Italian National Agency for New Technologies,
Energy and Sustainable Economic Development

High Performance Computing on CRESCO infrastructure: research activities and results 2017

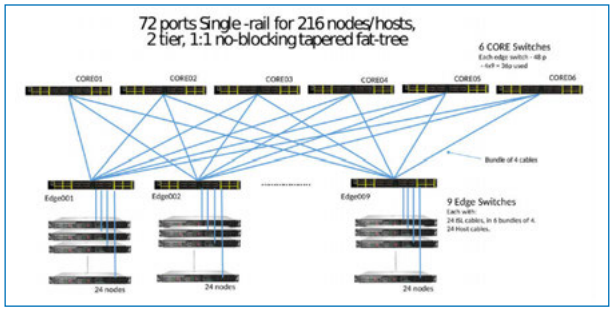

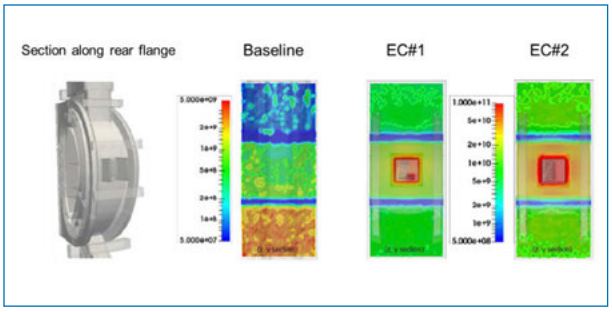

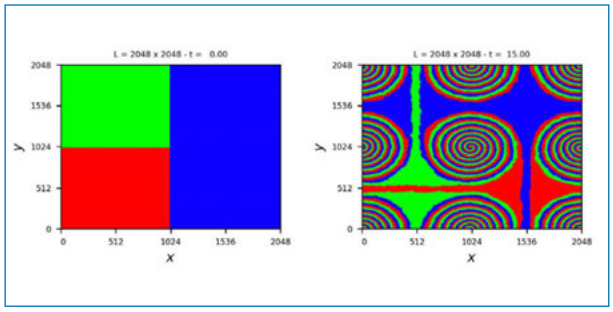

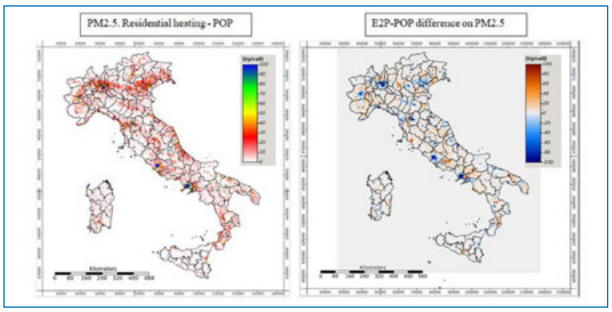

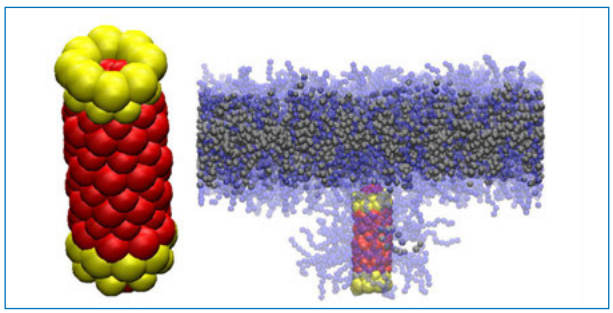

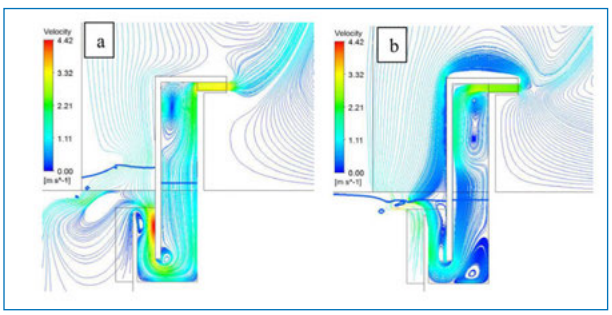

December 2017

High Performance Computing on CRESCO Infrastructure:
research activity and results 2017

Contributions provided by a selection of users of the CRESCO infrastructure

Scientific Editor: *Marcello Galli*, ENEA, DTE-ICT-HPC, Bologna Research Centre

Acknowledgements: We wish to thank *Gianclaudio Ferro* for providing the Reporter system (http://hdl.handle.net/10840/5791) to collect contributions and to build the Volume

Cover: *Amedeo Trolese*, ENEA, DTE-Rete, Frascati Research Centre

ISBN: 978-88-8286-373-9

Contents

Foreword

During the year 2017, the CRESCO high performance computing clusters have provided more than 30 millions hours of "core" computing time, at a high availability rate, to more than one hundred users, supporting ENEA research and development activities in many relevant scientific and technological domains. In the framework of joint programs with ENEA researchers and technologists, computational services have been provided also to academic and industrial communities.

This report, the ninth of a series started in 2008, is a collection of papers illustrating the main results obtained during 2017 using the CRESCO/ENEAGRID HPC facilities. The significant number of contributions proves the importance of the HPC facilities in ENEA for the research community. The topics cover various fields of research, such as materials science, efficient combustion, climate research, nuclear technology, plasma physics, biotechnology, aerospace, complex systems physics, renewable energies, environmental issues, HPC technology. The report shows the wide spectrum of applications of high performance computing, which has become an all-round enabling technology for science and engineering.

Since 2008, the main ENEA computational resources is located near Naples, in Portici Research Centre. This is a result of the CRESCO Project (Computational Centre for Research on Complex Systems), co-funded, in the framework of the 2001-2006 PON (European Regional Development Funds Program), by the Italian Ministry of Education, University and Research (MIUR).
The CRESCO Project provided the financial resources to set up the first HPC x86_64 Linux cluster in ENEA; a major computing installation for both the Italian and the International context: it ranked 126 in the HPC Top 500 June 2008 world list, with 17.1 Tflops and 2504 cpu cores. It was later decided to keep CRESCO as the name for all the Linux clusters in the ENEAGRID infrastructure, which integrates all ENEA scientific computing systems, and is currently distributed in six Italian sites. CRESCO computing resources were later upgraded in the framework of PON 2007-2013 with the project TEDAT and the cluster CRESCO4, 100 Tflops computing power. In 2017 the ENEAGRID computational resources consist of about 8000 computing cores (in production) and a raw data storage of about 1400 TB.

The success and the quality of the results produced by CRESCO stress the role that HPC facilities can play in supporting science and technology for all ENEA activities, national and international collaborations, and the ongoing renewal of the infrastructure provides the basis for an upkeep of this role in the forthcoming years.

In this context, 2015 is also marked by the signature of an agreement between ENEA and CINECA, the main HPC institution in Italy, to promote joint activities and projects. In this framework, CINECA and ENEA participated successfully to a selection launched by EUROfusion, the European Consortium for the Development of Fusion Energy, for the procurement of a several PFlops HPC system, beating the competition of 7 other institutions. The new system MARCONI-FUSION started operation in July 2016 at 1 Pflops computation power level which has been increased to 5 Pflops in the summer of 2017. The ENEA-CINECA agreement is a promising basis for the future development of ENEA HPC resources in the coming years. A new CRESCO6 cluster of 0.7 Pflops has been installed in 2018.

Dipartimento Tecnologie Energetiche,
Divisione per lo Sviluppo Sistemi per l'Informatica e l'ICT - CRESCO Team

SENSITIVITY OF STOMATAL CONDUCTANCE TO SOIL MOISTURE: IMPLICATIONS FOR TROPOSPHERIC OZONE

Alessandro Anav[1*], Alessandra De Marco[2]

[1] *Institute of Sustainable Plant Protection, National Research Council , Sesto Fiorentino, Italy*[1]

[2] *Italian National Agency for New Technologies, Energy and the Environment (ENEA), Italy*

ABSTRACT. Soil moisture and water stress play a pivotal role in regulating stomatal behaviour of plants; however, in the last decade, the role of water availability was often neglected in atmospheric chemistry modelling studies as well as in integrated risk assessments, despite through stomata plants remove a large amount of atmospheric compounds from the lower troposphere.
The main aim of this study is to evaluate, within the chemistry transport model CHIMERE, the effect of soil water limitation on stomatal conductance and assess the resulting changes in atmospheric chemistry testing various hypotheses of water uptake by plants in the rooting zone.
Results highlight how dry deposition significantly declines when soil moisture is used to regulate the stomatal opening, mainly in the semi-arid environments: in particular, over Europe the amount of ozone removed by dry deposition in one year without considering any soil water limitation to stomatal conductance is about 8.5 TgO_3, while using a dynamic layer that ensures plants to maximize the water uptake from soil, we found a reduction of about 10% in the amount of ozone removed by dry deposition (~7.7 TgO_3).

1 Introduction

Plant-level water cycling and exchange of air pollutants between atmosphere and vegetation are intimately coupled, thus any factor affecting root water absorption by plants is expected to impact the concentration of gases in the lower troposphere by changing deposition rates. A major part of dry deposition to vegetation is regulated by stomata opening which strongly depends on the amount of water available in the soil. Therefore a proper quantification of soil water content as well as a proper understanding of stomatal response to soil moisture are required for correctly quantifying the concentration of gases in the atmosphere.
In this study, we improve the dry deposition scheme within the chemistry transport model CHIMERE considering the effect of soil water limitation to stomatal conductance. Our main aim was to perform several different simulations testing various hypotheses of water uptake by plants at different soil depths in the rooting zone, based on the main assumption that roots maximize water uptake to fulfill resource requirements adsorbing water at different depths depending on the water availability.

[1] Corresponding author. E-mail: alessandro.anav@ipsp.cnr.it

2 Setup

CHIMERE (v2014b) is an Eulerian chemistry transport model model developed to simulate gas-phase chemistry, aerosol formation, transport and deposition at regional scale [1].
The gas-phase chemical mechanism used by CHIMERE is MELCHIOR2, which consists of 40 chemical species and 120 reactions. Meteorological forcing required by CHIMERE to calculate the atmospheric concentrations of gas-phase and aerosol species are provided by WRF (v3.6). For each soil layer WRF calculates the volumetric soil water content (θ) from the mass conservation law and the diffusivity form of Richards' equation:

$$\frac{\partial \theta}{\partial t} = \frac{\partial \theta}{\partial z}\left(D \frac{\partial \theta}{\partial z} \right) + \frac{\partial K}{\partial z} + F_\theta \qquad (1)$$

where D is the soil water diffusivity, K is the hydraulic conductivity, Fθ represents additional sinks and sources of water (i.e., precipitation, evaporation and runoff), t is time and z is the soil layer depth.
In our configuration the soil has a vertical profile with a total depth of 2 m below the surface and it is partitioned into four layers with thicknesses of 10, 30, 60, and 100 cm (giving a total of 2 m). The root zone is fixed at 100 cm (i.e. including the top three soil layers). Thus, the lower 100 cm of soil layer acts as a reservoir with gravity drainage at the bottom.
In order to have a large latitudinal gradient and assess the role of soil moisture across different climatic zones, we selected a domain extending over all Europe (except Iceland). Considering WRF we performed a simulation for the whole year 2011, with a spin up of 2 months to initialize all the fields, while we performed five different simulations with CHIMERE testing various hypotheses: 1) no soil moisture limitation to stomatal conductance (henceforth NO_SWC), 2) soil moisture from first soil layer (i.e. 0-10 cm depth, henceforth SWC_10cm), 3) soil moisture from middle soil (i.e., 10-40 cm depth, henceforth SWC_40cm), 4) soil moisture from the deeper soil layer of rooting zone (i.e., 0.4-1 m depth, henceforth SWC_1m) and 5) a dynamic layer (henceforth SWC_DYN) supporting the hypothesis that plants adsorb water at the depth with the higher water content availability.
Both WRF and CHIMERE have been compiled with the intel compiler and ran over CRESCO4 using 144 CPUs; the domain decomposition has been achieved with MPI.

3 Main results

The inclusion of soil water limitation in the stomatal conductance parameterization affects, at first, the surface resistance, that, in turn, affects the dry deposition velocity and thus the amount of air pollutants removed from the surface layer by dry deposition. Fig. 2 shows the mean percentage of change in O_3 dry deposition during the periods April-May-June (AMJ) and July-August-September (JAS) between the reference simulation (i.e. NO_SWC) and the simulations that take into account the soil moisture limitation to stomatal conductance. As the inclusion of soil water stress leads to a reduction of stomatal conductance, the amount of O_3 removed by dry deposition is always larger in the NO_SWC simulation than in the other simulations; this explains the negative pattern in the percentage of change in O_3 dry deposition in both the analyzed seasons. Looking at the spatial pattern (Fig. 2), we find the weaker differences in Norway, where soil moisture is barely limiting the stomatal conductance, while the larger differences occur in the Mediterranean basin (i.e. Spain, South France, Italy, Greece and Turkey). In fact, in these semi-arid regions the soil dries out quickly, especially during summer, and plants close their stomata during the warmer hours of the day to

prevent water loss, leading to a smaller amount of O_3 entering the leaves and thus removed by vegetation. This process is well displayed during JAS in the SWC_10cm simulation and to a lesser extent in the SWC_40cm, SWC_1m and SWC_DYN simulations: specifically, in Southern Europe the upper soil layer (i.e. 10 cm) dries out faster than the deeper ones during the warm and dry season, consequently, in the SWC_10cm simulation we find the stronger limitation of soil moisture to stomatal conductance and the highest reduction in O_3 dry deposition. In the other simulations we use a deeper rooting zone where plants can uptake water from the soil; during summer these layers are generally moister than the shallow layer, thus the stomatal conductance will be less limited by soil moisture and consequently the vegetation removes a larger amount of O_3 [2].

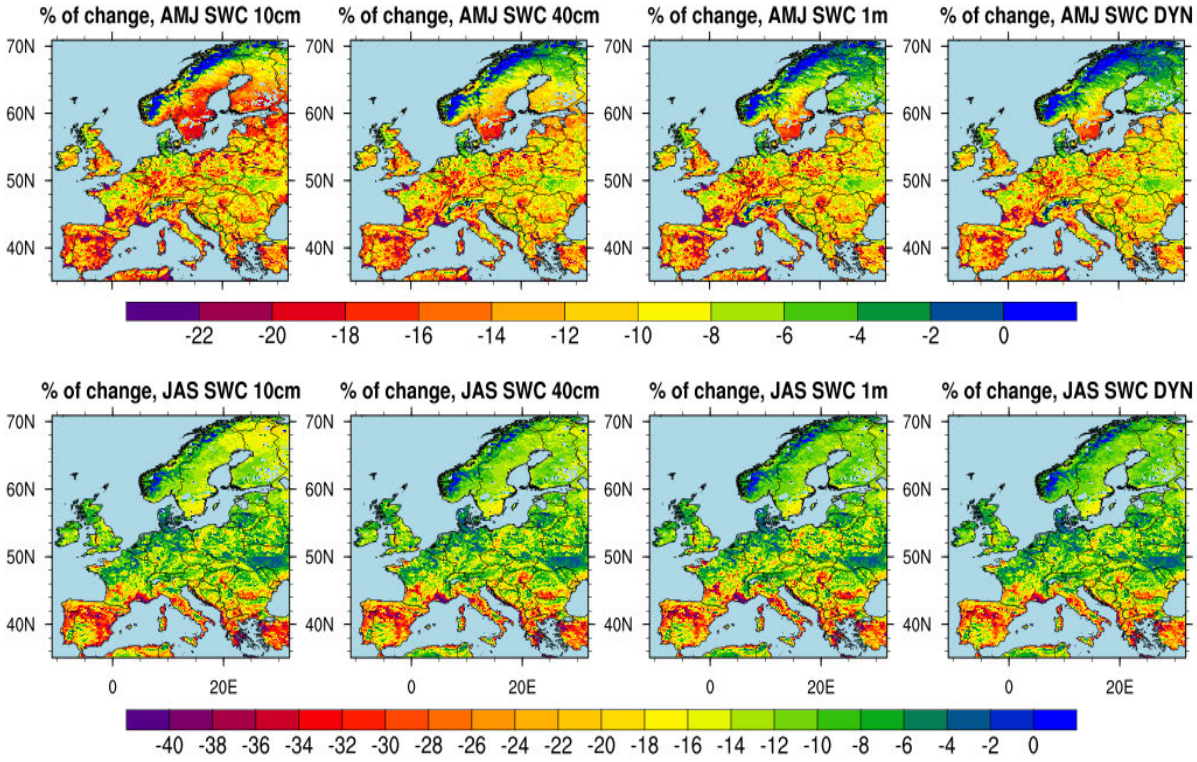

Fig.**1**: Percentage of change in the amount of O_3 removed by dry deposition over the land points (sea points are masked) computed in the time periods April-May-June (AMJ) and July-August-September (JAS). The percentage of change is defined as: [(Sim–Ref) /Ref)]*100, where Ref is the *NO_SWC* simulation and Sim represents the other simulations.

References

[1] L. Menut, et al. CHIMERE 2013: a model for regional atmospheric composition modeling. *Geoscientific Model Development* **6**, pp. 981-1028, (2014).

[2] A. Anav, et al. Sensitivity of stomatal conductance to soil moisture: implications for tropospheric ozone, *Atmospheric Chemistry and Physics* **18**, pp. 5747-5763, (2018).

DETECTION OF TDNA INSERTIONS IN *Chlamydomonas reinhardtii* AFTER TRANSFORMATION MEDIATED BY *Agrobacterium* AND ELECTROPORATION

Paola Mini[1], Olivia Costantina Demurtas[1], Silvia Valentini[1,2], Patrizia Pallara[1], Giuseppe Aprea[1]*, Paola Ferrante[1], and Giovanni Giuliano[1]

[1]*Italian National Agency for New Technologies, Energy and Sustainable Development (ENEA) Casaccia Research Center, Via Anguillarese 301, 00123 Roma, Italy.*

[2]*University of Rome "La Sapienza", Piazzale Aldo Moro, 5, 00185 Rome, Italy.*

ABSTRACT. In this report we briefly describe a comparative study of *Agrobacterium* and electroporation mediated transformation of *Chlamydomonas reinhardtii*.

1 Background

Chlamydomonas reinhardtii is a single-cell green alga which is widely used for functional genomics studies as well as for heterologous protein production. Anyway, despite recent advances in genetic engineering, the expression of foreign genes in the nuclear genome of wild-type *Chlamydomonas* remains challenging due to transgene rearrangement and silencing (*1–3*).

Agrobacterium tumefaciens is a pathogenic soil bacterium that has evolved the capacity to transfer a segment of DNA (TDNA) from the tumor-inducing plasmid into the nucleus of a plant cell. This ability is used in plant biology to transfer a gene of interest in plants. An advantage in using *Agrobacterium* for plant transformation is the reduction in transgene copy number, DNA rearrangements and transgene silencing (*4*, *5*).

Hence the opportunity to use *Agrobacterium* to transform *Chlamydomonas reinhardtii* looks appealing.

A transformation of *Chlamydomonas reinhardtii* by *Agrobacterium tumefaciens* has been reported in (*6*). The authors of this work claimed a transformation efficiency 50-fold higher than that obtained with the glass beads method. Further improvements of the transformation efficiency are described in a second paper (*7*). No data on the stability of expression over time of the reporter gene were shown in either case.

Our study aims to assess efficiency in *Chlamydomonas reinhardtii* transformation mediated by *Agrobacterium tumefaciens* in comparison with electroporation.

*Corresponding author. E-mail: giuseppe.aprea@gmail.com.

2 Sample preparation

We set up the pAgroLucR vector, optimized for *Agrobacterium*mediated *Chlamydomonas* transformation. This vector harbors the Paro gene, conferring paromomycin resistance and, and a reporter gene (luciferase, Luc). The vector was used to transform *Chlamydomonas* cw15 strain by electroporation and *Agrobacterium*.

Agrobacterium mediated transformation efficiency was 2.5 to 60 fold lower with respect to electroporation using the same plasmid. Also, while 100% of electroporated Paro resistant colonies tested are positive for the presence of the Paro gene in the PCR assay, only 65% to 97% of colonies obtained after *Agrobacterium* infection did so, indicating a high percentage of false positive transformants.

After that, the maintenance of the Luc transgene was assessed in the Paro-positive transformants. The results indicate that only 13%–16% of Paro resistant colonies obtained through *Agrobacterium* transformation carry a complete Luc gene, compared to the 26%–33% obtained through electroporation with the same vector. Thus, in contrast with the results obtained in higher plants, *Agrobacterium*-mediated transformation of *Chlamydomonas* does not reduce, compared to electroporation, the rearrangement of transgenes.

3 Insertions detection

In order to identify the insertion points in *Chlamydomonas* cw15 strain transformants obtained with the 2 different methods, we performed whole genomic sequencing of twenty transformants, ten obtained by *Agrobacterium* and 10 by electroporation using the pAgroLucR plasmid.

From each sample DNA, about 8 millions paired-end reads where obtained on average. Reads were cleaned of adapters and quality trimmed with Cutadapt (*8*) and Trimmomatic (*9*). A composite reference was prepared by combining *Chlamydomonas* genome v. 5.5 (*10*) and the pAgroLucR vector sequence. All libraries were aligned to the reference using Bowtie2 (*11*) as single ends, to avoid any bias due to pairing in the alignment results. In order to isolate the insertion signals, only pairs with a hit both on the alga genome and the vector were retained. Finally, for each transformed sample, all signals were compared to the wild type and insertion points were called with MACS2 (*12*).

Most of the insertions occurred in genes (5' and 3' UTR and exons) with only a minority occurring in intergenic regions. One *Agrobacterium* and three electroporation transformants carried insertions in multiple chromosomal regions.

4 Conclusions

In the present work we compared *Agrobacterium* mediated transformation and electroporation of *Chlamydomonas* in order to verify if the former method can reduce some problems of the latter such as the low levels of expression and the rearrangements of the transforming DNA. Our data show higher efficiency in electroporation mediated transformation for the Paro gene which undergoes selective pressure. Moreover, electroporation transformants perform better also as for the rearrangements of the Luc gene, which is not under selective pressure. All that is only partially compensated by the reduced Luc silencing in *Agrobacterium* transformants. Thus, differently from what observed in plants, *Agrobac-*

terium-mediated transformation does not present significant advantages in terms of higher or more stable expression. For further details, please refer to (*13*).

5 Acknowledgements

Part of the computing resources and the related technical support used for this work have been kindly provided by CRESCO/ENEAGRID High Performance Computing infrastructure and its staff (*14*). This work was supported by the Italian Ministry of Agriculture, Hydrobio project.

References

1. R. Barahimipour *et al.*, *Plant Molecular Biology*, ISSN: 15735028, DOI: 10.1007/s11103-015-0425-8 (2016).
2. E. Specht *et al.*, *Micro-algae come of age as a platform for recombinant protein production*, 2010, DOI: 10.1007/s10529-010-0326-5.
3. J. Neupert *et al.*, *Methods in molecular biology (Clifton, N.J.)* ISSN: 1940-6029, DOI: 10.1007/978-1-61779-558-9_4 (2012).
4. D. Valvekens *et al.*, *Proceedings of the National Academy of Sciences*, ISSN: 0027-8424, DOI: 10.1073/pnas.85.15.5536 (1988).
5. S. Dai *et al.*, *Molecular Breeding*, ISSN: 13803743, DOI: 10.1023/A:1009687511633, arXiv: arXiv:1011.1669v3 (2001).
6. S. V. Kumar *et al.*, *Plant Science*, ISSN: 01689452, DOI: 10.1016/j.plantsci.2003.11.012 (2004).
7. P. T. Pratheesh *et al.*, *Molecular Biotechnology*, ISSN: 15590305, DOI: 10.1007/s12033-013-9720-2 (2014).
8. F Krueger, *[http://www.bioinformatics.babraham.ac.uk/projects/trim galore/]*, DOI: http://www.bioinformatics.babraham.ac.uk/projects/trimgalore/ (2012).
9. A. M. Bolger *et al.*, *Bioinformatics* **30**, 2114–2120 (2014).
10. S. Merchant, *Science*, ISSN: 0036-8075, DOI: 10.1126/science.1143609 (2007).
11. B. Langmead *et al.*, *Nature methods* **9**, 357–359 (2012).
12. Y. Zhang *et al.*, *Genome Biology*, ISSN: 1465-6906, DOI: 10.1186/gb-2008-9-9-r137 (2008).
13. P. Mini *et al.*, *BMC Biotechnology*, ISSN: 14726750, DOI: 10.1186/s12896-018-0416-3 (2018).
14. G. Ponti *et al.*, presented at the Proceedings of the 2014 International Conference on High Performance Computing and Simulation, HPCS 2014, ISBN: 9781479953127, DOI: 10.1109/HPCSim.2014.6903807.

Ab initio optical properties study of metal decorated tetramerized pyridinic graphene

Francesco Buonocore[1]*, Nicola Lisi[1], and Olivia Pulci[2]

[1] *ENEA, Casaccia Research Centre, via Anguillarese 301, I-00123 S.Maria di Galeria, Rome, Italy*

[2] *Department of Physics, and INFN, University of Rome Tor Vergata, Via della Ricerca Scientifica 1, I-00133 Rome, Italy*

Abstract. We used QUANTUM ESPRESSO package installed on the high performance computer facility CRESCO to perform a first principles study of the stability, and of the electronic and optical properties of graphene with nitrogen doped vacancies. Moreover, we investigated the modifications induced by the chemisorption of Mg simple metal and Zn, Pd and Pt transition metals. We found that the metal decoration of the defects produces semi-metallic systems for any studied size of the cell and new sharp peaks appear in the optical conductivity in the visible range, thus strongly enhancing the optical response of graphene.

1 Introduction

Graphene is a semimetal and its broad band optical absorption is dominated by a 4.5 eV peak. Several experiments [1, 2, 3, 4] have shown that graphene, athough its single atom thickness, can efficiently absorb photons ranging from the visible to the infrared. Moreover, electrons can move into its lattice with the highest mobility. This makes light harvesting a possible field of application [5] for plenty of novel molecular configurations, where the energy of the radiation is transfered to the excited electron to and from molecular networks attached to the plane. Moreover, saturable absorption behavior was found to occur in graphene over a wide energy range of the incident photons. This property opened the way to nonlinear optics or optical limiting applications, such as Q-switched or mode-locked lasers [6, 7]. We considered the possibility to tune the optical properties of graphene by simultaneous: 1) carbon vacancy creation; 2) nitrogen doping and 3) metal decoration of pyridine-type vacancy defects used as anchoring sites. We investigated by first principles calculations the electronic and optical properties of graphene with tetramerized pyridinic defects (TPDs) as alone and modified by the chemisorption of Mg simple metal and Zn, Pd and Pt transition metals. A TPD is formed when a carbon dimer vacancy (di-vacancy) is created and each of the four carbon atoms two-fold coordinated left are substituted by nitrogen atom. Different concentrations of pyridinic defects are considered, ranging from 6.5×10^{13} to 1.8×10^{14} cm^{-2}.

*Corresponding author. E-mail: francesco.buonocore@enea.it.

2 Theoretical Methods

The equilibrium geometry, electronic band structure and optical properties were calculated within Density Functional Theory (DFT). The computational approach was based on a pseudo-potential plane-wave method using PWSCF code as implemented in the QUANTUM-ESPRESSO package [8], compiled with Intel Fortran compiler, Math Kernel Library (MKL) and Message Passing Interface (MPI) parallelization on the Cresco4 cluster of the high performance computer facility CRESCO [9], with a good scalability up to hundreds of cores. We used the generalized gradient approximation (GGA) with the Perdew, Burke and Ernzerhof (PBE) exchange-correlation functional [10]. We used for the 3×3 unit cell systems also the more computationally expensive screened hybrid functional of Heyd, Scuseria, and Ernzerhof (HSE) [11], which mixes the HartreeFock (HF) exchange with the GGA exchange and correlation in the short-range portion of the potential. Indeed, the HSE hybrid functional has been demonstrated to successfully predict the electronic properties of graphene derivatives [12]. We have verified that the results did not change taking into account spin-orbit and dispersion forces effects. The pseudo-potential plane-wave calculations were performed using Martins-Troullier norm-conserving pseudo-potentials [13]. All geometry optimizations were performed with cut-off for the wave functions of 80 Ry and 6×6×1 k-points Monkhorst-Pack grid. The systems were fully relaxed with a convergence threshold of 0.001 Ry/Å on the inter-atomic forces. Each unit cell was optimized by imposing that the stress on the cell is less than 0.04 GPa. The convergence of the total energy was better than 0.001 eV/atom. We created PDs in different supercells of graphene, as shown in Figure 1: we used the 3×3, 4×4 and 5×5 unit cell of the graphene which contained 18, 32 and 50 C atoms, respectively. In the graphene with TPD one di-vacancy was created by removing two C atoms (one carbon dimer) and substituting four C atoms with N atoms. The vacuum between each monolayer and its image was set to 20 Å. The optical conductivity was calculated with 72×72×1, 60×60×1 and 32×32×1 Monkhorst-Pack k-points grid for 3×3, 4×4 and 5×5 unit cell, respectively.

3 Results and conclusions

We modeled TPD in different supercells of graphene in such a way to investigate the dependence of electronic and optical properties on defects density. The band structure of graphene with TPD in 4×4 unit cell is shown in Figure 2a). TPD induced strong hybridization of nitrogen and carbon p-orbitals that modified the pristine electronic structure of graphene. Low dispersion bands associated to nitrogen p-orbitals have been found 1.2, 0.4 and 0.3 eV below the Fermi energy in the 3×3, 4×4 and 5×5 unit cells of graphene with TPD, respectively. The unoccupied bands showed mainly contributions from the carbon p-orbitals. The 3×3 and 4×4 unit cells are metallic, but decreasing the density of defects to the 5×5 unit cell the distinguishing semi-metal feature of graphene is recovered. Due to the presence of TPD defects, the symmetry of ideal graphene is broken and the energy levels are not the same in the inequivalent corner points K and K' and middle points M and M' of the Brillouin zone. The Dirac cone of graphene is severely distorted and moves away from the K point. We analyzed the in-plane optical conductivity focusing our attention into the main peaks in the visible energy range. The optical conductivity for the 4×4 unit cell, compared to that of perfect graphene, is shown in Figure 3a). We found broad peaks around 2.7, 2.8 and 2.45 eV for the 3×3, 4×4 and 5×5 unit cells and identified the electronic transition with the strongest contribution to the optical adsorption. The occupied states near the Fermi energy are associated to N atoms of graphene with TPD and do not give rise to any relevant adsorption in the visible energy range.

Considering the formation of the metal complex, we found that Zn, Pd and Pt complexes have comparable formation energy, while the Mg-decorated TPD graphene is the most stable complex. Pt is found to bind stronger than the other metals, while Zn forms the less strong bonds. The comparison with the

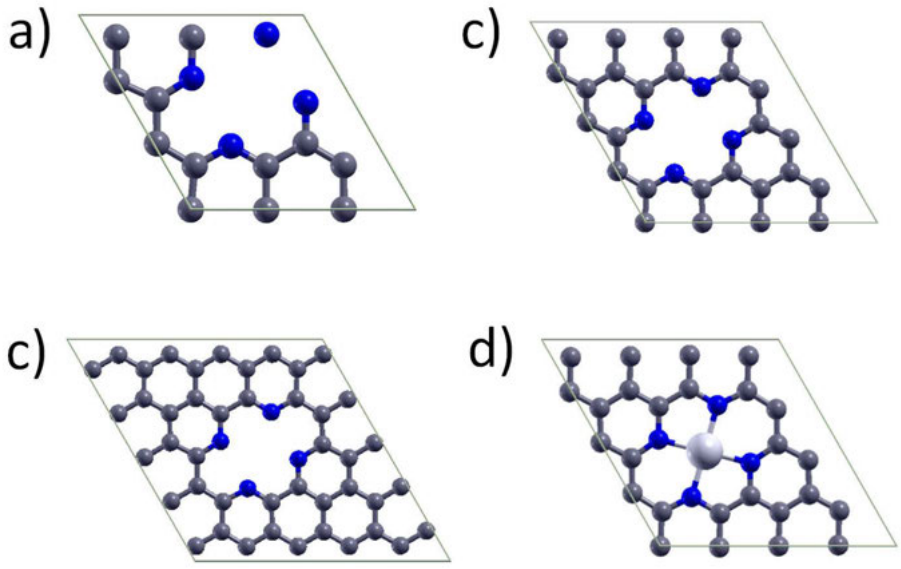

Figure 1: Atomistic models of graphene with tetramerized pyridine-type defect. a) 3×3, unit cell b) 4×4 unit cell, c) 5×5 unit cell, d) 4×4 unit cell of the metal decorated system. Gray, blue and light gray spheres are carbon, nitrogen and metal atoms, respectively.

cohesive energy of the corresponding bulk metal evidences the tendency to form complex rather than metal clusters.
TPD after metal decoration is semi-metallic, so that the peculiar electronic properties of Dirac fermions in graphene are kept. The band structures are reported in Figures 2b-d). The band structure for Pd-decorated TPD is not not shown here, but it is similar to that of the Pt-decorated system. The metal decoration quenches the bands associated to the nitrogen p-orbitals thanks to the passivation of nitrogen lone-pairs. The Fermi energy of Mg-, Zn-, Pd- and Pt-decorated graphene with TPD shift upwards until to cross the Dirac point in the proximity of the K' high symmetry point. The Dirac points are asymmetric, so that the Fermi velocities of the two linear branches are anisotropic. In the 4×4 unit cell the Fermi velocity can change until to 53% and 105% of graphene Fermi velocity. For Pt-decorated TPD we found that by increasing or decreasing the density of defects the Fermi velocity increases or decreases, respectively. The bands associated to Mg, Zn, Pd and Pt in the 4×4 unit cell are around -3.0, -1.3, -1.8 and -1.85 eV below Fermi energy, respectively. We found that the intensity of the metal contributions to the total DOS increases with the atomic number. The negative electron charge is moved from the metal atoms towards N and C atoms, so that after metal-decoration the pristine structure of graphene with TPD is enriched by electrons.

We found that a secondary energy gap exists for all of the metal-decorated TPDs investigated, with values ranging from 0.42 (Mg) to 0.49 (Pt) eV in the 4×4 unit cell and from 0.29 (Mg) to 0.54 (Pt) eV in the 3×3 unit cell, and tending to change from indirect to direct by increasing the atomic number. We found that the secondary gap of Pt-decorated TPD changes from indirect to direct moving from the 5×5 to the 3×3 unit cell, i.e., by increasing the density of defects. However, the Pd- and Pt-decorated TPD the value of the secondary energy gap has little dependence on the size of the unit cell. Besides the PBE exchange-correlation functional, we used the more computationally expensive HSE hybrid functional for

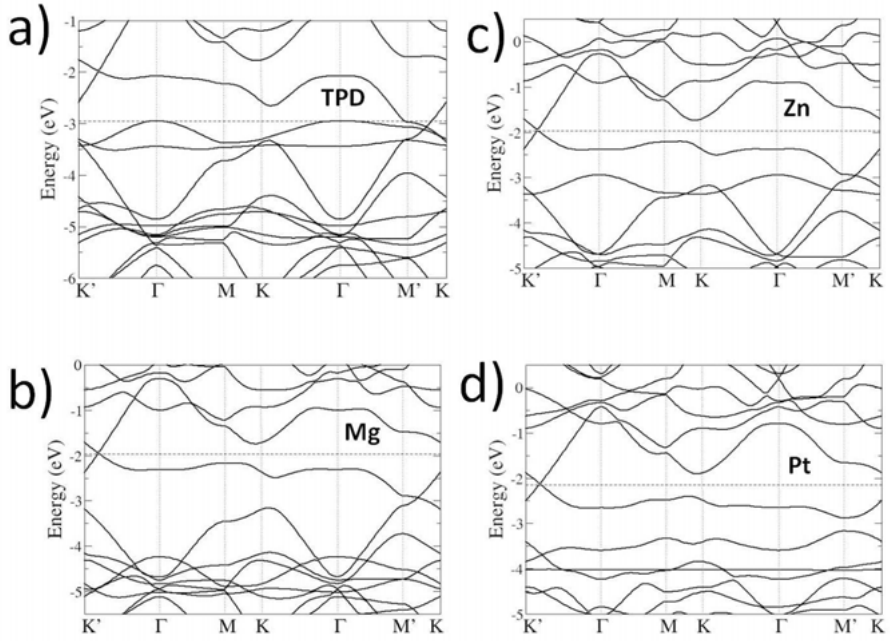

Figure 2: Band structures of a) isolated, b) Mg-, c) Zn- and d) Pt-decorated graphene with tetramerized pyridine-type defect 4×4 unit cell. The dotted horizontal line indicates the Fermi energy.

the 3×3 unit cell that has good performance in the evaluation of electronic and optical properties for graphene derivatives. The corrections to the PBE secondary energy gaps are in the range of 0.2-0.3 eV increase.

The main peaks in the visible range of the optical conductivity for Mg-, Zn-, Pd- and Pt-decorated TPD 4×4 (3×3) unit cell, shown in Figures 3b-c), are at 2.40, 2.44, 2.35, and 2.41 (2.15, 2.20, 2.17 and 2.21) eV, respectively. Metal-decoration introduces sharp features in the visible optical range absents both in ideal graphene and in graphene with TPD. Our calculations using the HSE hybrid funtional showed that the PBE optical underestimates optical transitions, at least for the 3×3 unit cell, of 0.6-0.65 eV. The optical transitions starting from the low dispersion band associated to Mg simple metal, lying at very low energy, are out of the visible range. On the other hand, we found optical transitions in the visible range and near the optical absorption peaks starting from the low dispersion band localized on Zn, Pd and Pt transition metals. From the analysis of the matrix elements associated to the optical transitions of 4×4 unit cell, the transition near M' high symmetry Brillouin zone point has been found to be the strongest among all of the viable electronic transitions and the optical transition associated to Pd and Pt localized states is nearby. The intensity and the position the main peak in the visible range, found at at 2.4 eV for 4×4 unit cell, is quite independent on the particular metal forming the complex, which plays the role of enhancing matrix element of the electronic transitions with that energy because of the hybridization of metal orbitals with C and N p-states. For Pt-decorated TPD the strongest optical transition is at Γ and the optical transition associated to Pt is nearby in the 5×5 unit cell while it is at M and the optical transition associated to metal is along $\Gamma - M'$ path in the 3×3 unit cell.

In conclusion, we investigated by first principles calculations the electronic and optical properties of graphene with TPDs as alone and modified by the chemisorption of Mg simple metal and Zn, Pd and Pt transition metals. We have demonstrated that it is possible to tune the optical properties of nitrogen doped graphene by metal decoration of vacancy defects used as anchoring sites. Our study suggests that this functionalized graphene derivative can be used in light harvesting and Q-switched or mode-locked

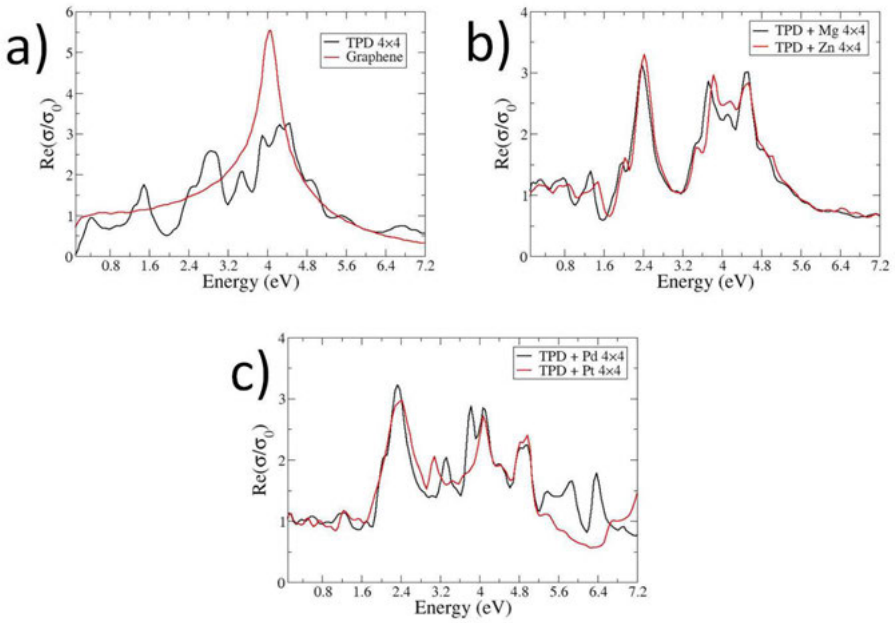

Figure 3: Real part of optical conductivity of a) pristine graphene and graphene with isolated tetramerized pyridine-type defect; b) Mg- and Zn-decorated as well as c) Pd- and Pt-decorated graphene with tetramerized pyridine-type defect (TPD) for 4×4 unit cell.

laser applications.

References

[1] R. R. Nair, P. Blake, A. N. Grigorenko, K. S. Novoselov, T. J. Booth, T. Stauber, N. M. R. Peres, and A. K. Geim. Fine structure constant defines visual transparency of graphene. *Science*, 320(5881):1308, 2008.

[2] F. Bonaccorso, Z. Sun, T. Hasan, and A. C. Ferrari. Graphene photonics and optoelectronics. *Nature Photonics*, 4:611, 2010.

[3] A. R. Wright, X. G. Xu, J. C. Cao, and C. Zhang. Strong nonlinear optical response of graphene in the terahertz regime. *Appl. Phys. Lett.*, 95:072101, 2009.

[4] F. Zhang, S. Han, Y. Liu, Z. P. Wang, and X. G. Xu. Dependence of the saturable absorption of graphene upon excitation photon energy. *Appl. Phys. Lett.*, 106:091102, 2015.

[5] K. J. Tielrooij, J. C. W. Song, S. A. Jensen, A. Centeno, A. Pesquera, A. Zurutuza Elorza, M. Bonn, L. S. Levitov, and F. H. L. Koppens. Photoexcitation cascade and multiple hot-carrier generation in graphene. *Nat. Phys.*, 9:248, 2013.

[6] Q. L. Bao, H. Zhang, Y. Wang, Z. H. Ni, Y. L. Yan, Z. X. Shen, K. P. Loh, and D. Y. Tang. Atomic-layer graphene as a saturable absorber for ultrafast pulsed lasers. *Adv. Funct. Mater.*, 19:3077, 2009.

[7] J. Ma, G. Q. Xie, P. Lv, W. Gao, P. Yuan, L. Qian, U. Griebner, V. Petrov, H. Yu, H. Zhang, and J. Wang. Wavelength-versatile graphene-gold film saturable absorber mirror for ultra-broadband mode-locking of bulk lasers. *Sci. Rep.*, 4:5016, 2014.

[8] P. Giannozzi, S. Baroni, N. Bonini, M. Calandra, R. Car, C. Cavazzoni, D. Ceresoli, G. L. Chiarotti, M. Cococcioni, I. Dabo, and et al. Quantum espresso: a modular and open-source software project for quantum simulations of materials. *J. Phys. Condens. Matter*, 21(39):395502, 2009.

[9] G. Ponti, F. Palombi, D. Abate, F. Ambrosino, G. Aprea, T. Bastianelli, F. Beone, R. Bertini, G. Bracco, M. Caporicci, and et al. The role of medium size facilities in the hpc ecosystem: the case of the new cresco4 cluster integrated in the eneagrid infrastructure. *IEEE HPCS*, 1030:6903807, 2014.

[10] J. P. Perdew, K. Burke, and M. Ernzerhof. Generalized gradient approximation made simple. *Phys. Rev. Lett.*, 77(18):3865, 1996.

[11] Jochen Heyd, Gustavo E. Scuseria, and Matthias Ernzerhof. Hybrid functionals based on a screened coulomb potential. *J. Chem. Phys.*, 118(18):8207–8215, 2003.

[12] Veronica Barone, Oded Hod, Juan E. Peralta, and Gustavo E. Scuseria. Accurate prediction of the electronic properties of low-dimensional graphene derivatives using a screened hybrid density functional. *Acc. Chem. Res.*, 44(4):269–279, 2011.

[13] Norman Troullier and José Luís Martins. Efficient pseudopotentials for plane-wave calculations. *Phys. Rev. B*, 43(3):1993, 1991.

SPATIAL DISAGGREGATION OF RESIDENTIAL WOOD COMBUSTION EMISSIONS USING DIFFERENT PROXY AND INVENTORY NUTS: SENSITIVITY STUDY

Mario Adani[2], Gino Briganti[1], Andrea Cappelletti[1], Luisella Ciancarella[2], Ilaria D'Elia[3], Massimo D'Isidoro[2], Mihaela Mircea[2], Antonio Piersanti[2]

[1] *ENEA - National Agency for New Technologies, Energy and Sustainable Economic Development, Pisa, Italy*

[2] *ENEA - National Agency for New Technologies, Energy and Sustainable Economic Development, Bologna, Italy*

[3] *ENEA - National Agency for New Technologies, Energy and Sustainable Economic Development, Rome, Italy*

ABSTRACT. This studyshows the impact of two different approaches for disaggregation of primary PM emitted by wood fuel combustion on the spatial distributions on particulate matter concentrations (PM)..

1 Introduction

The EU Directive 2008/50/EC promotes modelling techniques for assessing spatial distribution of the air pollution. The air quality (AQ) models are essential tools for developing emissions control plans needed to improve air quality levels and to preserve both human health and ecosystems. These models incorporate advection/dispersion drivers coupled with complex gas and aerosol chemistry solvers, and, therefore, require a lot of computational resources; supercomputing architectures, etc., like CRESCO infrastructure developed in ENEA. Directive 2008/50/EC is implemented at national level by Legislative Decree 155/2010, which states that ENEA provides every five years, model simulations of air quality at national level, using the national emissions inventory scaled at a district basis provided by ISPRA (http://www.isprambiente.gov.it/en/publications/reports/italian-emission-inventory-1990-2015.-informative-inventory-report-2017?set_language=en). In order to simulate air quality over Italy with the AMS-MINNI modelling system [8,9] , ENEA disaggregate spatially the provincial-based emission inventory, by using several proxies according to SNAP activity classifications. Due to technological and population habits changes, due to new legislation implemented to fulfil the European and international agreements, ENEA is continuously working to produce realistic distributions of emissions which are a fundamental input of air quality modelling system AMS-MINNI. This paper presents the impact of two methods used to determine the spatial distribution of primary PM emissions produced by wood fuel combustion.

The first method traditionally used in previous air quality simulations, uses a proxy depending on population distribution (POP), while the second one assumes that wood-burners are typically for houses (buildings with maximum) two floors and, therefore, the proxy is the spatial distribution of both 1&2-floor buildings fabric (E2P). The simulations performed with this two gridded emissions are compared to measured data (BRACE observation database [1]) and the performances are measured by means of statistical indexes, like Pearson's correlations and fractional bias [2].

2 Modeling set-up

2.1 Emission Manager

The emission processor EMMA is a set of scripts, makefiles and fortran executables which reads the yearly species-aggregated emissions on a particular administrative units level (NUTS) from a national inventory database and then projects them on the 3D+T grid of the domain. EMMA module operates on ENEA GRID environment in multi-scalar mode.
Starting from 2017, the traditional MINNI grid setup, including the five 4x4km sub-national grid (North Italy, Centre Italy, South Italy, Sicily and Sardinia), have been replaced by a unique national 4x4 km grid, speeding up the setup of EMMA procedures but increasing the computational GRID computation time. The master domain Italy (IT) 20x20 km is used to provide the boundaries and initial conditions for National (IT) 4x4 km.

	TMP (20km)	IT (4km)
NX	67	278
NY	75	308
NZ	16	16
Total (NX*NY*NZ)	80400	1369984
Disk space (GB)	103	1700
Cpu time (h)	6	48

Table 1: EMMA - Characteristics of the computational domain, disk space and Cpu time.

2.2 Meteorology

Meteorological fields to force air quality simulations are produced by means of the non-hydrostatic mesoscale meteorological model RAMS [3]. Three dimensional fields of temperature, pressure, geopotential, wind components and divergence, as well as 2-dimensional fileds of total cloud fraction, orography, sea surface temperature and precipitation have been provided at hourly temporal resolution over the grids described in Table 1. Fields from the global analyses from ECMWF (European Centre for Medium range Weather Forecasts) have been used as boundary conditions to RAMS.
The meteorological simulations have been performed using the CRESCO storage and computing facilities. In particular, the required resources were 480 cores for about two weeks to accomplish the whole year 2015 over CRESCO4 cluster, whith a disk usage of approximately 2.5TB.

2.3 Air quality dispersion model.

The simulations were conducted with the AMS-MINNI which include the air quality model FARM (Flexible Regional Atmospheric Model) [3] [4], developed by ARIANET s.r.l. (http://www.aria-net.it/) in Fortran 77/90 language. FARM is a three-dimensional Eulerian grid model with K-type turbulence closure that accounts for the transport, chemical reactions and ground deposition of atmospheric pollutants. The version used is 4.11.0, with SAPRC99 gas phase chemical mechanism [5] and AERO3 aerosol model[6], supporting hybrid MPI-OpenMP parallelization [7].
Boundary/initial conditions were provided by the CAMS model (https://atmosphere.copernicus.eu/) for air pollutants such as ozone, PM, etc. and EMEP-MSCE for the heavy metals and POPs.

All the input/output data of AQ model were stored in the gporq1_minni file system. Table 2 summarizes disk space and CPU time.

	TMP (20km)	IT (4km)
Disk space per day of simulation (GB/day)	1.2	20.5
Cpu time per day of simulation (h/day)	247	

Table 2: FARM - Disk space and Cpu time.

3 Discussion

The combustion of wood fuel for residential heating is one of the main contributions to PM emissions. The inventory databse (ISPRA) provides the yearly total PM emission for this anthropogenic activity at NUTS=3 level (districts). The Emission Manager processes this data and projects the total emitted PM to the current grid resolution (4km) using a proxy landuse data. The choice of the proxy is very important to calculate a realistic primary PM distribution on grid. A preliminary sensitivity study has been performed to analyze the effect of different proxy for wood fuel residential heating PM emissions. The differences between POP and E2P spatial distribution of emissions are summarized in Table 3 and shown in Figure 1.

PROXY	Inventory NUTS	Max (t/y/cell)	CODE	Comments
Population (POP)	NUTS=3 (Districts)	680	POP	Non-realistic emission peaks in urban centres appear
Up to 2 floors buildings (E2P)	NUTS=2 (Regions) and ISTAT classification	451	E2P	The 2013 ISTAT study on wood fuel consumption in Italian families has been used to replace NUTS=3 ISPRA disaggregation. The urban peaks disappear and the mass is moved towards rural zones but some hot spots are still present.

Table 3: Spatial disaggregation methods: POP and E2P.

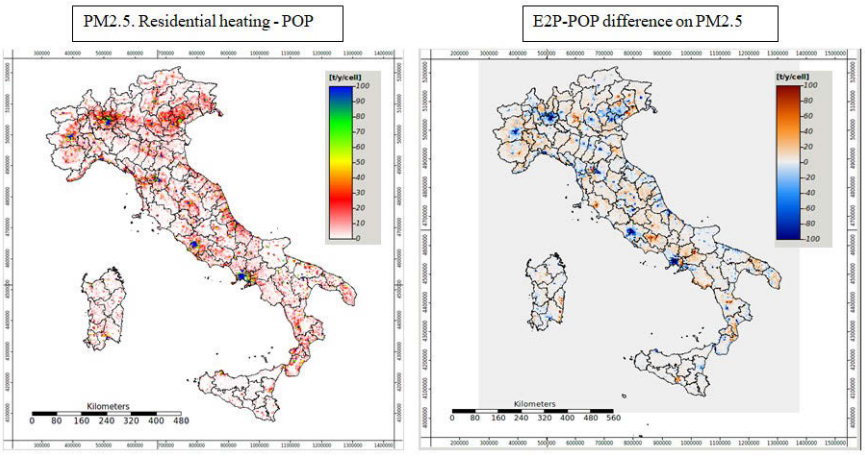

Figure 1: Distribution of PM2.5 emissions with POP (left) and difference between E2P and POP (right).

Statistical performance indexes (Figure 2) confirm the expected results seen from Figure 1, showing a significant decrement in absolute bias for E2P with respect to POP, in almost all the Lombardy stations. Pearson's correlation index shows just a slight decrease by using E2P, with respect to POP. Since the model resolution (4 km) is too coarse for resolving traffic stations dynamics only background stations have been considered.

Additional tests at lower resolutions (1 km) are in progress.

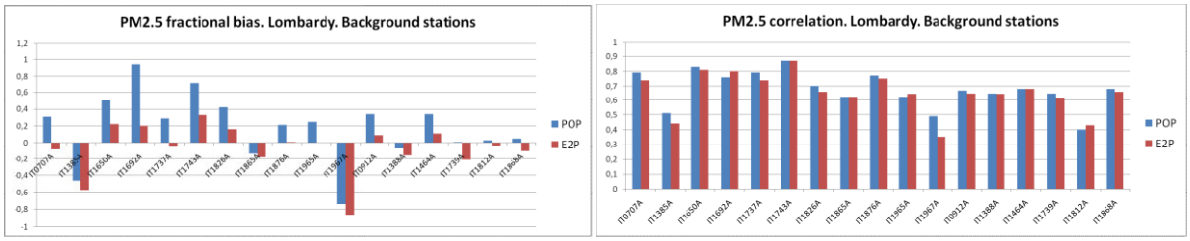

Figure 2: PM2.5 –simulations with POP and E2P approaches - performance measure for Lombardy background stations: annual fractional bias (left) and Pearson's correlation coefficient (right).

References

[1] http://www.brace.sinanet.apat.it/web/struttura.html

[2] "*Guidance on the use of models for the European Air Quality Directive A working document of the Forum for Air Quality Modelling in Europe*". FAIRMODE ETC/ACC report Version 6.2.

[3] Cotton, W. R., Pielke Sr., R. A., Walko, R. L., Liston, G. E., Tremback, C. J., Jiang, H., McAnelly, R. L., Harrington, J. Y., Nicholls, M. E., Carrio, G. G., McFadden, J. P., 2003. RAMS 2001: Current status and future directions. Meteorology and Atmospheric Physics, 82, 5-29, ISSN 0177-7971, http://dx.doi.org/10.1007/s00703-001-0584-9.

[4] Silibello C., Calori G., Brusasca G., Catenacci G., Finzi G. "*Application of a photochemical grid model to Milan metropolitan area"*. Atmospheric Environment **32** (11) (1998) pp. 2025-2038.

[5] Gariazzo C., Silibello C., Finardi S., Radice P., Piersanti A., Calori G., Cecinato A., Perrino C., Nusio F., Cagnoli M., Pelliccioni A., Gobbi,G.P., Di Filippo P. "*A gas/aerosol air pollutants study over the urban area of Rome using a comprehensive chemical tran sport model"*. Atmospheric Environment 41 (2007) pp. 7286-7303.

[6] Carter W.P.L. "*Documentation of the SAPRC-99 chemical mechanism for VOC reactivity assessment"*. Final report to California Air Resources Board, Contract no. 92-329, and (in part) 95-308, (2000).

[7] Binkowski F.S., Roselle S.J. "*Models-3 community multiscale air quality (CMAQ) model aerosol component- 1. Model description*". Journal of Geophysical Research 108 (2003) p. 4183, http://dx.doi.org/10.1029/2001JD001409, D6.

[8] Marras G., Silibello C., Calori G. "*A Hybrid Parallelization of Air Quality Model with MPI and OpenMP*". Recent Advances in the MPI: 19th European MPI Users Group Meeting, EuroMPI 2012, Vienna, Austria, September 23-26. Springer Berlin Heidelberg Editor.

Dynamics of poly(2-vinylpyridine) chains close to silica nanoparticles in nanocomposite system

S. Caputo[1]*, A. Pizzirusso[1], A. De Nicola[2], G.Munaò[1], G.Donati[1], Ying Zhao[3] and G. Milano[2]

[1] *Salerno University, Department of Chemistry and Biology "Adolfo Zambelli", 84084, Via Giovanni Paolo II, 132, Fisciano (SA), Italy*

[2] *Department of organic materials science, Yamagata University, 4-3-16, Jonan, Yonezawa, Yamagata-ken, 992-8510, Japan*

[3] *Institute of Nano-Photonics, School of Physics and Materials Engineering, Dalian Minzu University, Dalian 116600, China*

Abstract. We perform, for the first time, all atom molecular dynamics simulations of a polymer nanocomposite system made of a silica nanoparticle in a poly(2-vinylpyridine) melt. The aim is to obtain informations on the chain dynamics close to the nanoparticle, and far from it, by analysing the self-intermediate scattering function relaxation, calculated from atomistic trajectories.

1 Introduction

Interactions between polymers and nanoparticles can greatly influence physical-chemical properties of the resulting nanocomposite material respect to the pure polymers: one example is the glass transition temperature (Tg). It is known that strong polymer-nanoparticle interactions cause an increase in the Tg, while weak interactions tend to decrease it [1]: this is due to the difference in relaxation times between the polymer chains in the bulk and those close to the nanoparticle surface. However, in several cases, experiments show a negligible dependence of Tg on the interaction strength [2] . To clarify this conflicting situation, the experimental work needs to be supported by molecular simulations [1]; the latter show that the difference in relaxation times of the interfacial and bulk chains is not captured by the commonly employed Tg measurements. However, to the best of our knowledge, these simulations are based on generic bead-spring models, and therefore they are not easily comparable to real systems. Here we perform for the first time molecular dynamics atomistic simulations of a silica nanoparticle embedded in a poly(2-vinylpyridine) (P2VP) melt. This system has been chosen due to the extensive experimental probes reported [3]. By the analysis of the atomistic trajectories, we get information on the chain dynamics by means of the self-intermediate scattering function and other supplementary probes, such as gyration radius and end-to-end distances. Such informations should support the view that polymer chain dynamics in nanocomposites are heterogeneous and this has to be taken into account in the design of novel materials with tailored properties. We choose CRESCO supercomputing resources to perform simulations in accesible times.

*Corresponding author. E-mail: scaputo@unisa.it.

2 Models and simulation procedure

In the present work we perform all-atom molecular dynamics simulations of two polymeric systems, a poly(2-vinylpyridine) (P2VP) melt and a nanocomposite system including a silica nanoparticle embedded in the same polymer. Simulations have been carried out initially using the parallel version of the OCCAM MD code [4]. The main feature of this code is that the computation of pairwise nonbonded forces, which is the most demanding part of the calculation, is replaced by the interaction of particles with an external potential V(**r**) depending only on the local density (at a position **r**). Thus the molecular motion is reduced to the derivation of a partition function of a single molecule in an external field. The total nonbonded interaction energy of the system, in the field approximation, can be expressed in the following way:[5]

$$W[\{\phi(\mathbf{r})\}] = \int d\mathbf{r}(\frac{k_bT}{2}\sum_{KK'}\chi_{KK'}\phi_K(\mathbf{r})\phi_{K'}(\mathbf{r}) + \frac{1}{2\kappa}(\sum_K \phi_K(\mathbf{r}) - 1)^2) \qquad (\mathbf{1})$$

Where $\phi_K(\mathbf{r})$ is the density of species K at position r, $\chi_{KK'}$ are mean-field parameters for the interaction of a particle of type K with the density fields due to particles of type K, and κ is the compressibility. By using the so called saddle point approximation, the expression for the external potential can be derived from equation (1), giving:

$$V_K(\mathbf{r}) = \frac{\delta W[\{\phi_K(\mathbf{r})\}]}{\delta\phi_K(\mathbf{r})} = k_bT\sum_{K'}\chi_{KK'}\phi_{K'}(\mathbf{r}) + \frac{1}{\kappa}(\sum_K \phi_K(\mathbf{r}) - 1) \qquad (\mathbf{2})$$

For further details about the derivation and implementation of equation (2) the reader should refer to [6][7]
In this way we are able to equilibrate efficiently our polymeric systems, in that no atom superpositions are present. The structures thus generated can be used to run classical molecular dynamics, which in this case have been performed through the GROMACS package.[8]

3 Results and discussion

In a first instance we have simulated an all-atom poly(2-vinylpyridine) system in order to test if the proposed force-field parameters give the correct physical chemical properties. We have selected two different sets of parameters: the OPLS-AA force field[9] has been used to describe the pyridine groups, while for the aliphatic carbon and hydrogens parameters have been taken from a previous work[10]. First we generated a well-relaxed polymer system by using the OCCAM code[4], then classical MD simulation have been performed on this equilibrated configuration, first in NVT and then in NPT ensemble. All runs were carried out at the temperature of 293.15 K. The resulting calculated density is in agreement with the experimental one[11], within 3% error, thus validating the force field in use.

A similar procedure of equilibration and subsequent classical MD dynamics has been performed on the nanocomposite system containing a silica nanoparticle embedded in P2VP melt, at 453 K. Simulation are still running in the NPT ensemble, on CRESCO 4 cluster, in that it is necessary to produce at least 500 ns of trajectories, in order to be able to obtain a plot of the full relaxation of self-intermediate scattering function.

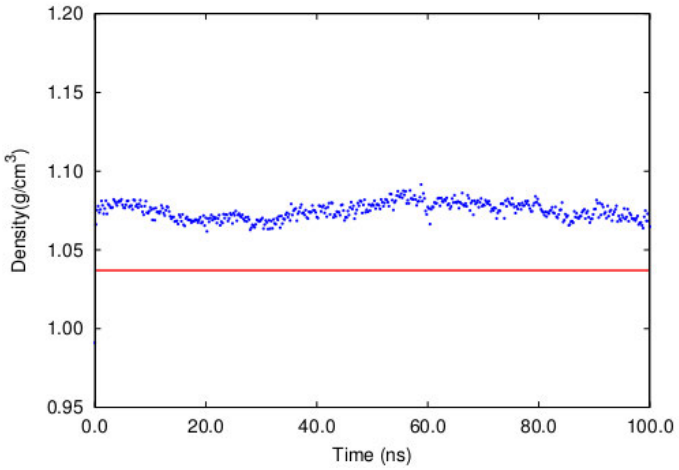

Figure 1: Plot of the calculated density over time (blue dots) and experimental density value for P2VP

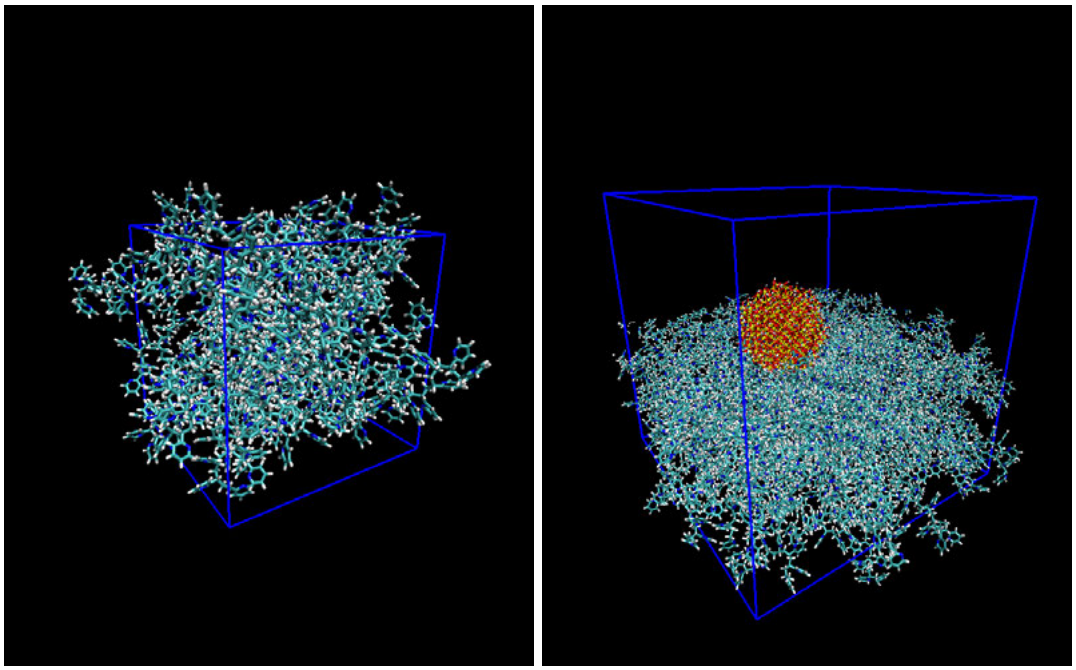

Figure 2: Snapshot of the pure P2VP polymer (left) and P2VP/SiO2 nanoparticle composite system (right)

References

[1] F. W. Starr, J. F. Douglas, D. Meng, and S. K. Kumar. *ACS Nano*, 10:10960, 2016.

[2] A. P. Holt, P. J. Griffin, V. Bocharova, A. L. Agapov, A. E. Imel, M. D.Dadmun, J. R. Sangoro, and A. P. Sokolov. *Macromolecules*, 47:1837, 2014.

[3] G. P. Baeza, C. Dessi, S. Costanzo, D. Zhao, S. Gong, A. Alegria, R. H.Colby, M. Rubinstein, D. Vlassopoulos, and S. K. Kumar. *Nature Communications*, 7:11368, 2016.

[4] Y. Zhao, A. De Nicola, T. Kawakatsu, and G. Milano. *J. Comput. Chem.*, 33:868, 2012.

[5] A. De Nicola, T. Kawakatsu, and G. Milano. *J. Chem. Theory. Comput.*, 10:5651, 2014.

[6] A. De Nicola, Y. Zhao, T. Kawakatsu, D. Roccatano, and G. Milano. *J. Chem. Theory. Comput.*, 7:2947, 2011.

[7] G. Milano and T. Kawakatsu. *J. Chem. Phys.*, 130:214106, 2009.

[8] M. J. Abraham, T. Murtola, R. Schulz, S. Pll, J. C. Smith, and B. Hess E. Lindahl. *Software X*, 1-2:19, 2015.

[9] W. L. Jorgensen and N. A. McDonald. *Theochem*, 424:145, 1997.

[10] F. Mller-Plathe. *Macromolecules*, 29:4782, 1995.

[11] D. N. Voylov, A. P. Holt, B. Doughty, V. Bocharova, H. M. Meyer III, S. Cheng, H. Martin, M. Dadmun, A. Kisliuk, and A. P. Sokolov. *ACS Macro Lett.*, 6:68, 2017.

Study of transport of runaway electrons in the presence of MHD perturbations with the Hybrid MHD Gyrokinetic Code

A. Casolari[1]*, S. Briguglio[2], G. Vlad[2]

[1] *Institute of Plasma Physics of the CAS, Za Slovankou 1782/3, 182 00 Prague, Czech republic*

[2] *ENEA C. R. Frascati, Via E. Fermi 45, CP I-65-00044 Frascati, Italy*

Abstract. Runaway electrons (RE) represent a serious issue for the operation of large tokamaks such as ITER. Suppression and control of the RE beam is a goal of primary importance in tokamak studies. The propagation of RE in the plasma volume is affected by the presence of magnetic perturbations, either caused by intrinsic MHD activity or artificially imposed by external coils. The successfull operation of future devices strongly relies on the success of numerical simulations in reproducing the complex dynamics of relativistic electrons in the presence of magnetic perturbations. The Hybrid MHD Gyrokinetic Code is designed to study the coupled dynamics of energetic particles and MHD modes in tokamaks. The relative simplicity of the code and the calculation speed make it a useful tool to gain first-order insight into the problem of RE propagation.

1 Introduction

During a disruption event, a fraction of the electrons can be accelerated to relativistic energies by large induced electric fields caused by the rapid cooling of the core region of the plasma column (thermal quence). After the collapse of the structure of magnetic flux surfaces during the thermal quench phase, the conservation of magnetic helicity prevents the complete removal of plasma current on short time scales. This causes magnetic flux surfaces to rapidly re-form, causing the onset of non-axisymmetric flux tubes, capable of confining energetic electrons, which would otherwise rapidly escape the plasma before reaching relativistic energies. Such confined electrons are thus accelerated to relativistic energies and their number can increase exponentially via successive collisions (avalanche effect).

Studies of RE transport in the presence of magnetic perturbations were motivated by the possibility of using resonant magnetic perturbations (RMPs) to mitigate the RE beam by increasing the RE losses. In the simplest picture, the electrons follow stochastic magnetic field lines and diffuse radially with the Rechester-Rosenbluth diffusion coefficient [5]. In reality, this represents an upper bound on the transport and RE confinement is usually better because of finite Larmor radius (FLR) and magnetic drift effects. In mixed magnetic topologies consisting of magnetic islands, intact magnetic surfaces and stochastic regions, this diffusion coefficient is not valid. In such circumstances, some fraction of the electrons will be trapped in magnetic islands, and the confinement time of these particles can equal the characteristic system evolution time. Understanding the physical processes responsible for the RE drift motion is essential to correctly model this process and to account for the experimental observations.

The most popular approach for this kind of studies is represented by particle simulations. At each time step, the electromagnetic fields are computed on the basis of momenta of the particle distribution

*Corresponding author. E-mail: casolari@ipp.cas.cz.

function (density and current) and particles are evolved according to the fields previously computed. In principle, each species of particles contained in the plasma (ions and electrons) can be represented by a corresponding numerical particle population. In practice, however, it can be worth reserving the particle representation to electrons, while describing the bulk plasma species by a fluid representation. This mixed approach is called a hybrid MHD-particle approach.

2 Characteristics of the code

In this work, we used the Hybrid MHD Gyrokinetic Code (HMGC) to study the RE transport in the presence of MHD perturbations in circular plasmas. HMGC was initially developed to study the interaction between energetic ions and Alfven modes [2], but it was later applied also to the study of the correlation between the Cherenkov signal associated with RE losses and the magnetic signal associated with MHD activity on FTU [3]. The code solves the MHD bulk plasma dynamics by integrating a reduced MHD system of equations, while the energetic particles dynamics is evolved by solving the gyrokinetic equation. The coupling between the MHD and the gyrokinetic modules is provided by the energetic particles contribution to the pressure tensor. The main limitations of HMGC are that it can only describe the dynamics in the case of circular cross section plasmas and that the equations evolving the particle dynamics are non-relativistic. Despite these limitation, the code's relative simplicity and its calculation speed make it a useful tool to gain first-order insight into the problem. In fact, HMGC represents a valid compromise between a sufficiently accurate MHD-particle interaction description and affordable computational resource requirements. Furthermore, many experimental regimes in presently operating devices, such as FTU and COMPASS, fall widely within the limits of validity of the code.

The code has been parallelized for distributed-shared memory architectures, the distributed-memory level being managed by the message-passing library MPI and the shared-memory level by the high-level parallel programming environment OpenMP. HMGC is written in Fortran90 language and it can be run on Linux machines and compiled by using the linux-intel compiler. The resources needed for HMGC simulations depend on the number of modes that need to be evolved by the MHD module and on the number of particles that are evolved by the kinetic module. For our purposes, we used two axisymmetric modes for the equilibrium and two non-axisymmetric modes for the perturbation. In the kinetic module, we used 150x32x8 cells and 2 particles per cell, for a total of 76800 particles. This choice for the number of particles turns out to be optimal to represent quite accurately the particle density in the plasma volume, withouth requiring too much computational time. Simulations performed with these settings lasted approximately 15 hours on 16 processors for 16 threads. This short computational time makes these settings ideal to run many simulations with different parameters.

3 Results

The purpose of this study was to understand the radial diffusion of RE in the presence of MHD perturbations. In particular, we were interested in the case of a (2,1) tearing mode evolving into a large magnetic island, to which a smaller (3,1) tearing mode is added later, either driven unstable by the toroidal coupling with the (2,1) or induced by external resonant perturbations. The reason behind this choice is that, for typical RE experiments, the (2,1) tearing mode is the most unstable MHD mode, while a small (3,1) mode can be driven unstable by the toroidal coupling. The fact that the $q = 3$ rational surface is relatively close to the edge, for typical experimental safety-factor profiles, suggests that an eventual overlapping between the (2,1) and the (3,1) modes can produce a significant loss of electrons. To be able to have more control over our simulations, we chose to evolve artificially the mode amplitude by starting from an initial seed, obtained from a linear run. The time evolution of the magnetic energy for the linear run and the amplitude of the seed perturbations are displayed in Fig1.

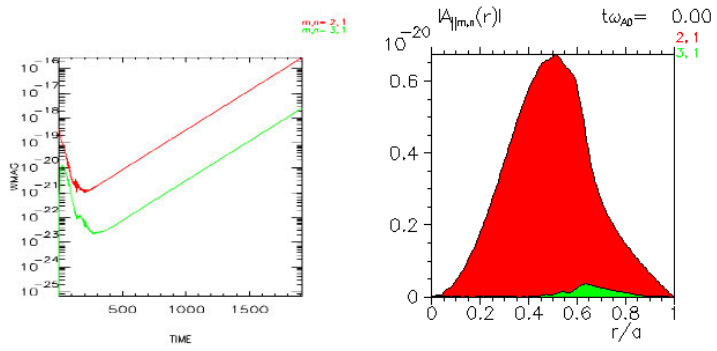

Figure 1: Magnetic energy associated to the linear growth of the (2,1) and the (3,1) tearing modes (left) and initial seed of the magnetic perturbation (right)

The artificial growth of the mode is obtained by bypassing the MHD module and by imposing that the mode aplitude grows linearly from the initial value to a final value, corresponding to the saturated amplitude. This linear growth is applied both to the (2,1) and the (3,1) modes but with a delay between the two amplitude ramps. The purpose of this delay is to be able to observe the different behavior of the energetic electrons in the presence of only the (2,1) magnetic island or both the islands, which eventually partially overlap. The time evolution of the magnetic energy and the final amplitude of the (2,1) and (3,1) modes is displayed in Fig.2.

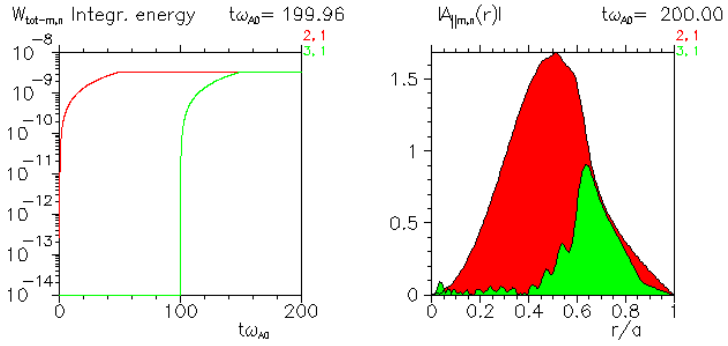

Figure 2: Magnetic energy associated to the artificial growth of the (2,1) and the (3,1) (left) tearing modes and final ampliude of the magnetic perturbation (right)

From numerical simulations, we observed that the electrons experience a large diffusion when the (3,1) mode is turned on and overlaps to the mode (2,1). This behavior can be ascribed to the formation of a stochastic layer in the position where the overlapping takes place. To evaluate this effect, we calculated the diffusion coefficient of the magnetic field lines by using the Hamiltonian theory. The values of the poloidal magnetic flux are extracted from the outputs of the code and the Hamiltonian equations are calculated to determine the trajectories of the magnetic field lines [1]. The diffusion coefficient of the magnetic field lines can be calculated by using the mean square displacement formula[4]: $D(r) = \frac{\epsilon}{\pi N} \sum_{i=1}^{N} (r_i - r)^2$, where $\epsilon = a/R_0$ is the inverse aspect ratio, N is the number of steps in the integration of the Hamiltonian equations, r_i is the radial position at each step and r is the initial position. All the lengths are normalized to a and the time is normalized to the Alfven time τ_A. By using the formula above for each radial position and for each instant, a space-time dependent diffusion coefficient $D(r,t)$ is obtained. By using this, the evolution of the electron density is determined by a diffusion equation: $\frac{\partial n}{\partial t} = \frac{\partial}{\partial r}\left(D(r,t)\frac{\partial n}{\partial r}\right)$. The comparison between the evolution of the density profile resulting from the simulation and the one computed with the diffusion equation is displayed in Fig.3.

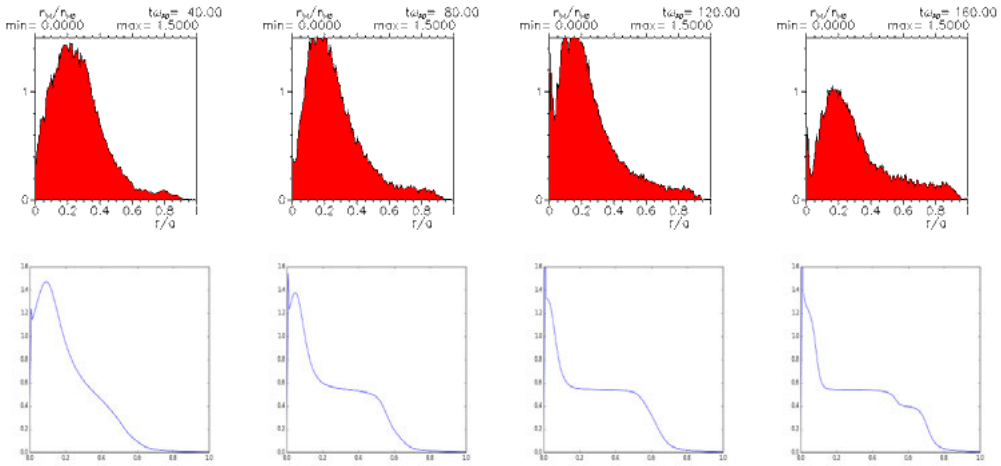

Figure 3: Comparison between the evolution of the density profile resulting from the simulation and the one computed with the diffusion equation at different time instants

The diffusive model suggests that the strongest contribution to the RE drift comes from the (2,1) mode, which causes a significant flattening of the density profile, with the (3,1) mode playing a minor role. According to the simulations, instead, only when the partial overlapping between the two modes occurs, a significant particle diffusion is observed. The disagreement between these results shows that the radial drift of the RE population cannot be accurately described by a purely diffusive model.

4 Conclusions

To study the behavior of relativistic electrons in the presence of magnetic perturbations is a difficult task, involving different phenomena (such as the FLR and drift effects) which must be correctly included in the models. The hibrid MHD-particle approach implemented in HMGC is capable of accounting for these effects without requiring large computational resources. The short computational time needed to run the simulations makes this code a very useful tool to perform parameter scans.

References

[1] Allen H Boozer. Hamiltonian representation of divergence-free fields. Technical report, Princeton Univ., NJ (USA). Plasma Physics Lab., 1984.

[2] S Briguglio, G Vlad, F Zonca, and C Kar. Hybrid magnetohydrodynamic-gyrokinetic simulation of toroidal alfvén modes. *Physics of Plasmas*, 2(10):3711–3723, 1995.

[3] F Causa, P Buratti, B Esposito, G Pucella, E Giovannozzi, L Jakubowski, K Malinowski, M Rabinski, MJ Sadowski, J Zebrowski, et al. Cherenkov emission provides detailed picture of non-thermal electron dynamics in the presence of magnetic islands. *Nuclear Fusion*, 55(12):123021, 2015.

[4] O Dumbrajs, V Igochine, H Zohm, et al. Diffusion in a stochastic magnetic field in asdex upgrade. *Nuclear Fusion*, 48(2):024011, 2008.

[5] AB Rechester and MN Rosenbluth. Electron heat transport in a tokamak with destroyed magnetic surfaces. *Physical Review Letters*, 40(1):38, 1978.

CODE PARALLELIZATION OF THE OPTIMISATION FOR THE LOCAL TRANSPORT'S ELECTRIFICATION

Giuseppe Chiapparo[1*] and Massimo Celino[2†]

[1] *University of Rome Tor Vergata, Computer Science, Rome, Italy*

[2] *ENEA, C. R. Casaccia, via Anguillarese 301, 00123 Rome, Italy*

ABSTRACT. To promote the use of electric buses in public transport networks, a careful analysis of the costs is needed to find the best implementation of the electrified sub-networks. Unfortunately this task has a very high computational cost, that has till now prevented its application in real cases on large cities and forced the use of heuristic and approximate algorithms. The availability of supercomputers like CRESCO, opens the possibility to face this class of problems. In order to fully exploit its huge computing power, we developed an optimisation algorithm to model a general public transport network. Then we have parallelized it to explore the entire set of possible solutions and find out the more convenient among the many feasible sub-networks. This goal has required the implementation of branch-and-bound techniques and a careful analysis of the performance. The first implementation of the parallel code has been used to address the public transport network of Florence.

1 Introduction

The goal of this project is to find the optimal solutions for the electrification of the public transport networks to check the reliability of heuristic and approximated approaches already used in this context. We developed several methods of optimisation through the analysis of the public transport sub-networks in the different recharge configurations of the vehicles. With the realisation of these models we verified the technical and economical feasibility for the autonomous power supply, using appropriate technologies for the recharge of the electric buses. This analysis is performed for the buses of a city with significant size. Our work is focused on the design and engineering of algorithms that explore the space of the possible recharge configurations on appropriate subset of the bus lines for the considered public transport network.

In order to realise an application software that computes the exact solution we needed to design and implement a parallel program with smart techniques of load balancing between the many computing resources of CRESCO. In fact, the main challenge of this work is to find an efficient load-balancing. The problem to resolve is: *given a budget for the initial investment, what bus lines could be electrified first and what kind of recharge architecture is the most suitable ?*

To get the exact solution of this optimisation problem, we used the exhaustive search approach. In this way we can analyse all the eligible solutions in order to find the optimal. However, the space of the solutions is such that, if we want examine a network with L lines and two architectures of recharge, we

*Corresponding author. E-mail: giuseppe.chiapparo@uniroma2.it.

†Corresponding author. E-mail: massimo.celino@enea.it.

should analyse a number of solutions equal to:

$$f(L) = \sum_{k=1}^{L} \binom{L}{k} \cdot 2^k \tag{1}$$

To estimate the value of $f(L)$ in equation (1), it's sufficient to think that if L is equal to 100 we should explore $5,153 \cdot 10^4$ solutions. This number is very high, and it is unthinkable to explore this space of solutions in a reasonable time and with a standard personal computer.

For this reason we implemented an algorithm that:

- Explores the space of the solutions in parallel mode [1].
- Explores each possible solution once and only once by only one processor.
- Exploits the computational resources of CRESCO.
- Uses branch and bound techniques, avoiding the analysis of the unfeasible sub-networks.

2 Algorithms and methods

The first step of this project was the design of an algorithm that explores the network in a parallel mode, analyses all the possible solutions with an approach of branch and bound and distributes the workload on many processors.

The second and main step was the creation of an algorithm that balance the workload in an efficient way on the processors. We implemented four static balance algorithms:

1. *Balancing fear lines.*
2. *Balancing of lines first less, last more.*
3. *Fixed balancing in depth.*
4. *Variable balancing in depth.*

Each algorithm is an optimised version of the previous. The first two algorithms don't distribute well the workload and they don't exploit all the computing resources of CRESCO. Instead, the best result is obtained by the "Variable balancing in depth". This algorithm can divide the workload on many processors and it can obtain a fair distribution of the workload.

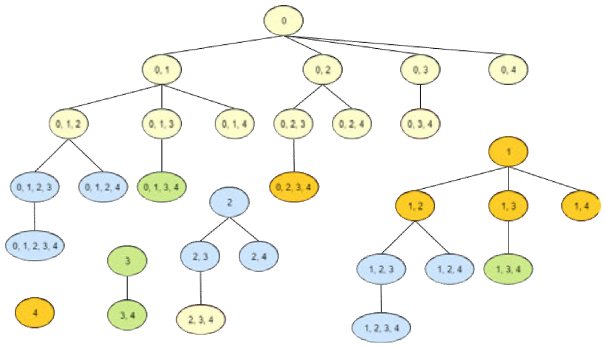

Figure 1: Example of load-balancing of the algorithm "Variable balancing in depth" with five lines and four processors. Each node represents a sub-network and each colour the processor that will analyse that sub-network.

For further details we can refer to the Report RdS/PAR2016 [4].

3 Computational details

We used CRESCO3 and CRESCO4 for the execution of our tests. The programming language that we chose to use is C++ with the communication protocol MPI among the processes [3]. The reason to use C++ rather than other languages is performance. The reason for that is that C++ offers a means of abstraction that has no performance overhead at run-time. This allows the writing of very efficient code that still has a very high abstraction level. In this way we can write efficient code with an high level of abstraction.

The program is designed to be executed on numerous nodes of the cluster and requires a communication protocol between the computers. We chose MPI because it is the standard for the communication among nodes belonged to a cluster of computers that executes a parallel program developed for systems with distributed memory.

4 Results and discussions

In order to verify our program we did many tests and we realised that the success of a test depends on many factors: the size of the analysed network, the budget for the initial investment, the chosen load-balancing algorithm, the hardware architecture (CRESCO3 or CRESCO4) and the maximum time for the experiment in the queue.

For this reason we did two types of tests:

1. **Preliminary test and experimental evaluations.**

   (a) *We tested the different types of load-balancing algorithms and we analysed the number of the sub-networks assigned to each processor.* In this way we understand that the load balancing algorithm "Variable balancing in depth." has the best results (for equal parameters and architecture of execution). The reason is due to the fear distribution of the workload rather than the previous algorithms.

   (b) *We tested many artificial networks with increasing number of lines.* When the number of lines increases, also the complexity of the computation increases. In fact, the problem is that: not only the number of feasible sub-networks increases, but also the size of these sub-networks increases. However, we tested the same instances but with a lower budget and we have analysed also networks with 130 bus lines.

2. **Test for the comparison with the heuristic algorithms and the analysis of the real case of Florence.**

   (a) *We tested different artificial networks with 30 lines and variable budget.* These tests show us that the execution time depends not only on the number of lines but also on the distribution of the investment costs for the bus lines. If the costs of the bus lines are lower than an other network with the same number of lines, the analysis will take more time.

   (b) *We tested the real network of Florence (85 lines) with increasing budget.* With these tests we analysed the best 15 sub-networks that we can electrify in the Florence network with an increasing budget (from 1 million of euro to 7 millions). These tests highlighted that with a budget of 7 millions, the best sub-networks contain 2, 3 or 4 bus lines.
   Moreover, in the 15 best sub-networks we obtained a positive value of the objective function

(see table 2). This means that with the electric buses we have an economic convenience. For example, with only 2 bus lines we'd gain $1\,547\,413,66$€.
We can notice that the time execution increases with the budget (see table 1). The reason of it is already discussed previously.
Finally, we can notice that the greater is the budget, the greater is the value of the objective function. Thus, the greater are the investments for the electric buses, the greater is the global gain.

Table 1: Test on the network of Florence

Budget (M€)	Time exec. (s)
2	1.98719
3	2.77997
4	26.5262
5	309.652
6	2843.34
7	21216.6

Table 2: Best sub-networks of Florence with budget 7M€

Obj. func. (€)	num. of lines	line1	line2	line3
1547413	2	7B	69B	-
1336217	3	18A	52B	69B
1325647	3	16A	52B	69B
1322930	3	52B	62A	69B
1319209	3	30A	52B	69B

5 Conclusion

We developed algorithms that can be executed on the parallel architectures of CRESCO and we balanced the workload between the different processors. These algorithms implement techniques of branch and bound, thanks to which we analysed networks with 130 bus lines and we obtained interesting results on the real network of Florence with 85 bus lines.

With this project we can compare the exact result with the results of heuristic algorithms that can be executed on a standard personal computer. Moreover, we proved that the power supply is beneficial in the case of the Florence instance.

However, we are planning the analysis of bigger networks than Florence, like Rome. In order to do it, we need to change our code architecture and use for the next year the *job array* technique [2]. This technology exploits better the resources of CRESCO. In fact, our problem is embarrassingly parallel and runs consisting of hundreds or thousands of similar calculations, each one executing the same program but with different inputs. With the job array technique we can submit all these jobs at once, and manage them as a single entity. This is the main further development for the next year, together with the analysis of more recharging architecture and bigger networks.

References

[1] Introduction to parallel computing, lawrence livermore national laboratory. https://computing.llnl.gov/tutorials/parallel_comp/.

[2] Job array. https://scicomp.ethz.ch/wiki/Job_arrays.

[3] Mpi documents. http://mpi-forum.org/docs/.

[4] Giuseppe Francesco Italiano. Sviluppo di algoritmi per l'ottimizzazione del processo di elettrificazione di reti di trasporto pubblico urbano attraverso l'analisi delle possibili configurazioni di ricarica su sottoinsiemi della rete di trasporto. *Accordo di Programma Ministero dello Sviluppo Economico - ENEA, Piano Annuale di Realizzazione 2016*, September 2017.

NEUTRONIC TRANSPORT ANALYSIS THROUGH OPENINGS IN IN-VESSEL COMPONENTS IN DEMO

A. Colangeli[1*], D. Flammini[1], F. Moro[1] and R.Villari[1]

[1] *ENEA, FSN Department, Via E. Fermi 45, 00044 Frascati, Rome, Italy* [1]

ABSTRACT. In the frame of this task within PMI program, nuclear analyses with MCNP5 code [1] and JEFF3.2 nuclear data library [2] have been performed to support design and integration of Electron Cyclotron (EC) and pellet fuelling lines. Different configurations of the various systems have been analysed and the impact on Tritium Breeding Ratio (TBR), neutron flux, nuclear heating and damage on Breeding Blanket (BB), Vacuum Vessel (VV) and Toroidal Field (TF) coil was studied as well nuclear loads on the integrated systems. Strategies to improve in-vessel components design and shielding capability have been suggested to reduce the interface with other systems [3]. In this paper results of the integration of the Pellet Fuelling line is reported.

1 Integration of the Pellet Fuelling Line

Different options for pellet fuelling lines (PFL) (fig.1) are under study for integration. Neutronic analyses have been performed on Helium Cooled Pepple Bed (HCPB) DEMO reactor for two possible configurations of a Guiding Tube bolted to the VV inner shell, that impacts the inboard blanket (IB) modules 5 and, marginally, 4. The two examined configurations are listed below (fig. 2):

1. 20 cm length for the guiding tube and 3° opening of IB5 at the end of the tube;
2. 40 cm length for the guiding tube and 3° opening of IB5 at the end of the tube.

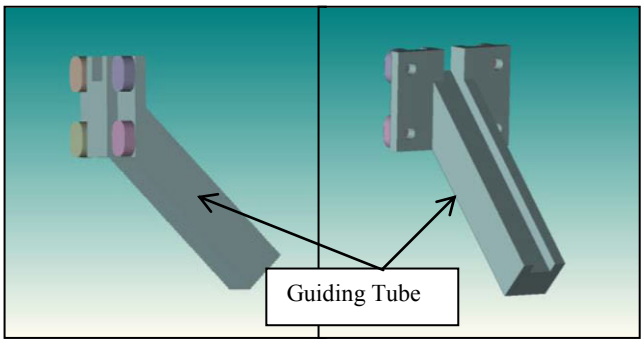

***Figure 1**:* Model of Cu Pellet Guiding Tube with bosses

[1] Corresponding author. E-mail: andrea.colangeli@enea.it

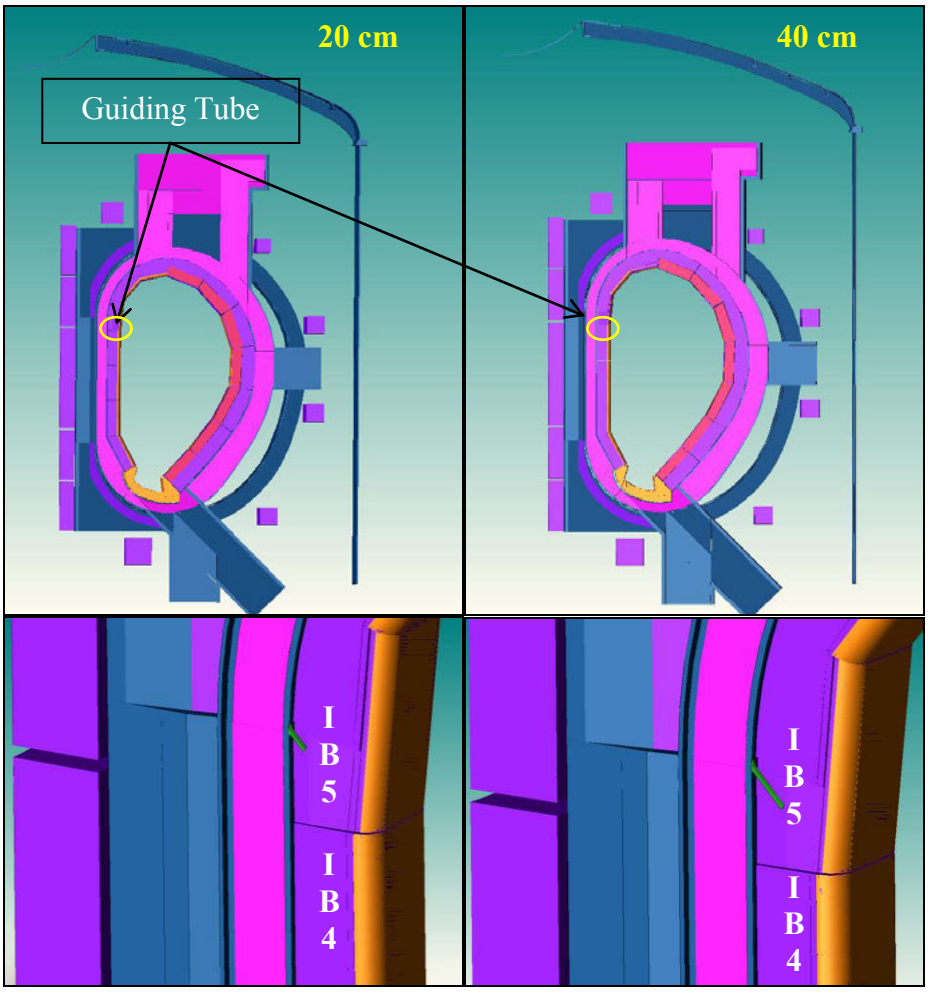

***Figure 2**:* HCPB MCNP 3D model of 20 and 40 cm configurations

2 Results

The impact of the guiding tube on the total nuclear heating is marginal. The maximum effect is observed in IB5 module, in the worst configuration (20 cm) for the left side caps (close to the gap) the calculated value is 3 times higher with respect to the Baseline and past pellet fuelling line tubes options [4, 5]. Regarding the nuclear loads on the Pellet Guiding Tube the maximum heating and damage in front positions are 0.9 W/cm^3 and 1.7 dpa/FPY for 20 cm configuration and 2.14 W/cm^3 and 2 dpa/FPY for 40 cm one. The nuclear loads decrease in the guiding tube connecting plate to 0.8 W/cm^3 (20 cm) and 0.72 W/cm^3 (40 cm). In this last configuration the reduction of 10% is due to the smallest opening of the IB5.
A great increase of damage in steel is observed on the VV inner shell due to the neutron streaming.
The maximum calculated damage is 3.91 and 3.42 dpa/6FPY for 20 and 40 cm configuration respectively (fig. 3) then the cumulated damage on VV is well above the limit of 2.75 dpa over 6 FPY for both configurations.

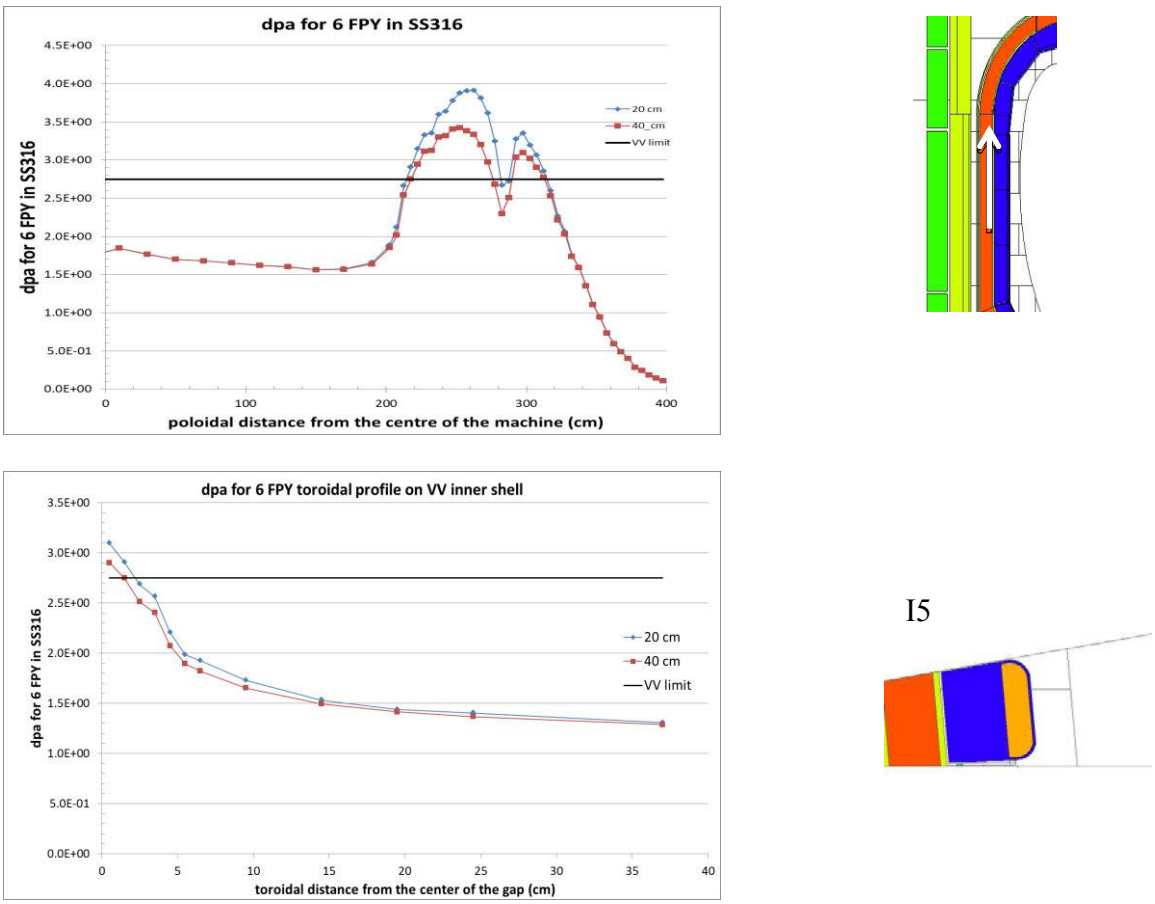

Figure 3: Neutron damage poloidal (top) and toroidal (bottom) profiles in dpa over 6 FPY in VV inner shell for 20&40 cm configurations

Then both configurations required efforts to decrease the nuclear loads on the VV inner shell. Some design variants by changing the angular opening of the guiding tube and the size of the connecting plate have been studied to reduce the zone of VV directly exposed to neutron streaming. The reduction of angular opening only is not effective to reduce the dpa level below the limit. The 40 cm configuration with opening reduction to 1° and extension of the connecting plates to 75 cm seems sufficient to protect VV (max dpa 2.66 over 6 FPY).

The integration of the pellet fuelling line requires a great computational efforts. For this reason the use MCNP MPI multiprocessor version installed on the CRESCO cluster, available in ENEA [6], was necessary.
Each MCNP run generates 5e9 particles, using 640 processor. Typical dimension of an MCNP output generated by CRESCO is 22 Mbyte and the overall studies required the analyses of some Gbyte data.

References

[1]] X-5 Monte Carlo Team: MCNP - A General Monte Carlo N-ParticleTransportCode, Version 5,LosAlamosNationalLaboratory, Los Alamos, New Mexico, USA, April 2003.

[2] JEFF3.2 nuclear data library, http://www.oecdnea.org/dbforms/data/eva/evatapes/jeff_32/.

[3] R. Villari,A. Colangeli, D. Flammini, F. Moro, D. Trombetta, Neutron transport analysis through openings in in-vessel components, Final Report WP PMI-3-3-T007 -2017.

[4] F. Cismondi, P. Agostinetti, C. Bachmann, W. Biel, L.V. Boccaccini, A. Bruschi, Chr. Day, A. Del Nevo, G. Di Gironimo, I. Fernandez, T. Franke, G. Grossetti, F. Hernandez, D. Iglesias, J. Keep, P. Lang, A. Loving , P. Norajitra, G. Mazzone, D. Marzullo, B. Ploeckl, R. Mozzillo, D. Rapisarda, M.Q.Tran, A. Vaccaro, R. Villari, J. H. You, C. Zeile, Progress in EU-DEMO In-Vessel Components integration, **124** (2017), 562-566**.**

[5] G. Grossetti1, L.V. Boccaccini, F. Cismondi, A. Del Nevo, U. Fischer, T. Franke, G. Granucci, F. Hernández, R. Mozzillo, D. Strauß, M. Q. Tran, A. Vaccaro, R. Villari, DEMO Port Plug Design and Integration studies, *Nuclear Fusion* **57**, 116068.

[6] http://www.cresco.enea.it/

Monte Carlo Simulations supporting Safaty Studies of PWR's and Irradiation Tests in Nuclear Research Reactors

P. Console Camprini[1]*and K.W. Burn[1]

[1]*ENEA, Fusion and Technology for Nuclear Safety and Security Department, 40129, Bologna, Italy*

Abstract. In the framework of the Development of Expertise in Nuclear Safety and Nuclear Reactor Design, studies are carried out within the Project B.3.1 LP1 of the Programmatic Agreement funded by the Italian Ministry of Economic Development − Annual Plan 2016. Evaluations concern mainly the following topics: Nuclear Safety analyses for Gen-II and Gen-III PWRs, preliminary studies related to some irradiation campaigns in the TAPIRO research reactor, code experience and verification in fast neutron systems supporting innovative Gen-IV reactors. PWR reactor evaluations have been carried out by substantially modifying the Monte Carlo MCNP6.1 source code to implement a new version of the in-house MCNP patch which utilizes the Direct Statistical Approach method to generate variance reduction parameters. Relevant updates have been implemented and a version based on the MCNP6.1 release has been produced. A customized pin-by-pin neutron fixed source has been prepared and tested in order to account for the impact of different fission spectra on ex-core responses: comparison spectra are the MCNP default, the ^{235}U and the ^{239}Pu fission spectra. In the framework of Project B.3.1 LP2 research activity, the simulations concern the TAPIRO facility located at ENEA Casaccia − selected as the irradiation facility by the OECD-NEA group of minor actinide management (EGIEMAM). Following the work of previous years, sensitivity calculations have been performed regarding the modification of the multiplication factor of the reactor due to the insertion of some samples containing minor actinides in experimental channels. Finally, the utilization of MCNP6.1 code has been tested on fast neutron spectrum simulations - supporting Gen-IV reactor design − of an irradiation experiment performed in the LR0 research reactor at CV-Rez Institute, in Prague.

1 Monte Carlo Code Development and DSA Methodology

The Monte Carlo approach to the simulation of nuclear reactors is a valuable tool since it allows to treat transport of neutral (and charged) particles within media, considering the interactions between radiation and matter according to the basic evaluated data with a continuous-energy description and scattering laws. Furthermore the geometry may be modelled accurately with neither spatial nor angular discretization. Responses of interest are tallied by means of a statistical approach operating over many samples, or particle histories.
This method is particularly valuable in cases where the desired response involves a small subgroup of particles that reach a portion of phase space which is normally difficult to reach. Such a class of problems − so called deep penetration problems − requires the use of techniques to encourage particles to move

*Corresponding author. E-mail: patrizio.consolecamprini@enea.it.

towards important regions and simultaneously not to waste time in populating parts of the calculational domain that are unimportant. These methods reduce the statistical variance of a certain response, or range of responses, while maintaining the average expected results as the simulation were carried out according to physical unbiased laws. These variance reduction (VR) techniques require parameters provided by an external program or an additional algorithm.
The research has been part of the Project B.3.1 LP1 funded by the Italian Ministry of Economic Development − Annual Plan 2016 − concerning the enhancement of the tools for safety analysis of nuclear reactor systems.
A first activity regarded the in-house ENEA VR algorithm, DSA [**?**] (Direct Statistical Approach) that formerly existed as a patch for the Monte Carlo code MCNP5-1.40 [**?**]. During this year it has been adapted to the latest MCNP6.1 [**?**] version; it has been updated firstly in order to match the new code structure and the source modifications according to Modern Fortran syntax and capabilities (mainly modules and derived types), secondly to unify the fixed source and eigenvalue versions and finally to implement some new capabilities.
As far as the eigenvalue capability is concerned, it has been found that the use of "superhistories" [**?**] is required if performing VR in reactor cores or fissile configurations. The iteration steps are enlarged in such a way that each of them is constituted by more than one fission generation between two consecutive normalization steps.
Moreover, the latest DSA version allows also to provide VR parameters through a superimposed mesh for both a Cartesian and cylindrical geometry − the phase space in which such parameters are expressed is independent of the problem geometry but instead fixed to a topology selected by the user.
Such code development requires open-ended computer resources for test runs in order to carry out the debugging and to check the code performance, including also runs on benchmark problems. Computing resources consisted of CRESCO4 nodes for time steps of 24 hours.

2 Simulations for Safety Studies of Gen-II and Gen-III PWRs

Within the framework of the collaboration agreement between ENEA and IRSN (l'Institut de Radioprotection et de Sûreté Nucléaire) France, studies have been performed on radiation transport within and outside the cores of Gen-II and a Gen-III pressurized water reactors (PWRs). This work has been part of the Project B.3.1 LP1 funded by the Italian Ministry of Economic Development − Annual Plan 2016 − concerning some applications of new methodologies to real cases of interest mainly through collaborations with other nuclear research institutes and safety authorities. The case study of an existing Gen-II nuclear reactor core has been the Tihange-II reactor located in Belgium. It has been selected for the large amount of experimental data obtained during the start-up phase and available in open scientific literature [**?**].
Concerning Gen-III designs, a model of an EPR-like (European Pressurized Reactor) system, provided by IRSN colleagues and matched to the needs of safety studies [**?**], has been utilized. This year attention has concentrated on the accurate evaluation of the radiation damage to the pressure vessel. The responses of interest are the neutron and gamma fluxes and related responses at a variety of locations: neutron and gamma fluxes have been evaluated at the core mid-plane at different angular positions (see figure 1), as well as at platform and below platform positions (see figure 2). At the same locations neutron and gamma DPA (Displacement Per Atom) have also been calculated.
Firstly a set of fixed-source problems has been evaluated. The source has been previously sampled according to an eigenvalue calculation, in order to obtain a fission source with different levels of description (homogeneous, assembly-by-assembly with a single axial profile, assembly-by-assembly with an axial profile for each assembly, pin-by-pin with an axial profile for each pin). The pin-by-pin source configuration has also been utilized for an analysis of the impact of the fission spectrum on all ex-core positions. Three spectra have been considered: MCNP6.1 default spectrum, ^{235}U fission and ^{239}Pu fission spectra.

All three calculations were conducted with the same set of VR parameters obtained with the DSA. These decoupled calculations (eigenvalue and source preparation + fixed source simulation) were then compared with a DSA eigenvalue run − in which both steps are executed in a single run [**?**].

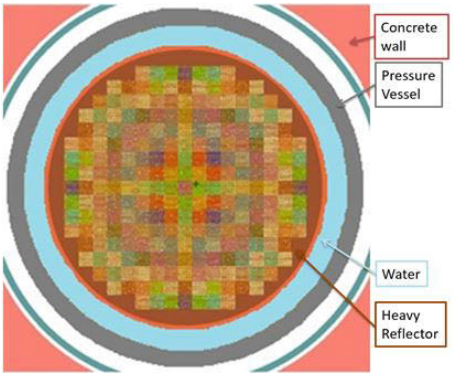

Figure 1: PWR Gen-III core cross-section (fuel assembly FA cross-section is highlighted)

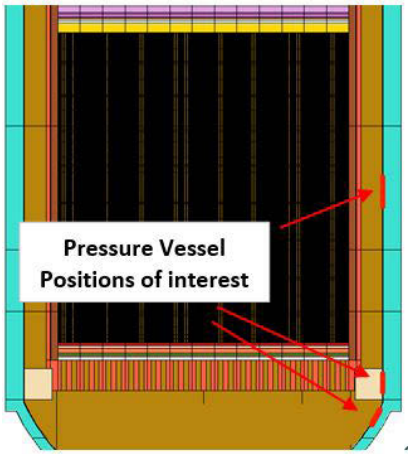

Figure 2: PWR Gen-III, vertical positions

The simulations required substantial computation resources provided by the CRESCO4 machines (the queues utilized permitted calculations of 24 and 144 hours). Using message-passing standard (mpi) according to OpenMPI protocol, generation of the VR parameters with the DSA required intensive communication between the nodes. Subsequent employment of the VR parameters in eigenvalue problems required some communications between the nodes, but substantially less than in the generation phase. Employment of the VR parameters in fixed-source calculations required still less node communication and points of rendez-vous were only at the end of a certain batches of source histories. Problems of this type turned out to be more scalable.

3 Irradiation Tests at LR0 Research Reactor

Design activity of Gen-IV nuclear reactors requires the utilization and the user experience of many simulation tools in order to predict the behaviour and performance of a nuclear installation for power generation and to describe and predict the plant characteristics throughout the plant lifespan.
The analysis has been part of the Project B.3.1 LP2 of the Programmatic Agreement funded by the Italian Ministry of Economic Development − Annual Plan 2016 − that involves the enhancement of expertise in the design of innovative Gen-IV nuclear energy systems, and particularly Lead-cooled Fast Reactors.
Simulations have concerned an irradiation experiment that was performed at the LR0 research reactor by CV-Rez researchers, in Prague, within a collaboration agreement with ENEA. Within an annular driver core with thermal neutron spectrum, a test section has been inserted for irradiation. The test section was made of a cylindrical shell, filled by solid lead enclosing 6 experimental fuel pins, meant for irradiation by propagation of neutrons through the lead.
The experiment has been reproduced by means of the Monte Carlo code MCNP6.1.
The system description was provided by CV-Rez and calculations were run in order to reproduce the gamma responses of some relevant detectors. The gamma source inside the experimental pins is indeed an indicator of their irradiation − notably of the capture and fission rates due to neutron flux. For this reason, the gamma emitters of interest were the following: ^{239}Np and ^{92}Sr [**?**]. The results of the calculations for the nuclide buildup have been compared with the experimental results. A reasonable

degree of agreement has been achieved and thus the capability of MCNP code to reproduce the neutrons propagation through lead turned out to be satisfactory.

4 Evaluations of TAPIRO Reactor Irradiation Campaign

Within the NEA Expert Group dealing with Integral Experiments for Minor Actinides Management (EGIEMAM), the TAPIRO [**?**] research reactor (figure 3), located at ENEA Casaccia, has been proposed as a relevant facility for integral experiments with a fast fission spectrum. The possibility to achieve a nearly-pure prompt fission spectrum in some positions close to the core is a key feature of this low power machine (5 kW). Thus, it is intended to perform irradiations of samples of minor actinides to obtain detailed neutron cross sections for absorption and fission. In this context ENEA proposed the AOSTA irradiation campaign [**?**].
Following analyses carried out in previous years, the motivation of the recent series of simulations was to understand if the insertion of some actinide samples appreciably changed the multiplication coefficient of the system − namely the first eigenvalue k_{eff}. The study is part of the Project B.3.1 LP2 funded by the Italian Ministry of Economic Development − Annual Plan 2016.
The AOSTA irradiation campaign considered two samples: OSMOSE and IRRM. Due to their geometrical dimensions, OSMOSE could be inserted in the Radial-1 and Tangential channels whilst the dimensions of the IRRM sample allowed insertion in the Radial-1, Tangential and Diametrical channels (see figure 4).

Figure 3: The TAPIRO facility hall

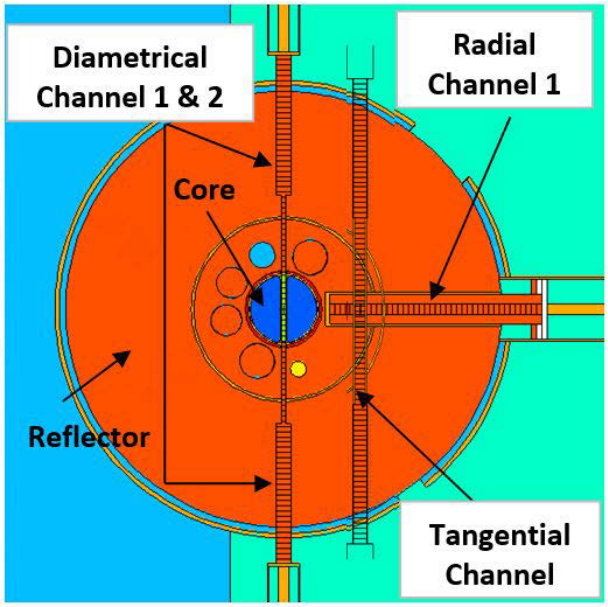

Figure 4: The TAPIRO MCNP model, mid-core plane and channels subdivided in cells for responses (tangential channel is actually positioned at a different depth)

The nuclides considered for the AOSTA irradiation campaign at TAPIRO are the following: ^{235}U, ^{238}U, ^{237}Np, ^{239}Pu, ^{240}Pu, ^{242}Pu, ^{241}Am, ^{243}Am, ^{243}Cm, ^{244}Cm, ^{245}Cm. Preliminary Monte Carlo calculations by means of the MCNP6.1 code yielded satisfactory and consistent results for insertion of OSMOSE samples: small differences compared to the reference core configuration and compatible with

safety regulations for tests in research reactors. These evaluations concerned direct calculations.
By contrast, very small variations in k_{eff} were induced by the insertion of IRRM samples. Such variations were so small that repeating the OSMOSE approach of differences between the results of two direct calculations was not feasible as the results were too noisy.
Therefore, it has been decided to take advantage of perturbation techniques and sensitivity methods through MCNP modules which utilize the adjoint flux and series expansion around a particular reference state. This second approach also involved a limited patching of MCNP. Satisfactory results were obtained in which the very small change in k_{eff} on inserting IRRM in the various channels was properly quantified [**?**].

Acknowledgement

The work on Gen-II and Gen-III PWRs was carried out in close collaboration with Institut de Radioprotection et de Sûreté Nucléaire (IRSN). In particular, IRSN supplied the MCNP geometric models and the responses of interest: for this the authors would like to thank Mariya Brovchenko and Isabelle Duhamel. Simulation of the LR0 irradiation campaign was possible thanks to data and specifications provided by CV-Rez research reactor team. The information to perform the simulations supporting irradiation in TAPIRO reactor was provided by Valentina Fabrizio and the ENEA colleagues of the research reactor laboratory team (FSN-FISS-RNR), under the guidance of Mario Carta.

Atomistic Model of Mesoporous Organosilica Materials

Antonio De Nicola[1]*, Antonio Pizzirusso[1], Ying Zhao[2] and Giuseppe Milano[1]

[1] *University of Salerno, Dip. Chimica e Biologia, 84084 Fisciano, SA, Italy*

[2] *Dalian Nationalities University, Institute of Nano-Photonics,116600 Dalian, China*

Abstract. The new class of mesoporous ogranosilicas materials (PMOs) attracts growing interest from different points of view including several research areas and applications. We present an atomistic model of *p*-phenylenesilica crystalline mesoporous structure with a hexagonal framework. OPLS-AA force field optimization is described.

1 Introduction

Periodic mesoporous organisilicas (PMOs) are a new class of materials[13] used in several applications such as: gas storage,[6] confined polymerization, molecular rotors,[6], selective adsorption,[17] catalysis,[7] adsorbent for pollutes from air and water,[18] and water desalination.[5]
Since 1999 when Inagaki,[10] Asefa[1] and Melde[15] reported firsts successful synthesis of bridge-bonded species (RO)3Si-R9-Si(OR)3, the synthesis of hybrid organic-inorganic materials has become well established. Today, PMOs materials are commonly produced by hydrolytic and polycondensation reactions of precursors of type (RO)3Si-R-Si(OR)3 known as sol-gel process.[9] PMOs with crystalline-like order in their walls[11] have organosiloxane units organized into ordered layers with molecular axes parallel to the mesochannel axis. Mesoporous organosilica crystalline structure exhibits a hexagonal framework with nanochannels having both, mesoscale periodicity and molecular order, as reported by Inagaki.[11] The combination of ordered organic/inorganic layers at wall nanochannel interface makes interactions of PMOs with guest species one of the key feature of adsorption/desorption properties from both, fundamental and applicative points of view.

2 Force Field and PMO Model

Due to the chemical similarity to the PMOs, OPLS-AA force field[12] have been tested to reproduce the PMOs crystalline precursor structure reported by Corriu[4]. On the basis of experimental X-Ray data[4], the Cartesian coordinates of PMOs precursor crystalline structure have been generated by using Mercury CSD 2.0 Code.[14] A single unit cell of 1,4-Bis(trihidroxysilil) Benzene (BTHB) has been duplicated five times in each *x,y,z,* direction, obtaining a periodic structure composed by 14400 atoms. The chemical structure of (BTHB) together with crystalline unit cell representation are reported in Figure 1.

*Corresponding author. E-mail: adenicola.chem@gmail.com.

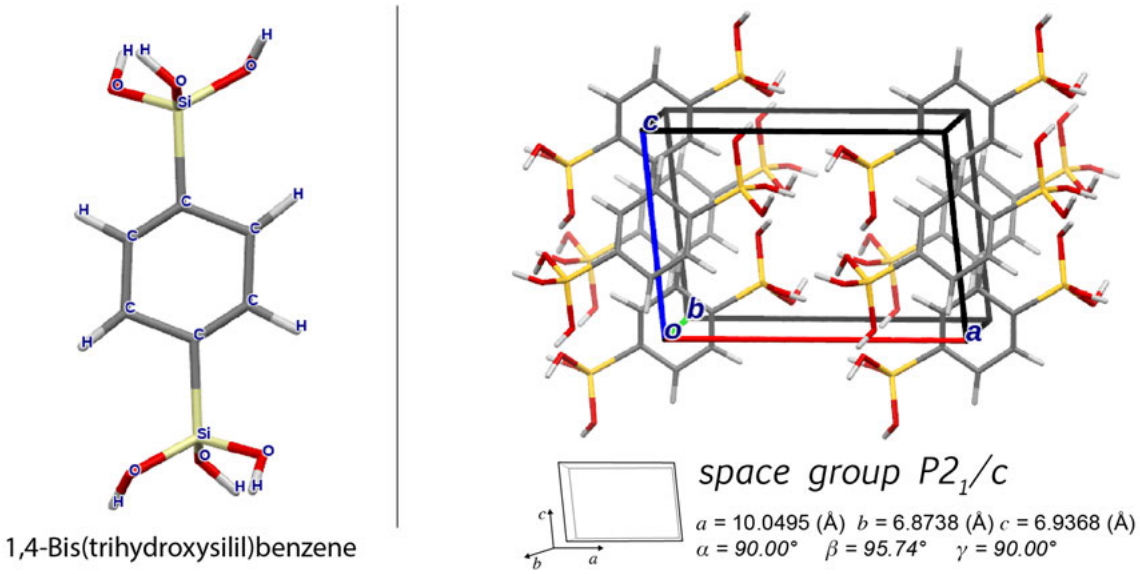

Figure 1: Chemical structure of BTHB on left. Crystalline unit cell, built from fractional atomic coordinates[4] in the right panel. Hydrogen atoms have been manually added by considering the bond distances and bending angle of the OPLS-AA force-field.[12]

2.1 OPLS-AA Force Field Optimization

OPLS-AA atomistic force-field[12] has been used for the majority of bonded and non bonded interactions, excluding those ones involving silicon atoms. In particular, bond and angle potential are calculated as:

$$E_{bond} = \sum_{bonds} K_B(r - r_{eq})^2 \tag{1}$$

$$E_{angle} = \sum_{angles} K_\theta(\theta - \theta_{eq})^2 \tag{2}$$

Where K_B is the bond constant of the harmonic potential, $r_{eq.}$ is the equilibrium distance between two bonded atoms, K_θ is the angle bending constant and θ_0 is the equilibrium angle between three consecutive bonded atoms.
The torsional intra molecular energy is calculated as the sum of first three terms of Fourier series as:

$$E(\phi) = \frac{V_1}{2}[1 + cos(\phi + f1)] + \frac{V_2}{2}[1 + cos(2\phi + f2)] + \frac{V_3}{2}[1 + cos(3\phi + f2)] \tag{3}$$

Where ϕ is the dihedral angle between for consecutive bonded atoms and V_1,V_2,V_3 are the Fourier coefficients series, instead *f1*, *f2*, *f3* are the angle phases.
The sum of Coulomb and Lennard-Jones (LJ) terms are used to represents the non-bonded interactions. The functional form of interaction energy for two molecules A and B is reported in the eq. 4:

$$E_{AB} = \sum_i^A \sum_j^B \left[\frac{q_i q_j e^2}{r_{ij}} + 4\epsilon_{ij} \left(\frac{\sigma_{ij}^{12}}{r_{ij}^{12}} - \frac{\sigma_{ij}^{6}}{r_{ij}^{6}} \right) \right] f_{ij} \tag{4}$$

where f_{ij} is equal to 0.5 (for $i, j = 1, 4$) and is equal to 1 for i, j grater than 4. All bonded and non-bonded parameters used in this work are listed in the Table S1 of Supporting Information. The

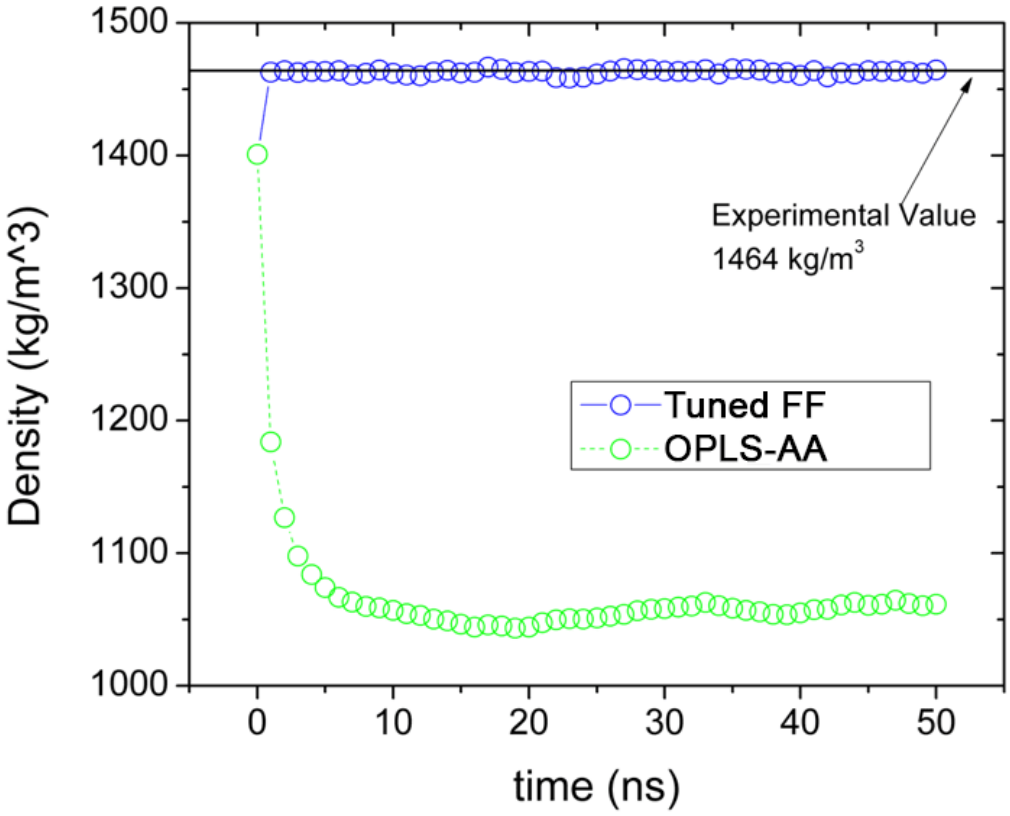

Figure 2: Comparison between mass density calculated by using OPLS-AA (green open circles) and the tuned force-field (blue open cirlce). The black line represents the experimental[4] value of 1464 Kg/m^3.

parameters involving silicon atoms, such as bond and angle parameters between Si-O, O-Si-O, Si-O-H groups, have been taken from the work of Barbier.[2] The initial system has been simulated for 1 ns in the NVT ensemble at 293 K and 1 atm by using GROMACS 4.5.4.[16] A time step of 2 fs has been used for all simulations. The temperature and pressure have been controlled by using Berendsen thermostat[3] with a τ_p of 10 fs. Periodic boundary conditions have been applied to all x,y,z directions. After an initial energy minimization (500 steps) by using the steep-descent algorithm, all bonds have been constrained by using the LINCS algorithm.[8] The non-bonded interactions were truncated at 1.0 nm. After a short NVT simulation, a production run of 100 ns (NPT ensemble with $\tau_p = 30$ fs) has been performed starting from the last NVT configuration.

By using the proposed model, we observed a high underestimation of the mass density, about + 28 %, together with a large deformation of the crystalline BTHB structure (Figure 2). Considering that the OPLS-AA force-field[12] is able to reproduce the bulk mass density of organic liquid molecules within an error of about 2-4 %, and, considering that Barbier[2] reported a correct reproduction of the mass density and crystalline structure of silica α-quartz, the main problem arises from the treatment of interactions between silicon atoms with phenyl carbon atoms. We decided to perform *ab initio* calculations to get suitable parameters of such interactions. In particular, on a single molecule of BTHB, DFT calculations have been performed to get bond lengths, bending and torsion angles. With the optimized force-field, as reported in Figure 2, the mass density is correctly reproduced.

2.2 PMO Structure

In the following is described the procedure to build the periodic mesoporous crystalline structure with hexagonal framework including explicitly nanochannels. In particular, we used as minimal brick element to build the whole structure, a single interconnected wall, as reported in Figure 3A. 12 replicas of the single wall (minimal brick element) have been oriented in a way to obtain a mesoporous repeating unit. Then, each wall has been properly connected, with others, by replacing pendant hydroxyl groups OH with Si-O-Si covalent bonds. The final repeating unit, containing a whole nanochannel, has reported in the Figure 3B (continuous black line). Connecting 4 repeating units, as depicted in the scheme of Figure 3B, the fully connected periodic crystalline structure is obtained. A snapshot of the structure is reported in the panel C of Figure 3.

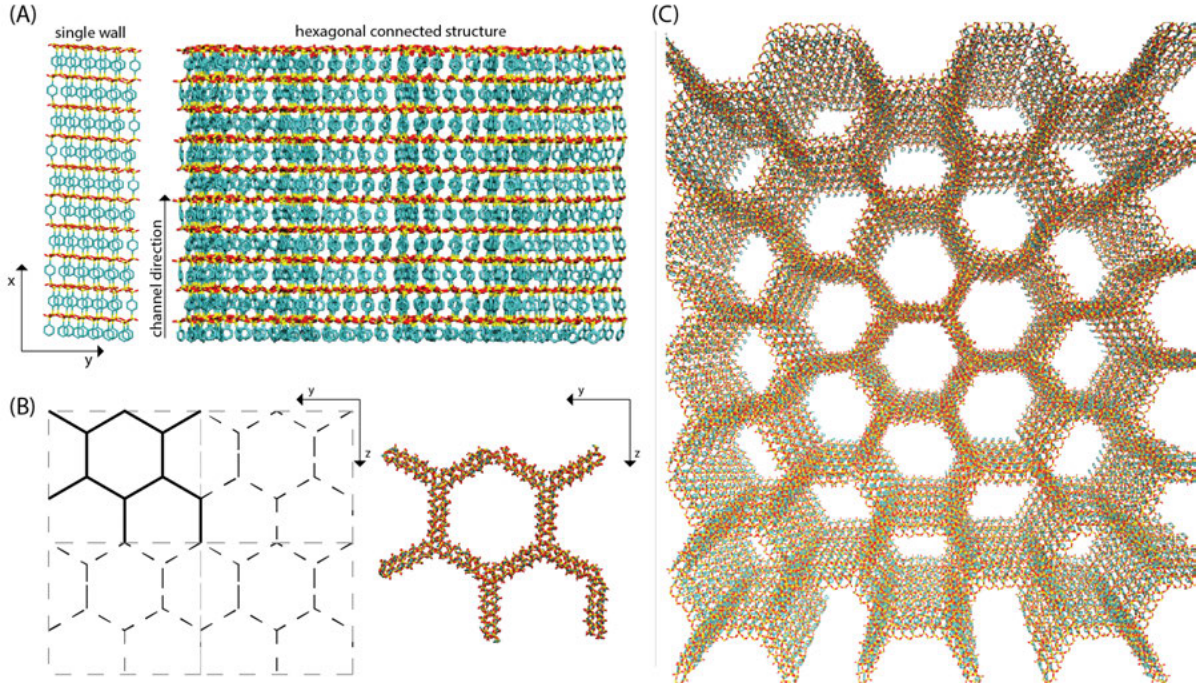

Figure 3: (A) View along channel direction of both: single wall and assembled hexagonal crystalline unit. (B) Scheme illustrating the repeating unit (black continuous line) and periodic images along *y,z* plane (segmented black line). The top view of the repeating unit structure is also reported. (C) Top view of periodic mesoporous structure in which nanochannels are reported. In all reported structures the hydrogen atoms have been omitted for clarity.

The final mesoporouse structure, obtained by following the described procedure, has been used as starting point for MD simulations. In particular, a minimization of structure (250 steps), using steep-descent algorithm, have been performed. On the minimized structure a short NVT simulation of 5 ns has been performed followed by a production NPT run of 100 ns.

3 Conclusions

We provided a validation and optimization of OPLS-AA force field to model at all atom level periodic crystalline mesoporous *p*-phenylenesilica. In particular, the mesoporous hexagonal framework structure, including explicitly nanochannels, have been validated on the reproduction of experimental periodic

distance distributions.[11] DFT calculations have been used to correctly parametrize torsional potential of phenyl rings belonging organic layers connected with inorganic silicon atoms.

References

[1] Tewodros Asefa, Mark J. MacLachlan, Neil Coombs, and Geoffrey A. Ozin. Periodic mesoporous organosilicas with organic groups inside the channel walls. *Nature*, 402:867 EP –, Dec 1999.

[2] Delphine Barbier, David Brown, Anne-Cécile Grillet, and Sylvie Neyertz. Interface between end-functionalized peo oligomers and a silica nanoparticle studied by molecular dynamics simulations. *Macromolecules*, 37(12):4695–4710, 2004.

[3] H. J. C. Berendsen, J. P. M. Postma, W. F. van Gunsteren, A. DiNola, and J. R. Haak. Molecular dynamics with coupling to an external bath. *Journal of Chemical Physics*, 81(8):3684–3690, 1984.

[4] Geneviève Cerveau, Robert J. P. Corriu, Bertrand Dabiens, and Jean Le Bideau. Synthesis of stable organo(bis-silanetriols): X-ray powder structure of 1,4-bis(trihydroxysilyl)benzene. *Angewandte Chemie International Edition*, 39(24):4533–4537, 2000.

[5] Yen Thien Chua, Chun Xiang Cynthia Lin, Freddy Kleitz, Xiu Song Zhao, and Simon Smart. Nanoporous organosilica membrane for water desalination. *Chemical Communications*, 49(40):4534–4536, 2013.

[6] Angiolina Comotti, Silvia Bracco, Patrizia Valsesia, Lisa Ferretti, and Piero Sozzani. 2d multi-nuclear nmr, hyperpolarized xenon and gas storage in organosilica nanochannels with crystalline order in the walls. *Journal of the American Chemical Society*, 129(27):8566–8576, 2007. PMID: 17579407.

[7] Hoffmann Frank, Cornelius Maximilian, Morell Jürgen, and Fröba Michael. Silica-based mesoporous organic-inorganic hybrid materials. *Angewandte Chemie International Edition*, 45(20):3216–3251, May 2006.

[8] Berk Hess, Henk Bekker, Herman J. C. Berendsen, and Johannes G. E. M. Fraaije. Lincs: A linear constraint solver for molecular simulations. *Journal of Computational Chemistry*, 18(12):1463–1472, 1997.

[9] Frank Hoffmann, Maximilian Cornelius, Jürgen Morell, and Michael Fröba. Silica-based mesoporous organic–inorganic hybrid materials. *Angewandte Chemie International Edition*, 45(20):3216–3251, 2006.

[10] Shinji Inagaki, Shiyou Guan, Yoshiaki Fukushima, Tetsu Ohsuna, and Osamu Terasaki. Novel mesoporous materials with a uniform distribution of organic groups and inorganic oxide in their frameworks. *Journal of the American Chemical Society*, 121(41):9611–9614, Oct 1999.

[11] Shinji Inagaki, Shiyou Guan, Tetsu Ohsuna, and Osamu Terasaki. An ordered mesoporous organosilica hybrid material with a crystal-like wall structure. *Nature*, 416:304, 2002.

[12] W. L. Jorgensen, D. S. Maxwell, and J. Tirado Rives. Development and testing of the opls all-atom force field on conformational energetics and properties of organic liquids. *Journal Of The American Chemical Society*, 118(45):11225–11236, 1996.

[13] Mahendra P. Kapoor, Qihua Yang, and Shinji Inagaki. Self-assembly of biphenylene-bridged hybrid mesoporous solid with molecular-scale periodicity in the pore walls. *Journal of the American Chemical Society*, 124(51):15176–15177, Dec 2002.

[14] Clare F. Macrae, Ian J. Bruno, James A. Chisholm, Paul R. Edgington, Patrick McCabe, Elna

Pidcock, Lucia Rodriguez-Monge, Robin Taylor, Jacco van de Streek, and Peter A. Wood. Mercury csd 2.0 - new features for the visualization and investigation of crystal structures. *Journal of Applied Crystallography*, 41(2):466–470, 2008.

[15] Brian J. Melde, Brian T. Holland, Christopher F. Blanford, and Andreas Stein. Mesoporous sieves with unified hybrid inorganic/organic frameworks. *Chemistry of Materials*, 11(11):3302–3308, Nov 1999.

[16] D. Van der Spoel, E. Lindahl, B. Hess, G. Groenhof, A. E. Mark, and H. J. C. Berendsen. Gromacs: Fast, flexible, and free. *Journal of Computational Chemistry*, 26(16):1701–1718, 2005.

[17] Yong Wei, Xiaomin Li, Renyuan Zhang, Yong Liu, Wenxing Wang, Yun Ling, Ahmed Mohamed El-Toni, and Dongyuan Zhao. Periodic mesoporous organosilica nanocubes with ultrahigh surface areas for efficient co2 adsorption. *Scientific Reports*, 6:20769 EP –, Feb 2016. Article.

[18] Wang Wendong, Lofgreen Jennifer E., and Ozin Geoffrey A. Why pmo?: Towards functionality and utility of periodic mesoporous organosilicas. *Small*, 6(23):2634–2642, Oct 2010.

ENHANCED STEAM METHANE REFORMING SIMULATION BY MEANS OF THE COMPUTATIONAL PARTICLE FLUID DYNAMICS (CPFD) METHOD

A. Di Nardo, G. Calchetti, S. Stendardo

ENEA - Italian National Agency for New Technology, Energy and Sustainable Economic Development
Energy Technology Department - Production, Conversion and Efficient Use of Energy Division - Process and Energy Systems Engineering Laboratory
Casaccia Research Center , Via Anguillarese 301, 00123 S. Maria di Galeria - Rome - ITALY

ABSTRACT. This paper reports the modelling and simulation results of the Steam Methane Reforming (SMR) looping process, using sorbent and catalyst materials, by means of the Computational Particle Fluid Dynamics (CPFD) method, with an Eulerian-Lagrangian approach. The method resulted to be very powerful with respect to simulation time and computational resources saving, also due to the capability of the Barracuda® code to make use of the Graphics Processing Units (GPUs).

1 Introduction

Steam reforming of natural gas is the predominant process for hydrogen production on large-scale industrial applications and power production. The simultaneous CO_2 sorption is a convenient method to enhance H_2 production, by shifting the reactions equilibrium beyond their conventional thermodynamic limits and leading to more favourable conditions: the produced CO_2 reacts with a calcium based sorbent to make a solid carbonate, thus driving the reforming and water-gas shift reactions toward products. In Steam Methane Reforming (SMR) the natural gas is catalytically converted to H_2 rich gas with a co-present sorbent powder in a fluidised bed reactor.

2 Chemical kinetics

In presence of fluidized bed composed of CaO sorbent and catalyst agent, the SMR chemical reactions can be schematized as follows [1]:

Gas-gas phase

$$CH_4(g) + H_2O(g) \rightleftharpoons CO(g) + 3H_2(g) \quad \Delta H_{298} = 206 \text{ kJ/mol}$$

$$CO(g) + H_2O(g) \rightleftharpoons CO_2(g) + H_2(g) \quad \Delta H_{298} = -41 \text{ kJ/mol}$$

$$CH_4(g) + 2H_2O(g) \rightleftharpoons CO_2(g) + 4H_2(g) \quad \Delta H_{298} = 165 \text{ kJ/mol}$$

Gas-solid phase

$$CO_2(g) + CaO(s) \rightleftharpoons CaCO_3(s) \qquad \Delta H_{298} = -178 \text{ kJ/mol}$$

The reaction rates of the gas phase and gas-solid processes were evaluated using literature models. In particular, the kinetic expressions reported in [1] have been used for the gas phase reactions.
The intrinsic kinetics of the gas phase reactions are:

$$r_1 = \frac{\frac{k_1}{P_{H_2}^{2.5}}\left[P_{CO}P_{H_2O} - \frac{P_{H_2}^3 P_{CO}}{K_{eq1}}\right]}{DEN^2} \qquad r_2 = \frac{\frac{k_2}{P_{H_2}}\left[P_{CO}P_{H_2O} - \frac{P_{H_2}P_{CO_2}}{K_{eq2}}\right]}{DEN^2} \qquad r_3 = \frac{\frac{k_3}{P_{H_2}^{3.5}}\left[P_{CH_4}P_{H_2O}^2 - \frac{P_{H_2}^4 P_{CO_2}}{K_{eq3}}\right]}{DEN^2}$$

$$DEN = 1 + K_{CO}P_{CO} + K_{H_2}P_{H_2} + K_{CH_4}P_{CH_4} + K_{H_2O}\frac{P_{H_2O}}{P_{H_2}}$$

and the kinetic constants are reported in Table 1.

Table 1: Adsorption and reaction rate constants of the gas-phase reactions.

Adsorption constants:

$K_j = B_j exp\left(\frac{-\Delta H_j}{RT}\right) \qquad j = CO, H_2, CH_4, H_2O$

Species	Bj (bar^{-1})	ΔHj (J/mol)
CO	8.23×10^{-5}	-70650
H_2	6.12×10^{-9}	-82900
CH_4	6.65×10^{-4}	-38280
H_2O	1.77×10^{5}	88680

Reaction rate constants:

$k_i = A_i exp\left(\frac{-E_i}{RT}\right) \qquad i = 1,2,3$

Reaction	A_i (mol $bar^{0.5}$/ gcat s)	E_i (J/mol)
1	1.174×10^{12}	240100
2	5.43×10^{2}	67130
3	2.833×10^{11}	243900

The previously developed particle grain model (PGM) in [2] and [3] has been used for the carbonation reaction and the sorption-enhanced comprehensive reacting system, respectively. This grain model describes the simultaneous reaction and diffusion process within the particle, as a function of radial position and time on stream. It has been adapted and integrated in the commercial code to evaluate the CO_2 uptake occurring in the investigated loop. The sorbent conversion is related to three fundamental steps: chemical reaction (carbonation) on the surface of the active oxide grains, diffusion through particle pores that progressively reduce their diameter and volume because of the larger molar volume of carbonates with respect to oxides, diffusion through the solid product layer (carbonate) that progressively builds up on calcium oxide grains according a shrinking core model. The PGM model described in [3] assumes that the granular material is made of spherical particles. As far as the whole sorption mechanism of carbon dioxide is concerned, the CaO grains are supposed to be carbonated through the development of a $CaCO_3$ outer layer becoming progressively more compact and penetrated with increasing resistance by CO_2 molecules, which are bound to react on the underlying CaO core surface. A shrinking core approach was applied to the sorbent grains, characterized by a first order surface reaction as proposed in [4] and a product layer diffusion coefficient decreasing exponentially as a function of CaO conversion; the sorption grains volume increases progressively, with simultaneous reduction of solid particle porosity, due to the difference between molar volume of $CaCO_3$ and CaO: their ratio is somehow larger than 2. In [3], the sorption rate expression, obeying the above requirements is derived in details:

$$\frac{\partial X}{\partial t} = \frac{\sigma_{CaO}^0 k_s (1-X)^{2/3}\left(C_{CO_2} - C_{CO_2,eq}\right)}{1 + \frac{N_{CaO}^0 k_s}{2D_{PL}}\delta_{CaO}^0 \sqrt[3]{1-X}\left(1 - \sqrt[3]{\frac{1-X}{1-X+Xz}}\right)} = \frac{r_{CBN}}{N_{CaO}^0} \qquad D_{pl} = D_{pl,0} exp\left(-aX_{CaO}{}^b\right)$$

and the model constants are reported in Table 2.

Table 2: PGM model constants.

CaO moles per unit particle volume, N^0_{CaO}	21.9	kmol/m^3
Molar volume ratio, $z = V_{CaCO_3}/V_{CaO}$	2.18	-
Initial CaO grain diameter, δ^0_{CaO}	0.100 10^{-6}	m
CaO grain surface per unit particle volume, σ^0_{CaO}	2.22 10^{7}	m^2/m^3
Rate constant, k_s	5.95 10^{-7}	m^4/(kmol s)
Initial value of CO_2 solid diffusion coefficient, $D_{PL,0}$	2 10^{-5}	m^2/s
a	22.5	-
b	0.03	-

3 Simulation method and results

In the CPFD method, the gaseous phase is considered as a continuous fluid with its own density, temperature and velocity whereas the solid phase is modelled by means of a discrete Lagrangian phase. The gaseous and solid phases are fully coupled to material, momentum and energy transfer. Particularly the commercial code Barracuda® uses the multiphase particle-in-cell (MP-PIC) method as particle-flow solver for the simulation of the fluidized bed reactor. According to the MP–PIC technique [5] [6], the physical particles have been grouped depending on some parameters (e.g. size, composition, volume, mass density) in computational particles (called parcels). As a consequence, it was possible to model the SER reformer reactor with a high number of particles and relative low computational burden, since collisions between the particles are not directly evaluated but modelled as spatial gradient calculated on the Eulerian calculation grid via interpolated functions. For an accurate interpolation of the Lagrangian phase on the Eulerian grid the size of the physical particles have to be small enough compared to the Eulerian grid. To speed simulations, the code provides a highly parallelized implementation of particle trajectory evaluation in the Graphics Processing Units (GPUs). This use of the GPUs of CRESCO has allowed to accelerate the simulations gaining insights in the investigated complex multi-particle system.

The reactor is a cylinder of 0.2 m of diameter and is 2 m high. The bed material is composed of 10.2 kg of calcined dolomite (CaO and MgO) and 3.6 kg of catalyst (alumina) particles. Particles radius is $9x10^{-5}$ and $7.5x10^{-5}$ m, respectively. The fluidising gas is composed of 80% H_2O, 19.4% CH_4, 0.4% CO_2 and 0.2% H_2, by volume, at 873 K and 1.2 bar, and enters the reactor in the range of velocity 0.2-0.4 m/s. The computational grid is made of 10000 Cartesian cells, adapted at the walls.

Parametric analysis upon gas velocity have been performed to study both the hydrogen production and CO_2 content of the decarbonized product gas. This has permitted to evaluate the operating condition window, in term of gas flow rate where the bed show a good performance in term of methane conversion. The model has been validated with the experimental data reported in [7], and the comparison has been reported in Fig. 1a, 1b. In order to monitor the evolution during the separation of CO_2 and the reforming of CH_4, sensitivity analysis with regards to the sorbent conversion has been conducted. As reported in Fig. 1a four different simulations were performed with different initial conversion of the sorbent (X). A value of X=0 represents the initial condition of the CO_2 uptake (fresh sorbent), whereas X=0.75 is the average condition at the end of the experimental run (spent sorbent). As Fig. 1a shows, a good agreement with the experimental results is obtained, particularly at lower and larger CaO conversion values. Fig 1b shows a parametric analysis with regards to the space velocity. It is apparent that the range value of velocity 0.2 – 0.4 m/s is the optimal operating condition for the production of a H_2 rich gas from SMR. Finally, the characterisation of the hydrodynamic behaviour of the fluidized bed has been analysed in details. Particularly, the bubble formation and its velocity has been evaluated (Fig. 1c). This has allowed us to monitor bubbles evolution in a fluidized environment.

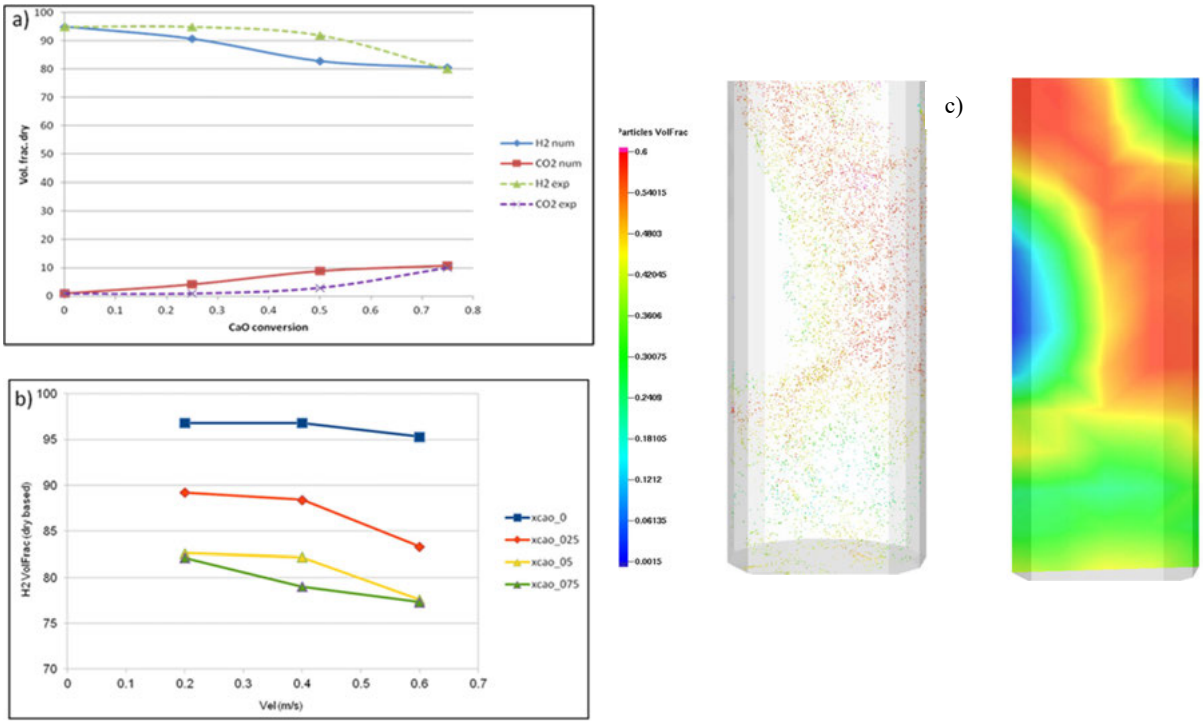

Fig.**1**: a) Experimental-numerical comparison, b) parametric analysis, c) particles volume fraction.

References

[1] J. Xu and J.F. Froment. Methane steam reforming, methanation and water-gas shift: I. Intrinsic kinetics. *AIChE J*ournal **35**, pp. 88–96, (1989).

[2] S. Stendardo and P.U. Foscolo. Carbon dioxide capture with dolomite: A model for gas–solid reaction within the grains of a particulate sorbent. *Chemical Engineering Science* **64**, pp. 2343–2352, (2009).

[3] S. Stendardo, L. Di Felice, K. Gallucci, P.U. Foscolo. CO_2 capture with calcined dolomite: the effect of sorbent particle size. *Biomass Conv. Bioref.* **1**, pp 149–161, (2011).

[4] S.K. Bhatia and D.D. Perlmutter. Effect of the product layer on the kinetics of the CO_2-lime reaction. *AIChE Journal*, **29**, pp. 79–86, (1983).

[5] M.J. Andrews and P.J. O'Rourke. The multiphase particle-in-cell (MP-PIC) method for dense particulate flows. *International Journal of Multiphase Flow* **22**, pp. 379–402, (1996).

[6] D.M. Snider. An incompressible three-dimensional multiphase particle-in-cell model for dense particle flows. *Journal of Computational Physics* **170**, no. 2, pp. 523–549, (2001).

[7] A. Di Carlo, I. Aloisi, N. Jand, S. Stendardo, P. U. Foscolo. Sorption enhanced steam methane reforming on catalyst-sorbent bifunctional particles: A CFD fluidized bed reactor model. *Chemical Engineering Science,* **173**, 428–442, (2017).

NEUTRONICS STUDIES FOR THE NOVEL DESIGN OF LOWER PORT IN DEMO

Davide Flammini[1], Andrea Colangeli[1,2], Fabio Moro[1], Rosaria Villari[1]

[1]*ENEA, Fusion Technical Unit, Nuclear Technologies Laboratory, Via Enrico Fermi 45, 00044 Frascati, Rome, Italy*

[2]*Department of Basic and Applied Sciences for Engineering, SAPIENZA – University of Rome, via Scarpa 14*

ABSTRACT. The conceptual design activity of the Demonstration Fusion Power Reactor (DEMO) is in progress within the EUROfusion Consortium. In this work neutronics studies are presented for a novel design of the lower port (LP). Two possible configurations of the LP have been investigated: the vacuum pumping port, with the pumping unit located inside the port, and an empty port designed for remote handling. For both configurations 3-dimensional Monte Carlo calculations have been performed with MCNP5 to assess the neutron flux inside and around the port and the nuclear heating in sensitive components. Different shielding configurations have been considered, by adding shielding blocks at the lower port entrance. Single and double wall port walls and closure plates with different thickness have been studied to reduce nuclear loads and neutron flux.

1 Introduction

The conceptual design activity of the Demonstration Fusion Power Reactor (DEMO) is in progress within the EUROfusion Consortium. The lower port (LP) in DEMO is of paramount importance because of its structural, operational and maintenance functions [1]. Previous version of the lower port (DEMO 2015) had a dedicated vertical LP for pumps, while the divertor replacement was foreseen by the main lower port, 45° inclined with respect to the horizontal plane. The present baseline model (EU DEMO1 2017 [2]) foresees a single 45° LP, while, in the novel design, the inclination has been reduced and a kink at a radial position close to the toroidal field (TF) coils connects the port to a horizontal duct. This study is devoted to the neutronics analysis of components around the novel design of the LP. In particular, two possible configurations of LP have been analysed: LP for vacuum pumping (VP), a configuration in which the LP hosts a vacuum torus pumping unit, i.e. the metal foil (MF) pump and the linear diffusion (LD) pump, and a configuration in which the LP is dedicated to the remote handling (RH), so it is completely empty. Additional shielding elements have been integrated in the structure to reduce the radiation streaming through the pumping duct that can produce very large nuclear loads.
MCNP [3] calculations have been performed using the 3-D 11.25° sector 2017 baseline DEMO, updated to have a 22.5° model in which the new LP design has been integrated instead of the baseline LP (see figure 1). For both VP and RH configurations, several variants have been analysed. Variants differ for the insertion of several shielding blocks, for the dimension and composition of the port walls and for the thickness of the port plug. In figure 1 the CAD of the LP is reported. JEFF 3.2

nuclear data library [4] has been used in the calculations. A total of 5 different input files have been used, for each of them $3 \cdot 10^9$ source neutrons have been simulated, in coupled neutrons and gamma transport. Calculations were performed on CRESCO4 cluster, using 512 cores.

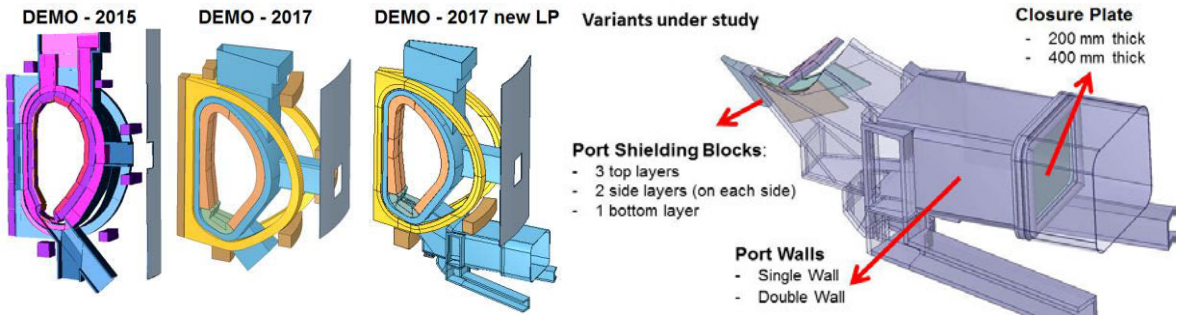

Fig. 1: CAD models of the DEMO-2015, DEMO 2017 baseline and DEMO with new LP, whole sector (left) and of the LP, with variants under analysis (right).

Closure plate, shielding blocks and port walls are all made of SS-316-LN. Single port walls (SW) are 60 mm thick. Double port walls (DW) are two 60 mm thick walls with 100 mm of water in between them, represented with a homogenized mixture.

2 Results and discussion

Nuclear quantities have been tallied with cell and mesh track length estimators to calculate flux or nuclear heating. Nuclear heating includes the energy deposited by neutrons (generated from both plasma and nuclear reactions) and by photons (generated by nuclear reactions). Meshes have 10x10x10 cm^3 voxels and the relative statistical uncertainties are within 10%, at 1 σ, in all the region of interest (i.e. inside the LP). REF configuration refers to LP without shielding and with single wall, V1 uses all the additional shielding elements and a double wall structure, V2 has single wall and additional shielding. In figure 2 the neutron flux maps are shown for VP and RH configurations. In table 1 the neutron flux behind the closure plate is reported.

Table 1: Neutron flux behind the Closure Plate. Statistical uncertainty is ± 8% in the worst case.

Variant	Neutron flux ($n/cm^2/s$)	Ratio to VP_REF
VP_REF	$1.16 \cdot 10^{10}$	1.00
VP_V1	$9.1 \cdot 10^{8}$	0.08
VP_V2	$9.5 \cdot 10^{9}$	0.82
RH_REF	$2.9 \cdot 10^{10}$	2.50
RH_V1	$4.0 \cdot 10^{9}$	0.34

Nuclear heating density has been calculated on the shielding blocks, when present, on the vacuum pumping unit, separately on the LD pump and on the MF pump, and on the conductor of the TF coil, in the region around the LP. These results are summarized in table 2, where the average values on the whole components are reported. The maximum nuclear heating density for MF pump is 420 W/m^3 in REF configuration and a small variation is observed among the variants.

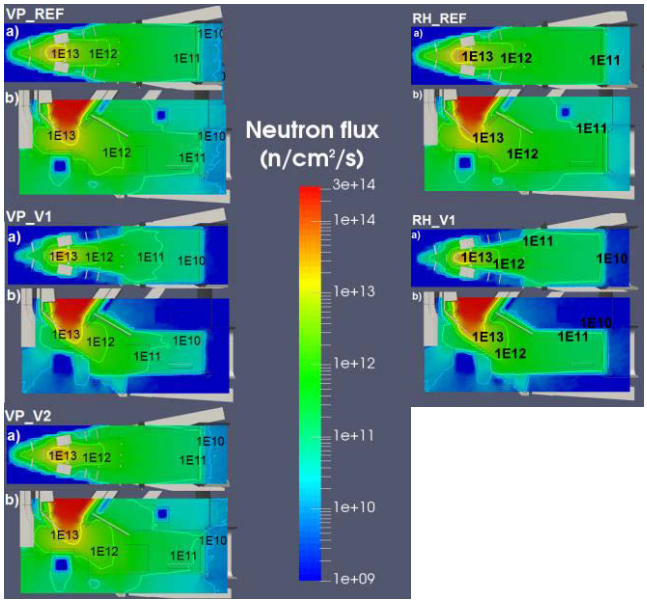

Fig. 2: Neutron flux maps for VP and RH configurations, REF, V1 and V2 variants. Vertical cut along the central axis (b) and horizontal cut along the red line (a).

Much larger nuclear heating densities are observed in the shielding blocks. In this case the nuclear heating does not depend on the configuration or on the variant, because the shielding blocks are mostly subjected to a direct irradiation from the pumping duct.
In the case of the CP we observe a behavior which is similar to that of the neutron flux: the vacuum pumping unit acts as a shield, reducing the loads on the CP.

Table 2: Nuclear heating density on specific components for the LP configurations. Statistical uncertainties are within 1%.

Config.	Nuclear Heating density (W/m^3)x10^3					
	Pumps		Shielding blocks			CP
	MF	LD	Top	Side	Bottom	
VP_REF	0.42	0.17	-	-	-	0.37
VP_V1	0.40	0.15	24.3	66	17.7	0.15
VP_V2	0.31	0.13	24.4	60	-	0.30
RH_REF	-	-	-	-	-	1.25
RH_V1	-	-	24.1	65.1	17.7	0.59

Nuclear heating density on the TF coil conductor has been calculated as well. The nuclear loads on this component are of paramount importance because the operation of the reactor is dependent from this quantity. In particular, a strict design limit has been fixed at 50 W/m^3 [5]. In order to assess the nuclear loads as a function of the poloidal position, the TF coil conductor has been segmented in 6 cells (see figure 3). Results are reported in table 3, only for VP, being RH values within the statistical uncertainty.

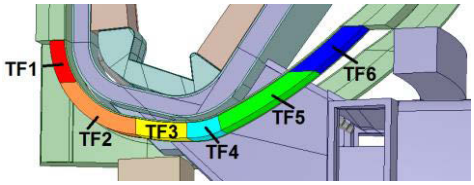

Fig. 3: Segmentation of TF coil conductor.

Table 3: Nuclear heating density in TF coil conductor segments. Statistical uncertainty is ± 10% in the worst case.

Segment	Nuclear heating density (W/m^3)		
	REF	**V1**	**V2**
TF1	180	19	176
TF2	$4.51 \cdot 10^3$	705	$4.66 \cdot 10^3$
TF3	$1.54 \cdot 10^4$	$3.30 \cdot 10^3$	$1.50 \cdot 10^4$
TF4	$5.05 \cdot 10^3$	386	$3.74 \cdot 10^3$
TF5	$1.21 \cdot 10^3$	44	781
TF6	345	9.38	266

Nuclear heating density in TF coil conductor results well above the design limit. The most critical part is segment #3 located poloidally in correspondence of the pumping duct with a value 300 times the limit in REF and V1 configuration. The effectiveness of the DW in reducing the load is clearly visible on this segment: it allows a decrease of the nuclear heating density of about a factor 5, i.e. 60 times the limit. The effect of the shielding blocks is also marginal: a reduction of about -40% is observed but only in TF4 and TF5, comparing REF and V2. The segments in which the design limit is respected are TF1 and TF6 in all variants, and TF5, but only in V1 variant.

In summary, two configurations of the novel design of DEMO LP have been analysed. The double wall structure is very effective in lowering the neutron flux thanks to the presence of water inside the walls. Instead the nuclear heating inside the port is not strongly dependent from the wall configuration. The nuclear heating of the shielding blocks is less than 10^5 W/m^3, but, being exposed to direct irradiation from plasma, large gradients are expected, so that active cooling should be considered. On the vacuum pump, the nuclear heating density is below 500 W/m^3 in the worst case. Also the heating of the port closure plate is very low, being 370 W/m^3 at its peak value. Nuclear heating on TF coil conductor has been calculated and it comes out to be a major issue: in the best possible variant a value 60 times the limit is observed. Additional studies to reduce the nuclear heating of the TF coil are required.

References

[1] C. Gliss, et al., Initial integration concept of the DEMO lower horizontal port, 30th Symposium on Fusion Technology, September 2018, Giardini Naxos.

[2] EU DEMO1 2017 (IDM link: https://idm.euro-fusion.org/?uid=2NE9JA)

[3] X-5 Monte Carlo Team MCNP – A general Monte Carlo N-particle Trans-port Code, Version 5, Los Alamos National Laboratory, LA-UR-03-1987, 2003, https://mcnp.lanl.gov/.

[4] The JEFF-3.2 Nuclear Data Library, http://www.oecd-nea.org/dbforms/data/eva/evatapes/jeff_32/ NUCLEAR ENERGY AGENCY, OECD

[5] U. Fischer et al., Neutronics requirements for a DEMO fusion power plant, Fusion Engineering and Design 98-99 (2015) 2134-2137. doi:10.1016/j.fusengdes.2015.02.029.

MODELING OF ENERGETIC PARTICLE DRIVEN INSTABILITIES USING HYBRID MAGNETOHYDRODYNAMICS-GYROKINETIC CODES

Sergio Briguglio[1], Giuliana Fogaccia[1*],Gregorio Vlad[1] and Tao Wang[2]

[1]*ENEA, Dipartimento FSN, C. R. Frascati, via E. Fermi 45, 00044 Frascati (Roma), Italy*

[2]*Institute for Fusion Theory and Simulation and Department of Physics, Zhejiang University, Hangzhou, People's Republic of China*

ABSTRACT. The main activities in 2017, regarding numerical simulation of interaction between Alfvén modes and energetic particles in nuclear fusion devices and using CRESCO HPC facilities, are described. In Sec.1 a possible mechanism to transfer the power associated with fusion-generated alpha particles to the thermal ions through the interaction with high- and low-frequency waves, is investigated; in Sec.2 results related to the code HYMAGYC, for a realistic shaped cross section model scenario, are show and retain the effects of the radial orbit extent (FOW), finite Larmor radius (FLR) and magnetic compression; in Sec.3 the results of a set of simulations of Alfvén modes driven by an energetic particle population have been considered, with the specific aim of comparing energetic particle radial transport between single-*n* and multiple-*n* simulations (*n* being the toroidal mode number); finally, in the last section, linear stability properties and shear Alfvén fluctuation spectra of a typical DTT reference scenario are investigated by HMGC code.

1 Investigation of the mechanism of alpha channelling

Alpha channelling, originally proposed by N. Fisch in 1992, is a mechanism to transfer the power associated with the fusion-generated alpha particles to the thermal ions through the interaction with an externally excited wave, rather than relying on classical electron slowing down that requires the fusion plasma to be at equipartition (Te≥Ti). In its simplest form, the mechanism relies on the interaction between fusion alphas and a high-frequency wave (typically a mode-converted Ion Bernstein Wave). The high-frequency wave extracts the kinetic energy associated with perpendicular motion through a resonant interaction that breaks the magnetic moment invariance. The extraction of energy is associated with a radial diffusion towards the plasma edge.
The goal of the investigation is to put on a firm theoretical basis the idea of alpha channelling and to determine the optimal operating conditions for its demonstration on present experiments in view of the potential application to ITER and DEMO.
An explicit analytical form for the alpha particle distribution function under the effect of a high-frequency wave has been obtained by solving the Fokker-Planck equation in the presence of a single high-frequency wave[1].

This distribution function has been adopted as the initial distribution function in hybrid MHD-particle simulations performed by the XHMGC code. A numerical population of more than 300 milions of particles has been evolved by means of a 24-hours simulation on 24x16 Cresco4 cores. It has been shown that Alfvén modes can be driven unstable by the free energy sources yielded by the phase-space gradients presented by the alpha particle distribution. Further investigation is in progress, in order to assess whether the Alfvén modes are able to 1) extract a signifiant fraction of

the residual kinetic energy from the alpha particle distribution; 2) displace the exhausted alphas by a large fraction of the minor radius; 3) transfer the energy extracted form the alphas to the bulk ions.

2 Activity related to the code HYMAGYC, for a realistic shaped cross section AUG model scenario

The activities related to the code HYMAGYC have continued in 2017 studying the effects of the energetic particles Finite Larmor Radius (FLR) and the effect of the magnetic compression, for a realistic shaped cross section AUG model scenario [2].
The AUG reference case has been identified and analyzed, in the previous year, in collaboration with the NLED Enabling Research group, both characterizing the Alfvén continua for different toroidal mode numbers (n=1,2,3) and studying the global, ideal MHD TAEs present in such equilibrium. A maxwellian energetic particle population of deuterium was assumed, characterized by a dimensionless thermal velocity $v_{th,H}/v_{A0}\approx 0.257$, being v_{A0} the on-axis Alfvén velocity and corresponding to a temperature value $T_H=0.093$ MeV, constant along the radial coordinate.
In the HYMAGYC code, the equations of motion of the energetic particles always retain the radial orbit extent (Finite Orbit Width, FOW effect), while the FLR effect may or may not be considered, both in the energetic particles equations of motion and in the computation of energetic particles pressure tensor. When considering the FLR effects, several scalar quantities, proportional to perturbed fields, must be computed in the position of each particle along the Larmor orbit, and, then, averaged over the gyroangle. The magnetic compression effect can also be retained, by taking into account in the equations of motion of the energetic particles the perpendicular (to the equilibrium magnetic field) component of the perturbed vector potential δA.

In Figure 1 the power spectrum of the electrostatic potential $|\phi(\omega,s)|^2$ in the plane $(\omega/\omega_{A0},s)$ is shown for the reference AUG case with n=1 and $T_H=0.093$ MeV; here ω/ω_{A0} is the frequency normalized to the on-axis Alfvén frequency, and s is the radial coordinate (the square root of the poloidal flux function normalized to unity at the edge). An unstable Reversed Shear Alfvén Eigenmode (RSAE) driven by the energetic particles appears as the most unstable mode, being localized in frequency at $\omega/\omega_{A0}=0.081$, just below the lower Alfvén continuum, and radially at s=0.39 close to the location of the minimum of the q-profile.

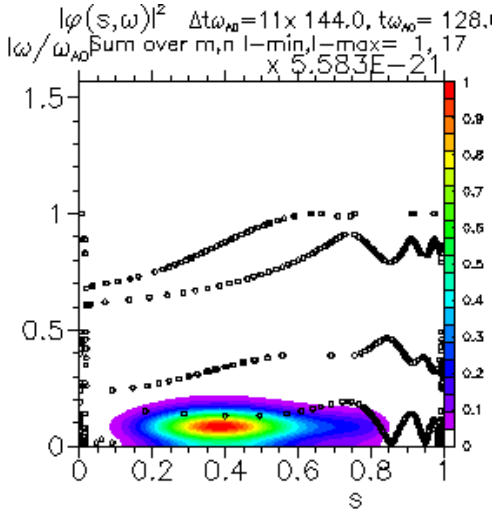

Fig.1: power spectrum of the electrostatic potential $|\phi(\omega,s)|^2$ in the plane $(\omega/\omega_{A0},s)$; also the Alfvén continua are shown (circle symbols).

The growth rate of the n=1 RSAE vs. the energetic particle temperature is shown in Figure 2 (blue curve). Similar trends are obtained for n=2 and n=3 (red and black curves, respectively), where an Energetic Particle Mode (EPM) is observed as the most unstable one. The modes are localized, radially, close to the maximum of the energetic particle pressure gradient.

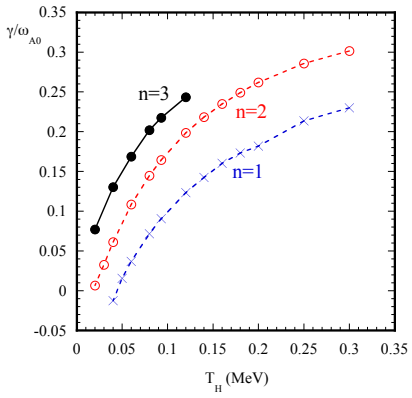

Fig.2: growth-rate vs. T_H, for the most unstable n=1 (blue curve), n=2 (red curve), n=3 (black curve) modes.

Starting from the simulation of Figure 1, in which only the FOW effect is retained, other simulations have been performed, considering, one by one, the effect of magnetic compression and the FLR effect in the equations of motion of the energetic particles. The most unstable mode observed is always a RSAE, with small variations about radial localization, frequency and growth rate (see Table 1). Both the FLR and the $A_\perp$ effects appear to be stabilizing.

	s	ω/ω_{A0}	γ/ω_{A0}
FOW	0.39	0.081	0.091
$A_\perp$	0.36	0.060	0.060
FLR in equations of motion	0.38	0.083	0.078

Table 1: radial localization s, normalized frequency ω/ω_{A0}, and growth rate γ/ω_{A0}, retaining only FOW effects, and one by one the contribution of the perturbed perpendicular vector potential or the FLR effects in equations of motion.

3 Comparison of energetic particle radial transport between single-n and multiple-n simulations of Alfvénic modes

The results of a set of simulations of Alfvén modes driven by an energetic particle population have been considered, with the specific aim of comparing energetic particle radial transport between single-*n* and multiple-*n* simulations (*n* being the toroidal mode number). The hybrid reduced $O(\varepsilon^3_0)$ MHD gyrokinetic code HMGC [3, 4, 5] is used ($\varepsilon_0 \equiv a/R_0$ being the inverse aspect ratio of the torus,

with a and R_0 the minor and major radius, respectively), retaining both fluid (wave-wave) and energetic particles nonlinearities. The code HMGC retains self-consistently, in the time evolution, the wave spatial structures as modified by the energetic particle (EP) term. These set of simulations have taken benefit from the EUROfusion Project HYMHDGK on Marconi-fusion HPC.

A model equilibrium has been considered, rather than a specific experimental device, with the aim of studying how the dynamics of the EP driven Alfvénic modes changes when considering single-n or multiple-n simulations, while keeping all the other parameters fixed. A circular, shifted magnetic surface, static equilibrium has been considered, characterized by a large aspect ratio (ε_0=0.1) and a parabolic safety factor profile $q(r)=q_0+(q_a-q_0)(r/a)^2$ with q_0=1.1 and q_a=1.9 being the on-axis and edge safety factor, respectively. A bulk ion density profile $n_i(r) \propto (q_0/q(r))^2$ has also been assumed, in order to have the toroidal gap radially aligned, for all the mode considered. Regarding the EPs, an isotropic Maxwellian distribution function has been considered.

Simulations with toroidal mode numbers $1 \leq n \leq 15$ have been considered. For the specific energetic particle drive considered, single-n simulations (see Fig. 3, left frame) are either stable (n=1), or weakly unstable (n=2,3,13,14,15), or strongly unstable ($4 \leq n \leq 12$), with $4 \leq n \leq 12$ modes exhibiting similar growth-rates, while n=4 the largest saturated amplitude. A variety of modes are observed (TAEs, upper and lower KTAEs, EPMs) during the linear growth phase. All the strongly unstable modes ($4 \leq n \leq 12$) exhibit pronounced (both up and down) frequency chirping at saturation [6, 7, 8, 9, 10, 11]. Nevertheless, no appreciable global modification of the energetic particle density profile is observed at saturation for the unstable modes.

A multiple-n simulation is also shown in Fig. 3, right frame, to be compared with the single-n ones. The same Fourier toroidal mode spectrum of the set of single-n simulations has been considered (Fig. 3, left frame). Note that the n=0 Fourier component has been considered to be fixed in time; all the numerical parameters of the multiple-n simulation have been kept the same of the single-n ones, i.e., equilibrium, spatial grids and energetic particle parameters. The multiple-n, fully nonlinear simulation exhibits an appreciable broadening of the energetic particle radial density profile at saturation, thus showing an enhanced radial transport w.r.t. the single-n simulations. Moreover, the sub-dominant modes are strongly modified by the nonlinear coupling, which results both from the MHD and from the energetic particle terms.

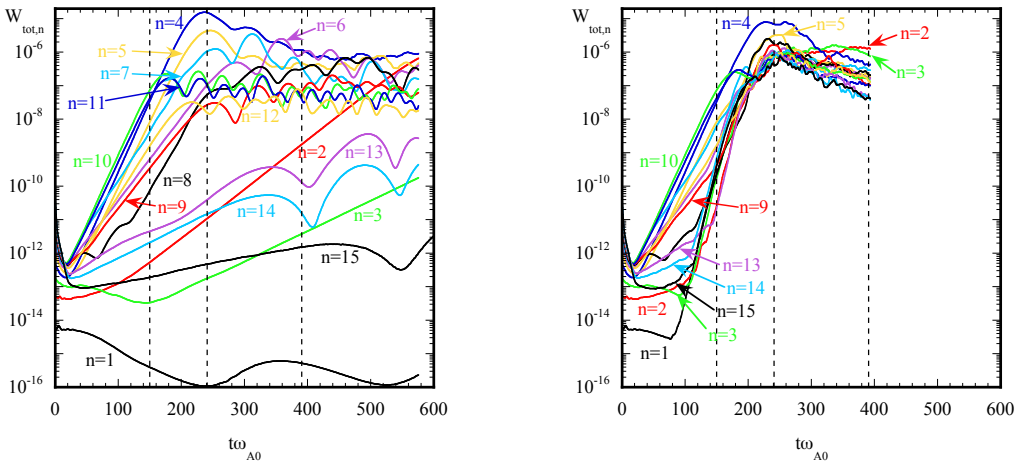

Fig.3: Single-n simulations (left frame) compared with the multiple-n simulation (right frame): time evolution of the total (kinetic plus magnetic) MHD energy content for each toroidal mode number n considered $W_{tot;n}$

Acknowledgments: This work has been carried out within the framework of the EUROfusion Consortium and has received funding from the Euratom research and training programme 2014-2018 under grant agreement No 633053. The views and opinions expressed herein do not necessarily reflect those of the European Commission. Part of the computing resources and the related technical support used for this work have been provided by the EUROfusion High Performance Computer (Marconi-Fusion) hosted by CINECA Bologna (Italy) and part by the CRESCO/ENEAGRID High Performance Computing infrastructure and its staff.

4 Resonant energetic particle orbit width and Alfvénic fluctuation linear stability property in the Divertor Tokamak Test facility

Analytical theory [12] predicts that for Alfvénic fluctuations in tokamaks, the maximum drive of energetic particles (EPs) for changing toroidal mode number n occurs when the perpendicular (w.r.t. equilibrium magnetic field) wavelength of the underlying fluctuation is of the order of characteristic orbit width of resonant EPs, because of orbit averaging. In the study of shear Alfvén fluctuation linear stability property of a Divertor Tokamak Test (DTT) facility [13] reference scenario by HMGC, resonant EP magnetic drift orbit width ρ_d is estimated numerically by test particle method, and it is shown to be responsible for the high most unstable mode number found in the simulations [14]. This further confirms the anticipation from analytical theory, and is consistent with the DTT target design.

The test particles are initialized as a sample of resonant EPs, by fixing two constants of motions (M,C) and distributing radially. Test particle ρ_d is estimated by its unperturbed orbit in the equilibrium magnetic field. For magnetically trapped particles, ρ_d could be easily given as $\rho_d = ½ (r_{outer} - r_{inner})$, where r_{outer} and r_{inner} are respectively, the outer and inner radial coordinates when the particle crosses the equatorial plane along one orbit. However, this method cannot be simply applied to passing particles, due to the fact that the two crossings occur on opposite sides of the tokamak equatorial plane. Thus, finite Shafranov shift $\Delta(r)$ must be taken into account, and ρ_d could be estimated as $\rho_d = ½ (r_{outer} - r_{inner}) \pm \Delta(r_\psi)$, with plus and minus signs apply for counter- and co-passing particles, respectively. Here, r_ψ is the radial coordinate of the flux surface, and could be given by $r_\psi = ½ (r_{outer} + r_{inner})$. Fig. 4 shows the radial profiles of ρ_d for trapped, co- and counter-passing test particle populations, in a n = 6 TAE case driven unstable by collective resonant interactions with both trapped and passing EPs. In addition, ρ_d of passing test particles without Δ correction are also shown for comparison. We can see that without the Δ correction, the same method of trapped particles gives a rather significant error for passing particles, and the two profiles of co- and counter-passing test particles converge when the Δ correction is taken into account.

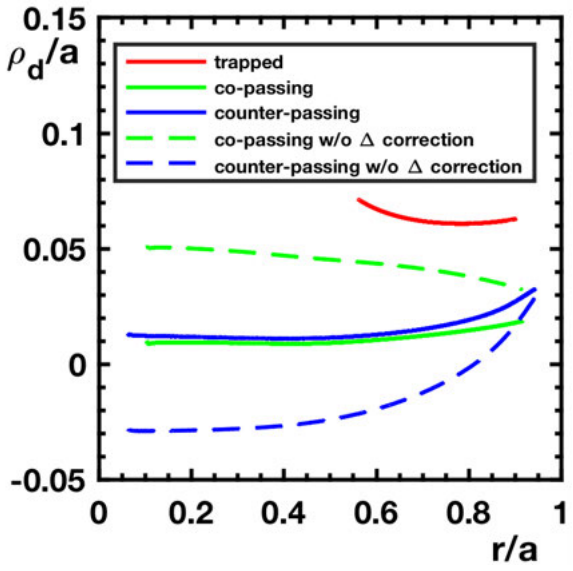

Fig. 4: Numerically estimated ρ_d of trapped (red solid curve), co-passing (green solid curve) and counter-passing (blue solid curve) test particles. ρ_d of co-passing (green dashed curve) and counter-passing (blue dashed curve) test particles without Δ correction are also shown for comparison.

From Fig. 4, we can also see that there is a clear difference of trapped and passing resonant EP orbit widths, which suggest a significant difference of most unstable mode numbers excited by their respective wave-EP resonances. In the study of linear stability properties of the TAE-like modes, the most unstable mode number is found to be n ~ O(10), as shown in Fig. 5(a). This is consistent with the criterion k ρ_d ~ 1 for the most unstable mode number, where k is the perpendicular wave number, and could be estimated from the mode structures. Fig. 5(b) shows numerical calculations of k ρ_d for resonant trapped, co- and counter-passing EPs. We could see that the most unstable mode number excited by wave-EP resonant interactions with trapped EPs is n ~ O(10), and the one due to resonances with passing EPs is n > 10. Thus, the most unstable mode number n ~ O(10) found in our simulations lies in between of the two limits, and is consistent with the resonance analysis as well as the ordering of ρ_d. This is also consistent with the DTT objectives, as DTT aims at creating DEMO relevant plasma edge conditions, and the characteristic EP orbit width in DTT is expected to be significantly smaller than in present day devices.

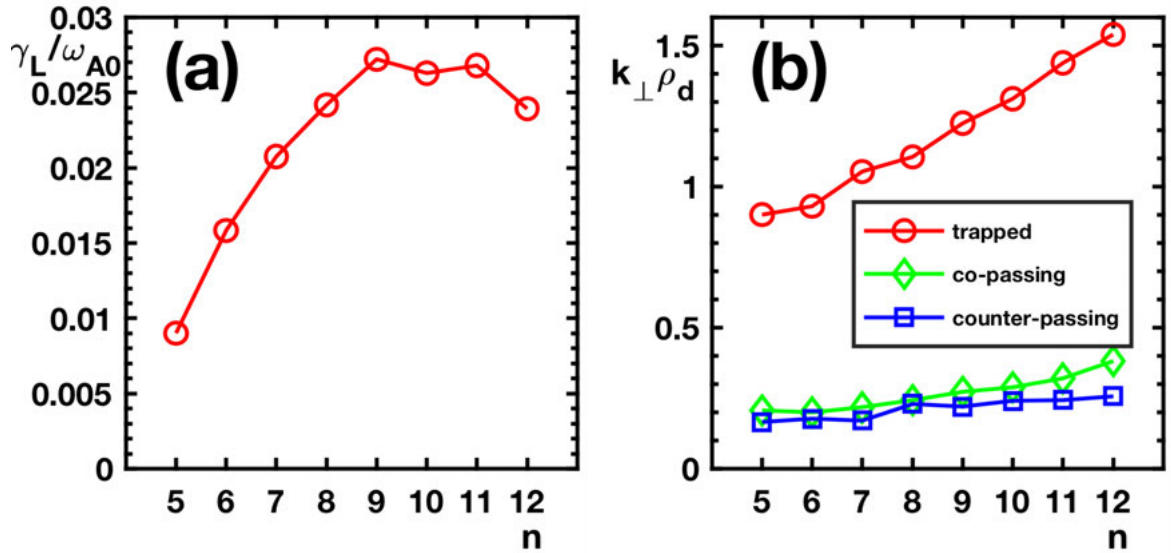

Fig. 5: (a) Linear growth rate γ_L of the TAE-like modes as a function of n; (b) numerical calculations of k ρ_d versus n for resonant trapped (red), co-passing (green) and counter-passing (blue) EPs, in the same cases considered in panel (a).

References

[1] Cianfrani F., Romanelli F. "*On the optimal conditions for alpha-channelling*", Nuclear Fusion **58**, (2018) 076013 (16pp)

[2] Lauber P. et al., NLED- AUG reference case, http://www2.ipp.mpg.de/~pwl/NLED_AUG/data.html

[3] Briguglio S., Vlad G., Zonca F. and Kar C. "*Hybrid magnetohydrodynamic-gyrokinetic simulation of toroidal Alfvén modes*", 1995 Physics of Plasmas, 2 3711-3723

[4] Vlad G., Kar C., Zonca F. and Romanelli F. "*Linear and non-linear dynamics of Alfvén eigenmodes in tokamaks*", 1995 Physics of Plasmas, 2 418-441.

[5] Wang X., Briguglio S., Chen L., Di Troia C., Fogaccia G., Vlad G. and Zonca F. "*An extended hybrid magnetohydrodynamics gyrokinetic model for numerical simulation of shear Alfvén waves in burning plasmas*", 2011 Phys. Plasmas, 18 052504

[6] Chen L. and Zonca F. "*Physics of Alfvén waves and energetic particles in burning plasmas*", 2016 Rev. Mod. Phys. 88 015008, DOI: 10.1103/RevModPhys.88.015008

[7] Zonca F., Chen L., Briguglio S., Fogaccia G., Vlad G. and Wang X. "*Nonlinear dynamics of phase space zonal structures and energetic particle physics in fusion plasmas*", 2015 New J. Phys. 17 013052

[8] Vlad G., Fusco V., Briguglio S., Fogaccia G., Zonca F. and Wang X. "*Theory and modeling of electron fishbones*", 2016 New J. Phys. 18 105004

[9] Berk H.L., Breizman B.N. and Petiashvili N.V. "*Spontaneous hole-clump pair creation in weakly unstable plasmas*", 1997 Phys. Lett. A 234 213

[10] Breizman B.N., Berk H.L., Pekker M., Porcelli F., Stupakov G.V. and Wong K.L. "*Critical nonlinear phenomena for kinetic instabilities near threshold*", 1997 Phys. Plasmas 4 1559

[11] Berk H.L., Breizman B.N., Candy J., Pekker M. and Petiashvili N.V. "*Spontaneous hole–clump pair creation*", 1999 Phys. Plasmas 6 3102

[12] Zonca F. and Chen L. *Theory of toroidal Alfvén modes excited by energetic particles in tokamaks. Phys. Plasmas* **3**, 323 (1996).

[13] Albanese R., Pizzuto A., WPDTT2 Team, and DTT project proposal contributors. The DTT proposal. A tokamak facility to address exhaust challenges for DEMO: Introduction and executive summary. *Fusion Eng. Des.* **122**, 274 (2017).

[14] Wang T., Qiu Z., Zonca F., Briguglio S., Fogaccia G., Vlad G., and Wang X. "*Shear Alfvén fluctuation spectrum in Divertor Tokamak Test facility plasmas*". PHYSICS OF PLASMAS 25, 062509 (2018).

A First Numerical Experiment of High-Pressure Methane Oxy-Combustion in a Supercritical CO2 Environment

E. Giacomazzi[1]*, D. Cecere[1], N.M. Arcidiacono[1] and F.R. Picchia[1]

[1]*ENEA, DTE-PCU-IPSE, S.P. 081, Via Anguillarese 301, 00123, Rome, Italy*

Abstract. The aim of this work is to investigate the role of radiant transfer of energy in turbulent non-premixed methane oxy-combustion in an atmosphere rich in CO2 at supercritical conditions by means of Large Eddy Simulation. A simple shear-layer configuration typical of slot burners is considered: the fuel is CH4 and flows through the central slot, the oxidant O2/CO2 (90both sides of the slot, and a pilot flame is imposed at the inlet between the two streams of reactants to force ignition. Another CO2 stream coflows.

1 Introduction

The Radiative Transfer of Energy (RTE) is a very important mechanism in several applications. Emission and absorption coefficients of gases increase proportionally to the concentration of the participating species, and hence to the mixture pressure for a given species mass or molar fraction. Besides, the spectral coefficients vary with temperature but also with pressure. Increasing pressure results in spectral line broadening, mainly due to molecular collisions (since the gas density increases) [4], up to wider and more overlapping lines than at lower pressures: the result is that the gas becomes grayer (opaque).

This work is devoted to numerical simulation of methane oxy-combustion in supercritical carbon dioxide at 300 bar. The numerical simulations are performed by means of the in-house parallel code HeaRT and ENEAs supercomputing facility CRESCO [6]. Fully compressible Navier-Stokes equations coupled to the Peng-Robinson cubic equation of state for real gases in its improved translated volume formulation are solved adopting the Large Eddy Simulation approach. The dynamic Smagorinsky and the LTSM [3] subgrid scale models are used for turbulence and combustion closures. Among the diffusive mechanisms only the Dufour effect is neglected; transport properties are accurately calculated. A simplified chemical mechanism consisting of 4 reactions and 6 species developed for oxycombustion is adopted [1, Table 2]. The M1 radiant transfer of energy model is adopted without considering turbulence-radiation interactions. The radiant transfer of energy is also taken into account by means of the M1 diffusive model. For the time being, turbulence-radiation interaction is neglected, although it is expected to play an important role in flame cooling at the highpressure conditions of the present simulations. Another simplification is the adoption of the individual species Planck mean absorption coefficients typically used at atmospheric pressure. Since they are expected to increase by increasing pressure, the effect of multiplying them by 1000 is investigated.

*Corresponding author. E-mail: eugenio.giacomazzi@enea.it.

2 The Geometry and Conditions

The numerical experiment here simulated has a nominal pressure around 300 bar and consists in a simple shear-layer; the flow is confined by means of two no-slip adiabatic walls (at left and right of the domain). At the bottom of the computational domain there is the inlet, while the outlet is located at the top. Simulations are perfomed in a two-dimensional framework to reduce computational time. The domain Y x Z is 8 x 10 mm, Y and Z being the transversal and the streamwise dircetions, respectively: it is discretised by means of 396 x 700 nodes.

The fuel is CH4 and is injected centrally at 50m/s and 388K; its width is 4 x 10^{-4} m. The oxidant O2/CO2 mixture flows on both sides of the methane, and a pilot flame is imposed at the inlet between the two streams of reactants to force ignition. Each oxidant jet flows at 100 m/s and 450 K; their width is 1.95 x10^{-4} m. The pilot flames imposed at the inlet exhibit a temperature distribution ranging from 900 to 2049 K and a coherent distribution of chemical species; such data come from separate calculations previously performed; these hot gases flow at 5m/s and are 10^{-4} m widen. Adjacent to each of the oxidant streams, there is a coflowing stream of CO2 at 50 m/s and 973 K.

Three simulations are performed. The first, without considering the radiant transfer of energy (case NO-RTE); the second, switching on the M1 model with two different levels of absorption: in the case named 1 x k_P the individual species Planck mean absorption coefficients used at atmospheric pressure are adopted, while in the case 10^3 x k_P they are intensified by a factor 10^3.

2.1 Effect of Radiant Transfer of Energy

Comparing results obtained without considering the RTE model with those obtained using different intensification factors of the Planck mean absorption coefficients, very little differences appear in the flame. This happens despite the large differences in the radiation source/sink term of the energy transport equation shown in Fig. 1 (left). This behaviour can be easily understood by comparing the energy budgets of the different terms contributing to the total energy transport and shown in Fig. 1 (right). The order of magnitude of the work done by the gravity force is 10^5 W/m^3; the viscous work is of the order of 10^8 W/m^3; since they are order of magnitudes lower than the other terms, they are not shown. Then, in the ordered list of budgets there is the radiative source term with 10^{10} W/m^3, followed by the heat diffusion term with 10^{11} W/m^3. It can be concluded that in the present simulation the effect of radiant transfer of energy is negligible even with the intensifying factor 10^3 for the k_P . However, accurate calculation of the Planck mean absorption coefficients from high-resolution spectroscopic databases is necessary to really understand if the intensification factor 10^3 here adopted is justifiable, sufficient or not. Besides this, it is reminded that turbulence/radiation interaction has not been taken into account in this work, although its contribution is expected to be enhanced in high-pressure combustors [5, 2].

It is observed that radiation cooling is active in the hottest regions of the flame but it produces a negligible effect, i.e., peak temperatures do not decrease due to radiation transport. As a matter of fact, the competition between the enhanced radiative cooling expected and the enhanced chemical kinetics (both due to the high pressure) is here dominated by chemistry, in agreement with the heat release budget that is four order of magnitudes greater than the radiative budget. Instantaneous distributions of the radiative source/sink term show that it is localized in thin layers. Although not shown, the results evidenced that radiative cooling (associated to negative values of S_{rad}) in this flame is limited to a very thin layer localized around the stoichiometric mixture fraction and it is more frequent in the hot products side.

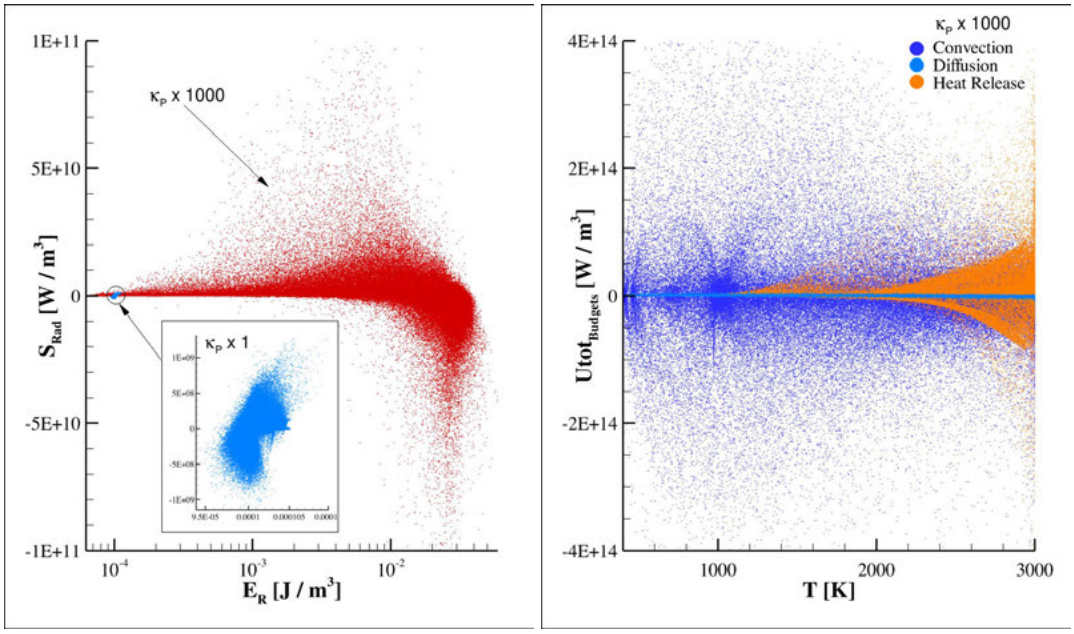

Figure 1: Instantaneous distributions of the radiative source term in the total energy transport equation versus the radiant energy density for two intensifying factors of the Planck mean absorption coefficient κ_P (left). Instantaneous distributions of energy budgets related to convection, diffusion and heat release terms contributing to the total energy transport equation (right); contributions from viscous and gravity force works are lower and hence not reported.

Once clarified that in the present simulations the effect of radiation is negligible, lets examine the structure of the flame. The flame is stably anchored, showing small reacting pockets mainly aligned in the streamwise direction close to the injection, and evolving into larger scale reacting regions moving downstream, as revealed by the temperature snapshot in Fig. 2 (left). The reacting structures are thinner than those typically encountered at lower pressures: this is due to the accelerated chemical kinetics promoted by the high-pressure condition. The methane distribution associated to the same instant is reported in Fig. 2 (right) showing that the jet is corrugated by turbulence without exhibiting any laminar region on its boundaries. High-momentum O2 ligaments penetrate the methane jet as well as CH4 fingers also develop into the coflowing stream, thus producing isles of fuels later developing in reacting pockets.

References

[1] J. Andersen, C.L. Rasmussen, T. Giselsson, and P. Glarborg. Global combustion mechanisms for use in CFD modelling under oxy-fuel conditions. *Energy & Fuels*, 23:1379–1389, 2009.

[2] T. Ebara, N. Iki, S. Takahashi, and W.H. Park. Effect of Radiation Reabsorption on Laminar Burning Velocity of Methane Premixed Flame Containing with Steam and Carbon Dioxide. *JSME International Journal Series B - Fluids and Thermal Engineering*, 49(2):260–264, 2006.

[3] E. Giacomazzi, D. Cecere, F.R. Picchia, and N. Arcidiacono. Sviluppo di un Modello LES per Fiamme Turbolente Premiscelate / Development of an LES model for turbulent premixed flames.

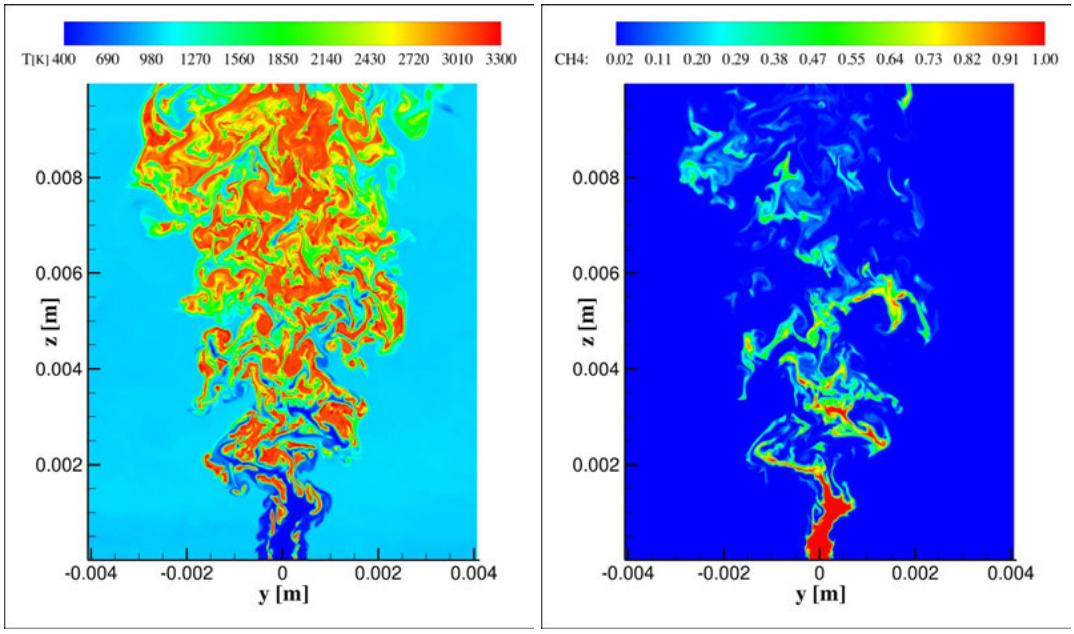

Figure 2: Case $10^3 \times \kappa_P$. Instantaneous distribution of temperature and methane mass fraction.

PAR2013, Ricerca di Sistema, Accordo di Programma tra ENEA ed il Ministero dello Sviluppo Economico RdS/2013/255, ENEA (UTTEI-COMSO), Roma - Italy, October 2014.

[4] J.R. Howell, R. Siegel, and M.P. Menguc. *Thermal Radiation Heat Transfer*. CRC Press, Taylor & Francis Group, 5th edition, 2010.

[5] J.B. Moss and C.D. Stewart. Spectrally Resolved Measurements of Radiative Heat Transfer in a Gas Turbine Combustor. *Experimental Thermal and Fluid Science*, 28(6):575–583, 2004.

[6] G. et al. Ponti. The role of medium size facilities in the HPC ecosystem: the case of the new CRESCO4 cluster integrated in the ENEAGRID infrastructure. In *Proceedings of the 2014 International Conference on High Performance Computing and Simulation*, volume HPCS 2014 N. 6903807, pages 1030–1033, 2014.

A CFD SIMULATION OF A FULL-SCALE U-OWC BREAKWATER

Luana Gurnari[1], Pasquale Filianoti[1], Sergio Camporeale[2], Marco Torresi[2], and Filippo Scarpetta[2]

[1]*Università "Mediterranea" degli studi di Reggio Calabria, Dipartimento DICEAM, Loc. Feo di Vito, 89122 Reggio Calabria, Italia. E-mail: filianoti@unirc.it, luana.gurnari@unirc.it*
[2] Politecnico di Bari, Dipartimento DMMM, via Orabona 4, 70125 Bari, Italia. E-mail: *filippo.scarpetta@poliba.it, marco.torresi@poliba.it, sergio.camporeale@poliba.it*

ABSTRACT In order to analyse the interaction between the waves and the U-OWC, in terms of reflection and absorption coefficients, as well as the overall performance of the system, a CFD simulation of a full-scale U-OWC breakwater has been carried out, aiming to simulate the flow field in front of breakwater and inside the OWC device, taking into account the characteristics of the air turbine adopted as power take-off device. In order to reduce the huge need of computational resources, CFD unsteady simulation have been carried out in a two-dimensional (2D) reference frame by solving the Reynolds-Averaged Navier-Stokes (RANS) equations, where the water-air interaction is taken into account by means of the Volume Of Fluid (VOF) model. To overcome the problems related to the simulation of the air turbine in the 2D domain, the connection between the chamber and the external ambient is modelled as a porous zone, where analytical equations able to represent the air flow in the duct and across the turbine have been adopted. The numerical simulation was carried out through CRESCO platform, using the cresco3 cluster. In this work, we used the cresco5_16h24 code with 48cores (16x3). Several simulations with different wave characteristics were made.

1 The numerical experiment

In the field of research on renewable energy sources, many different technical concepts exploiting wave energy are presently under study [1], [2]. One of the most promising research field is focused on Oscillating Water Column (OWC) devices (see, e.g., Falcao et al. [3], [4]) that can be either integrated inside a breakwater (onshore) or arranged as a floating device [5]. In general, an OWC device consists of a chamber that is partially submerged in sea water, having inside an air column trapped above a water column. In order to verify its energy conversion performance, an OWC device must be designed and tested by considering the operation of the PTO system. In particular, the relationship between the PTO damping and the OWC hydrodynamics can be used to improve the efficiency of the OWC. Moreover, in the case of U-OWC devices, the PTO damping affects the ability of the device to operate in resonance conditions with the incident sea waves (e. g. [6]). Numerical modelling is useful for carry out an evaluation of the performance of OWC operating under different values of PTO damping for different incident wavelengths. Didier et al. [7] explored the use of porous media theory to develop a numerical model of the PTO damping effect by means of a linear pressure drop law on a simplified representation of the OWC device as a thin cylinder. U-OWC devices (Boccotti, [8] and [9]) belongs to the family of OWCs, with some modifications in respect to conventional ones. They are breakwaters in reinforced concrete embodying an OWC with an additional vertical duct on the wave-beaten side. The vertical duct is connected to the OWC between a U-duct. Recently, U-OWC devices have been installed in the Port of Civitavecchia (Rome, in Italy), located in the Tyrrhenian Sea [6]. The relevant characteristics of the plant are shown in the cross section shown in Fig. 1a. The width of the duct and of the absorbing cell is 1.6m and 3.2m,

respectively; the length of the duct is 7m, the height of the chamber over the mean water level is 9.4m. The absorbing cells are independent, with a constant width of 3.87m. The computational domain is composed by a wave-flume, having a piston-type wavemaker placed in the left extremity and a U-OWC breakwater in the right extremity of the numerical domain (see Fig. 1b). The spatial discretization of the computational domain (see Fig. 1c) was made by a hybrid mesh, formed by rectangular elements in the overall length of the flume, whereas near the U-OWC device triangular elements were adopted. The mesh has approximately 300,000 cells. The part of the computational domain indicated by a red rectangle in Figure 1c, was set as "porous zone" in order to model the pressure difference between the chamber and the external ambient due to the oscillating flow. The "porous zone" is characterized by viscous and inertial losses which are used to reproduce the actual pressure losses in the air duct according with the following procedure that aims at identifying the parameters of the "equivalent" porous zone model.

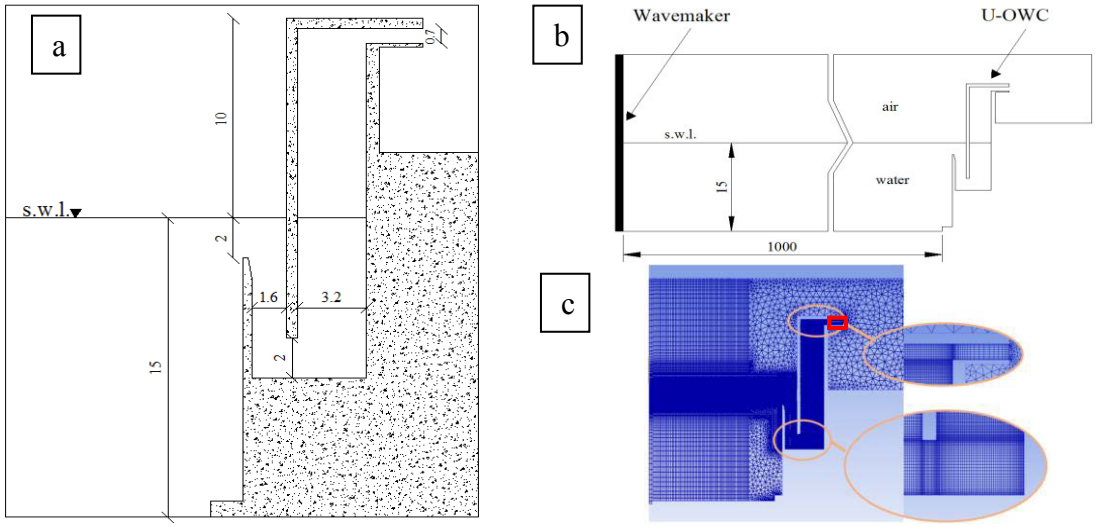

Fig.1. **a)** Cross section of the caisson of the breakwater converter installed at Civitavecchia Harbour (measures are in meter). **b)** Sketch of the computational domain (measures are in meter) **c)** spatial discretization of the computational domain. The conduit contoured by a red rectangle is modelled as porous zone to account the turbine presence.

The numerical approach is based on a two-dimensional CFD simulation using the commercial code Ansys Fluent 14.5. The water-air interaction is taken into account by means of the Volume Of Fluid (VOF) model. In the VOF model, two or more fluids (or phases) are not interpenetrating and the fraction of the volume of a phase in a cell is compute as the volume fraction. The volume fraction in the cells that lie near the interface between two phases is calculated by the Geometric Reconstruction scheme. In this approach, the interface between fluids was represented through a piecewise linear interpolation. Both air and water flow fields are assumed to be unsteady and are computed solving the Reynolds-Averaged Navier-Stokes (RANS) equations. These equations are discretized according to a Finite Volume approach, adopting a pressure-based algorithm in its implicit formulation.

In this work, we used the Standard k-ω turbulence model. The k-ω model includes two extra transport equations to represent the turbulent properties of the flow. This allows a two-equation model to consider effects like the convection and the diffusion of turbulent energy. The first transported variable is turbulent kinetic energy, k. The second transported variable is the specific dissipation, ω, that determines the scale of the turbulence, whereas the first variable, k, determines the energy in the turbulence. The SIMPLE (Semi-Implicit Method for Pressure Linked Equations) scheme has been used for the pressure-velocity coupling. It is a segregated algorithm that uses a relationship between velocity and pressure corrections to enforce mass conservation and to obtain the pressure field. In order to obtain the spatial discretization of the convection terms in the governing equations,

we used the Green-Gauss Cell-Based method to gradient evaluation and PRESTO! (PREssure STaggering Option) scheme for pressure equation. The other convection-diffusion equations (e.g. momentum or energy equation) were discretized by means of the Second Order Upwind scheme. Regarding the temporal discretization, a time step $\Delta t=T/1000$, being T the wave period, was used. This time step dimension has been selected in order to keep the Courant Number value much lower than 1, improving the solution convergence. The numerical simulation was carried out using the cresco3 cluster. Was been used cresco5_16h24 code splitting the domain into 48 cores.

2 The hydrodynamic analysis

In this work, we carried out a numerical simulation assigning a sinusoidal motion to the left wall of the wave flume, in order to reproduce a wave train with height H= 3.5m and period T = 8s (see sea state number 7 in [6]). To verify the share of the incident wave flux absorbed by the U-OWC, we calculated the energy flux in different sections along the wave flume. Figure 2a shows the instantaneous energy flux of the incident waves, Φ_{in}, evaluated at two wavelengths far from the wavemaker. The mean energy flux of the incoming waves train (i.e. the waves generate by the wavemaker) is approximatively equal to 52.1 kW/m.

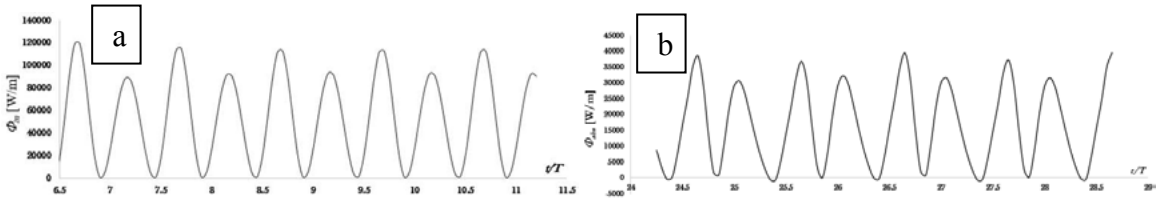

Fig.2. a) The energy flux of the incident waves measured at a fixed vertical section along the wave flume. **b)** The energy flux crossing the outer opening of the vertical duct of the U-OWC breakwater.

The instantaneous energy flux absorbed by the plant, Φ_{abs}, measured at the outer opening of the vertical duct, is shown in Fig. 2b. The time average energy flux absorbed by the plant is about 16.9 kW/m that is about 32% of the incoming wave energy flux. CFD simulation allows to perform a detailed analysis of the streamlines within the U-OWC device. Figures 3a and 3b show the streamlines at the occurrence of maximum water inflow and maximum outflow from the device, respectively.

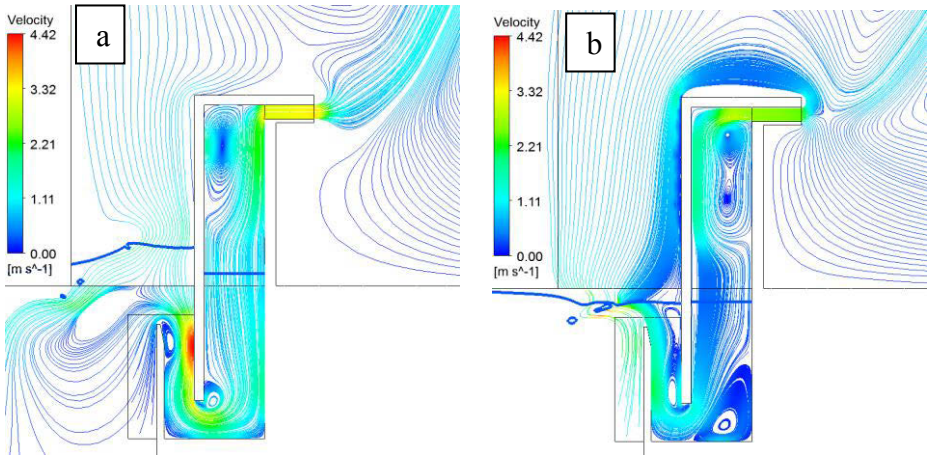

Fig.3 a) Streamlines inside and near the U-OWC device registered at the occurrence of maximum water inflow into the device **b)** Streamlines at the occurrence of maximum water outflow

As we can see in Fig. 3a, vortexes are generated near the vertical duct mouth, near the lower opening of the chamber and near the roof of the chamber.
These vortexes cause energy dissipation inside the device, reducing the amount of energy suitable for the turbine conversion. Also, in Fig. 3b we can see the presence of vortexes, which in this case are in larger number and bigger

3 Conclusions

The proposed CFD model allows a detailed analysis of the interaction between a U-OWC device and incident waves, for what concerns both the external wave field and the air and water flow inside the plant. The wave period of the simulated waves is far from the resonance condition. Indeed, the energy absorption is about 32% of the incoming wave energy flux. The analysis of the streamlines inside the device highlighted the need to improve the design of both the vertical duct upper opening and the U-duct to limit fluid dynamics losses. Indeed, about 30% of the absorbed wave energy is wasted in losses in water flow while 70% is available as pneumatic power for the turbine.
Finally, the porous medium model adopted as "equivalent model" of the air turbine in 2D CFD simulations worked successfully. It has been verified that the equivalent linear viscous losses in the porous medium, related to the turbine operation, are greater than continuous and minor head losses. The 2D CFD model adopted in this work permits to set up 1D numerical model suitable to match the plant characteristics and the PTO system with the local wave climate of the plant. Once fixed main parameters, the 2D CFD proves to be a useful tool to improve the plant performance by optimizing the plant geometry and fine tuning it with waves.

References

[1] Falcão A. F. de O, (2003). "First-generation wave power plant: current status and R&D requirements", Proc. of OMAE2003; 22nd International Conference on Offshore Mechanics and Arctic Engineering, Cancun, Mexico.
[2] Falnes J., (2002). "Ocean Waves and Oscillating Systems". Cambridge University Press. ISBN 0-521-01749-1., 288 pp.
[3] A. F. O Falcao, J. C. C. Henriques, Oscillating-water-column wave energy converters and air turbines: A review, Renewable Energy, Volume 85, 2016, Pages 1391-1424.
[4] A.F.O Falcao, J. C. C. Henriques, L. M. C. Gato, R. P. F. Gomes, Air turbine choice and optimization for floating oscillating-water-column wave energy converter, Ocean Engineering, Volume 75, 1 January 2014, Pages 148-156.
[5] http://www.oceantecenergy.com/
[6] F. Arena, V. Fiamma, V. Laface, G. Malara, A. Romolo, F. M. Strati, Monitoring of the U-OWC under construction in Civitavecchia (Rome, Italy), Proceedings of the 11th European Wave and Tidal Energy Conference (EWTEC), 6-11 September 2015, Nantes, France.
[7] Didier, E., Paixao Conde, J.M., Teixeira, P.R.F., 2011. Numerical simulation of an oscillating water column wave energy convertor with and without damping, in: Proc., International Conference on Computational Methods in Marine Engineering.
[8] P. Boccotti, Design of breakwater for conversion of wave energy into electrical energy, Ocean Engineering, Volume 51, 1 September 2012, Pages 106-118.
[9] P. Boccotti, Comparison between a U-OWC and a conventional OWC, Ocean Engineering, 34(5-6), pp. 799-805, 2007.

AB-INITIO MOLECULAR DYNAMICS STUDY OF *c-Si/a-Si:H* INTERFACES

Michele Gusso[1]*, Massimo Celino[2], Simone Giusepponi[2], Philippe Czaja[3] and Urs Aeberhard[3]

[1]*ENEA, C.R. Brindisi, S.S. 7 Appia km 706, 72100, Brindisi, Italy*

[2]*ENEA, C.R. Casaccia, via Anguillarese 301, 00123, Rome, Italy*

[3]*IEK-5 Photovoltaik, Forschungszentrum Jülich, 52425 Jülich, Germany*

ABSTRACT. Ab-initio molecular dynamics (MD) is performed to generate a realistic a-Si:H/c-Si interface structure with very low defect-state density by performing a high-temperature annealing. Some structural quantities are monitored during the MD. In particular the evolution of the bonds and the localization of the H atoms. The final structure has a low density of defects and the interface region is completely defect free.

1 Introduction

Silicon-based hetero-junction solar cells are a promising possibility for future industrial standard photovoltaic technologies. At the heart of this technology is the interface between the crystalline silicon (c-Si) and the thin passivating hydrogenated amorphous silicon film (a-Si:H). Since the physical processes occurring at this interface determine the characteristics of the entire photovoltaic device, it is of fundamental importance to understand and control transport and recombination propertires at the hetero-junction interface. The first step of an atomistic simulation of such photovoltaic device consist in building a reliable interface model that exhibits the experimentally observed features. Quantum based atomistic description are computational challenging and thus performed in the frame of the European Centre of Excellence EoCoE [4]. To this aim we started from a model already reported in [1] obtained after $35ps$ of Born-Oppenheimer MD with Quantum Espresso at $T = 300K$ and continue the MD annealing with CP2k up to 900 K and then, with a fast quenching, back to 300K. The system is made of a thin layer of hydrogenated amorphous silicon passivating a crystalline (001) silicon surface for a total of 368 atoms (320 Si and 48 H) in a $15.46x15.46x38.69\mathring{A}^3$ cell. The system is described in detail in [1]. Fig. 1 shows the configuration of the interface at the end of the molecular dynamics annealing. Here we describe the evolution of some structural characteristics of this model. A full account of the geometrical and electronic properties and their evolution during the annealing is reported in [2].

2 Molecular Dynamics Simulations

Born-Oppenheimer molecular dynamics (BOMD) simulations using the Quickstep code of the CP2K package [5] with norm-conserving Goedecker-Tetter-Hutter pseudopotentials with PBE-GGA exchange-

*Corresponding author. E-mail: michele.gusso@enea.it.

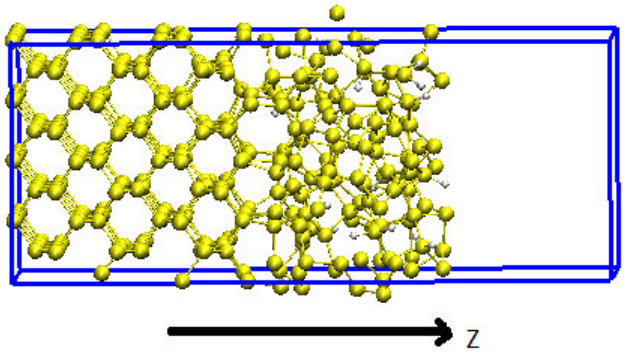

Figure 1: The c-Si/a-Si:H interface at the end of the molecular dynamics annealing

correlation functional were performed. A TZV2P basis set optimized from molecular calculations was used. All MD simulations were performed in the NVT ensemble and the electronic calculations restricted to the Γ-point, which is justified by the size of the super cell. The temperature was controlled by a Nosé thermostat. The system was subjected to a long high-temperature annealing in order to resolve the great number of structural defects present in the initial configuration. Table 1 reports the temperatures and duration of the annealing steps. In total 243420 time steps of $1fs$ (i.e. $243.4ps$) were made. The simulation was performed using 256 cores of the CRESCO4 machine and each MD step lasted on average $19s$ so that the total simulation needed about 54 days to be completed. Thus the wall clock time (WCT_years) was 38 core x years. In the following figures we describe the evolution of some structural parameters. Since the most important goal of the MD was the healing of the numerous defects present in the initial configuration we first show (Fig. 2) the evolution of the number of undercoordinated (coordination less than 4) or overcoordinated (coordination greater than 4) Si atoms. We used a geometric definition of bond: an atom is bonded to another one if their distance in less than a certain cutoff distance. For the cutoff we chose $2.85\mathring{A}$ for the Si-Si bond and $1.70\mathring{A}$ for the Si-H bond [3]. Note also that in this and all the following figures the curves are averaged using a time window of $300fs$ in order to smooth the rapid fluctuations of the reported quantities. It can be seen that there is a fast decrease of defects in the first few ps of the MD run. Then the number of defects (under or overcoodinated Si atoms) increases during the $500K$ step probably due to a rearrangemnets of the

Table 1: Temperatures and duration of the annealing steps

Annealing steps	T(K)	time(ps)
1	300	60
2	500	40
3	700	40
4	900	40
5	700	20
6	500	21.8
7	300	21.6

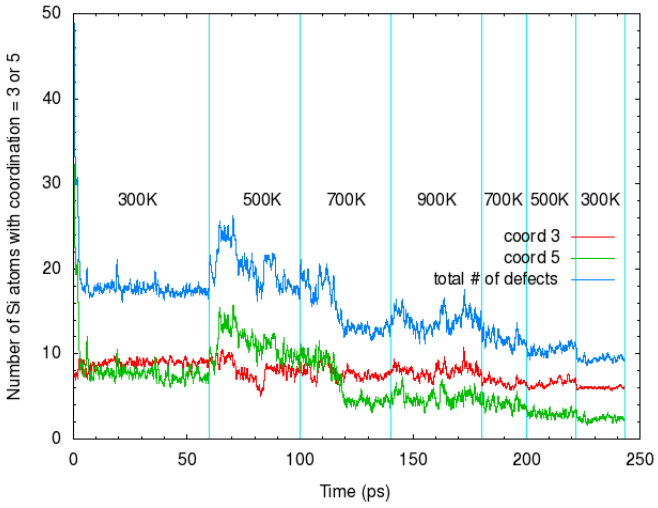

Figure 2: Number of Si atoms with coordination equal to 3 or 5 and the sum of the two curves (total number of defects) during the MD simulation.

structure, followed by a further decrease in particular during the final part of the $700K$ step and the (very fast) quenching back to $300K$. Considering that the sample has a free surface it is also important to verify the spatial localization of the defects. Fig. 3 reports the number of Si atoms with coordination not equal to four in 3 different region of the structure: the interface defined as the layer with $z_{int} \pm 2.8\mathring{A}$ where z_{int} is the approximate z-position of the crystalline-amorphous interface (at about $15.6\mathring{A}$), the surface region defined as the layer with z coordinate greater than $L_z - 2.8\mathring{A}$ being L_z the length of the structure (approximately $27.2\mathring{A}$) and the bulk a-Si:H region as the layer between the interface and the surface region. It can be seen that at the end of the simulation the interface region is defect free, the bulk region of the amorphous layer is almost defect free while most of the defects are concentrated at the free surface of the amorphous layer. Fig. 4 reports the dynamics of the z center of mass of H atoms.

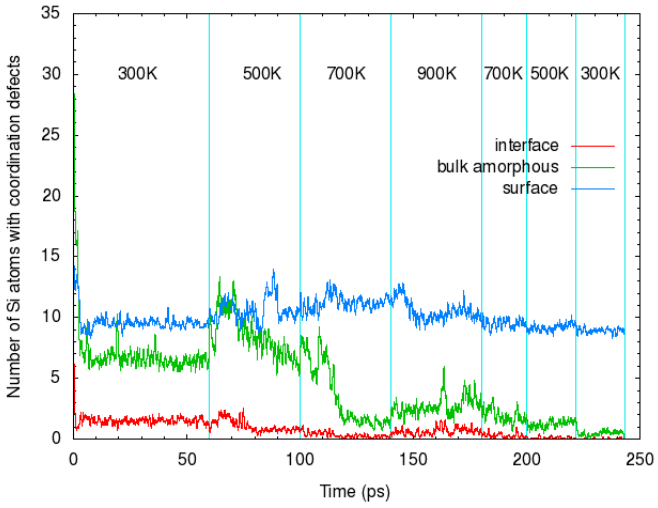

Figure 3: Number of Si atoms with coordination not equal to 4 in three different region of the sample during the MD simulation.

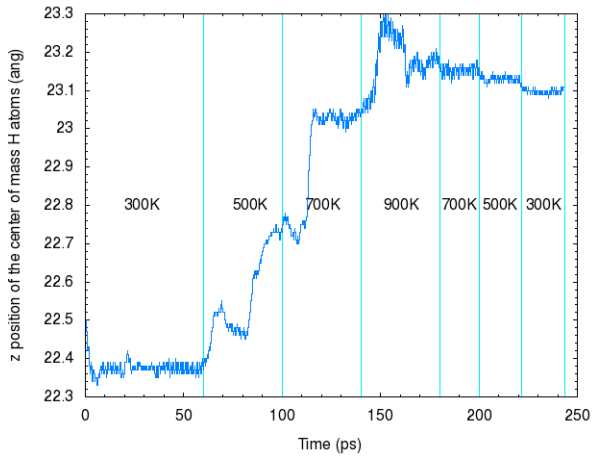

Figure 4: Z center of mass of the H atoms during the MD simulation.

There is a movement of H atoms toward the free surface. Indeed at the end of the dynamics there is no accumulation of H atoms at the interface. This means that the healing of the defects is mostly driven by reorganization of the Si atoms and not by H-passivation. Besides it can be shown (not shown in the figure) that the jumps of the z center of mass of H atoms are almost always due to the breaking of one Si-H bond.

3 Conclusions

Using ab-initio MD a realistic a-Si:H/c-Si interface structure with very low defect-state density was obtained. A short report of the evolution of the structural characteristics of the model during the MD was reported. For a detailed description of the structural but also electronic properties of this model refers to ref [2], while in [3] some general considerations for MD simulation of hydrogenated silicon materials can be found. The authors gratefully acknowledge funding from the European Commission Horizon 2020 under grant agreement No. 676629 (EoCoE project [4]).

References

[1] S. Giusepponi M. Celino M. Gusso U. Aeberhard and P. Czaja. Ab-initio study of c-Si/a-Si:H interface for PV technology. *High Performance Computing on CRESCO infrastructure: research activities and results 2016*, pages 113–116, 2017.

[2] P. Czaja U. Aeberhard M. Celino S. Giusepponi and M. Gusso. Computational characterization of a-Si:H/c-Si interfaces. *Journal of Computational Electronics*, (accepted), 2018.

[3] P. Czaja M. Celino S. Giusepponi M. Gusso and U. Aeberhard. Ab initio study on localization and finite size effects in the structural, electronic, and optical properties of hydrogenated amorphous silicon. *Computational Materials Science*, 155:159–168, december 2018.

[4] https://www.eocoe.eu/.

[5] http://www.cp2k.org/.

DYNAMICAL PHASE TRANSITIONS IN DISSIPATIVE STRONGLY-INTERACTING ATOMIC ENSEMBLES

Carlos Pérez-Espigares[1], Igor Lesanovsky[1], Juan P. Garrahan[1] and Ricardo Gutiérrez[1,2*]

[1] *School of Physics and Astronomy and Centre for the Mathematics and Theoretical Physics of Quantum Non-equilibrium Systems, University of Nottingham, Nottingham NG7 2RD, UK*

[2] *Complex Systems Group & GISC, Universidad Rey Juan Carlos, 28933 Móstoles, Madrid, Spain*

ABSTRACT. The physics of highly-excited (Rydberg) atoms is governed by blockade interactions that hinder the excitation of atoms in the proximity of a previously excited one. This leads to a dynamic heterogeneity similar to that observed in glassy soft matter, where fast- and slow-evolving regions coexist. In this work, we establish theoretically the existence of a glassy dynamical regime in a dissipative system of Rydberg atoms, which is associated with a dynamical first-order transition between an active phase of low density, and an inactive phase in which excited atoms are dense. We first explore the phenomenology via continuous-time Monte Carlo simulations, then perform a numerical diagonalizations of the relevant dynamical operators. We finally develop an analytical mean-field approach that allows us to understand the mechanism underlying the transition.

1 Introduction

The study of cold-atomic ensembles allows the exploration of many-body effects relevant to condensed-matter and statistical physics in experimentally accessible settings. Among these systems, gases of highly-excited (Rydberg) atoms constitute a versatile platform due to their strong and tunable interactions. Their physics, which currently intensely explored experimentally and theoretically, is governed by blockade effects reminiscent of the exclusion effects of glassy soft matter. The dynamics is highly heterogeneous, with regions that evolve rapidly while others remain stuck for long times [2].

In this work [3], we show that the heterogeneous dynamical behavior of Rydberg gases is due to the emergence of a glassy regime stemming from an underlying dynamical phase transition — those systems lies at a coexistence point between an active and an inactive phase. The inactive space-time regions that appear as the transition is approached from the active side are analogous to vapor bubbles in a liquid near liquid-vapor coexistence. We perform a detailed investigation of the dynamical phase diagram as a function of the interaction strength using continuous-time Monte Carlo simulations and operator diagonalization techniques. We further develop a mean-field theory that provides insight into the phase transition mechanism. Our work consolidates the understanding of collective dynamical phenomena in dissipative Rydberg gases and establishes a direct connection to soft-matter physics. Furthermore, our formalism can be applied for uncovering collective dynamical behavior in other driven dissipative spin systems, such as e.g. electrons and nuclei in non-equilibrium nuclear magnetic resonance.

*Corresponding author. E-mail: ricardo.gutierrez@urjc.es.

2 Model

We consider a driven dissipative system of L atoms in a 1D chain. At each site lies an atom that can be in its ground state $|\downarrow\rangle$ or in a high-lying (Rydberg) excited state $|\uparrow\rangle$. The (van der Waals) interaction between atoms j and k is non-negligible only if both are excited, and is then $V_{jk} = C_\alpha/|r_j - r_k|^6$, where r_j gives the position of j. The $|\downarrow\rangle \leftrightarrow |\uparrow\rangle$ transition is resonantly driven by a laser field with Rabi frequency Ω, and the system is affected by dephasing noise with a rate γ. In the large dephasing limit, $\gamma \gg \Omega$, a classical stochastic dynamics emerges [2], with rates for transitions $|\downarrow\rangle_j \leftrightarrow |\uparrow\rangle_j$ that, after a convenient rescaling of time, become $\tilde{\Gamma}_j = [1 + (R^6 \sum_{k\neq j} n_k/|r_k - r_j|^6)^2]$. Here, $n_j = |\uparrow\rangle_j\langle\uparrow|$ and $R = (2C_\alpha/\gamma)^{1/\alpha}$ gives the blockade length [2, 1].

3 Dynamical phase transition: numerical study of finite-size systems

We start with a numerical exploration of the dynamics. In the upper and lower part of Fig. 1, we show representative trajectories for $R = 1$ and $R = 3$ respectively, obtained via continuous-time Monte Carlo simulations. Extensive use of our C code has been made possible by the access to the Cresco supercomputer in Portici. While for $R = 1$ the dynamics is homogeneous and characterized by a single time scale, for larger R we observe an alternation of relatively dilute regions that evolve quite rapidly and regions that evolve along much longer time scales. This observations are confirmed by the inspection of many other trajectories and two-time correlation functions $\langle n_j(t)n_j(0)\rangle$.

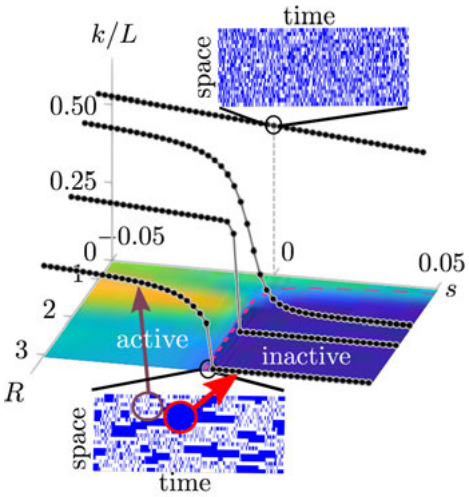

Figure 1: **Dynamical first-order phase transition in Rydberg gases.** Activity $k(s)/L$ as a function of the tilting field s and the blockade length R. Black curves correspond to $R = 1, 1.5, 2$ and 3; results for a range of R are displayed in the color map at the base. Trajectories for $R = 1$ (upper panel) and $R = 3$ (lower panel) are displayed. Blue and white indicate excited and ground state atoms, respectively.

This phenomenology is shown to arise from a dynamical trajectory phase transition, which is probed through a dynamical order parameter, namely, the activity per unit time $k = K/t$, which quantifies the number of state changes K in a trajectory of duration t. The phase diagram is obtained via a thermodynamics of trajectories approach, which allows us to infer the presence of dynamical phase transitions through the the probability distribution of the activity $P(k)$. For long times, this probability satisfies a large deviation principle $P(k) \approx e^{-t\phi(k)}$, where $\phi(k)$ is the so-called large deviation function. Often it

is more convenient to study the moment generating function $Z(s) = \langle e^{-stk} \rangle \approx e^{t\theta(s)}$, where the scaled cumulant generating function (SCGF) $\theta(s)$ is the Legendre transform of $\phi(k)$. In this framework, s acts as a control parameter that allows for the exploration of dynamical regimes that are unlikely to be observed as spontaneous fluctuations. We focus our study on the SCGF $\theta(s)$, whose non-analyticities correspond to transitions between dynamical phases. It is given by the eigenvalue with the largest real part of the so-called tilted generator $\mathbb{W}_s = \sum_{j=1}^{L} \left[\tilde{\Gamma}_j (e^{-s} \sigma_j^x - 1) \right]$ that gives the evolution biased by the field s, which "tilts" the systems towards more (if $s < 0$) or less (if $s > 0$) active dynamics. For $s = 0$, the unbiased dynamics is recovered. This generator is numerically diagonalized using our own C codes that perform a modified version of the Lanczos algorithm.

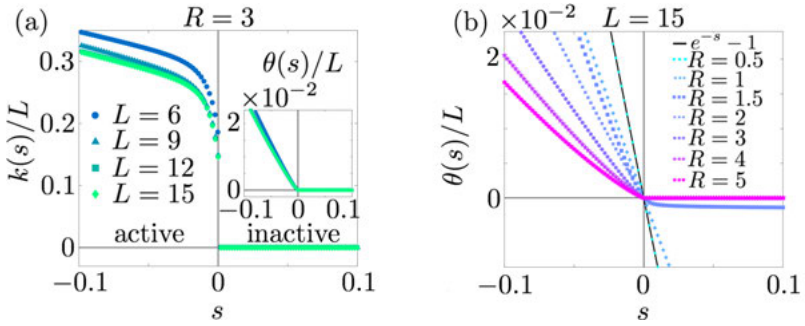

Figure 2: **Finite-size diagonalization results.** (a) Activity $k(s)/L$ (main panel) and SCGF $\theta(s)/L$ (inset) as functions of s for $R = 3$ and different L. (b) $\theta(s)$ in a system of $L = 15$ sites for different R.

In Fig. 1 we show the activity $k(s)/L$ as a function of R and s. We observe a qualitative change at $s = 0$: whereas for small R the change from active ($s < 0$) to inactive ($s > 0$) is smooth, a discontinuity develops for $R \geq 2$. This indicates the presence of a first-order dynamical phase transition, which is below theoretically established at the mean-field level. The dynamics observed in the trajectory for $R = 3$ (more generally, $R > 2$) arises from the coexistence of space-time regions. The activity density $k(s)/L$ shown in Fig. 1 is obtained from the SCGF $\theta(s)$, as $k(s)/L = -\theta'(s)/L$. The numerical diagonalization of $\mathbb{W}_s$ needed for obtaining the SCGF has been performed for a system of size $L = 15$, as larger sizes are prohibitive due to the exponential growth of the generator. We illustrate the finite-size behavior of the activity for $R = 3$ in Fig. 2 (a), where $k(s)/L$ converges to a size-independent curve for $L > 10$. The SCGF itself is shown in Fig. 2 (b), also for $L = 15$, which displays a smooth dependence on s for $R < 2$, and becomes Poissonian for $R = 0.5$, when the system is virtually non-interacting.

4 Dynamical phase transition: mean-field analysis

To shed further light on the problem, we introduce a variational free energy $\mathcal{F}_{|V\rangle}(s) = -\langle V|\mathbb{W}_s|V\rangle$, for normalized states $|V\rangle$, whose minima are dynamical phases. We focus on the subspace of (uncorrelated) states $|V\rangle = \bigotimes_j |v\rangle_j$ for $|v\rangle_j = \sqrt{p}\,|\uparrow\rangle_j + \sqrt{1-p}\,|\downarrow\rangle_j$. Since they are parametrized by the excitation density p, the free energy will be denoted $\mathcal{F}(p, s)$. The SCGF is approximated by minus the minimum of the variational free energy, $\theta_{\rm mf}(s) = \max_{|V\rangle}[\langle V|\mathbb{W}_s|V\rangle] = -\min_p[\mathcal{F}(p, s)]$, with

$$\mathcal{F}(p,s) = -\sum_{j=1}^{L} (\bigotimes_{l\neq j} \langle v|) \tilde{\Gamma}_j (\bigotimes_{m\neq j} |v\rangle_m)_j \langle v|(e^{-s}\sigma_j^x - 1)|v\rangle_j = -L\,\Gamma_{\rm mf}\left[2\,e^{-s}\sqrt{p(1-p)} - 1\right]. \quad (1)$$

The expression corresponding to the mean-field (de-)excitation rates $\Gamma_{\rm mf}$ can be found in Ref. [3].

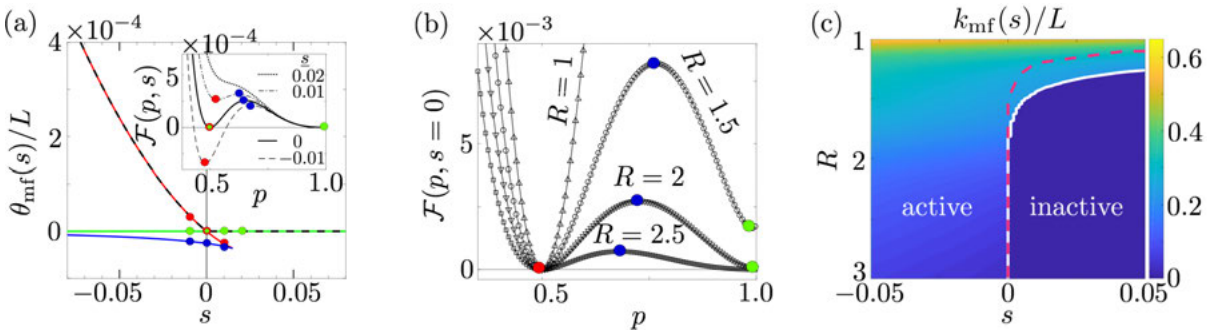

Figure 3: **Mean-field analysis.** (a) (Negative) free energy $-\mathcal{F}(p,s)$ for $R=3$ evaluated at the stationary points including two maxima (red and green lines) and one minimum (blue line), and SCGF $\theta_{\rm mf}(s)/L$ (dashed black line). *Inset*: $\mathcal{F}(p,s)$ as a function of p around $s=0$. (b) $\mathcal{F}(p,s=0)$ around the critical R. (c) Activity $k_{\rm mf}(s)/L$ as function of s and R.

The extrema of $\mathcal{F}(p,s)$ for a given s are found numerically. For $R \lesssim 1.25$ there is only one minimum, while for $R > 1.25$ there are two, and one maximum. In Fig. 3 (a) we show $-\mathcal{F}(p,s)$ for $R=3$ evaluated at each of these extrema and the SCGF $\theta_{\rm mf}(s)$. In the inset, the smaller minimum of $\mathcal{F}(p,s)$ for $s<0$ is seen to become the larger one for $s>0$, which results in the non-analytic behavior of $\theta_{\rm mf}(s)$ at $s=0$, where they are equally deep. Furthermore, we see a discontinuity from $p\approx 0.5$ for $s<0$ to $p\approx 1$ for $s>0$, with a metastable region for $s \gtrsim 0$ that ends in a spinodal point. This establishes the existence of a first-order dynamical phase transition at $s=0$. The dependence of $\mathcal{F}(p,s)$ on the blockade length R, on the other hand, is shown in Fig. 3 (b). The glassy phase is entered beyond $R=2$, as two minima are present at $s=0$, indicating the coexistence of active and inactive regions, while for smaller values of R there is just a single global minimum. For $1.25 \lesssim R \lesssim 2$ a second local minimum develops that becomes as deep as the first one for slightly positive s. As a result, the transition appears slightly away from $s=0$, signaling the presence of fat tails in $P(k)$. For larger R the transition moves towards $s=0$, and saturates at $R\approx 2$, see the white line in Fig. 3 (c).

5 Conclusions

Our formalism provides key theoretical insight into the heterogeneous dynamics of dissipative Rydberg gases, which was only vaguely understood thus far. Our results may be useful for engineering new dynamical regimes in cold atomic ensembles, which are currently explored in many laboratories worldwide for the study of collective quantum phenomena.

References

[1] R. Gutiérrez, J. P. Garrahan, and I. Lesanovsky. Self-similar nonequilibrium dynamics of a many-body system with power-law interactions. *Phys. Rev. E*, 92(6):062144, 2015.

[2] I. Lesanovsky and J. P. Garrahan. Kinetic constraints, hierarchical relaxation, and onset of glassiness in strongly interacting and dissipative Rydberg gases. *Phys. Rev. Lett.*, 111(21):215305, 2013.

[3] C. Pérez-Espigares, I. Lesanovsky, J. P. Garrahan, and R. Gutiérrez. Glassy dynamics due to a trajectory phase transition in dissipative Rydberg gases. *arXiv:1804.03070*, 2018.

MONTE CARLO MODELING OF d – t NEUTRON GENERATOR: IMPROVEMENT AND EXPERIMENTAL VALIDATION OF A MCNPX INPUT DECK

Giada Gandolfo[1], Luigi Lepore[1*]

[1] *Sapienza - University of Rome, Department of Basic and Applied Sciences for Engineering, Via Antonio Scarpa, 14 - 00161 Rome, Italy*

Abstract. The improvement of a Thermo Scientific MP320 neutron generator Monte Carlo N-Particles eXtended input deck, already developed in a first provisional version, was carried out thanks to the availability of new experimental data. The improved version is currently utilized at ENEA Casaccia Research Center for optimizing measurements related to explosives, drugs, and fissiles detection by fast neutrons. Improvement of the generator's model was mainly due to industrial radiographies of the neutron generator by 160 kV X-ray-tube-based imaging system, which provided detailed drawings of the internal layout of the device allowing a better reproduction of the internal configuration inside the MCNPX model. Accurate validation of the generator's model was obtained by comparing simulated results vs. experimental tests in a free-in-air condition, reducing neutron scattering as more as possible. The aim of this work is explaining all the steps that led to those results, suggesting a procedure that might be extended to different models of neutron generators.

1 Introduction

In a previous paper [16] the authors described the first development of the MCNPX (Monte Carlo N-Particles eXtended) [5] input deck of Thermo-Scientific MP-320 neutron generator [18], focusing on neutrons' emission rate obtained at a single angular position. Further developments, obtained thanks to a better knowledge of the generator's internal structure, now allow reproduction of the whole angular emission rate.

By means of the current improved version it was possible to optimize the CBRNE [1] experimental activities carried out at the Nuclear Material Characterization and Nuclear Waste Management Laboratory at ENEA Casaccia Research Centre [2]. In particular, the Differential Dye-away Time Analysis (DDTA) [14] experiments described in [7] [15], and, in general, Fast Neutron Analysis (FNA) [6] for explosive determination.

The MP-320 generator was used in d-t mode. It is worth to remark that notwithstanding the angular isotropy of the d-t fusion neutrons produced at the generator's internal target, the successive interaction of neutrons with generator's structures produces appreciable angular anisotropy of emitted neutrons [15]. It is necessary such anisotropy to be quantified for the definition of the optimal set-up of the

*Corresponding author. E-mail: luigi.lepore@uniroma1.it.

aforementioned measurement techniques. As described in § 2, the availability of digital radiographic system allowed to carry on a precise modelization of the internal structure of MP-320 which has been the basis for an accurate Monte Carlo reproduction of neutron emission angular anisotropy.

It is worth to remark that this work mainly deals with what happens inside the generator, in order to reproduce the correct neutron angular distribution to be implemented into the simulation code of measurement techniques. As a consequence, this work acts as a novelty respect to other papers on neutron generator simulations which dealt with distribution of fusion products [21], or calculation of neutron fluxes outside structures for shielding and/or moderation [11], and radiation protection issues around the generator itself [10].

It is useful to remark that Thermo Scientific MP-320 can be provided either for d-t and d-d fusion sources. It is rugged, very compact, portable and light in weight. It is based on a deuterium-tritium sealed source and it is designed for laboratory or field applications. Neutron production rate has a maximum of 10^8 neutron per second, and output can be continuous or pulsed, the latter ranging from 250 Hz to 20 kHz.

2 Methodology

For input deck realization, the MCNPX code has been used in its version MCNPX 2.7.0 [5]. Notwithstanding the code is able to transport deuterium and tritium ions inside the matter, it does not manage fusion reactions. For overcoming such a difficulty, a subroutine based on a fusion source model developed by Pillon et al. [12] has been added to the code, requiring re-compilation of MCNPX source code. More details about the way the d-t source has been integrated inside the neutron generator simulation can be found in Remetti et al. [16], which describes the first provisional version of the MP320's MCNPX input deck.

Having integrated Pillon's model into MCNPX, and having considered the successive interactions of fusion neutrons inside the generator, it was possible to achieve a reliable Monte Carlo model of the Thermo Scientific MP-320 neutron generator [18], capable to reproduce the real neutron emission from the device. The key issue for such result was the accuracy of the generator's internal components simulation.

The availability of the Gilardoni FEP ME Cargo radiographic system [3] allowed to deepen the investigation about the internal configuration of the Thermo Scientific MP-320 neutron generator, if compared with the previous guessed model by the author in [16]. Figure 1 shows the radiography of the device by the 160 kV X-ray-tube-based imaging system, and the virtual radiography of the neutron generator built into the MCNPX input deck. The device's operation manual [19] [4], and useful information from Vogt [20], and Stubbers et al. [17] helped to analyze and evaluate the radiographic readout.

New considerations emerged from such visualization of the internal configuration, with a better definition of components and their function. In particular, with reference to Figure 1, the guessed internal structure sections can be referenced as follow: 1) Cockcroft-Walton high-voltage source; 2) electric connections to the sealed-tube neutron generator; 3) sealed-tube neutron generator; 3.1) tritiated target section; 3.2) deutons Penning source; 3.3) deuterium gas reservoir.

Starting from the radiography readout, the MCNPX input deck of the neutron generator has been adjusted during the sequence of the simulations, in order to reproduce the neutron flux vs. the azimuth angle as rated by the manufacturer [9]. In the previous work carried out on the subject [16], about 45 sequential trials have been run to achieve a model capable of reproducing the real emission by the device. Here, 17 sequential trials have been run to get the MCNPX model searched for: the information obtained from radiography reduced the number of trials to one third, if compared with [16]. Moreover, results appear to be more accurate, even at some angles where the previous model was not completely

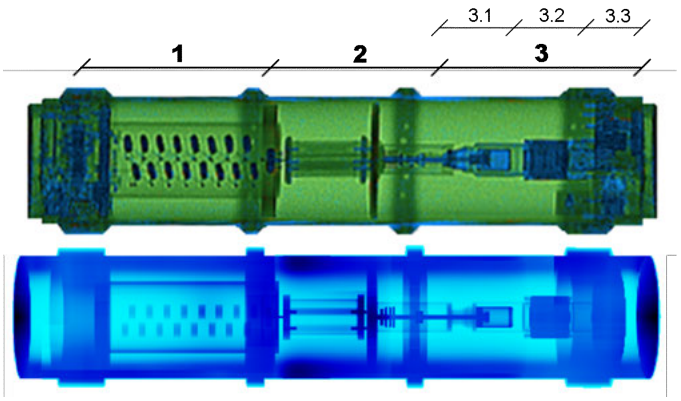

Figure 1: Up: Thermo Scientific MP-320 neutron generator radiography via a 160 kV X-ray-tube-based imaging system. Down: virtual radiography from the neutron generator model built into the MCNPX input deck. In particular, in the guessed internal structure sections: 1) Cockcroft-Walton high-voltage source; 2) electric connections to the sealed-tube neutron generator; 3) sealed-tube neutron generator; 3.1) tritiated target section; 3.2) deuton Penning source; 3.3) deuterium gas reservoir.

satisfactory. The availability of the device's internal configuration and the representation (into the MCNPX input deck) of the internal layout closer to the reality is undoubtedly the key issue for the goodness of the simulation results here shown.

About computational power, the 17 sequential trials did not require particular efforts. For instance, 0.5 core · h per run was sufficient to get significant results with low errors (<10%), because generator's geometry is quite small. Instead, high computational power may be needed when the user has to simulate the technique involving the use of neutrons. For instance, shielding, large geometries, high resolution in the energy and time domains, usually require the availability of HPC (High Parallel Computing) resources to achieving significant results in reasonably short time.

2.1 Development of the neutron generator model

As materials are concerned, copper, iron, aluminum and aluminum oxide (alumina), especially in massive components, were assumed to be important for neutrons' scattering inside the device, while thin parts were neglected.

With reference to Figure 2, from the neutron generator MCNPX model, neutron fluxes calculated are discretized in 72 values, with a 5°-step in the θ angular coordinate. Comparison with manufacturer's data, and point isotropic source hypothesis for the neutron generator are also represented.

With respect to the point isotropic source hypothesis for the neutron generator angular emission over all energies, maximum deviations from isotropy of the neutron flux vs. azimuthal angle are expected at $\theta = 90°$ and $\theta = 270°$, corresponding to the end-caps of the generator tube, due to materials (copper, alumina, glass, etc.) that neutrons could interact with. A removal from such angular 'bin' is expected in favor of emission over other angles, according to the scattering phenomena that fusion neutrons undergo with the device internal components.

The neutron generator MCNPX model here discussed was targeted to reduce such discrepancies, as to reproduce the device's real emission as better as possible.

Figure 3 shows deviation data of the neutron fluxes' angular distribution vs. manufacturer's data. A comparison with the previous MCNPX model [16], is also reported to enlighten that the newer MCNPX

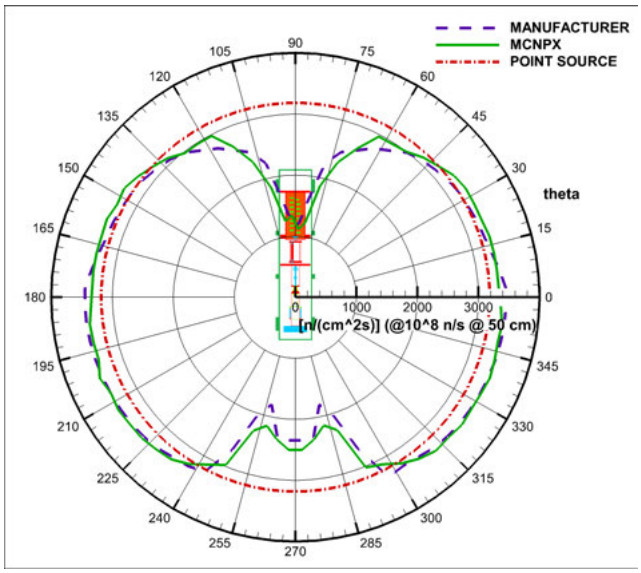

Figure 2: Comparison between the uncollided angular neutron emission over all energies by the MP320 neutron generator (@ 50 cm far from the center of the target) and the flux calculated by the MCNPX model of the device. For comparison, the uncollided angular neutron flux corresponding to the hypothesis of isotropic point source is added.

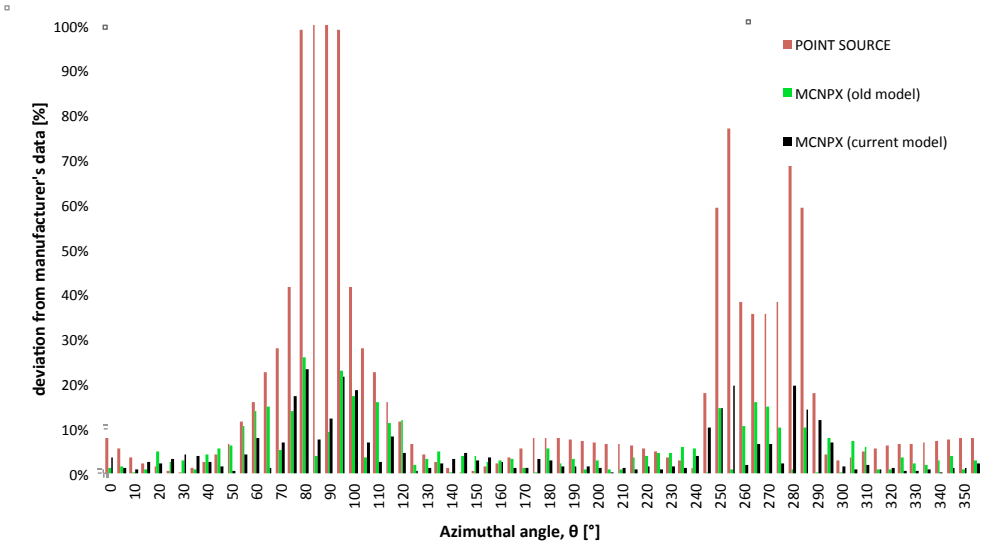

Figure 3: Deviation of the neutron fluxes' angular distribution vs. manufacturer's data. Bold black: comparison between the uncollided angular neutron emission over all energies by the MP320 neutron generator (@ 50 cm far from the center of the target) and the flux calculated by the MCNPX model of the device here proposed. Light green: comparison between the uncollided angular neutron emission over all energies by the MP320 neutron generator (@ 50 cm far from the center of the target) and the flux calculated by the MCNPX old model [16]. Red: comparison between the uncollided angular neutron emission over all energies by the MP320 neutron generator (@ 50 cm far from the center of the target) and the point-isotropic source hypothesis.

model here discussed provides more accurate results. From a numerical point of view, assuming that the uncollided angular neutron emission over all energies by manufacturer [9] is the real emission from the device, the following can be stated:

- when the point isotropic source hypothesis is considered, 48 of 72 values shows deviations below 10%; 6 of 72 values shows deviations between 10% and 20%; 18 of 72 values shows deviations greater than 20%;
- when the neutron generator MCNPX model in [16] is considered, 56 of 72 values shows deviations below 10%; 14 of 72 values shows deviations between 10% and 20%; 2 of 72 values shows deviations greater than 20%;
- when the neutron generator MCNPX model here proposed is considered, 61 of 72 values shows deviations below 10%; 7 of 72 values shows deviations between 10% and 20%; 4 of 72 values shows deviations greater than 20%.

The availability of the radiographic information for the Thermo Scientific MP-320 neutron generator was the key issue to improve simulation results obtained in [16]. The previous version for the MCNPX input deck was giving acceptable results when working with irradiation of samples placed at $\theta = 0°$ in large spaces, i.e. where neutron scattering phenomena on the sample are intrinsically reduced by the poor geometrical efficiency.

It is worth to remark that at ENEA Casaccia Nuclear Material Characterization Laboratory and Nuclear Waste Management [2], the neutron generator is used unshielded, because fast-neutrons interrogation of samples is needed. In such a condition, it is important to characterize the Thermo Scientific MP-320 neutron generator angular emission over all values for the theta coordinate for a better utilization in spaces or bunkers that cannot be considered as 'large', where scattering phenomena from-building-structures-to-samples are not negligible. e.g. a 30 cm wall-thick concrete bunker, 8 m long, 4 m large, 3 m height, cannot be considered 'large', because the scattered component of the comprehensive neutron flux on the sample in not negligible. MCNP calculations run to optimize some measurements setup [15] showed that when the sample is placed at $\theta = 0°$, 50 cm far from the neutron generator's target, the 10 to 14 MeV component of the neutron flux on the sample reaches 70% at maximum, while the other 30% is represented by the scattered contribution from the wall to the sample, due to the fact that the bunker cannot be considered as 'large'.

The issue becomes more significant when the distance between the neutron generator and the sample position is increased. i.e. the 10 to 14 MeV component of the neutron flux on the sample vs. the scattered component, rapidly decreases when the sample is placed more far: at 2 m distance, the 10 to 14 MeV region ranges from 30% to 40% according to the orientation of the neutron generator inside the room, while the scattered component of the neutron flux on the sample dominates. The way to manage a fast-neutron irradiation, and reduce the scattered component on the sample is to: i) employ of the neutron generator in 'large' spaces, with concrete walls, ceiling, and floor as much as possible far from the neutron generator and the sample (reduction of the comprehensive geometrical efficiency regarding neutrons that are backscattering on the sample); ii) reducing the mass of materials that may cause neutron scattering (e.g. buildings in bare metal are preferable to concrete buildings, although radiation protection issues should require shielding materials); iii) reducing the distance between the neutron generator and the sample to be irradiated (enhancement of the geometrical efficiency for the fast-neutrons' component of the neutron flux to the sample).

The example above clarify why an accurate characterization of the MP-320 neutron generator is needed, and the most accurate reproduction of the device's emission in the MCNPX code is searched for. It is evident from Figure 2 and Figure 3 that the agreement between MCNPX calculations and the data given by the supplier is now more satisfactory if compared with previous results presented in [16].

3 Conclusion

The application of the methodology previously described to the Thermo-Scientific MP-320 neutron generator led to the identification of a working MCNPX input deck of the device capable to reproduce the neutron emission in very good agreement vs. manufacturer's data, as well as vs. experimental tests. The present work, in comparison with [16], benefits from radiographic information of the neutron generator itself via a 160 kV X-ray-tube-based imaging system. The sketch of the internal layout allowed a more accurate evaluation of the generator internal configuration: such data has been the key-point to improve results in [16].

An experimental setup, here not described for the sake of brevity, was implemented, in order to check the entity of the anisotropy of the angular emission rate and for verifying values of the angular neutron flux, 50 cm far from the generator's target with a $\theta = 22.5°$-step in the theta angular coordinate, at the nominal neutron yield of the device, corresponding at the settings 80 kV voltage for the accelerator, and 60 µA for the deuteron beam.

The correspondence of the experimental vs. simulated data has been obtained, using the generator at its maximum power where neutron production rate was certified by the manufacturer: the matching is found into a confidence interval within 10%.

The capability of the code allows the user to simulate also the behavior of the device vs. time when it is used in pulse mode, rather than in continuous neutrons emission. Moreover, it allows the user to run several trial simulations to optimize measurement technique's geometry and parameters, powering the generator only to check some correspondence between simulated and measured values at some key-stages of the technique's optimization process. Feasibility studies and sensitivity analysis can be implemented in a systematic way, saving precious device's lifetime.

The procedure shown before is very versatile. It can be applied whatever the neutron generator, in order to retrieve a working MCNPX input deck to be implemented for any users' needs.

Currently, at ENEA Casaccia Research Center, the realized MCNPX input deck is available for all the experiments that foresee the use of a fast neutron interrogation source. Further, it will be used in future works on waste assessment and CBRNE (Chemical Biological Radioactive Nuclear and Explosive) activities [1].

Acknowledgment

The authors would like to express special thanks to Dr. Mario Pillon for his disposability in dialogue and his technical competences in discussing the radiographic data of the Thermo Scientific MP-320 neutron generator.

Thanks go to the Institute of Radiation Protection of ENEA [2] for providing the calibrated Berthold LB6411 neutron counter used in the experimental campaigns.

A special thanks goes to all ENEA-UTICT technicians working on HPC system used into this work. The computing resources and the related technical support used for this work, and all future uses, are provided by CRESCO/ENEAGRID High Performance Computing infrastructure [13]. CRESCO/ENEAGRID High Performance Computing infrastructure is funded by ENEA, and by Italian and European research programmes [8].

References

[1] End-user driven demo for cbrne, website. . Last access: April, 29^{th} 2018.

[2] Enea, italian national agency for new technologies, energy and sustainable economic development, website. . Last access: April, 29^{th} 2018.

[3] Gilardoni s.p.a., fep me cargo. . Last access: April, 29^{th} 2018.

[4] W. L. Araujo and T. P. Campos. Design of a high dc voltage generator and d-t fusor based on particle accelerator. In *2011 International Nuclear Atlantic Conference - INAC 2011*. Belo Horizonte, MG, Brazil, 2011.

[5] J. F. Briesmeister. *MCNP - A general purpose Monte Carlo code for neutron and photon transport*. Los Alamos National Laboratory, Report LA - 12625, New Mexico, United States, 1993.

[6] Andy Buffler. Contraband detection with fast neutrons. *Radiation Physics and Chemistry*, 71(3):, 3, 853 – 861,, 2004. 9th International Symposium on Radiation Physics (ISRP-9).

[7] Nadia Cherubini, Alessandro Dodaro, Giada Gandolfo, Luigi Lepore, Giuseppe A. Marzo, Ermanno Piccinelli, and Romolo Remetti. Field prototype of the enea neutron active interrogation device for the detection of dirty bombs. *Challenges*, 7:, 2(17),, 2016.

[8] ENEA,. Enea cresco website. . Last access: April, 29^{th} 2018.

[9] F. Prezzavento. Private communication, 2016.

[10] John W. Hayes, Erin Finn, Larry Greenwood, and Rick Wittman. Characterization of a thermo scientific d711 d-t neutron generator located in a low-scatter facility. *Nuclear Instruments and Methods in Physics Research Section A: Accelerators, Spectrometers, Detectors and Associated Equipment*, 741:57 – 66, 2014.

[11] Jeff Katalenich, Marek Flaska, Sara A. Pozzi, and Michael R. Hartman. High-fidelity mcnp modeling of a d–t neutron generator for active interrogation of special nuclear material. *Nuclear Instruments and Methods in Physics Research Section A: Accelerators, Spectrometers, Detectors and Associated Equipment*, 652(1):120 – 123, 2011. Symposium on Radiation Measurements and Applications (SORMA) XII 2010.

[12] M Pillon, M Angelone, M Martone, and V Rado. Characterization of the source neutrons produced by the frascati neutron generator. *Fusion Engineering and Design*, 28:683 – 688, 1995. Proceedings of the Third International Symposium on Fusion Nuclear Technology.

[13] G. Ponti, F. Palombi, D. Abate, F. Ambrosino, G. Aprea, T. Bastianelli, F. Beone, and R. Bertini. The role of medium size facilities in the hpc ecosystem: the case of the new cresco4 cluster integrated in the eneagrid infrastructure. In *Proceedings of the 2014 International Conference on High Performance Computing and Simulation*, number no. 6903807, pages 1030–1033. Bologna, Italy, 2014.

[14] A.-C. Raoux, A. Lyoussi, C. Passard, C. Denis, J. Loridon, J. Misraki, and P. Chany. Transuranic waste assay by neutron interrogation and online prompt and delayed neutron measurement. *Nuclear Instruments and Methods in Physics Research Section B: Beam Interactions with Materials and Atoms*, 207(2):, 2, 186 – 194,, 2003.

[15] Romolo Remetti, Giada Gandolfo, Luigi Lepore, and Nadia Cherubini. In field application of differential die-away time technique for detecting gram quantities of fissile materials. *Nuclear Instruments and Methods in Physics Research Section A: Accelerators, Spectrometers, Detectors and Associated Equipment*, 870:, 123 – 130,, 2017.

[16] Romolo Remetti, Luigi Lepore, and Nadia Cherubini. Development and experimental validation of a monte carlo modeling of the neutron emission from a d-t generator. *Nuclear Instruments and Methods in Physics Research Section A: Accelerators, Spectrometers, Detectors and Associated Equipment*, 842:7 – 13, 2017.

[17] R. A. Stubbers, B. E. Jurczyk, D. A. Alman, Coventry M. D., and Schaus M. J. Long life high efficiency neutron generator, February 2011. . U.S. patent document US2011/0044418A1. U.S. Commissioner of Patents, Washington, D.C. 20231, USA.

[18] ThermoFisher Scientific,. Mp 320 neutron generators. . Last access: April, 29^{th} 2018.

[19] ThermoFisher Scientific,. Mp320 neutron generator - operation manual, 2014.

[20] J. R. Vogt. *Accelerator System for Activation Analysis - A comparative Survey*, pages 161–176. Springer, Boston, US, 1968.

[21] U. Wiacek and J. Dankowski. Monte carlo modelling of distributions of the d- d and d- t reaction products in a dedicated measuring chamber at the fast neutron generator. *Nuclear Instruments and Methods in Physics Research Section B: Beam Interactions with Materials and Atoms*, 349:96 – 102, 2015.

Dependence on Pseudopotentials of Ab-Initio Molecular Dynamics Simulations of High Temperature GeO_2

Giorgio Mancini[1]*, Massimo Celino[2], Andea Di Cicco[1] and Emanuela Covino[1]

[1] *Università Di Camerino, Sezione di Fisica della Scuola di Scienze e Tecnologie, Via Madonna delle Carceri 9B, 62002 Camerino (MC), Italia*

[2] *ENEA, Ente per le Nuove Tecnologie, l'Energia e lo Sviluppo Economico Sostenibile, C. R. Casaccia, Via Anguillarese 301, 00123 Roma, Italia*

Abstract. Two series of *first-principles* molecular dynamics simulations have been carried out in the framework of the density functional theory on a large system consisting of 240 GeO_2 atoms. The entire temperature range 10-4000K has been covered by *ab-initio* simulations on the same initial configuration using two different norm conserving pseudopotentials with the BLYP exchange-correlation functional. The results are compared with experimental data.

1 Introduction

Thanks to its higher electron and hole mobilities together with its lower operating voltages, germanium is gaining increasing consideration to became a material of election for the production of less energy-demanding solid state devices. As a consequence, the interest for further investigations of its properties has recently been renewed by many scientists. In this context molecular dynamics (MD) simulations have firmly become a valuable means to flank, and possibly integrate, experimental results. The possibility to get information that are difficult, if not practically impossible to access by direct experimental measurements, calls for effective reliability of MD simulations. The computing power available nowadays makes it possible to implement more sophisticated models to run on larger systems than just a few years ago, allowing for richer, more detailed and accurate results; *first-principles* or *ab-initio* MD is credited with being an important step in this direction. Nevertheless, thorough comparisons of MD results with experimental data are of primary importance, since the simulations can be trusted for additional information only if known quantities are correctly reproduced. In the present paper we illustrate the results we have obtained by *ab-initio* MD simulations carried out using the Car-Parrinello Molecular Dynamics software (CPMD) [1, 2, 3] to study the properties of GeO_2. The CPMD approach, based on the density functional theory, uses plane waves and pseudopotentials to represent valence and core electrons, thus the choice of functionals, plane waves cut-offs, pseudopotentials and integration timesteps, has an important impact on computational times, hardware resources and, of course, on results. In a preceding paper [4] we presented a comparison of CPMD simulations for GeO_2 at 3000K carried out using different kinetic energy cut-offs for plane waves expansions, showing that an appropriate choice (60 Ry in our case, allowing for a 10a.u. timestep) gives the same results on shorter runs, less processors and memory than the commonly suggested higher values (80-90Ry, 3a.u. timestep). Anyway, for

*Corresponding author. E-mail: giorgio.mancini@unicam.it.

ease of comparison with other authors, we continued with the only 90Ry cut-off to reach 4000K [5]. As for the functionals and pseudopotentials, we adopted norm conserving pseudopotentials with the BLYP exchange-correlation functional using the TroullierMartins parametrization in the Kleinman-Bylander separable form for the core-valence interactions [6]. Our simulations, entirely carried in the *first-principles* frame constituted by CPMD, gave the the positions of the first $g_{\alpha\beta}(r)$ shown in the second column of Table 1 [5]. These values are in perfect agreement with the ones obtained by mixed classical/*ab-initio* simulations, e.g. [7], and in good agreement with classical MD and experimental results [8, 9]. When using the same pseudopotentials, the slight differences with experimental data are commonly attributed to the differences in the initial configurations and preparations. It is worth noticing that a long enough equilibration at higher temperatures than the melting point should lead the system to retain no memory of the initial conditions, so that – it was our opinion – the subsequent outcomes only depend on pseudopotentials. We have verified this point repeating the entire set of *ab-initio* simulations on the same initial GeO_2 configuration using separable, dual-space gaussian pseudopotentials due to Goedecker et al. [10], so as to check for correspondence, if any, of the results from distinct potentials. Pseudopotential(s) due to Trullier-Martins and Goedecker will be respectively indicated as T-M and GOE from now on.

2 Computational resources

The calculations were performed using the facilities and services available at the ENEA GRID infrastructure (Italy). Molecular Dynamics simulations have been carried out using CPMD v3.15.3 running on CRESCO4 cluster. 800GB of disk storage has been granted on the PFS/gporq1_256k file system.

3 Simulations details

A second cycle of CPMD simulations was performed on the same initial GeO_2 system we started from previously [4]: 240 atoms positioned at random in a cubic simulation box of edge 15.602Å to give a density ρ= 3.66 gr/cm^3. Apart from switching from T-M to GOE and setting a higher kinetic energy cut-off (actually set at 100Ry) required by GOE for plane-waves expansion, we left the other parameters untouched: BLYP-GGA generalized gradient approximation for the exchange and correlation parts of the total energy, 400a.u. for the fictitious electronic mass, 1000cm^{-1} and 10000cm^{-1} for the characteristic frequencies of ions and electrons, respectively, and 3a.u. for the timestep. After initial plane-waves and geometry optimisations, Car-Parrinello molecular dynamics simulations were carried out on the system heated up from 10K to 4000K by steps of 200K using a massive thermostatting for the ions (a Nosé-Hoover chain thermostat placed on each ionic degree of freedom [3, 11, 12]). A second Nosé-Hoover chain thermostat was set on the electronic degrees of freedom to prevent electrons from provoking improper ions damping or leaving the Born-Oppenheimer surface. GOE constantly demanded 40% longer execution times than T-M at 90Ry did during all simulations. At 4000K, as we did for M-T, we allowed for a long, final equilibration through 600,000 time steps (3 a.u. each one), amounting to 44ps. The determination of the appropriate cut-off value of 100Ry was performed in the same way we chose it for T-M, strictly abiding by the prescriptions given in the CPMD user's manual for such a choice. Nevertheless, just for pure curiosity, we timed some executions times for GOE at 150Ry on CRESCO4 cluster: they were 280% longer than T-M.

4 Results

Liquid GeO_2 at 4000K, well over the melting point, presents wider, lower first peaks for $g_{\alpha\beta}(r)$ than at 300K, but their positions are expected to remain the same if cooled down to 300K. The results we present here are shown against the experimental data measured at 300K (as a matter of fact, for ease of comparison, we digitalized an experimental data curve by hand, so it results noisy with respect to the more accurate curves in [8, 9]). As shown in Fig.1 and Table 1, the Goedecker pseudopotentials

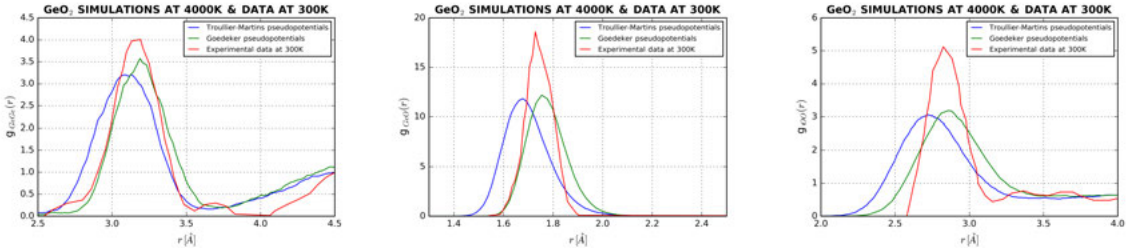

Figure 1: Pair distribution functions from simulations and experimental data

led to evident different results than the Troullier-Martins ones; in particular all interatomic distances by GOE are longer than T-M, and closer to experimental values. We showed that Troullier-Martins pseudopotential for germanium gave very accurate results when compared to experimental data [13, 14, 15], so it seems reasonable to attribute the different results for GeO_2 to the MT pseudopotential for the oxygen: an hypothesis still to be thoroughly investigated, but strenghten at the moment by the fact that the largest displacement in the first $g_{\alpha\beta}(r)$ peaks is due to the oxygen and amounts to three times the other ones [Table 1].

Table 1: Positions of the first $g_{\alpha\beta}(r)$ peaks and coordination numbers from Troullier-Martins and Goedecker pseudopotentials

	Troullier-Martins@4000K	Goedecker@4000K	Experimental@300K
r_{GeGe}	3.12 Å	3.18 Å	3.16 Å
r_{GeO}	1.69 Å	1.75 Å	1.73 Å
r_{OO}	2.75 Å	2.86 Å	2.83 Å
z_{GeGe}	4.1	4.1	4.1
z_{GeO}	4.0	4.0	3.8
z_{OO}	6.9	6.9	6.7

A series of short simulations (labelled GOE→T-M for short) imposing M-T potentials to the results from GOE, showed the higher mobility of the first peaks of $g_{GeO}(r)$ and $g_{OO}(r)$ that moved to the M-T positions. A smaller displacement was observed for $g_{GeGe}(r)$, probably due to the short simulation time [Fig.2]. All GOE→T-M pair distribution functions showed lower and wider peaks than both GOE and T-M. Similar considerations applied to the structural properties, as shown in Fig.3 comparing the results for the static structure factors $S_{\alpha\beta}(q)$ and S(q) from GOE, T-M and GOE→T-M simulations.

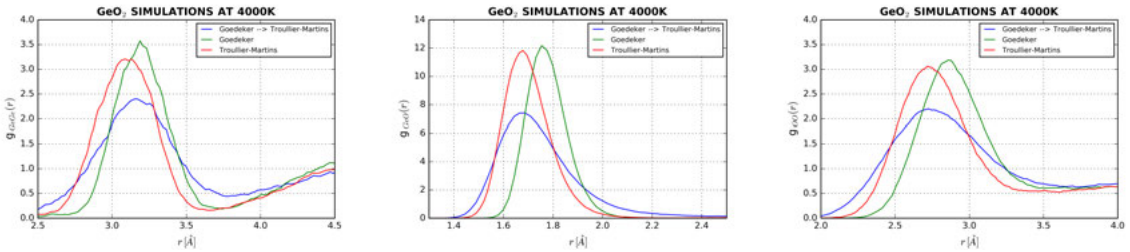

Figure 2: Pair distribution functions from original and crossed GOE→T-M pseudopotentials

As for coordination numbers, both approaches gave the same results [Table 1] (the data - not reported here - clearly showed for GOE the same plateaux as M-T, just shifted towards shorter distances).

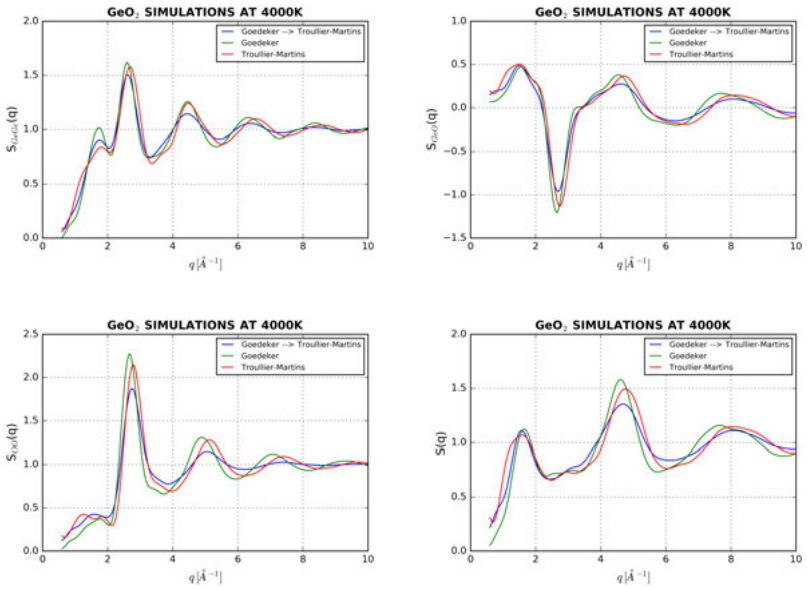

Figure 3: Structure factors from original and crossed GOE→T-M pseudopotentials

5 Conclusions

Trouellier-Martins pseudopotentials led to shorter distances than experimental ones both when used through the entire 10-4000 K simulations range and when cross-applied to the wider distanced configuration resulting from Goedecker pseudopotentials at 4000K . In this last aspect, we somewhat imitate the mixed approach consisting in using classical MD results as starting points for *first-principles* simulations, showing that even a short simulation evolved to the same shorter distances than experimental ones as reported in [5, 7], making it impossible for us to reproduce the results shown in [8] although they too were obtained from wider starting configurations at high temperature, using the same software (CPMD). The results we have presented clearly show that *first-principles* CMPD simulations of high temperature GeO_2 using Goedecker pseudopotentials led to improved results with respect to Troullier-Martins ones. The positions of the first peaks of the pair distribution functions closely reproduced the

experimental values. This result is expected to remain as such when the system will be quenched back down to room temperature to finally get an amorphous GeO_2 sample.

References

[1] R. Car and M. Parrinello. Unified approach for molecular dynamics and density-functional theory. *Physical Review Letters*, 55(22):2471–2474, 1985.

[2] CPMD v3.13.2 copyright ibm corp 1990-2008, copyright mpi fr festkrperforschung stuttgart 1997–2001.

[3] The CPMD Consortium. Car-Parrinello Molecular Dynamics: An ab-initio Electronic Structure and Molecular Dynamics Program. Manual for CPMD version 3.15.1.

[4] G. Mancini and M. Celino. Ab-initio Carr-Parrinello simulations of high temperature GeO_2: a comparison of the effects of plane waves cut-off and time step choice. *High Performance Computing on CRESCO infrastructure: research activities and results 2015*, pages 6–9, November 2016. ISBN: 978-88-8286-342-5.

[5] G. Mancini, M. Celino, and A. Di Cicco. Molecular dynamics of GeO_2: Car-Parrinello simulations in the range 10-4000k. *High Performance Computing on CRESCO infrastructure: research activities and results 2016*, pages 117–121, November 2017. ISBN: 978- 88-8286-362 2-3.

[6] N. Troullier and J. L. Martins. Efficient pseudopotentials for plane-wave calculations. *Physical Review B*, 43:1993–2006, 1991.

[7] T. Tamura, G-H. Lu, R. Yamamoto, and M. Kohyama. First-principles study of neutral oxygen vacancies in amorphous silica and germania. *Physical Review B*, 69:195204–195213, 2004.

[8] M. Hawlitzky, J. Horbach, S. Ispas, M. Krack, and K. Binder. Comparative classical and ab-initio molecular dynamics study of molten and glassy germanium dioxide. *Journal of Physics: Condensed Matter*, 20:285106–285121, 2008.

[9] P.S. Salmon, A.C. Barnes, R.A. Martin, and G.J. Cuello. Structure of glassy GeO_2. *Journal of Physics: Condensed Matter*, 19:415110–415132, 2007.

[10] S. Goedecker, M. Teter, and J. Hutter. Separable dual-space gaussian pseudopotentials. *Physical Review B*, 54:1703–1710, 1996.

[11] S Nosé. A molecular dynamics method for simulations in the canonical ensemble. *Molecular Physics*, 52:255–268, 1984.

[12] S.A Nosé. A unified formulation of the constant temperature molecular dynamics methods. *The Journal Of Chemical Physics*, 81:511–519, 1984.

[13] G. Mancini, M. Celino, and A. Di Cicco. Ab-initio study of amorphous germanium. *High Performance Computing on CRESCO infrastructure: research activities and results 2012*, pages 87–92, March 2014. ISBN: 978-88-8286-302-9.

[14] G. Mancini, M. Celino, and A. Di Cicco. First-principles study of amorphous germanium under pressure. *High Performance Computing on CRESCO infrastructure: research activities and results 2013*, pages 97–105, December 2013. ISBN: 978-88-8286-312-8.

[15] G. Mancini, M. Celino, F. Iesari, and A. Di Cicco. Glass polymorphism in amorphous germanium probed by first-principles computer simulations. *Journal of Physics: Condensed Matter*, 28:15401–15406, 2016.

First principle surface conductivity and susceptibility of monolayer TMDs

Margherita Marsili[1]*, [2], Joshua D. Elliott [2] and Olivia Pulci[3]

[1] *Laboratoire des Solides Irradiés, École Polytechnique, CNRS F-91128 Palaiseau, France*

[2] *Dipartimento di Fisica e Astronomia "Galileo Galilei", Univeristà degli Studi di Padova, via Marzolo 8, I-35131, Padova Italy*

[3] *ETSF and Dipartimento di Fisica, Università di Roma Tor Vergata, Via della Ricerca Scientifica 1, ' I-00133 Rome, Italy*

Abstract. In view of computing the surface susceptibility and surface conductivity for the series of transition-metal dichalcogenides monolayers we perform a preliminary study on MoS_2, the most studied and characterized of them. As they are know to be crucial for the description of the absorption spectrum of monolayer MoS_2, the dielectric function inlcuding excitonic effects is obtained at the Bethe-Salpeter Equation level and for Mo spin-orbit interactions are included; we also apply an empirical correction for zero-point vibrations. Excellent agreement with experimental ellipsometry measurements is obtained.

1 Motivation

In addition to spin-orbit interactions, strong excitonic effects are known to heavily influence the optical response of monolayer (ML)-MoS_2. An appropriate theoretical framework is required for the description of excitons: within many-body perturbation theory (MBPT) electron-hole interactions are included via solution of the Bethe-Salpeter Equation (BSE) [7]; the BSE has previously been employed to reproduce experimental optical spectra for ML- few-layer- (FL) and bulk-MoS_2 [6].

The favorable optical absorption properties of ML-MoS_2 have given rise to a lengthy and diverse list of potential applications, which serves to intensify research in this area. However, they have also overshadowed, at least from a theoretical perspective, the investigation of other optical properties accessible via MBPT. In particular, the real part of the macroscopic dielectric function, $\varepsilon_1(\omega)$, is of interest as this can be directly related to experimental ellipsometry measurements of the surface susceptibility.

2 Methods and computational details

Optical properties of the a given system may be obtained from the frequency-dependent macroscopic dielectric function, $\varepsilon_{\mathrm{M}}(\omega)$, in the limit of long wavelength: $\mathbf{q} \to 0$. When including electron-hole

*Corresponding author. E-mail: margherita.marsili@polytechnique.edu.

interactions $\varepsilon_{\mathrm{M}}(\omega)$ is expressed as [10]

$$\begin{aligned}\varepsilon_{\mathrm{M}}(\omega) &= 1 \lim_{\mathbf{q}\to 0} -v_0(\mathbf{q}) \sum_{\lambda\lambda'} \left[\sum_{n_1 n_2} \langle n_1 | e^{-i\mathbf{q}\cdot\mathbf{r}} | n_2 \rangle \frac{A_\lambda^{(n_1,n_2)}}{E_\lambda - \omega - i\eta} \right. \\ &\times \left. S^{-1}_{\lambda\lambda'} \sum_{n_3 n_4} \langle n_4 | e^{-i\mathbf{q}\cdot\mathbf{r}} | n_3 \rangle A_\lambda^{(n_1,n_2)} \left(f_{n_4} - f_{n_3}\right) \right] \end{aligned} \tag{1}$$

where v_0 is the bare Coulomb interaction, λ and λ' label eigenstates of the effective two-particle BSE hamiltonian with respective energies: E_λ and coefficients in terms of single-particle transitions: $A_\lambda^{(n_1,n_2)}$, finally, n_i are the single-particle Kohn-Sham states (see [10]).

As already detailed in references [8], since it is convenient to expand electronic wavefunctions in a basis of plane-waves there is a requirement for the use of periodic boundary conditions (PBCs). Ensuing simulations of two-dimensional sheets in PBCs actually compute an artificial crystal structure with an interlayer spacing L in the direction of the surface normal, thus the computed ε is a called a superlattice quantity [8], even in the limit of large L where interactions between periodic images are negligible, from now on we label such quantities with subscript SL.

The in-plane (denoted by superscript $\|$) surface conductivity, $\sigma^{\|}_{\mathrm{2D}}(\omega)$, may be directly related to the $\varepsilon^{\|}_{\mathrm{SL}}(\omega)$ by [4, 8]:

$$\sigma^{\|}_{\mathrm{2D}}(\omega) = -i\varepsilon_0\omega L \left[\varepsilon^{\|}_{\mathrm{SL}}(\omega) - 1\right]. \tag{2}$$

and from it the surface conductivity σ and susceptibility χ can be obtained as:

$$\sigma = \mathrm{Re}\, \sigma^{\|}_{\mathrm{2D}}(\omega),\ \chi = \frac{\mathrm{Im}\, \sigma^{\|}_{\mathrm{2D}}(\omega)\, \lambda}{2\pi c \varepsilon_0} \tag{3}$$

In the first step of our procedure, we have used Density Functional Theory (DFT) as implemented in *pw.x* of the Quantum Espresso suite [2, 3]. A primitive hexagonal cell with a lattice parameter of 3.15 Åin accordance with reference [11] has been used, in addition to remove any unphysical interactions between periodically replicated images a vacuum separation of 25.2 Å has been employed. Kohn-Sham wavefunctions, computed within the Local Density Approximation (LDA), have been expanded in a basis of plane waves with an energy cutoff of 60 Ry (816 eV). The atomic cores were treated using fully-relativistic norm-conserving pseudopotentials, including the Mo semicore 4p, 4d,and 4s states in the valence band.

For our BSE calculations we follow reference [9], applying a 0.925 eV scissor operator and a stretching factor of 1.2 to the valence and conduction band energies. Moreover, given the emergence of zero-point vibrational (ZPV) effects in the solution of the temperature-dependent BSE [9, 1] we also apply a rigid -100 meV shift to our BSE energies.

3 Results, convergence and outlook

The imaginary part of the macroscopic dielectric function, $\varepsilon_2(\omega)$, for ML-MoS_2 has been widely reported on owing to the fact that it is directly relatable to the optical absorption of the direct band gap, which is well within the visible part of the electromagnetic spectrum ($\approx$ 2 eV) and therefore has relevance in renewable energies technology. Yet, on the other hand, the real part of the macroscopic dielectric function, $\varepsilon_1(\omega)$, that can provide information about the surface susceptibility, has received almost no attention from the theoretical community. Consequently, it remains for us to verify that $\varepsilon_1(\omega)$ computed

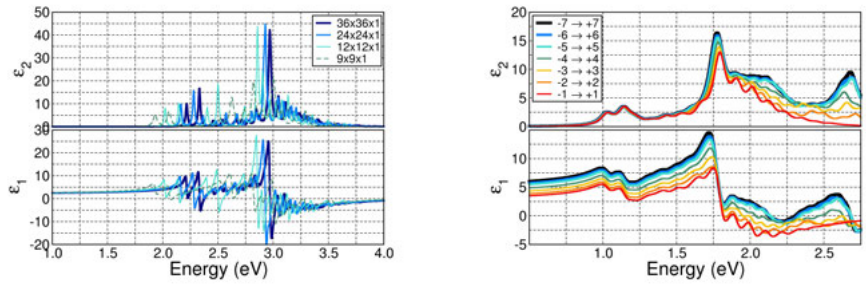

Figure 1: Left panel: convergence of $\varepsilon_1(\omega)$ and $\varepsilon_2(\omega)$ with respect to the irreducible Brillouin zone sampling. Right panel: convergence with respect to the number of bands included in the single-particle transition basis (starting to count from the highest occupied and low-occupied ones).

using the BSE is converged with the same accuracy as $\varepsilon_2(\omega)$ and comparable with experimental results.

Typically, in the convergence of $\varepsilon_{\mathrm{SL}}^{\parallel}$ one should consider the total number of **G**-vectors, the number of empty states, the integration of the first Brillouin zone (BZ) and the transition space in which excitations occur. In our case, the convergence of both the real and imaginary parts of $\varepsilon(\omega)$ with respect to the calculation parameters was most sensitive to (i) the k-point sampling of the BZ and (ii) to the number of bands that were considered when building the excitonic Hamiltonian in the single-particle transition space. Examining first the k-point convergence, which is plotted in the left panel of Fig. 1, it can be seen that both $\varepsilon_1(\omega)$ and $\varepsilon_2(\omega)$ exhibit similar behaviour with increasing k-point mesh densities. Indeed, both reach a satisfactory level of convergence for a $24 \times 24 \times 1$ grid. While convergence is similar for the the BZ sampling, we note that $\varepsilon_1(\omega)$ requires markedly more single particle transitions in order to reach convergence, even at low energies (see right panel Fig. 1). The excitonic peaks in the imaginary part of the spectrum are converged for a transition space which includes four states spanning the HOMO-1 $\rightarrow$ LUMO+1, yet to reach satisfactory convergence of the real part, a range spanning HOMO-6 $\rightarrow$ LUMO+6 is required.

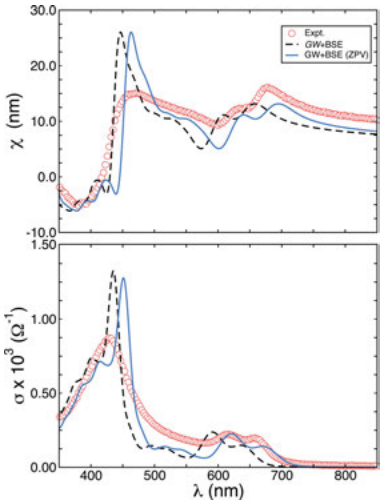

Figure 2: Comparison of optical constants χ (above) and σ (below) of ML-MoS_2 as a function of photon wavelength obtained via ellipsometry measurement [5] (red circles) and our GW-BSE calculations (solid line).

Transformation of the 3-dimensional $\varepsilon^{\parallel}_{\mathrm{SL}}(\omega)$ accordance with equations (2) & (3) yields the final spectrum, plotted with black dashed lines in Fig. 2. The features show a generally good agreement with experimental data obtained via ellipsometry measurements [5] for both the surface conductivity and susceptibility. Although, it can be seen that with respect to the experimental data, our computed spectrum is blue-shifted by approximately 20 nm. Better agreement in the positions of the excitonic peaks is obtained by taking into account the effects of zero-point vibrations (ZPV) [9]. Solutions of the temperature dependent BSE suggest at 100 meV shift to lower energies as a result of ZPVs. Applying the same rigid shift to our spectra yields improved agreement with the experimental results (see blue solid line Fig. 2).

References

[1] Elena Cannuccia and Andrea Marini. Effect of the quantum zero-point atomic motion on the optical and electronic properties of diamond and trans-polyacetylene. *Phys. Rev. Lett.*, 107:255501, Dec 2011.

[2] P Giannozzi, O Andreussi, T Brumme, O Bunau, M Buongiorno Nardelli, M Calandra, R Car, C Cavazzoni, D Ceresoli, M Cococcioni, N Colonna, I Carnimeo, A Dal Corso, S de Gironcoli, P Delugas, R A DiStasio Jr, A Ferretti, A Floris, G Fratesi, G Fugallo, R Gebauer, U Gerstmann, F Giustino, T Gorni, J Jia, M Kawamura, H-Y Ko, A Kokalj, E Kkbenli, M Lazzeri, M Marsili, N Marzari, F Mauri, N L Nguyen, H-V Nguyen, A Otero de-la Roza, L Paulatto, S Ponc, D Rocca, R Sabatini, B Santra, M Schlipf, A P Seitsonen, A Smogunov, I Timrov, T Thonhauser, P Umari, N Vast, X Wu, and S Baroni. Advanced capabilities for materials modelling with quantum espresso. *Journal of Physics: Condensed Matter*, 29(46):465901, 2017.

[3] Paolo Giannozzi, Stefano Baroni, Nicola Bonini, Matteo Calandra, Roberto Car, Carlo Cavazzoni, Davide Ceresoli, Guido L Chiarotti, Matteo Cococcioni, Ismaila Dabo, Andrea Dal Corso, Stefano de Gironcoli, Stefano Fabris, Guido Fratesi, Ralph Gebauer, Uwe Gerstmann, Christos Gougoussis, Anton Kokalj, Michele Lazzeri, Layla Martin-Samos, Nicola Marzari, Francesco Mauri, Riccardo Mazzarello, Stefano Paolini, Alfredo Pasquarello, Lorenzo Paulatto, Carlo Sbraccia, Sandro Scandolo, Gabriele Sclauzero, Ari P Seitsonen, Alexander Smogunov, Paolo Umari, and Renata M Wentzcovitch. Quantum espresso: a modular and open-source software project for quantum simulations of materials. *Journal of Physics: Condensed Matter*, 21(39):395502 (19pp), 2009.

[4] John D. Jackson. *Classical Electrodynamics*. John Wiley & Sons, 1999.

[5] Gaurav Jayaswal, Zhenyu Dai, Xixiang Zhang, Mirko Bagnarol, Alessandro Martucci, and Michele Merano. Measurement of the surface susceptibility and the surface conductivity of atomically thin mos2 by spectroscopic ellipsometry. *Opt. Lett.*, 43(4):703–706, Feb 2018.

[6] Hannu-Pekka Komsa and Arkady V. Krasheninnikov. Effects of confinement and environment on the electronic structure and exciton binding energy of mos_2 from first principles. *Phys. Rev. B*, 86:241201, Dec 2012.

[7] Richard M. Martin, Lucia Reining, and David M. Ceperley. *Interacting Electrons: Theory and Computational Approaches*. Cambridge University Press, 2016.

[8] Lars Matthes, Olivia Pulci, and Friedhelm Bechstedt. Influence of out-of-plane response on optical properties of two-dimensional materials: First principles approach. *Phys. Rev. B*, 94:205408, Nov 2016.

[9] Alejandro Molina-Sánchez, Davide Sangalli, Kerstin Hummer, Andrea Marini, and Ludger Wirtz. Effect of spin-orbit interaction on the optical spectra of single-layer, double-layer, and bulk mos_2. *Phys. Rev. B*, 88:045412, Jul 2013.

[10] Giovanni Onida, Lucia Reining, and Angel Rubio. Electronic excitations: density-functional versus many-body green's-function approaches. *Rev. Mod. Phys.*, 74:601–659, Jun 2002.

[11] Diana Y. Qiu, Felipe H. da Jornada, and Steven G. Louie. Optical spectrum of mos_2: Many-body effects and diversity of exciton states. *Phys. Rev. Lett.*, 111:216805, Nov 2013.

STUDY OF ADVANCED CONFIGURATIONS ON TOKAMAK EAST WITH THE EMC3-EIRENE CODE

Carlo Meineri[1*]

University of Padova and ENEA, Via Enrico Fermi, 45, 00044 Frascati, ROMA, ITALIA [1]

Heat exhaust is one of the most challenging issues to be addressed for tokamak magnetic confinement fusion research. EMC3-EIRENE is a Monte-Carlo code package studying the heat and particle transport in the Scrape Of Layer (SOL) and the 3-D effects acting on plasma in a Tokamak. It has been installed on Cresco to study alternative advanced divertor configuration, i.e. quasi snowflake (QSF) at EAST (Experimental Advanced Superconducting Tokamak), China.

1 Advanced magnetic configuration: SF and QSF

The hardest goal to obtain in a reactor design is to reduce the heat and particle loads on the plasma facing components; a promise solution for this problem would be probably the using of alternative magnetic configurations, such as the snowflake divertor (SF), or a two-null nearby divertor configuration (QSF). The SF configuration, figure 1 on the right, is characterized by a second-order null (x-point) in the poloidal magnetic field (B_p), where both B_p itself and its spatial derivatives vanish (B_p = 0, GradB_p = 0).

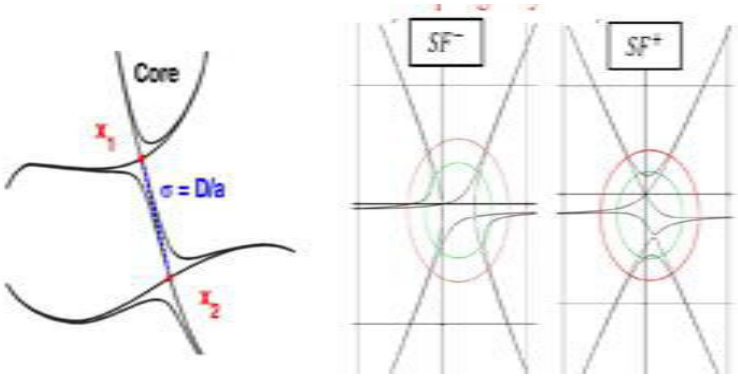

Fig.1: Alternative magnetic configurations

This splits the separatrix near the null into six segments: two of them enclose the confined plasma and four lead to the machine wall (the divertor legs). The poloidal cross-section of the obtained magnetic flux surfaces with hexagonal null-point has the appearance of snowflake. The QSF, figure 1 on the left, instead places the second x-point near the plate, causing flared field lines there, which spreads the heat over a larger area and increases the line connection length.

[1] Corresponding author. E-mail: carlo.meineri@enea.it.

1.1 EAST experiments

Initial experiments on the experimental advanced superconducting tokamak (EAST) [1] in 2014 have been motivated from the goal to test the promises/potential of a QSF by first proving that it can be created and effectively controlled on a large superconducting device. Magnetic and plasma characteristics of QSF, figure 2, have been studied in ohmic discharges with a plasma current $I_P \sim 250\ kA$, a toroidal magnetic field $B_t \sim 1.8\ T$, an edge safety factor $q_{95} \sim 8$, and $P_{NBI} = 500\ kW$ of NBI heating where the plasma current has been purposely kept low for safety reasons.

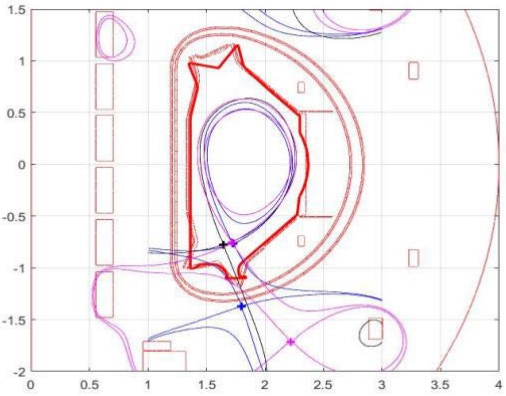

Fig 2: Poloidal cross section of three magnetic configuration: black profile SN, blu line a QSF with a second null at distance of 60 cm, and in violet a very far second null

2 EMC3-EIRENE tool

The EMC3 [2] code is a 3D Monte-Carlo numerical tool, which solves a set of stationary Braginskii fluid equations for the plasma density, the parallel momentum and the temperature of electrons and ions, adapted for typical fusion edge plasma conditions. It is coupled iteratively to the 3D kinetic Monte-Carlo code EIRENE to calculate the source terms of equations. The code has the aim to study all the cases where the problem became intrinsically 3D, for example in presence of RMP coils to control ELMS or gas puffing at local position. So it would be create a 3D grid, figure 3, where the EMC3 code instead of solving a linear matrix for the unknown quantities at the grid points, it follows Monte Carlo particles, which undergo convective and diffusive processes in parallel and cross-field directions, if the magnetic field line vectors are defined everywhere.

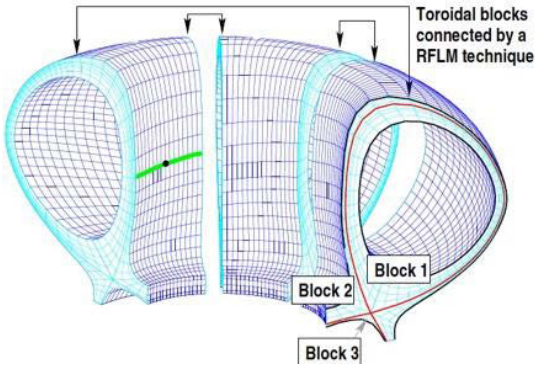

Fig 3: 3D field [3] aligned grid for a poloidal divertor configuration with 3 toroidal blocks, where each toroidal block is made up of 3 sub-blocks. The toroidal blocks are continuous in real space, but shifted apart in this figure to highlight the grid structure

The code provides separate function modules for the specific tasks, figure 4, needing to be composite and iterate for the convergence of the simulation

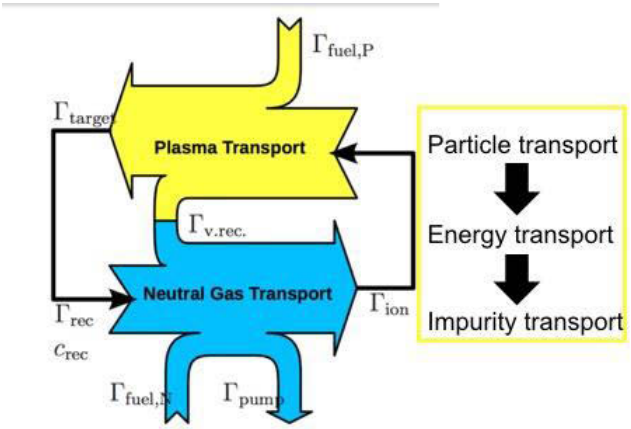

Fig 4: Scheme of the process for a single complete iteration. In yellow the EMC3 code and in blue EIRENE.

2.1 code compiling and program analysis tool

The source code is managed by Simulation Group of IPP at Munich Germany, and FZJ, Julich, Germany. The code is written in Fortran and optimize to work in parallel, it's compiled on Cresco4 with mpif90 and OpenMpi-Intel as library for parallel calculation. A positive test Benchmark was done on Cresco, comparing results with EAST and IPP server.
A study of parallelization Efficiency was done at IPP, with fixed particles, figure 5, where it is possible to understand that after 200 cpus the Speedup tend to saturate. In the future it will be done a similar study on Cresco.

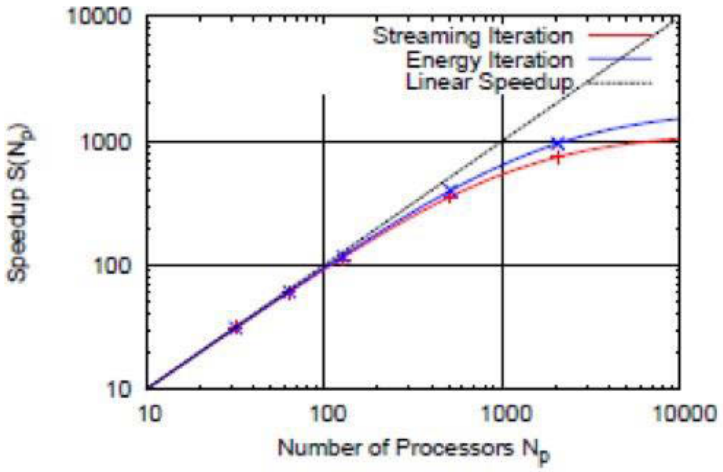

Fig 5: Studying of parallelization efficiency, where the blue line represent the iteration inside the simulation linked with particle transport, the red line energy transport; they are compared with a linear case (black line)

Python is the main language program to analyse the output-data. It has been written GUI interface to interpret the data and compare with experimental results.

3 First simulation on QSF configuration

The experimental input power to the SOL used in the simulations have been: $P_{sol} = 431.7\,kW$ in the SN and $P_{sol} = 414.5\,kW$ for the QSF case (a slightly higher radiation has been observed in QSF discharge). Electron density at outer mid-plane (OMP) separatrix has been taken from the reflectometer diagnostic to be $n_{sep} = 6 \cdot 10^{18}\,m^{-3}$ for both QSF and SN discharges. No impurity has been considered. It has been choose for the transport coefficients, $D_{\perp} = 0.4\ {}^{m^2}/_{s}$ for the main ions, and $\chi_{\perp} = 0.8\ {}^{m^2}/_{s}$ for electron and ion temperature. The purpose was to obtain the decay power length $l_q = 2\ cm$, experimental expect for these plasma currents by EAST scaling. It has been done a density scan between $n_{sep} = 3 \cdot 10^{18}\,m^{-3}$ to $n_{sep} = 6 \cdot 10^{18}\,m^{-3}$ to evaluate if the second null has not only a geometrical effects (locally expansion of flux tube) but also a physical effect with main ion-neutral interaction.

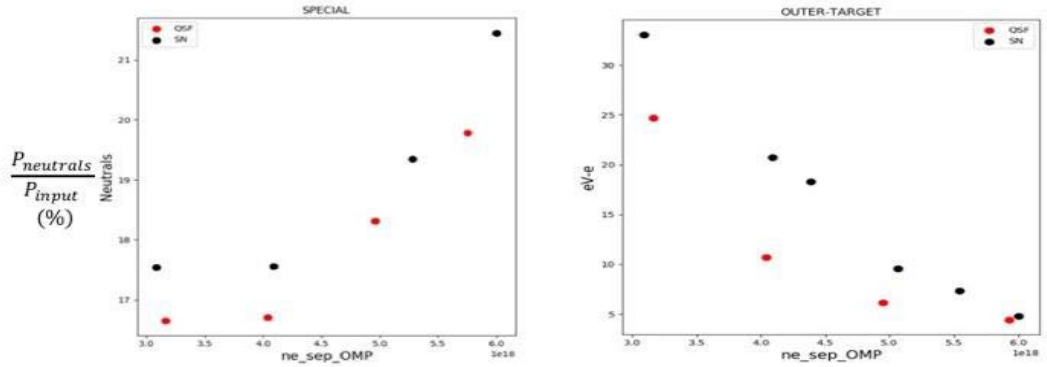

Fig.6: Fraction of power transferred to neutral particles (charge exchange and elastic collisions) on the left and Electron temperature at separatrix at OUTER-TARGET on the right. The black dots represent the SN case and the red one the QSF case.

In figure 6, on the left, It showed the fraction of power (in %) transferred to neutral particles (charge exchange and elastic collisions). It clears that both magnetic configurations have the same trend (some differences in order of 1% needing to investigate in the future varying transport coefficients), showing that at these densities, almost all the mitigation for QSF can be attributed to the flux expansion (defined as the ratio of the elementary area normal to the magnetic field at the target to that at the X-point). In Fig 6, on the right, it showed the Electron temperature at separatrix at OUTER-TARGET, where the SN cases is in black, and QSF case is in red. It is clear that QSF case decreases more rapidly than SN case, arriving a temperature near the limit where recombination became important. The next step is the investigation of the same case with carbon impurity, and to compare with simulation with an Higher P_{sol}.

References

[1] **G. Calabrò** et al., EAST alternative magnetic configurations: modelling and first experiments, *Nucl. Fusion* **55** (2015).

[2] **Y Feng** et al., Monte Carlo fluid approaches to detached plasmas in non-axisymmetric divertor configurations, *Plasma Phys. Control. Fusion* **59**, 034006, (2017).

[3] **Frerichs, Heinke Gerd**, Three-dimensional plasma transport in open chaotic magnetic fields: A computational assessment for tokamak edge layers, THESIS

THE ITER RADIAL NEUTRON CAMERA IN-PORT SYSTEM: NUCLEAR ANALYSES IN SUPPORT OF ITS DESIGN DEVELOPMENT

Fabio Moro[1]*, Basilio Esposito[1], Daniele Marocco[1], Salvatore Podda[1], Davide Flammini[1], Andrea Colangeli[1,2], Rosaria Villari[1]

[1]*ENEA, Department of Fusion and Nuclear Safety Technology, I-00044, Frascati (Rome), Italy*

[2]*Department of Basic and Applied Sciences for Engineering, SAPIENZA – University of Rome, Rome, 00161, Italy*

ABSTRACT. The ITER Radial Neutron Camera (RNC) is a multichannel detection system hosted in the Equatorial Port Plug 1 (EPP 1). It is designed to measure the uncollided neutron flux from the plasma, providing information on the neutron emissivity profile and total strength. The RNC structure consists of two sub-systems based on fan-shaped arrays of cylindrical collimators: the ex-port system, covering the plasma core with 2 sets of lines of sights lying on different toroidal planes, and the in-port system, enclosed in a dedicated cassette within the EPP1 diagnostic shielding module, for the measurement of neutrons generated in the plasma edge. Due to the harsh environment in which it has to operate, the design of the in-port RNC system is particularly critical both from the measurements point of view (low signal to noise ratio induced by the high level of scattered neutrons at the detector positions) and from the structural point of view. The manuscript presents the results of the neutronic analyses performed with the MCNP Monte Carlo code with the aim of optimizing the in-port RNC design in order to enhance the diagnostic measurement performance and evaluating the nuclear loads that have to be withstand by its structural elements, detectors and associated components

1 Introduction: the ITER Radial Neutron Camera

The Radial Neutron Camera (RNC) is a key ITER diagnostic system designed to measure the uncollided 14 MeV and 2.5 MeV neutrons from deuterium-tritium (DT) and deuterium-deuterium (DD) fusion reactions, through an array of detectors covering a full poloidal plasma section along collimated lines of sights (LOSs) (figure 1). Its main function is to estimate the neutron emissivity/α source profile and the total neutron source strength, providing spatial resolved measurements of several parameters needed for fusion power estimation, plasma control and plasma physics studies [1, 2]. The present RNC layout is composed by two fan-shaped collimating structures viewing the plasma radially through vertical slots in the diagnostic shielding module of ITER Equatorial Port 1 [3]. The ex-port structure, devoted to the plasma core coverage, extends from the Port Interspace to the Bioshield Plug: it consists of a massive shielding unit hosting two sets LOSs lying on different toroidal planes, leading to a total of 20 interleaved LOSs equipped with scintillators. The in-port structure (fig. 1) consists of a removable cassette, integrated inside the port plug with two sets of three LOSs each, looking at the plasma edges.

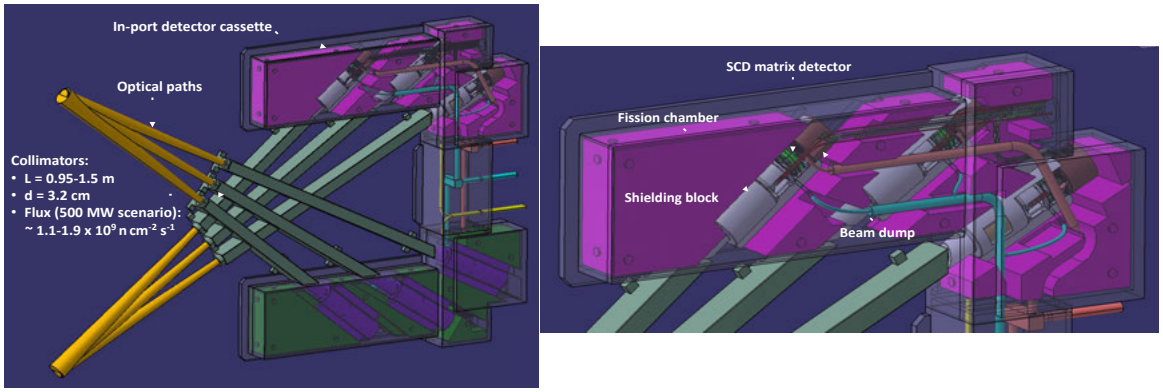

Fig. 1. ITER in-port RNC subsystem (left) and details of the inner structure (right).

The in-port RNC has to guarantee the required measurement performances in very severe operating conditions. The present study aims at addressing the main issues due to the effect of the nuclear loads on the in-port sub-system, both from the measurement capability and structural point of view, providing guiding criteria for its design development.

2 The in-port RNC: MCNP modelling and integration

The present design of the in-port subsystem is presents 6 LOSs, equipped with Single Cristal Diamond (SCD) matrix detectors and ^{238}U Fission Chambers (FC) as back-up detectors in high-power DT operations, resulted to be the most reliable in fulfilling the ITER measurement requirements. The detectors are embedded in a stainless steel (SS) case including water-cooling features for the SCDs (to be employed during the baking phase), beam dumps, a dedicated calibration system (^{239}Pu, ^{241}Am, ^{244}Cm α source for SCDs and ^{252}Cf source for FCs [5]) and are connected to the vacuum vessel by means of SS cylindrical collimators and optical paths penetrating through the port plug. All the detection system is enclosed in a SS cassette that also provide with electrical, vacuum and cooling feedthroughs. The empty space inside the cassette is filled with sintered Boron Carbide (B_4C) as shielding material to moderate the radiation streaming. The equivalent MCNP model of the In-port RNC has been generated through the conversion of a previously simplified engineering CAD model, by means of the SuperMC [6] code automatic modeling features and successively integrated in the ITER MCNP C-model Diagnostic Generic Equatorial Port Plug (DGEPP, fig. 2).

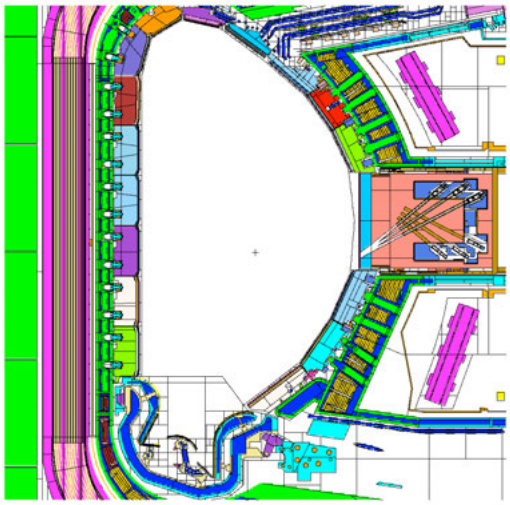

Fig. 2. In- port RNC model integrated in the ITER C-Model.

The 3D ITER model so far described has been used to perform specific nuclear analyses aimed at the optimization of the In-port inner components design by means of the MCNP6 transport code [7], coupled with the FENDL3.1d [8] nuclear data libraries. The calculations have been performed using the standard ITER plasma source provided with the C-model (inductive H-mode, 10 MA/5.3T, 500 MW fusion power, neutron yield: 1.773×10^{20} neutrons/sec). The complexity of the model and the necessity of statistically reliable results (statistical error below 10%) required the use of the MCNP MPI multiprocessor version installed on the CRESCO cluster. Each MCNP run generates 1e10 particles (neutrons, photons or both depending on the nuclear responses evaluated), using 800 processors for a total computing time of about 2.2e5 seconds. The typical dimension of a single output file is approximately 300 Mbyte, so the study required the analysis of some Gbyte data.

2 Measurement performance enhancement

The In-port RNC LOSs look at the plasma edges, where the neutron emissivity is significantly lower with respect to the plasma core; moreover the equatorial port plug is characterized by a consistent scattered neutron streaming that decrease the signal-to-noise ratio at the detectors. A dedicated study has been carried out aimed at investigating the optimal shape of the penetrations to enhance the measurement performances. As a first approach, the cut-outs in the Diagnostic Shielding Module have been designed as cylindrical extensions of the collimators up to the First Wall. In the present analysis, the effect of conically-shaped penetrations on the neutron spectra at the detectors position have been studied. Results are reported in figure 3, where the consistent enhancement of the signal-to-noise due to the conical penetrations with respect to the cylindrical ones is highlighted.

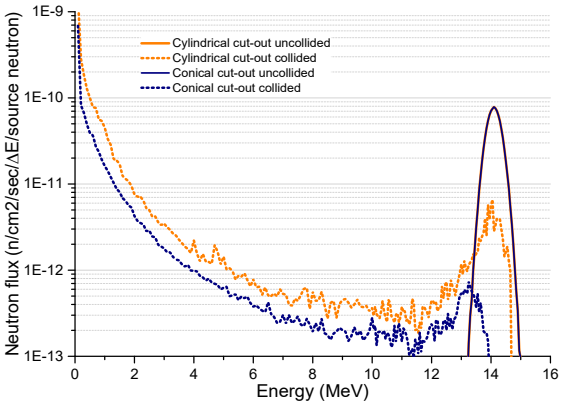

Fig. 3. Breakdown of the neutron spectra for the conical and cylindrical collimators.

As mentioned above, sintered B_4C (density 2.52 gr/cm^3) has been selected as shielding material for the In-port cassette and for the beam bumps. This choice has been driven, taking into consideration its high neutron capture cross section (through (n,γ) reactions) and physical properties. The main drawback in the use of B_4C is the consistent production of prompt photons that can have a harmful effect on the measurement, increasing the spectra background. The average gamma flux at the detectors position for the In-port subsystem is ~2.4×10^9 γ/cm^2/sec; the parametric study performed point out that, with a 2.5 mm layer of Lead wrapped around the detector boxes, a reduction of about 60% of the gamma flux impinging on the detectors can be achieved.

2 Nuclear loads assessment

The evaluation of the nuclear loads on the In-port RNC components is fundamental to verify its structural integrity during Normal Operations Condition (NOC), ensure proper functioning and

provide guidelines for the design optimization of the diagnostic system. Figure 4, left panel, shows a section of the total neutron flux maps across the upper LOSs: the highest values have been obtained for the front part of the collimators tubes (~$5x10^{11}$ n/cm^2/sec), while at the detectors position the maximum neutron flux is $8.5x10^9$ n/cm^2/sec and $7.6x10^9$ n/cm^2/sec for the fission chamber and diamond respectively. A variation of about 2 orders of magnitude in the neutron flux has been assessed from the most exposed area of the cassette (closer to the FW) to the back region, where it drops to ~10^8 n/cm^2/sec.

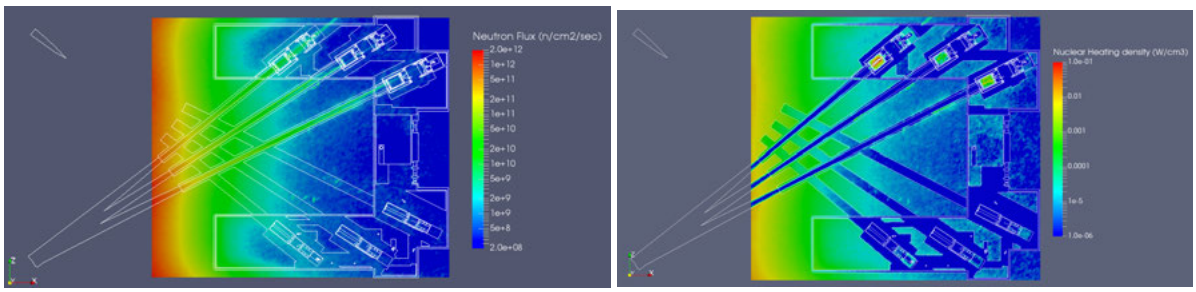

Fig. 4. Sections of the neutron flux (left) and nuclear heating density maps (right).

Nuclear heating calculations have been performed taking into account both the contributions of neutrons and secondary gamma, providing data for thermal and thermo-mechanical analyses. The nuclear heating density map (figure 4, right panel) shows a variation of about 4 orders of magnitude between the front and back area of the cassette (about $4.3x10^{-3}$ W/cm^3 and $2.3x10^{-7}$ W/cm^3 respectively). A particularly critical issue is the reduction of the heat load on the diamonds detectors: experimental studies [9] showed that SCD detectors, equipped with proper electrical contacts, are able to operate in a stable and reliable way, over long periods and under continuous neutron irradiation at temperature up to 150 °C. According to the present calculations, the heat load density on the SCD detectors is ~$8x10^{-5}$ W/cm^3: using this data as input for thermal analyses, the diamonds temperature during NOC results to range between 137 °C - 151 °C. With the present In-port RNC layout, a reduction of the maximum temperature of the SCD by increasing the thermal conductivity with the surrounding components,without enabling the cooling system.

References

[1]D. Marocco et al., Combined unfolding and spatial inversion of neutron camera measurements for ion temperature profile determination in ITER, Nucl. Fusion, 51, (2011), 053011.
[2]D. Marocco et al., Neutron measurements in ITER using the Radial Neutron Camera, Journal of Instrumentation, 7, (2012), C03033.
[3]F. Moro et al., Nuclear analysis of the ITER radial neutron camera architectural options, Fus. Eng. Des., 123 (2017), 1033-1038.
[4]D. Marocco et al. System level design and performances of the iter radial neutron camera, 26th IAEA Fusion Energy Conference, Kyoto, 2016.
[5]M. Cecconello et al., Strategy and guidelines for the calibration of the ITER radial neutron camera, this conference.
[6]Y. Wu, FDS Team, CAD-based interface programs for fusion neutron transport simulation, Fus. Eng. Des. 84 (2009) 1987 – 1992
[7]X-5 Monte Carlo Team: MCNP - A General Monte Carlo N-Particle Transport Code, Version 5, LANL report LACP-03-0245, (2005).
[8]FENDL-3.1d: Fusion Evaluated Nuclear Data Library ver.3.1d, https://www-nds.iaea.org/fendl/, (2018)
[9]R. Pilotti et al., Development and high temperature testing by 14MeV neutron irradiation of single crystal diamond detectors, Journal of Instrumentation, 11 (2016), p 1-9.

EFFECTIVE INTERACTIONS IN POLYMER NANOCOMPOSITES

Gianmarco Munaò[1]*, Antonio Pizzirusso[1], Antonio De Nicola[2], Stefano Caputo[1], Greta Donati[1], Ying Zhao[3] and Giuseppe Milano[1,2]

[1]*Dipartimento di Chimica e Biologia, Università di Salerno, Via Giovanni Paolo II, 132, I-84084, Fisciano (SA), Italy.*

[2]*Department of Organic Materials Science, Yamagata University, 4-3-16 Jonan Yonezawa, Yamagata-ken 992-8510, Japan.*

[3]*Dalian Minzu University, Institute of Nano-Photonics, School of Physics and Materials Engineering, 116600, Dalian, China.*

ABSTRACT. In this contribution we present a simulation study of the effective interactions in a coarse-grained model of silica nanoparticles merged in a polystyrene matrix by using the hybrid particle-field molecular dynamics approach. In particular, we investigate the potential of mean force between the nanoparticles, which are considered both ungrafted and grafted with further polystyrene chains. The resulting interactions are strongly attractive if the nanoparticles are ungrafted, becoming progressively more repulsive upon increasing the grafting density. A deeper insight into the microscopic mechanisms underlying the effective interactions is gained by calculating the three-body contribution to the PMF; in such a way it is possible to compare our results with simulation and experimental morphological diagrams, finding a good correspondence between the behavior of the PMF and various self-assembled phases. In particular, it emerges that the knowledge of three-body effects is crucial for identifying the nature of self-assembled nanostructures, like strings, connected sheets or small clusters.

1 Introduction

Polymer composites containing nanosized particles are currently the object of a intensive investigation, for the capability of these material to generate new potential technologies [1]. In this context, the stability of the resulting nanocomposite material is of primary importance, since the addition of nanosized fillers into the polymer matrix can significantly influence its overall behavior. In particular, the potential of mean force (PMF) between the nanoparticles embedded in the polymer is the most investigated issue when studying the stability of polymer nanocomposites [2]. In the present study, we investigate the behavior of a coarse-grained (CG) model of a nanocomposite constituted by Silica nanoparticles (NPs) dispersed in a Polystyrene (PS) matrix by means of the hybrid particle-field molecular dynamics representation (MD-SCF) [3]. The NPs are considered both bare and grafted with further PS chains. The main target of this study is to provide an accurate representation of the effective interactions among NPs in the polymer melt; this is an issue of crucial importance for the dispersion state of the NPs, that is in turn the main factor determining the final properties of the polymer nanocomposite. In addition, we have explicitly included in the calculation of the PMF the contribution due to multi-particle effects such

*Corresponding author. E-mail: gmunao@unisa.it.

as three-body interactions, whose importance has been already highlighted in experimental works [4] when facing the issue of self-assembly of grafted NPs in polymer melts. In order to obtain accessible simulation times for a proper calculation of two- and three-body PMF we thus make use of CRESCO supercomputing resources.

2 Simulation details

The simulation approach that we adopt in the present study for studying CG systems is based on a combination of a standard molecular dynamics approach and a self-consistent field theory [5] for the calculation of non-bonded potentials. The resulting scheme is known as hybrid particle-field model [6]: according to such an approach, the hamiltonian of a system comprised by M molecules can be split as:

$$\hat{H}(\Gamma) = \hat{H}_0(\Gamma) + \hat{W}(\Gamma) \tag{1}$$

where Γ represents a point in the phase space and the symbol $\hat{}$ indicates that a given quantity is a function of the microscopic state corresponding to Γ. In Eq. 1, $\hat{H}_0(\Gamma)$ is the Hamiltonian of a system with molecules experiencing only intramolecular interactions, whereas $\hat{W}(\Gamma)$ is the contribution due to the other non-bonded interactions. The latter can be calculated as an external potential $V(r)$ on single particles, which is due to the density field. The details of the derivation of $V(r)$ can be found elsewhere [6]. According to this derivation, the mean field solution for the potential acting on a particle of type K at position r, $V(r)$ is:

$$V_K(\mathbf{r}) = k_B T \sum_{K'} \chi_{KK'} \Phi_{K'}(\mathbf{r}) + \frac{1}{\kappa}(\sum_{K} \Phi_K(\mathbf{r}) - 1) \tag{2}$$

where k_B is the Boltzmann constant, T is the temperature, $\chi_{KK'}$ are the mean field parameters for the interaction of a particle of type K with the density field due to particles of type K' and the second term on the right-hand side of Eq. 2 is the incompressibility condition, κ being the compressibility. Also, $\Phi_K(\mathbf{r})$ and $\Phi_{K'}(\mathbf{r})$ are the density functions of the CG beads of type K and K', respectively. The value of $\chi_{KK'}$ has been fixed to 5.25, in agreement with a previous MD-SCF study of the same model [3].

As for the calculation of the two-body PMF, for each system we have prepared a set of 30 independent initial configurations, each one corresponding to a pair of NPs placed at a fixed distance from each other and embedded in the polymer matrix. One simulation has been performed for each configuration, where the NPs were allowed to freely rotate but not to translate, in order to keep their mutual distance fixed. Forces on the centers of mass of the two NPs have been computed each 0.4 ps and averaged over 80 ns. The resulting PMF has been calculated by integrating the obtained forces. The three-body PMF has been computed by placing a third NP in the simulation box and repeating the procedure employed for the calculation of the two-body contribution by keeping fixed the position of the third NP.

3 Results

The total collection of the investigated systems for the calculation of the two-body PMF between a pair of ungrafted or grafted NPs is reported in Tab. 1: for clearly identifying the various cases, we have labeled each system with a different symbol. We consider several values of free and grafted chain length (L_f and L_g, respectively) for two different grafting densities ρ_g, corresponding to two different

Table 1: Nanocomposite systems considered in the calculation of the two-body PMF. Each case is labeled by a different symbol. The grafting density is in chains/nm^2. The box lengths are $L_x = 22$ nm, $L_y = L_z = 12.5$ nm.

Grafting density (ρ_g)	Grafted chains (N_g)	Grafted chains length (L_g)	Free chains (N_f)	Free chains length (L_f)
0	0	-	1044	20
0	0	-	104	200
0.5 (+)	25	80	854	20
1.0 ($*$)	50	20	944	20
1.0 ($\times$)	50	80	644	20
0.5 ($\circ$)	25	80	17	1000
1.0 ($\square$)	50	20	19	1000
1.0 ($\triangle$)	50	80	13	1000
0.04($\bullet$)	2	40	1028	20
0.1 ($\blacksquare$)	5	80	995	20
0.4 ($\blacktriangle$)	20	20	99	200

numbers of grafted chains N_g. The number of free chains N_f is also allowed to vary. Note that the simulation box has been taken rectangular, with the long side oriented along the axis connecting the centers of mass of the two NPs. The two-body PMF between a pair of ungrafted NPs is found to be remarkably attractive, regadless the values of L_f; conversely, the two-body PMF between a pair of grafted NPs is repulsive for high grafting densities ($\rho_g \geq 0.5$ chains/nm^2) and attractive for low grafting densities ($\rho_g \leq 0.5$ chains/nm^2). This amounts to assume that in a system comprising many NPs, the latter are well dispersed in the first case and phase separated in the second case. A comparison with experimental [7] and numerical [4] studies on the same systems shows that for low grafting densities the appearance of nanostructured aggregates (small clusters, connected sheets or strings) is expected. In order to gain further insight on the nature of the effective interactions we have calculated also the three-body contribution to the PMF (see the procedure described in the previous section). We have found that for high ρ_g the three-body PMF is even more repulsive than the two-body counterpart, while for low ρ_g the resulting interactions show the existence of both attractive and repulsive contributions, depending on the range of the interaction. The contemporary presence of these two effects is compatible with the appearance of the self-assembled structures, as reported in Fig. [4]. As visible, the well dispersed condition, observed in the upper part of the diagram and characterized by high values of N_g and L_g, can be generally well described by the behavior of the two-body PMF; conversely, for a proper understanding of the nanostructures observed in the lower part of the diagram we need to consider the subtle interplay between two-body and three (or multi) body interactions. Experimentally obtained images of the specific nanostructures are also reported. The investigation of multi-body contribution to the PMF in polymer nancomposites with such a degree of accuracy has been possible thanks to the CRESCO Supercomputing resources, and for this purpose we have performed extensive molecular simulations of the cresco queues cresco3_h144, cresco4_h144 and small_h144. A computational study on the calculation of the PMF between atomistic NPs (to be used as a first step to fully characterize effective interactions in high-density polymer nanocomposites) has been recently published on *EPJ E* Journal, in which we thank the HPC team of Enea (http://www.enea.it) for using the ENEA-GRID and the HPC facilities CRESCO (http://www.cresco.enea.it) in Portici.

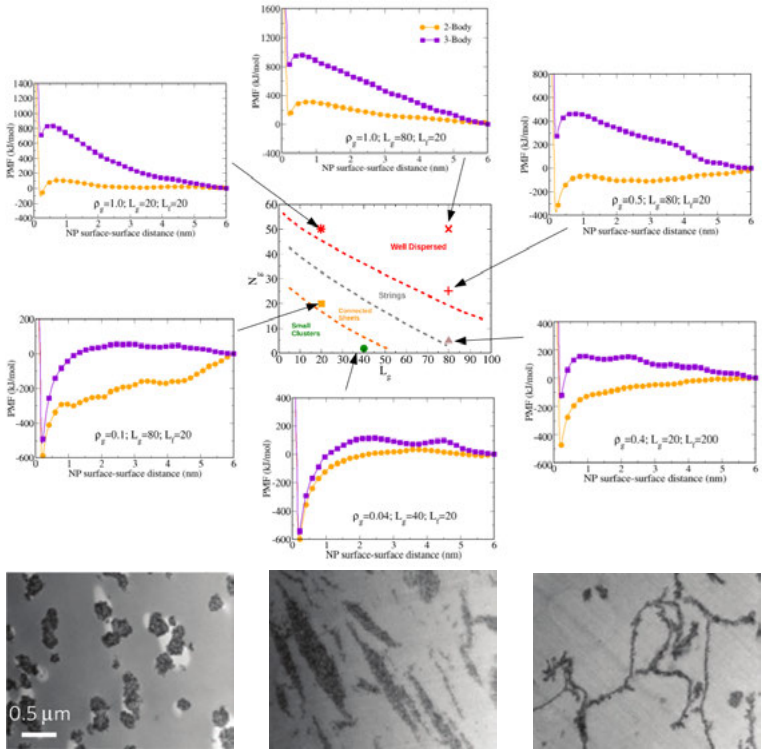

Figure 1: Top: schematic morphology diagram for grafted NPs embedded in a PS matrix, drawn by considering the three-body PMF. Different colors are used for well dispersed, strings, connected sheets and small clusters regions. The dashed lines separating the different regions are indicative guides for the eye. The behaviors of two-body and three-body PMF are also reported for enhancing their relation to the morphology diagram. Bottom: trasmission electron microscopy images of the corresponding self-assembled structures, redrawn from Akcora et al. [4]. The scale bar is indicated in the first image of the panel.

References

[1] C. Chevigny, J. Jestin, D. Gigmes, R. Schweins, E. Di Cola, F. Dalmas, D. Bertin, and F. Bouè. "wet-to-dry" conformational transition of polymer layers grafted to nanoparticles in nanocomposite. *Macromolecules*, 43:4833, 2010.

[2] D. Meng, S. K. Kumar, J. M. D. Lane, and G. S. Grest. Effective interactions between grafted nanoparticles in a polymer matrix. *Soft Matter*, 8:5002, 2012.

[3] A. De Nicola, T. Kawakatsu, F. Müller-Plathe, and G. Milano. Fast relaxation of coarse-grained models of polymer interphases by hybrid particle-field molecular dynamics: Polystyrene-silica nanocomposites as an example. *Eur. Phys. J. Special Topics*, 225:1817, 2016.

[4] P. Akcora, H. Liu, S. K. Kumar, J. Moll, Y. Li, B. C. Benicewicz, L. S. Schadler, D. Acechin, A. Z. Panagiotopoulos, V. Pyramitsyn, V. Ganesan, J. Ilavsky, P. Thiyagarajan, R. H. Colby, and J. F. Douglas. Anisotropic self-assembly of spherical polymer-grafted nanoparticles. *Nat. Mater.*, 8:354, 2009.

[5] T. Kawakatsu. *Statistical Physics of Polymers*. Springer, Berlin, 2004.

[6] G. Milano and T. Kawakatsu. Hybrid particle-field molecular dynamics simulations for dense polymer systems. *J. Chem. Phys.*, 130:214106, 2009.

[7] S. K. Kumar, N. Jouault, B. Benicewicz, and T. Neely. Nanocomposites with polymer grafted nanoparticles. *Macromolecules*, 46:3199, 2013.

AIR QUALITY MODELING FOR ASSESSMENT OF HEALTH RISKS FROM INDUSTRIAL FACILITIES. A STUDY ON A NEW-GENERATION COAL-FIRED POWER PLANT

Antonio Piersanti[1]*, Mario Adani[1], Gino Briganti[1], Andrea Cappelletti[1], Luisella Ciancarella[1], Giuseppe Cremona[1], Massimo D'Isidoro[1], Carmine Lombardi[2], Francesca Pacchierotti[3], Felicita Russo[1], Marcello Spanò[3], Raffaella Uccelli[3], Lina Vitali[1]

[1] *ENEA, National Agency for New technologies, Energy and Sustainable Economic Development, Laboratory of Atmospheric Pollution, via Martiri di Monte Sole 4, 40129 Bologna, Italy*

[2] *retired*

[3] *ENEA, National Agency for New technologies, Energy and Sustainable Economic Development, Laboratory of Biosafety and Risk Assessment, Via Anguillarese 301, 00123 Santa Maria di Galeria - Rome, Italy*

ABSTRACT. An assessment of potential carcinogenic and toxic health outcomes related to atmospheric emissions from the new-generation coal fired power plant of Torrevaldaliga Nord, in central Italy, has been conducted. The AMS-MINNI model of atmospheric chemistry and dispersion was run on the reference year 2010 in the area of the plant, producing airborne concentrations of a set of pollutants of significant health concern. Two model simulation were carried out, one for the overall ambient concentrations and another one for the sole contribution of the plant to airborne concentrations, allowing to assess the relative contribution of the power plant to the risk from all sources. Inhalation cancer risks and hazard quotients, for each pollutant and for each target organ impacted via the inhalation pathway, were calculated and mapped on the study domain. The proposed method can support health risk assessment of large industrial sources, with a prospective approach focused on potential future health impacts.

1 Introduction

We carried out a prospective risk assessment of potential health outcomes from the new-generation coal fired power plant of Torrevaldaliga Nord, in central Italy, in collaboration with the plant operators (ENEL s.p.a.). The basis is a prospective approach following the official Italian guidelines and internationally standardized risk assessment procedures.
An air quality modeling procedure was applied, using the AMS-MINNI [1] chemical transport model on the year 2010 with a differential approach, allowing to calculate pollutant concentrations both from all emission sources and from the sole power plant. This kind of approach is more comprehensive than air quality modeling approaches for risk assessment available in literature, since the evaluation of pollutant concentrations both for the entire area and for the individual plant takes into account, at the same time, three demanding aspects: a complete model representation of transport and chemical processes in atmosphere, a complete emission inventory of the area and large computing resources for a long-term simulation.

The plant is located about 50 km North-West of Rome, in the town of Civitavecchia. It is included in the list of industrial plants of national strategic relevance. The plant is conducted by ENEL s.p.a., a world major player in power generation and the largest producer of electric power in Italy, and is the second largest running power plant in Italy (1980 MW installed power capacity). The plant, in operation since 1984 on oil fuel, was converted to clean coal fuel in 2006-2007, restarted in 2008 and restored to full operation in 2010, with 4,075,569 tons of coal consumption and 11,603,020 MWh of net power fed into the grid. Coal is transported by ships, transferred by hermetic conveyor belts in 2 sealed coal storing domes, to feed 3 high-efficiency ultra-supercritical boilers with low NOx burners. Flue gases are treated with selective catalytic reduction (SCR) system for NOx decomposition, fabric filters (FF) for PM abatement, and a flue gas desulfurization (FGD) system with a wet limestone-gypsum scrubber for SOx removal. Flue gases are conveyed to a stack of 250 m height and 5.75 m exit diameter.

Fig.**1**: 3D photo-reconstruction of Torrevaldaliga Nord power plant (credits: Google Earth).

2 Methods

The emissions input data for the model simulations came from the Italian National Emission Inventory at NUTS level 3 (provinces), referred to the year 2010, published in May 2015 by ISPRA [2]. Data for large industrial sources are on the basis of different official registers, for supporting modeling applications, but are not available to the public. The inventory data for the plant were checked, against both public and private (ENEL) information available on the plant and considering the available scientific literature on similar plants. Almost all values were confirmed except for arsenic and selenium, significantly higher in the inventory. We decided to keep unchanged the inventory values of arsenic and selenium in this study, even if they are considered more inaccurate than other pollutants and leading to likely overestimated values of risks.
The meteorological and emission pre-processors and the chemical-transport model were run on a spatial domain of 120 km x 110 km, covering the power plant and the Rome area, with a horizontal

spatial resolution of 1 km x 1 km and a time resolution of 1 hour, for the year 2010. Boundary conditions for pollutants concentrations were provided from the official national MINNI model run for the year 2010, at 4 km x 4 km resolution. A comprehensive evaluation of model results has been performed in the target area, comparing modeled values with observations from public and private monitoring networks.
The risk assessment methodology followed the Italian law provisions and the reference levels for each of the main pollutants emitted from the plant were selected from the most valuable national and international scientific literature (World Health Organization, United States Environmental Protection Agency, California Environmental Protection Agency). For carcinogenic pollutants the inhalation dose was calculated as:

$$Dose = \frac{c_{air} * Rate * A * EF * ED * 1x10^{-6}}{AT}$$

where Dose is the dose absorbed through inhalation (mg/kg-day), c_{air} is the pollutant concentration in air ($\mu g/m^3$), Rate is the daily breathing rate (l/kg body weight-day), A is the inhalation absorption factor, EF is the exposure frequency (days/year), ED is the exposure duration (years), AT is the time period over which exposure is averaged (days).
The inhalation risk was calculated as:

$$R = Dose * SF$$

where SF = inhalation slope factor ($(mg/kg\text{-}day)^{-1}$), i.e. the additional lifetime (70 years) cancer risk for a standard man of 70 kg body weight and 20 m^3/day respiratory volume associated to an exposure of 1 $\mu g/m^3$ of a carcinogen in the air:

$$SF = UR * \frac{70\,kg}{20\,m^3/day} * 1000\,\mu g/mg$$

where UR represents the inhalation unit risk $(\mu g/m3)^{-1}$ for each pollutant.
For non-carcinogenic pollutants, the inhalation hazard quotient (HQ) was computed as follows:

$$HQ = \frac{c_{air}}{RfC} * 1000$$

Formulas were applied using modeled c_{air} values. Relying on concentration data availability on the modeling grid, also R and HQ were computed on the same domain and at the same spatial resolution.
R and HQ were calculated both for the area, keeping into account all emission sources in the modeled concentrations (R_{area} , HQ_{area}), and for the power plant, using the AQM differential approach (R_{plant} , HQ_{plant}). The most harmful atmospheric pollutants were selected, according to the availability of emission inventory data and of quantified risks in international scientific literature: benzene, benzo(a)pyrene, benzo(b)fluoranthene, benzo(k)fluoranthene, indeno(1,2,3-cd)pyrene, arsenic, cadmium, mercury, nickel, lead, selenium, particulate matter (PM10 and PM2.5), ammonia, nitrogen dioxide, ozone, sulphur dioxide.

3 Results

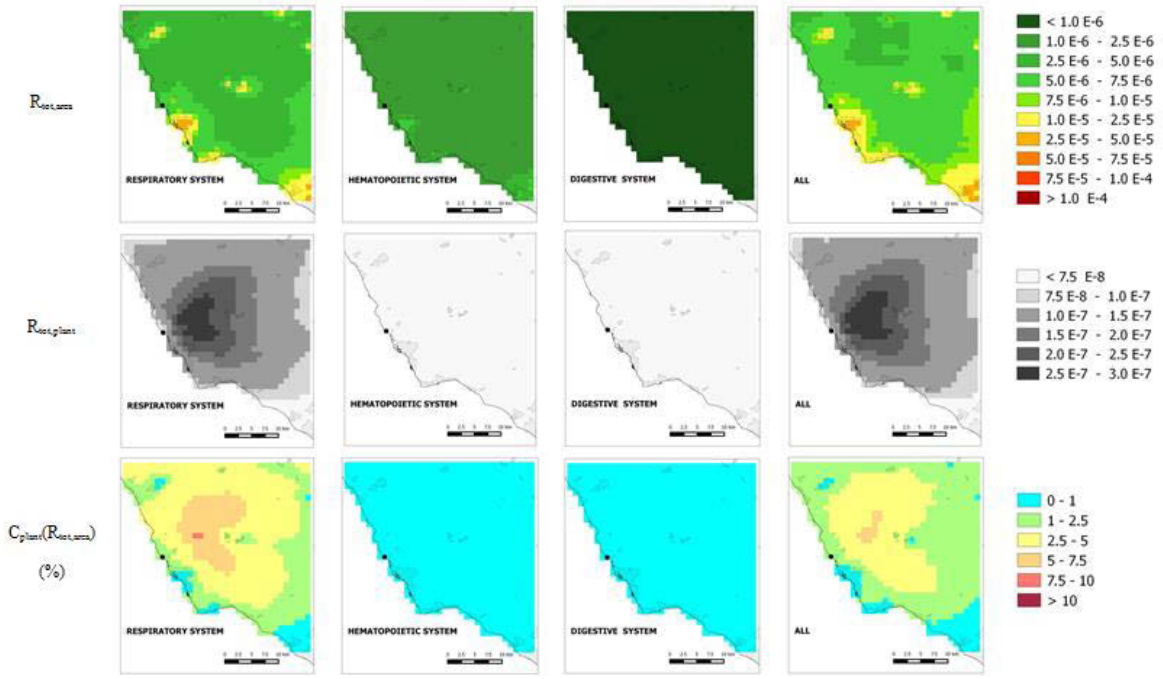

Fig. 2: cumulative carcinogenic risk from all sources ($R_{tot,area}$ - upper row), from the plant ($R_{tot,plant}$ - median row) and relative contribution of the plant to the risk from all sources ($C_{plant}(R_{tot,area})$ - lower row). Risk maps are shown for each target organ (columns) and overall (rightmost column).

In Fig. 2 the cumulative carcinogenic risk maps for all sources ($R_{tot,area}$) and for the sole power plant ($R_{tot,plant}$), and the relative contribution to the overall risk ($C_{plant}(R_{tot,area})$) are reported for each organ/apparatus (respiratory, hematopoietic, digestive) and for the overall risks. The maps of $R_{tot,area}$ show local maxima on the urban areas. The respiratory apparatus is the most impacted, with peak values between 2.5 x 10^{-5} and 5 x 10^{-5} (orange cells) and a prevalence of areas under 7.5 x 10^{-6} (green cells). The hematopoietic and the digestive systems show considerably lower risks, below 7.5 x 10^{-6}. The maps of $R_{tot,plant}$ show the "footprint" of the plant emissions fallout. The impact area covers the inland towards East and North-East, with values between 1 x 10^{-7} and 3 x 10^{-7} (last 4 shades of grey) in an area of about 300 km^2. The main target is the respiratory system. As already observed for the total area, also the plant-related risks for the hematopoietic and the digestive systems are considerably lower, below 7.5 x 10^{-8} (white cells). The shape of the contribution $C_{plant}(R_{tot,area})$ is similar, extended in East and North-East directions, and the maxima are located about 15 km far from the plant, with values of about 7.7% for the respiratory system (light red cells). However, $C_{plant}(R_{tot,area})$ decreases on urban areas including Civitavecchia, due to a higher contribution of other emitting sources to $R_{tot,area}$. Overall, the inhalation cancer risk from the power plant resulted always lower than resulted lower 3 x 10-7, well below the threshold of 10^{-6} which is the most protective value of the range considered acceptable by several International Agencies involved in risk assessment and management.

Analogous maps were calculated for hazard from non-carcinogenic pollutants, for all sources ($HQ_{tot,area}$) and for the sole power plant ($HQ_{tot,plant}$), and the relative contribution to the overall risk ($C_{plant}(HQ_{tot,area})$).). As far as the plant contribution is concerned, the maps of $HQ_{tot,plant}$ show a similar footprint compared to carcinogenic risks, extended in East and North-East directions, with maxima of about 0.03 for the respiratory system (darkest blue cells), located about 10 km far from the plant, and of about 0.02 for the cardiovascular system.

The proposed method was developed targeting the fulfilment of Italian law obligations on health damage and provides a tool for prospective human health risk assessment of large industrial sources, with an air quality model taking into account all emission sectors, atmospheric chemistry and the specific contribution of the plant.
More details are available in [3].

The computing resources and the related technical support used for the air quality simulations have been provided by CRESCO/ENEAGRID High Performance Computing infrastructure and its staff.

References

[1] Mircea M., Ciancarella L., Briganti G., Calori G., Cappelletti A., Cionni I., Costa M., Cremona G., D'Isidoro M., Finardi S., Pace G., Piersanti A., Righini G., Silibello C., Vitali L., Zanini G. . Assessment of the AMS-MINNI system capabilities to simulate air quality over Italy for the calendar year 2005. *Atmospheric Environment* **84**, pp. 178-188, (2014).

[2] Istituto Superiore per la Protezione e la Ricerca Ambientale (ISPRA), 2015. Disaggregazione dell'inventario nazionale 2010 – versione completa. http://www.sinanet.isprambiente.it/it/sia-ispra/inventaria/ , last accessed June 1, 2015.

[3] A. Piersanti, M. Adani, G. Briganti, A. Cappelletti, L. Ciancarella, G. Cremona, M. D'Isidoro, C. Lombardi, F. Pacchierotti, F. Russo, M. Spanò, R. Uccelli, L. Vitali. Air quality modeling and inhalation health risk assessment for a new generation coal-fired power plant in Central Italy. *Science of The Total Environment* **644**, pp. 884-898, (2018). DOI: 10.1016/j.scitotenv.2018.06.393.

Calculation of beam quality correction factors for reference dosimetry in radiotherapy photon beams

Maria Pimpinella*, Luca Silvi and Massimo Pinto

ENEA-FSN-INMRI, National Institute of Ionizing Radiation Metrology, 00123 Rome, Italy

ABSTRACT. The Monte Carlo (MC) method was applied to calculate the beam quality correction factors, k_Q, needed for reference dosimetry in external beam radiotherapy using ionization chambers calibrated in a reference Co-60 gamma beam. The k_Q factors were calculated by simulating the response in terms of absorbed dose to water of a Farmer type ionization chamber with an air sensitive volume of 0.6 cm^3. Long computation times are needed to fulfil the accuracy requirement of radiotherapy dosimetry, therefore a preliminary study was made to select the most appropriate transport parameters and calculation methods for accurate and efficient MC calculations.

1 Introduction

A central point for a successful radiotherapy treatment is the accuracy of the estimate of absorbed dose delivered to the patient according to international dosimetry recommendations. A consistent quality assurance procedure requires absorbed-dose-to-water (D_w) measurements in reference conditions as the first step. An important source of uncertainty in D_w measurement is the difference between the calibration and the user's beam that can affect the detector response to some extent. D_w measurements in radiotherapy beams produced by clinical accelerators are currently made by means of ionization chambers calibrated in a Co-60 gamma beam. Chamber-specific beam quality correction factors (k_Q) are used to correct the calibration coefficient for the different response in the clinical beam. The international dosimetry protocol IAEA TRS 398 [1] provides sets of k_Q values for the most widely used ionization chambers (Q indicates the beam energy). Those k_Q factors were calculated according to an analytic expression derived from the cavity theory and using theoretical and experimental key data available at the time of the protocol publication in 2000. Nowadays, advances in computer technology and availability of Monte Carlo (MC) software packages allowing accurate simulation of clinical beams and detector response [2,3] make calculation of k_Q factors possible with reduced uncertainty, compared to the values published in the IAEA TRS 398.
This report describes calculation algorithms, simulation geometries, and radiation transport parameters for the calculation of k_Q factors for radiotherapy photon beams by means of the EGSnrc MC toolkit [4].

2 Methods

2.1 Definition of k_Q

According to the IAEA TRS 398 [1] the beam quality factor is defined as:

$$k_Q = \frac{D_{w,Q}/M_Q}{D_{w,Co-60}/M_{Co-60}} \quad (1)$$

where D_w is the absorbed dose to water at the measurement point and M is the chamber signal (i.e. the collected charge) corrected for the influence quantities (temperature, pressure, ion recombination etc.). Considering that the absorbed dose to a medium is the energy deposited by radiation per unit mass, and assuming that the conversion of the energy deposited in the chamber sensitive volume into collected charge is independent of energy, eq. (1) can be rewritten as

$$k_Q = \frac{D_{w,Q}/D_{ch,Q}}{D_{w,Co-60}/D_{ch,Co-60}} \quad (2)$$

where D_{ch} is the absorbed dose to air in the chamber active volume. All the quantities in equation (2) can be obtained by simulating the radiation transport in water and the ionization chamber irradiation in the reference conditions specified in table 1 [1].

Influence quantity	*Reference value*	
	Co-60 gamma beam	*4 MV – 25 MV photon beams*
Phantom material	water	Water
Measurement depth	5 g/cm^2	10 g/cm^2
Field size at phantom surface	10 cm x 10 cm	10 cm x 10 cm

Table.1- Reference conditions for dosimetry in high energy photon beams

2.2 Calculation details

The EGSnrc system (https://nrc-cnrc.github.io/EGSnrc/) [4] installed on the cluster CRESCO4 in shared mode was used. The geometry package egs++, with the C++ class library, was used to model the NE 2571 ionization chamber, including a 1 mm thick PMMA waterproof sheet. D_w and D_{ch} in eq.(2) were calculated using the *egs_chamber* application [5]. D_w was obtained as absorbed dose in a small disk of water (1 cm radius, 0.025 cm thick) and D_{ch} as absorbed dose to air in the chamber cavity (about 0.6 cm^3) placed at the reference depth in a cube of water with side 30 cm (Fig.1).

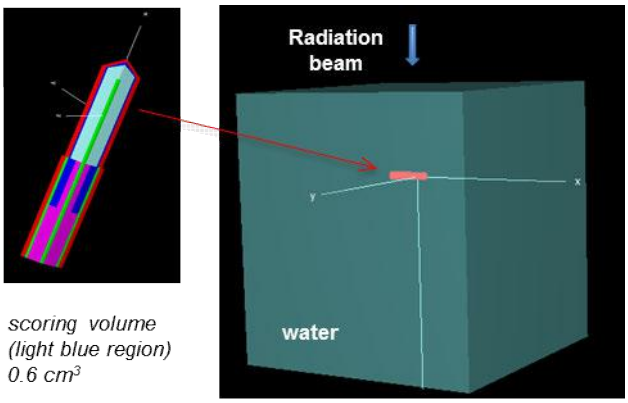

Fig.**1**: Model of a Farmer type ionization chamber (left) and computational geometry (right) for Monte Carlo simulations of the chamber irradiation in a water tank 30 cm x 30 cm x 30 cm.

Considering the small scoring volumes (0.08 cm^3 disk of water and 0.6 cm^3 air cavity) compared to the whole simulation geometry (27000 cm^3), it is clear that only a small fraction of interaction events in water can contribute to the dose scoring in the volumes of interest. In the energy range of this work, the mean free path of primary photons is between 10 cm and 50 cm and the typical range for secondary electrons is below 2 cm. Therefore, for most secondary electrons, the distance between the point of production and the scoring cavity is larger than their range. Following these particles causes a waste of time and variance reduction techniques (VRT) are needed to obtain in reasonable time a statistical uncertainty of calculated doses below 0.1%. Among the VRTs implemented in EGSnrc, the range-based Russian Roulette (RR) and the photon cross section enhancement (XCSE) were applied. The RR allows to terminate the trajectory of electrons not directly contributing to the dose scoring. Using the XCSE, the photon cross section can be increased by a given factor in a region surrounding the scoring cavity so to conveniently increase the number

of electrons set in motion by the incident photons while keeping constant the number of transported photons. The calculation efficiency can be defined as:

$$\varepsilon = \frac{1}{T\,\sigma^2} \qquad (3)$$

where T is the total computational time and σ^2 is the estimated variance of the calculated quantity. Since efficiency strongly depends on the XCSE factor and the extension of the enhancement region, a preliminary study was made to select the most appropriate parameters to be used.
Concerning the transport parameters, many options are available in EGSnrc. All the options for the most accurate interaction models were turned on when calculating k_Q (table 2). The default values were gradually changed and the impact on calculation results and time was evaluated for the Co-60 beam and for two clinical energies. The energy cut-off for electrons and photons were set to the minimum value allowed in EGSnrc (1 keV).

Transport parameter	*Default value*	*Adopted value*
Photon cross section	xcom	mcdf-xcom
Pair cross sections	BH	NRC
Bound Compton scattering	norej	On
Radiative Compton corrections	Off	On
Rayleigh scattering	Off	On
Photonuclear attenuation	Off	On
Brem cross sections	BH	NIST
Electron Impact Ionization	Off	On

Table.2- Transport parameters with settings different from the default values.

3 Results

Tests on the XCSE implementation showed that the highest efficiency gain is obtained for the Co-60 beam and the optimal XCSE factor tends to decrease with energy (Fig. 2). Based on these results, the XCSE factor was set to 128 for Co-60 and 6 MV beams and to 64 from 10 to 25 MV.

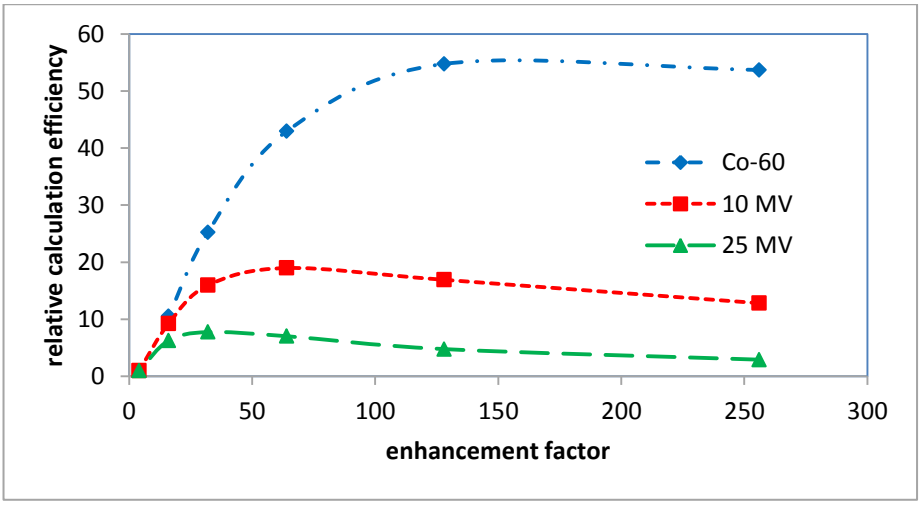

Fig.**2**: Efficiency gain as a function of XCSE factor for calculating the absorbed dose in the air cavity of the NE 2571 ionization chamber at reference depth in 30x30x30 cm^3 water phantom. The XCSE region extends 2 cm beyond the ionization chamber.

XCSE was applied in a region extending 2 cm beyond the scoring voxels and, given a target uncertainty, the simulation time was reduced by a factor ranging from 55 to 8.
Changing the transport parameters from the default values mainly resulted in an increase of simulation time. The maximum increase (about 10%) was observed in Co-60 beam and it was mostly caused by turning on the radiative Compton corrections. The corresponding time increase was about 4% at 10 MV and below 1% at 25 MV. Variations in the calculated absorbed doses due to adoption of the transport parameter values in table 2 ranged from -0.1% to 0.3% but, the final effect on k_Q values was within 0.15%, since variations partially cancelled out in the ratio.
Figure 3 shows the k_Q factors calculated for the NE 2571 chamber in comparison with the values published in the IAEA TRS 398. Differences are typically below 0.5% and therefore well within the 1% combined standard uncertainty associated to the TRS 398 values but, it should be noted that the MC values tend to be systematically lower than the protocol values. Work is in progress for analysing the above differences also extending the MC calculation of k_Q factors to reference class ionization chambers of different models.

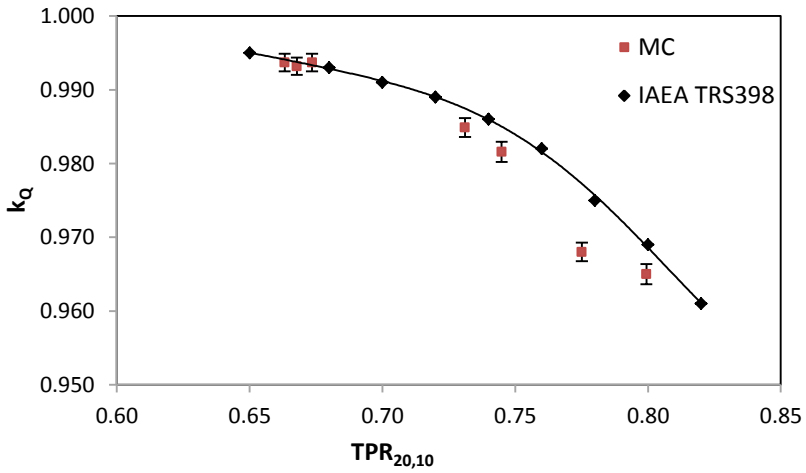

Fig.3: Monte Carlo calculated k_Q factors for the NE 2571 ionization chamber compared to the values recommended in the IAEA TRS 398.

Acknowledgments

This work is part of the RTNORM research project which has received funding from the EMPIR programme, grant 16NRM03 'k_Q factors in modern external beam radiotherapy applications to update IAEA TRS-398', co-financed by the Participating States and from the European Union's Horizon 2020 research and innovation programme.

References

[1] ANDREO P., BURNS D.T., HOHLFELD K., HUQ M., KANAI T., LAITANO R. F., SMYTH V., VYNCKIER S. "*Absorbed dose determination in external beam cancer therapy; An International Code of Practice for Dosimetry Based on Standards of Absorbed Dose to Water*". IAEA-TRS 398 (2000) (Vienna: IAEA)
[2] MUIR B.R., ROGERS D.W.O. "*Monte Carlo calculation of k_Q, the beam quality conversion factor*". Med. Phys. **37** (2010) pp 5939-50
[3] SEMPAU J., ANDREO P., ALDANA J., MAUZIER J., SALVAT F. "*Electron beam quality correction factors for plane-parallel ionization chambers in high energy photon beams: Monte Carlo calculations using the PENELOPE system"*. Phys. Med. Biol. **49** (2004) pp 4427-44
[4] KAWRAKOW I., MAINEGRA-HING E., ROGERS D.W.O., TESSIER F., WALTERS B.R.B. "*The EGSnrc Code System: Monte Carlo simulation of electron and photon transport"*. NRCC Report PIRS-701 (2013)
[5] WULFF J., ZINK K., KAWRAKOW I. "*Efficiency improvements for ion chamber calculations in high energy photon beams*". Med. Phys. **35** (2008) pp 1328-36

FREE ENERGIES IN TX-100/DPPC BILAYERS

A. Pizzirusso[1]*, G. Munaó[1], S. Caputo [1], G. Donati[1], A. De Nicola[2], Y. Zhao[3] and G. Milano[1,2]

[1] *Salerno University, Department of Chemistry and Biology "Adolfo Zambelli", 84084, Via Giovanni Paolo II, 132, Fisciano (SA), Italy.*

[2] *Department of Organic Materials Science, University of Yamagata, 4-3-16 Jonan Yonezawa, Yamagata-ken 992-8510, Japan.*

[3] *Dalian Minzu University, Institute of Nano-Photonics, School of Physics and Materials Engineering, 116600, Dalian, China.*

ABSTRACT. We examine at molecular level the extraction mechanism of lipid membrane in presence of Triton TX-100, by means of hybrid Molecular Dynamics - Self Consistence Field (MD-SCF) Computer Simulation. The work made from TX-100 to extract lipids is computed through Potential Mean Force approach. The resulting free energy profiles indicate that DPPC can be extracted more easily increasing the amount of TX-100 on the membrane surface.

1 Introduction

Membrane solubilization by interaction with detergents is a crucial step in several technological applications, and it is connected to characterization of integral membrane proteins [1, 2, 3, 4, 5]. The use of detergents, that are able to extract proteins from their native membrane, allows the investigation of macromolecular interactions between membrane proteins [6]. Studies using detergents for the isolation of proteins in specific membrane domains have so far revealed important physiological understanding in processes such as surface signaling [7], cell adhesion [7, 8, 9, 10], and intracellular sorting [11, 12].

On the basis of a recent publication [13] in which the solubilization mechanism of lipid bilayers in the presence of Triton X-100 (TX-100) has been investigated at molecular level, we studied the work made by TX-100 to extract membrane proteins as free energy profile. At the same time and thanks to the large time and length scales accessible by the hybrid particle-field formulation and CRESCO supercomputing resources, the complex process of protein extraction is here reported. For this purpose we are chosen three systems that differ from TX-100 concentration in a DPPC bilayer. In particular, we consider three different systems: The first of pure DPPC bilayer, a second of a bilayer composed of a ratio TX-100/DPPC =0.43 (close to the saturation ratio R_e^{sat} limit [14]), where TX-100 is randomly distributed on both the leaftlefts. The third system is a bilayer of a ratio TX-100/DPPC =1.0 (close to the experimental solubilization ratio R_e^{sol} limit [14]), where TX-100 is also randomly distributed.

*Corresponding author. E-mail: apizzirusso@unisa.it.

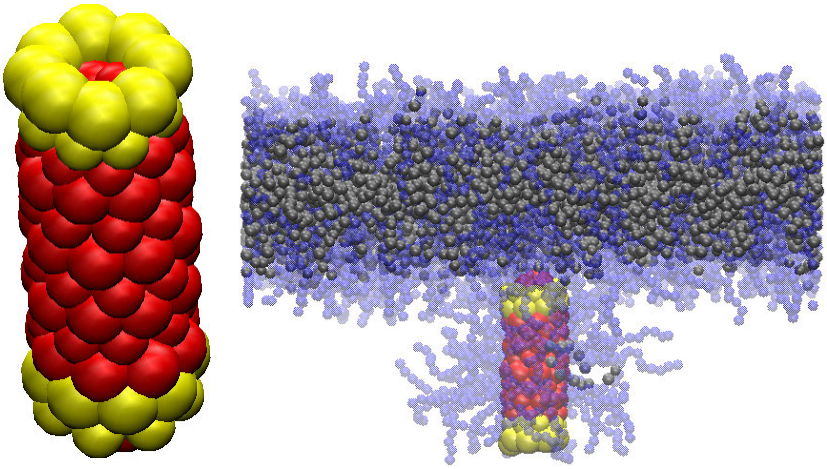

Figure 1: [Left] Double-walled nanotube as membrane protein where the central hydrophobic block is decipted in red and two hydrophilic terminal parts are coloured in yellow. [Right] CNT on a TX-100/DPPC=1.00 Bilayer placed at z=-5.25 nm of its center. TX-100 is coloured in blue and DPPC in gray.

2 Simulation Details

2.1 Coarse Grained Mapping and Potential Mean Force

For the mapping adopted of DPPC and TX-100 Coarse Grained models we refer to what is described in the our recent article [14], while the protein of membrane is mimic by a double-walled carbon nanotube (CNT), having a cylindrical shape of 4.0nm length and 1.3 nm diameter. The protein model is thus composed of a total of 132 beads with a central hydrophobic block and two hydrophilic terminal parts (see Figure 1 [Left]).

With the aim to generate a free energy profile act to describe the request work to extract the membrane protein as function of the TX-100 concentration, we propose a set of independent initial configurations (49 for each concentration), corresponding to a CNT placed at a fixed distance from the bilayer. In particular, placing CNT at progressively increasing distances from the bilayer center of mass (c.o.m, with a step of $\Delta z = 0.25nm$), we are able to evaluate the net force experienced by each of them. The potential of Mean Force (PMF) can been thus calculated according to the equation:

$$U(z) = -\int_{z_{max}}^{z_{min}} F(z)dz \tag{1}$$

where $U(z)$ is the potential of mean force and $F(z)$ is the force experienced by CNT, while z_{max}=6.0 nm and z_{min}=-6.0 nm from the c.o.m. of the bilayer are the limits of the integral.
According to this procedure, the CNT is symmetrically placed on both the leaflefts of the bilayer (see for instance, Fig.1 [Right] where CNT is placed on the down-leafleft of bilayer). For this purpose long simulations runs ($\simeq 800\ ns$) are required for 40980 particles of each sample.

2.2 MD-SCF Approach

The main feature of the hybrid MD-SCF approach is that the calculation of intermolecular non-bonded forces and potentials, representing the most computationally demanding part of MD simulations, can be substituted by a calculation of external potentials dependent on the local density (at position $\mathbf{r}$) [15]. According to the idea of SCF theory, a multi-body problem, such as molecular motion, can be reduced to a problem of deriving the partition function of a single molecule in an external potential $V(\mathbf{r})$ and to obtain a convenient expression of $V(\mathbf{r})$ and its derivatives.
In the framework of SCF theory, a molecule is regarded to be interacting with the surrounding molecules through a mean field, rather than direct interactions among the molecules. Assuming that the density dependent interaction potential W, where each species is specified by the index K, takes the form:

$$W[(\phi_k(\mathbf{r}))] = \int d\mathbf{r} \left(\frac{K_B T}{2} \sum_{KK'} \chi_{KK'} \phi_K(\mathbf{r}) \phi_{K'}(\mathbf{r}) + \frac{1}{2\kappa} (\sum_K \phi_k(\mathbf{r}) - \phi_0)^2 \right) \tag{2}$$

where $\phi K(r)$ is the coarse-grained density of species K at position r and $\chi_{KK'}$ are the mean field parameters for the interaction of a particle of type K with the density fields due to particles of type K'. It can be shown using the so-called saddle point approximation that the external potential is given by:

$$V_K(\mathbf{r}) = \frac{\delta W[(\phi_k(\mathbf{r}))]}{\delta \phi_K(\mathbf{r})} = K_B T \sum_{K'} \chi_{KK'} \phi_{K'}(\mathbf{r}) + \frac{1}{\kappa} \left(\sum_K \phi_k(\mathbf{r}) - \phi_0 \right) \tag{3}$$

To connect the particle and field models for the proposed hybrid MD-SCF scheme, it is necessary to obtain a smooth coarse-grained density function directly from the particle positions. Such function can be obtained using a mesh-based approach, which must also be able to give the density derivatives required to calculate the forces acting on molecules. The derivation of eq. 3 and the implementation of this approach are reported elsewhere [16, 15].

All simulations reported in the present report have been performed by using the version of OCCAM MD code where the Potential Mean Force is implemented inset.

3 Simulation Results

Configurations of simulation of $\simeq 1\mu s$ long are reported in Figure 2, where CNT is symmetrically placed on both the monolayers at a given distance. We found a more amount of TX-100 around the membrane protein increasing the concentration of TX-100, and consequently the Carbon Nanotube is easier to extract. In Figure 3 we reported the free energy profiles (as the calculation of the potential of mean force) that confirm the easier extraction of the CNT. The hole of free-energy in fact decreases as function of TX-100 concentration, and the work required from TX-100 to extract the carbon nanotube is less. For obtaining accessible simulation times to understand this assumption at molecular level, we opted thus for CRESCO supercomputing resources.

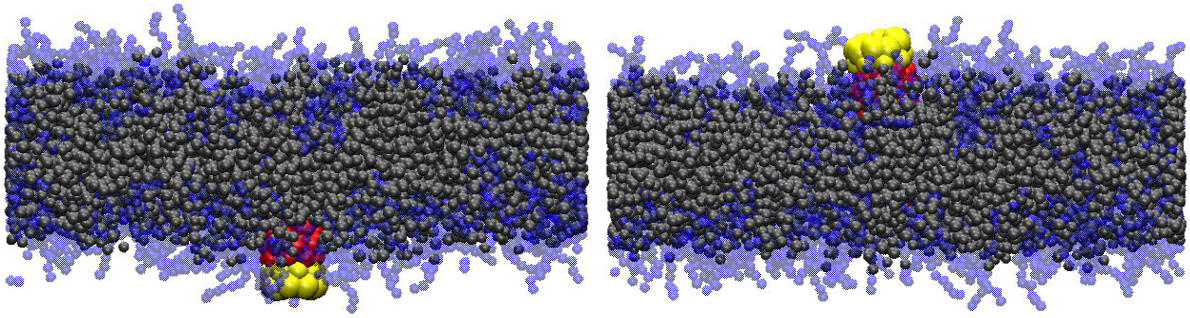

Figure 2: CNT in TX-100/DPPC=0.43 Bilayer at 2.25 nm of its center. CNT is symmetrically placed top and down the bilayer at z=2.25 nm.

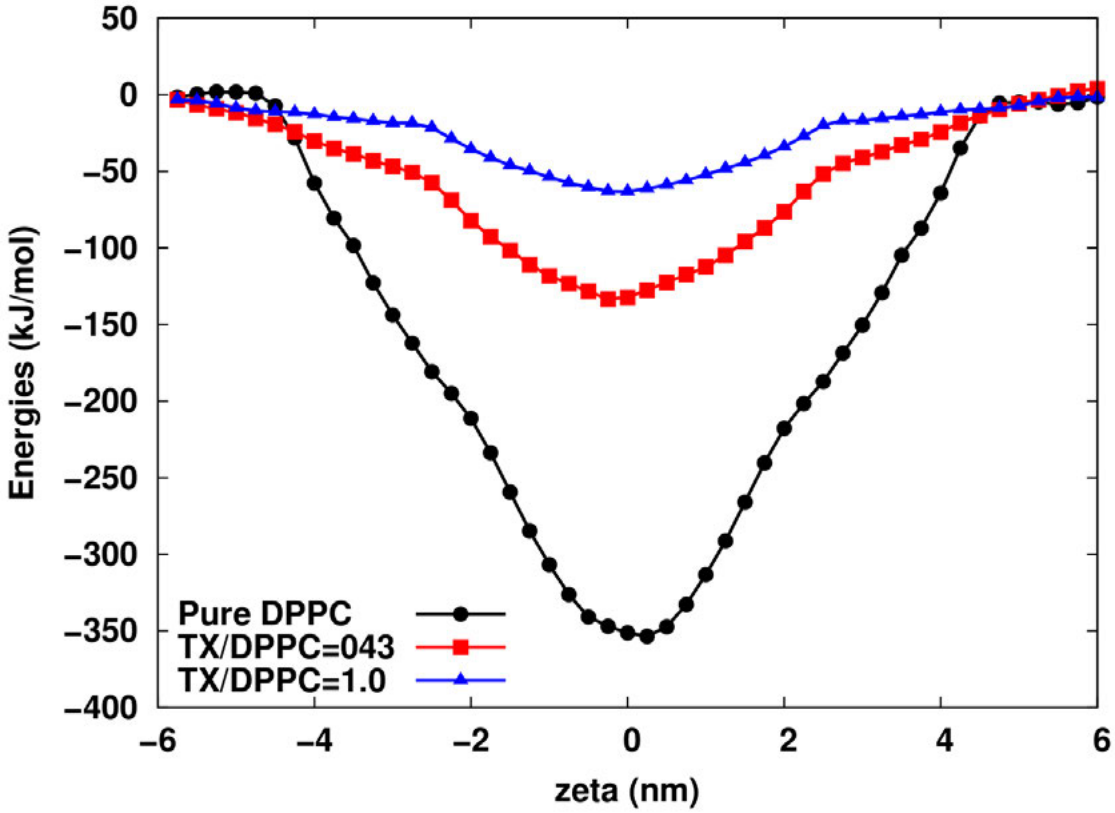

Figure 3: Free energy profiles computed as as the calculation of the potential of mean force, as function of distance of the center of lipid membrane (z=0) and at different concentration of TX-100 in bilayer.

References

[1] Helenius A. and Simons K. *Biochim. Biophys. Acta*, 415:29–79, 1975.

[2] E. A. Dennis. *Arch. Biochem. Biophys.*, 175:764–773, 1974.

[3] E. London and D. A. Brown. *Biochim. Biophys. Acta, Biomembr.*, 1508:182–195, 2000.

[4] J. Lasch. *Biochim. Biophys. Acta, Rev. Biomembr.*, 1241:269–292, 1995.

[5] C. Rosano and M. Rocco. *FEBS J.*, 277:3190–3202, 2010.

[6] M. le Maire, P. Champeil, and J. V. Möller. *Biochim. Biophys. Acta, Biomembr.*, 1508:86–111, 2000.

[7] D. A. Brown and E. London. *J. Biol. Chem.*, 275:17221–17224, 2000.

[8] L. Hinck, I. S. Näthke, J. Papkoff, and W. J. Nelson. *Journal of Cell Biology*, 125:1327–1340, 1994.

[9] I. Rabinovitz and A. M. Mercurio. *Journal of Cell Biology*, 139:1873–1884, 1997.

[10] A. Bernkop-Schnürch and G. Walker. *Critical Reviews in Therapeutic Drug Carrier Systems*, 18:459–501, 2001.

[11] D. A. Brown and E. London. *Annual Review of Cell and Developmental Biology*, 14:111–136, 1998.

[12] S. Pfeiffer, S. D. Fuller, and K. Simons. *1985*, 101:470–476, The Journal of Cell Biology.

[13] A. Pizzirusso, A. De Nicola, G. J. A. Sevink, A. Correa, M. Cascella, T. Kawakatsu, M. Rocco, Y. Zhao, M. Celino, and G. Milano. *Phys. Chem. Chem. Phys.*, 19:29780–29794, 2017.

[14] E. Schnitzer, D. Lichtenberg, and M. M. Kozlov. *Chem. Phys. Lipids*, 126:55–76, 2003.

[15] Milano G. and Kawakatsu T. *J. Chem. Phys.*, 130:214106, 2009.

[16] De Nicola A., Zhao Y., Kawakatsu T., Roccatano D., and Milano G. *J. Chem. Theory Comput.*, 7:2947–2962, 2011.

SAMPL6 host-guest blind predictions using a non equilibrium alchemical approach

Piero Procacci[1]*

Dipartimento di Chimica, Università di Firenze, Via della Lastruccia 3, I-50019 Sesto Fiorentino, Italy

Abstract. In this paper, we compute, by means of a non equilibrium alchemical technique, called Fast Switching Double Annihilation Methods (FSDAM), the absolute standard dissociation free energies of the the octa acids hots-guest systems in the SAMPL6 challenge initiative. FSDAM is based on the production of canonical configurations of the bound and unbound states via enhanced sampling and on the subsequent generation of hundreds of fast non-equilibrium ligand annihilation trajectories. The annihilation free energies of the ligand when bound to the receptor and in bulk solvent are obtained from the collection of work values using an unbiased estimate based on the Crooks theorem for driven non equilibrium processes. The FSDAM blind prediction, relying on the normality assumption for the annihilation work distributions, ranked among the best of all submitted blind predictions that were not adjusted with a linear corrections obtained from retrospective data on similar host guest systems. Improved results for FSDAM can be obtained by post-processing the work data assuming mixtures of normal components.

1 Introduction

Host-guest systems have been proposed in the SAMPL challenges[1] as effective substitutes for protein ligand systems in the evaluation of computational methods of predicting binding affinities. Typical host molecules in the SAMPL initiatives are cavitands like the octa acids (OA) and the tetra-endo-methyl octa-acids (TEMOA). These systems are supposed to mimic just the binding site pockets in proteins for hosting small flexible guest molecules, sparing the demanding task of simulating the whole protein and/or identifying the relevant binding sites on the protein surface. While SAMPL6 guests (termed as G0 to G7 in SAMPL6 see Ref. [1] for details) may exhibit a complex conformational pattern (e.g. G2 with axial/equatorial conformations of the 1-4 substituents on the six-membered ring, or G4 with five rotatble sp_3 bonds and, in principle, 243 different conformations), OA and TEMOA are relatively rigid systems, hence further alleviating the problem of canonically sampling the conformations of the binding sites in real proteins.

We used the so-called Fast Switching Double Annihilation technique (FSDAM).[2] FSDAM is the only non-equilibrium technique used in the SAMPL6 challenge. This method is based on the production of canonical configurations of the bound and unbound states via enhanced sampling (Replica Exchange with Solute Tempering, REST stage) and on the subsequent generation of hundreds of fast non-equilibrium (NE) ligand annihilation trajectories (Fast non equilibrium annihilation, FNEA stage) producing a bound and unbound work distributions. The annihilation free energies of the ligand when bound to the receptor and in bulk solvent, are straightforwardly obtained from the collection of NE work values

*Corresponding author. E-mail: procacci@unifi.it.

using an unbiased estimate, firmly based on the Crooks theorem for driven NE processes [3], in the assumption that the observed annihilation work distributions can be described by a normal distribution or by a mixture of Gaussian components.[4] The absolute binding free energies are recovered by the differences of the annihilation free energies of the ligand in bulk and in the bound state, plus a standard volume and finite-size corrections.

FSDAM is specifically tailored[5] for non uniform memory access systems, implemented via a two layer OpenMP/MPI parallelism, in such a way that the distributed memory layer manages the production of the simultaneous REST or FNEA trajectories, corresponding to weakly communicating MPI instances, each parallelized with a strong scaling scheme implemented on the OpenMP layer within the intra-node multi-cores shared memory environment. A single FNEA job can engage thousands of cores with nearly ideal parallel efficiency, producing a total simulation time of hundreds of nanonseconds in few wall clock minutes. On a per host-guest pair basis, the whole calculation required, for the REST stage, $\simeq$ 35 ns sampling (on the target state) using 8 replicas for both the bound and unbound systems and, for the FNEA stage, a cumulative $\simeq$ 250 ns for the bound and unbound state for a total simulation time on the sixteen host-guest system of $\simeq$8.5 μs of simulation performed in few wall-clock days on on the ENEA-CRESCO3 cluster and the Marconi Broadwell High Performing Computing (HPC) systems.

The paper is organized as follows. In the Section 2 we describe in detail the methodology used in the FSDAM SAMPL6 prediction. In Subsection 2.1, we briefly revise the theoretical basis of the FSDAM. The basic simulations details are provided in the subsection 2.2. FSDAM results for binding free energies based on the normality assumption of the work distributins are presented in the Section 3. In the subsection 3.1, we first report in detail the data concerning the single prediction that was submitted to the SAMPL6 challenge, critically analyzing the results with respect to the various source of errors. Conclusive remarks are presented in the last section.

2 Theoretical and methodological aspects of FSDAM

The theoretical background of FSDAM has been thoroughly described elsewhere[2, 4, 5]. Here we provide a brief theoretical summary, focusing mostly on the technical details used in implementing this methodology on a HPC systems.

2.1 FSDAM theory

Likewise its equilibrium counterpart[6] (FEP- or TI-based), this alchemical methodology accomplishes the determination of the binding free energy by computing the difference between the decoupling free energies of the ligand in the solvated complex and in bulk solvent. As outlined in the introduction, each of these two independent calculations is in turn done in two steps: i) a replica exchange simulation with torsional tempering (REST stage) of the fully coupled ligand state, aimed at harvesting canonical (equilibrium) configurations of the systems; ii) a transformative stage based on NE simulations (FNEA stage), whereby the ligand, starting from the configurations sampled in the corresponding REST stages, is rapidly annihilated in a swarm of concurrent and independent NE trajectories each yielding a NE work and eventually an annihilation work distribution.

Provided that the annihilation NE work distributions $P_b(W)$ and $P_u(W)$ from the FNEA stages are normal, according to the Crooks theorem[3] the corresponding annihilation free energies can be straightforwardly recovered using an unbiased estimated based on the mean and variance of the work distributions, i.e.

$$\Delta G_{b/u} = \langle W_{b/u} \rangle - \frac{1}{2}\beta\sigma^2_{b/u} \tag{1}$$

where the indices b, u refer to the bound or unbound states and where $\langle W_b \rangle$ and $\langle W_u \rangle$ are mean value of the ligand decoupling work in the bound state and in bulk solvent and σ_b^2, σ_u^2 are the corresponding variances.

It can be shown[4], that the FSDAM expression for the standard dissociation free energy is given by

$$\Delta G_0 \quad = \Delta G_b - \Delta G_u + RT \ln \left(\frac{V_{\text{site}}}{V_0} \right) \tag{2}$$

where V_0 is the standard state volume. In Eq. 1, the σ-related energies $\frac{1}{2}\beta\sigma_{b/u}^2$ have a straightforward physical interpretation: they represent the dissipation in the NE process of the annihilation of the ligand in the bound and unbound state. Hence, the wider are the normal distributions, the more dissipative the NE annihilation process is. The binding site volume, V_{site}, is computed in the REST stage from the oscillations of the guest in the binding pocket of the host.[4]

2.2 Simulation details and sample preparations

Atomic type assignment and partial atomic charges on the ligands were computed using the PrimaDORAC web interface.[7] PrimaDORAC computes the AM1-BCC charges on the AM1 optimized geometry of the ligand and assigns the atomic types according to the recently released GAFF2 general parameterization for organic molecules. Following the indications of the organizers, all the carboxylate groups on the host molecules OA and TEMOA and on the guest molecules were assumed to be deprotonated, so that the guest and the host molecules bear a net charge of -1e and -8e respectively. The solvent was treated explicitly using the TIP3P model. Long range electrostatic were treated using the Smooth Particle Mesh Ewald (SPME) method, with an α parameter of 0.37 Å^{-1}, a grid spacing in the direct lattice of about 1 Å and a fourth order B-spline interpolation for the gridded charge array. As no counterions were included, charge neutralization in charged bound and unbound systems is implicitly done in SPME using a uniform neutralizing background plasma. Bonds constraints were imposed to X-H bonds only, where X is an heavy atom. All other bonds were assumed to be flexible. The pressure was set to 1 atm using a Parrinello-Rhaman Lagrangian with isotropic stress tensor while temperature was held constant to 298 K using three Nosé Hoover-thermostats coupled to the translational degrees of freedom of the systems and to the rotational/internal motions of the solute and of the solvent. The equations of motion were integrated using a multiple time-step r-RESPA scheme with a potential subdivision specifically tuned for bio-molecular systems in the NPT ensemble.[5]. The long range cut-off for Lennard-Jones interactions was set to 13 Å in all cases.

Using the starting host and guest structures provided by the organizers, the preparation of the bound states for each host-guest pair was done by generating one hundred random host-guest structures within a COM-COM docking radius of 5 Å, followed by energy minimization in implicit solvent using the AGBNP model.[8] The so obtained least energy host-guest structures were then oriented along the inertia frame of the guest molecule and explicit water molecules at a density of 1 g/cm^3 were added in a cubic MD box whose side-length was computed so that the minimum distance between host or guest ligand atoms belonging to neighboring replicas was larger than 24 Å in any direction. After removal of overlapping water molecules, the bound state systems contained about 1250 solvent molecules for a volume of approximately 40000 Å^3 corresponding to a side-length of $\simeq$ 34 Å. For water and box volume equilibration, a preliminary 50 ps constant pressure, constant temperature simulation was run for each of the so prepared solvated complexes. The starting structures of the guest molecules in bulk solvent were prepared by inserting the structures provided by the organizers in a box of side-length 26 Å, containing TIP3P molecules at the density of 1g/cm^3.

The above procedure for generating the bound and unbound starting structures and the corresponding input file for subsequent REST and FNEA stages was completely automatized by an application script program. All simulations in this study are done using the program ORAC.[5]

2.3 REST stage

The REST simulations of the bound state was run on the HPC system by launching, in a single parallel job, four independent Hamiltonian replica exchange simulation with eight solute tempered replicas in the Generalized Ensemble (GE) for a total of 32 MPI instances. Each REST battery sampled 96 configurations taken at regular interval in a simulation time of 7.8 ns, hence accumulating 384 solvated bound state configurations in a total simulation time of 31.2 ns. For the free guest REST simulation, we used again 4 independent batteries of eight exchanging replicas, each lasting 1 ns, for a total simulation time of 4.0 ns, sampling 240 solvated guest molecules configurations. Each GE walker in the bound and unbound states used 6 threads on the OpenMP strong scaling layer, so that the hybrid OpenMP/MPI parallel REST jobs engaged a total 192 cores. Only the torsional potential of host and guest system was scaled throughout the GE up to 0.1 in both cases, corresponding to a solute "torsional" temperature of 3000 K. The scaling protocol in the eight replicas GE range [1-0.1] was set according to the scheme described in Ref. [9]. Exchanges were attempted between neighboring replicas at each long time step (i.e. each 15 fs), yielding a mean acceptance ratio throughout the GE of no less that 50%, in all cases. All REST computations were completed on the CRESCO3-ENEA HPC platform in few wall clock days.

2.4 FNEA stage

For each host-guest pair, in the FNEA stage a swarm of fast independent ligand annihilation trajectories were started from the phase-space points sampled in the REST stage for the unbound and bound guest molecules. The total number of independent NE trajectories were 384 for the decoupling of the ligand in the bound state and 240 for the decoupling of the ligand in bulk solvent. The annihilation protocol of the τ lasting NE processes was common to all host-guest systems and stipulates that the electrostatic interactions between the ligand and the environment are linearly brought to zero at $t = \tau/2$, while the Lennard-Jones interactions are switched off in the range $\tau/2 < t < \tau$ using a soft-core Beutler potential regularization as λ is approaching to 1 corresponding to the the decoupled state. The alchemical work along the alchemical path was computed as described in Ref. [2].

As done in REST, also in the FNEA stage parallel execution is performed using a straightforward hybrid OpenMP-MPI approach, with NE non communicating annihilation trajectories handled at the MPI level and a force decomposition scheme implemented with 9 threads on the shared memory OpenMP layer. As in past FSDAM studies on ligand-receptor or host-guest, the duration of each of NE independent decoupling trajectories adopted in this paper are of few hundreds of picoseconds (from 90 to 720 ps) for both the solvated bound state and the free ligand in bulk solvent. Each host-guest FNEA computation required 3240 and 2160 cores (bound and unbound state, respectively) on the Marconi-Broadwell HPC system[10] for few to few tens of wall clock minutes depending on the selected annihilation time. From the collection of annihilation works, the bound state and unbound state normalized work histograms probability were computed, namely $P_b(W)$ and $P_u(W)$, respectively. The normality of these distribution is assessed using the Anderson-Darling (AD) quadratic test.[11] The Anderson-Darling test A^2 is defined as $A^2 = \sum_{i=1}^{n} \frac{2i-1}{n}[\ln(\Phi(w_i) + \ln(1 - \Phi(w_{n+1-i})]$, where Φ is the Gaussian cumulative distribution function with sample mean and variance and w_i are the work values sorted in ascending order. The critical value of A^2 at the level $\alpha = 0.05$ is 0.752.[12] As shown in Table 1, the work distributions for the unbound state of all eight ligands amply passed the AD test for normality. The AD test was passed with a confidence level of 95% for 8 out of 16 bound state distributions and exceeded the critical value by more than 0.5 in only two cases, both referred to the highly flexible G7 guest molecule when bound to OA or TEMOA. In Table 1, we observe in general higher A^2 values for the TEMOA bound state, indicating that the extra methyl moieties decorating the crown of the host do have a significant impact on the host-guest free energy surface and, correspondingly, in the subsequent NE guest annihilation work.

3 Results and discussion

3.1 The FSDAM blind prediction on OA and TEMOA systems

All data for delivering our blind prediction of the octa-acids SAMPL6 challenge are collected in Table 1. The Table reports all the computed quantities that are needed in the FSDAM expression 2 for

OA bound states					
system	$\langle W \rangle$	$\frac{1}{2}\beta\sigma^2$	$RT\ln(V_{\rm site}/V_0)$	ΔG_{fs}	AD test
G0-OA	98.4 ± 0.17	2.1 ± 0.32	-2.73	1.62	0.514
G1-OA	96.6 ± 0.11	1.4 ± 0.18	-2.57	1.62	0.235
G2-OA	100.8 ± 0.14	1.9 ± 0.24	-2.72	1.62	0.350
G3-OA	98.0 ± 0.13	1.5 ± 0.22	-2.69	1.62	0.619
G4-OA	103.2 ± 0.21	2.9 ± 0.52	-2.46	1.62	0.784
G5-OA	95.9 ± 0.16	1.8 ± 0.33	-2.78	1.62	0.419
G6-OA	97.1 ± 0.16	2.2 ± 0.37	-2.70	1.62	0.891
G7-OA	97.2 ± 0.12	3.0 ± 0.44	-2.88	1.62	**2.019**

TEMOA bound states					
system	$\langle W \rangle$	$\frac{1}{2}\beta\sigma^2$	$RT\ln(V_{\rm site}/V_0)$	ΔG_{fs}	AD test
G0-TEMOA	96.7 ± 0.17	2.9 ± 0.41	-2.62	1.62	0.744
G1-TEMOA	99.1 ± 0.13	1.6 ± 0.28	-2.85	1.62	0.961
G2-TEMOA	93.6 ± 0.23	4.1 ± 0.54	-2.63	1.62	0.571
G3-TEMOA	98.9 ± 0.19	2.4 ± 0.38	-2.89	1.62	1.208
G4-TEMOA	105.0 ± 0.16	2.3 ± 0.36	-2.85	1.62	0.344
G5-TEMOA	95.5 ± 0.16	2.0 ± 0.32	-3.08	1.62	1.152
G6-TEMOA	99.5 ± 0.18	2.1 ± 0.29	-2.83	1.62	0.853
G7-TEMOA	94.7 ± 0.28	7.8 ± 0.83	-2.59	1.62	**6.084**

unbound states					
system	$\langle W \rangle$	$\frac{1}{2}\beta\sigma^2$	$RT\ln(V_{\rm site}/V_0)$	ΔG_{fs}	AD test
G0	88.1 0.11	0.6 ± 0.09	-	0.10	0.414
G1	87.3 0.08	0.3 ± 0.04	-	0.10	0.437
G2	85.6 0.09	0.4 ± 0.06	-	0.10	0.286
G3	89.3 0.07	0.3 ± 0.06	-	0.10	0.396
G4	88.7 0.11	0.6 ± 0.11	-	0.10	0.287
G5	87.2 0.08	0.4 ± 0.08	-	0.10	0.503
G6	88.6 0.10	0.6 ± 0.09	-	0.10	0.320
G7	86.9 0.09	0.4 ± 0.08	-	0.10	0.330

Table 1: Raw FSDAM data for the SAMPL6 octa-acids challenge. All energy entries are in kcal mol^{-1}. Standard dissociation free energy can be computed, assuming normality for all work distributions, from the reported energy contribution using Eqs. 1, 2. The finite size correction, ΔG_{fs} due to the net charge of the guest molecules, has been computed following Ref. [2] In the last column the A^2 value for the AD test for normality is reported.

the evaluation of dissociation free energy of a guest-hots pair. The errors in the evaluation of the moments $\langle W \rangle$ and σ^2 are standardly computed using bootstrap with resampling. The last column in the Table refers to the A^2 value computed with the AD test form normality on the corresponding work distributions. We see that AD failed patently in two cases only (highlighted in bold font in Table 1), both belonging to the bound state and both involving the G7 guest molecule, and that, in general,

bound state distributions involving OA satisfy better the normality DA test. On this basis, since Eq. 2 has been used for all computed work distributions, we may expect a better performance for the OA prediction set with respect to the TEMOA host-guest pairs. In Figure 1, we show the correlation diagram between experimental[1] and FSDAM computed standard dissociation free energies for the OA (left) and TEMOA (right) systems. We may say in general that our FSDAM blind prediction, with a RMSD of less than 2.5 kcal mol^{-1}, has an excellence ranking among all submitted genuine blind predictions (i.e without adjusted free energies based on retrospective data). FSDAM ranked in 4-th place for OA with a mean RMSD below 2 kcal mol^{-1} and in 5-th place for TEMOA with a mean RMSD below 3 kcal mol^{-1}.

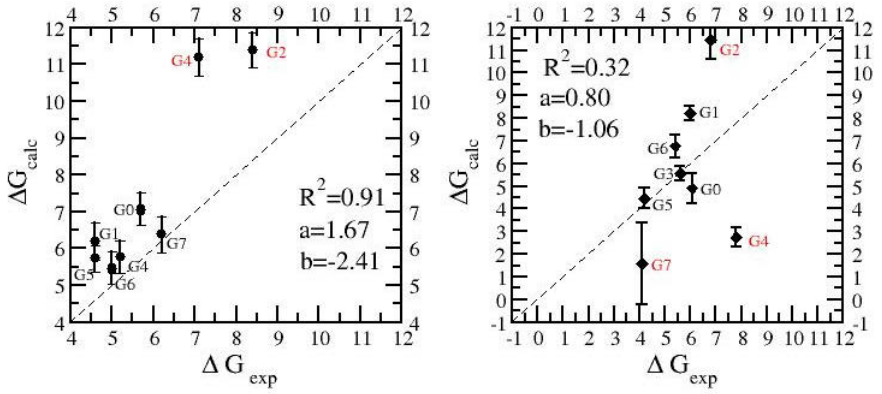

Figure 1: Correlation diagram between experimental and calculated dissociation free energies (kcal mol^{-1}) for the OA (left panel) and TEMOA (right panel) host-guest pairs. The normal assumption and Eq. 2 was used in the estimate and τ was set to 360 ps in the FNEA stage for both the bound and bulk state. The quantities a and b are the slope and intercept, respectively, of the regression line. The dashed line with $a = 1$ and $b = 0$ corresponds to perfect match.

4 Conclusion

In this paper, we have computed, by means of a non equilibrium alchemical technique (termed FSDAM), the absolute dissociation free energy for the octa-acids host-guest systems provided by the SAMPL6 initiative. FSDAM is based on the production of canonical configurations of the bound and unbound states via replica exchange with solute tempering (REST stage), followed by the generation of hundreds of fast non-equilibrium ligand annihilation trajectories (FNEA stage), eventually producing a collection of bound and unbound annihilation work values. The annihilation free energies of the ligand when bound to the receptor and in bulk solvent, are straightforwardly obtained from the collection of NE work values using an unbiased estimate, firmly based on the Crooks theorem for driven NE processes in the assumption that the NE work are normally distributed. The absolute binding free energies are recovered by the differences of the annihilation free energies of the ligand in bulk and in the bound state, corrected by a standard state and finite size terms.

In general our FSDAM SAMPL6 blind prediction, with a RMSD of less than 2.5 kcal mol^{-1}, has a satisfactory ranking among all submitted genuine blind predictions (i.e without adjusted free energies based on retrospective data). In a paper submitted to the forthcomong special issue of the Journal of Computed Aided Molecular Design dedicated to the SAMPL6 initiative, we show that results can be improved by using a generalization of the FSDAM approach based on the assumption that the

annihilation work samples are distributed according to a mixture of normal components rather than being represented by a single Gaussian distribution.

Possible future improvements of the FSDAM technique could involve the setting up of bidirectional approaches based on ligand annihilation and growth processes.

References

[1] Drug Design Data Resource (D3R), SAMPL6: Host-guest binding and physical property prediction. Information available at https://drugdesigndata.org/about/sampl (accessed 15 March 2018); Full free energy data available at https://drugdesigndata.org/upload/community-components/d3r/workshop2018/presentations/DavidMobley2018_SAMPL_overview.pdf (accessed 15 April 2018).

[2] Robert B. Sandberg, Martina Banchelli, Carlo Guardiani, Stefano Menichetti, Gabriella Caminati, and Piero Procacci. Efficient nonequilibrium method for binding free energy calculations in molecular dynamics simulations. *J. Chem. Theory Comput.*, 11(2):423–435, 2015.

[3] G. E. Crooks. Nonequilibrium measurements of free energy differences for microscopically reversible markovian systems. *J. Stat. Phys.*, 90:1481–1487, 1998.

[4] Piero Procacci. I. dissociation free energies of drug-receptor systems via non-equilibrium alchemical simulations: a theoretical framework. *Phys. Chem. Chem. Phys.*, 18:14991–15004, 2016.

[5] Piero Procacci. Hybrid MPI/OpenMP Implementation of the ORAC Molecular Dynamics Program for Generalized Ensemble and Fast Switching Alchemical Simulations. *J. Chem. Inf. Model.*, 56(6):1117–1121, 2016.

[6] Lingle Wang, Yujie Wu, Yuqing Deng, Byungchan Kim, Levi Pierce, Goran Krilov, Dmitry Lupyan, Shaughnessy Robinson, Markus K. Dahlgren, Jeremy Greenwood, Donna L. Romero, Craig Masse, Jennifer L. Knight, Thomas Steinbrecher, Thijs Beuming, Wolfgang Damm, Ed Harder, Woody Sherman, Mark Brewer, Ron Wester, Mark Murcko, Leah Frye, Ramy Farid, Teng Lin, David L. Mobley, William L. Jorgensen, Bruce J. Berne, Richard A. Friesner, and Robert Abel. Accurate and reliable prediction of relative ligand binding potency in prospective drug discovery by way of a modern free-energy calculation protocol and force field. *J. Am. Chem. Soc.*, 137(7):2695–2703, 2015.

[7] Piero Procacci. Primadorac: A free web interface for the assignment of partial charges, chemical topology, and bonded parameters in organic or drug molecules. *J. Chem. Inf. Model.*, 57(6):1240–1245, 2017.

[8] R. M. Levy E. Gallicchio. Agbnp: An analytic implicit solvent model suitable for molecular dynamics simulations and high-resolution modeling. *J. Comput. Chem.*, 25:479–499, 2004.

[9] S. Marsili, G. F. Signorini, R. Chelli, M. Marchi, and P. Procacci. Orac: A molecular dynamics simulation program to explore free energy surfaces in biomolecular systems at the atomistic level. *J. Comput. Chem.*, 31:1106–1116, 2010.

[10] Consorzio Interuniversitario del Nord est Italiano Per il Calcolo Automatico (Interuniversity Consortium High Performance Systems) http://www.cineca.it (accessed 22 January 2018).

[11] T. W. Anderson and D. A. Darling. A test of goodness of fit. *J. Am. Stat. Ass.*, 49:765–769, 1954.

[12] M.A. Stephens. Test of fit for the logistic distribution based on the empirical distribution function. *Biometrika*, 66:591–595, 1979.

VALIDATION CAMPAIGN OF NEUTRONIC CODES FOR LFR SYSTEMS ON CRESCO HPC

Massimo Sarotto[1*], Giacomo Grasso[2]

[1]*ENEA FSN-SICNUC-PSSN, C.R. Saluggia, Strada per Crescentino 41 – 13040 Saluggia (VC)*[1]

[2]*ENEA FSN-SICNUC-PSSN, C.R. "E. Clementel", Via Martiri di Monte Sole 4 – 40129 Bologna*

ABSTRACT. When addressing the core design (and in perspective the licensing) of a new reactor concept as the Lead Fast Reactor (LFR), a thorough validation of neutronic calculation codes (and data libraries) is deemed necessary to prove, to the largest extent, the validity of the results and the appropriateness of the design methodologies and tools. This work reports some examples of the results obtained in the validation activities carried out for the ERANOS deterministic code - ported to CRESCO HPC - in the framework of the programmatic agreement (AdP PAR 2015-17) between ENEA and MiSE. The LFR concept chosen as reference is the ALFRED European Demonstrator and the experimental measurements needed for the validation were performed during the EURATOM FP7 FREYA project in the VENUS-F zero-power reactor.

1 Introduction

The Lead-cooled Fast Reactor (LFR) is one of the six reactor concepts contemplated within the framework of the Generation IV International Forum (GIF) [1] and one of the three advanced reactors chosen by the European Sustainable Nuclear Industrial Initiative (ESNII) [2]. Among the leading criteria (*e.g.*, enhanced safety, reliability, economic competitiveness and proliferation resistance), the sustainability can be well addressed because of the fast spectrum allowing the closure of the fuel cycle (by reducing of about 2 orders of magnitude the U consumption, the actinide mass going to geological disposals and the fuel waste long-term radio-toxicity).
Within this promising perspective, the EURATOM 7th Framework Program (FP7) launched:

- the Lead-cooled European Advanced DEmonstration Reactor (LEADER) project, whose main goal was a preliminary design of the Advanced LFR European Demonstrator (ALFRED) [3];
- the Fast Reactor Experiments for hYbrid Applications (FREYA) project, in which some experiments representative of the ALFRED concept were foreseen in the VENUS-F zero-power reactor, located at the SCK•CEN research centre in Mol, Belgium [4].

In LEADER, ENEA had the responsibility to coordinate the core design studies, which continued successively - within the frameworks of the Programmatic Agreement between ENEA and MiSE (AdP) and of the Fostering ALFRED CONstruction international consortium (FALCON) [5] - by providing a refined model of the core [6]. In FREYA, ENEA had the responsibility in the design of a VENUS-F core dedicated to ALFRED, by exploiting the possibility to perform integral tests and local measurements of neutronic parameters representative of the LFR. These experiments represented a valuable support for the validation of neutron transport codes - both deterministic and Monte Carlo - adopted for the ALFRED core design and, in perspective, for licencing purposes.
This report draws on the campaign of validation activities carried out during the AdP PAR 2015-17 for the ERANOS deterministic code. It describes briefly:

- the main characteristics of the ERANOS system (ported to the CRESCO HPC) in §2;
- the main features of the VENUS-F core layout representative of ALFRED in §3;
- some examples of the Calculation-to-Experiment ratio (C/E) values obtained, together with some examples of the successive in-depth sensitivity and uncertainty analyses.

[1] Corresponding author. E-mail: massimo.sarotto@enea.it.

2 The ERANOS system code (ported on CRESCO)

The European Reactor ANalysis Optimised calculation System (ERANOS) is a modular system and consists of data libraries, deterministic codes and calculation procedures developed within the European collaboration on fast reactors over the past 20 years [7]. The different modules perform several functions to analyse reactivity, fluxes, burn-up, reaction rates, etc. of a nuclear system that can be described by 1D, 2D and 3D geometry models. The macroscopic cross-sections representing the different zones of the VENUS-F core/reactor (§3) were calculated by means of the European Cell Code (ECCO) [8]. Starting from the JEFF-3.1 [9] and ENDF/B-VI.8 [10] nuclear data libraries available in the ECCO/ERANOS environment, the cross-sections were:

- produced by means of a 1968 energy-group-structure, and successively condensed by ECCO in structures at 15, 33 and 49 groups (depending on the application);
- used for full-core calculations performed with the TGV module [11], where the variational nodal method is adopted to solve the transport equation in a XYZ geometry model of the reactor.

Despite the fact that ERANOS is a serial code, it is installed on the HPC clusters of the CRESCO infrastructure to take profit of several features, such as: the fast processors and a wide amount of RAM (*i.e.*, short execution times), the high number of available nodes (*i.e.*, different instances of the code can run in parallel *e.g.*, for parametric investigations) and the advantages deriving from a shared resource (*i.e.*, an official-centralized copy of ERANOS that is verified and constantly updated, along with the associated neutron data libraries).

3 The VENUS-F experiments devoted to LFR

In order to provide measurements representative of the LFR neutronic parameters, the VENUS-F reactor was refurbished by installing core components, radial and axial reflectors in solid lead. The left part of Fig. 1 shows the core layout made of 12×12 square assembly positions: the Fuel Assemblies (FAs, red) are radially surrounded by Lead Assemblies (LAs, blue) and a square casing in Stainless Steel (SS, yellow). The right part of Fig. 1 shows that the fissile zone is axially embedded by lower and top plates in SS (magenta) and surrounded by lead reflectors with different levels of Pb purity (yellow, green and blue). The bottom left part of Fig. 1 shows that the FA is a 5x5 square matrix inserted in a SS-Pb box (magenta-blue) made of 13 U metallic rods enriched at 30 wt.% in U^{235} (orange), 4 Aluminium Oxide (Al_2O_3) rods (green) and 8 lead blocks simulating the LFR coolant (purple).

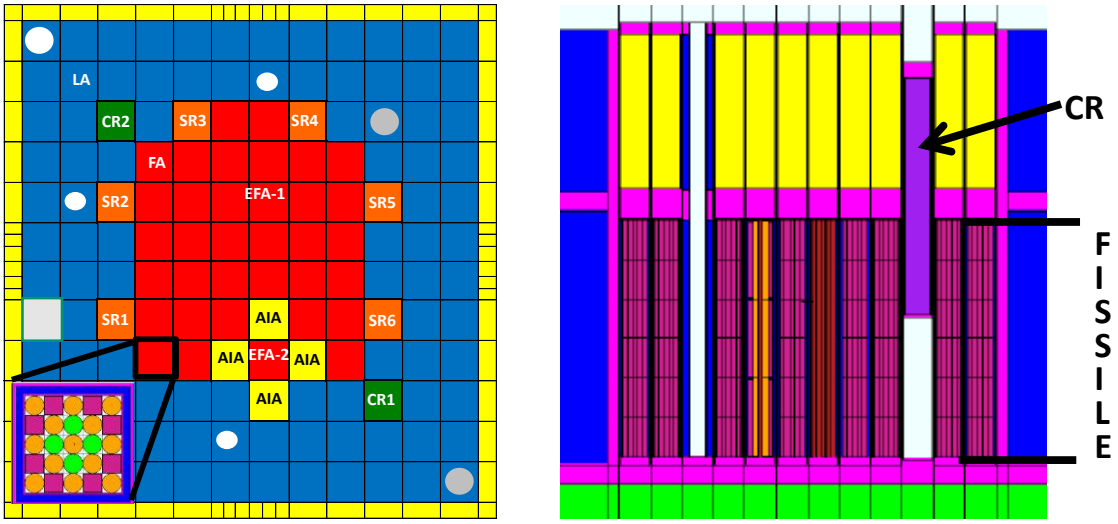

Fig.1: Horizontal (left) and vertical (right) views of the VENUS-F layout representative of ALFRED.

To reproduce the neutronic behaviour of the oxide fuel designed for ALFRED, some additional moderating assemblies – made only by Al_2O_3 rodlets (# 25) and called Alfred Inert Assemblies (AIAs) – were inserted in the VENUS-F layout and disposed as a chess around an Experimental FA (named EFA-2 in Fig. 1) where the ALFRED spectrum was reproduced [12]. The EFA is a standard FA with an U rod replaced by an empty SS guide tube for the measurement equipment insertion. For the reactor control and scram, the core is equipped with six fuel follower Safety Rods (SRs) and two Control Rods (CRs), whose reactivity worth was accurately measured and simulated (§4).

4 Some C/E results and further in-depth analyses

In the FREYA experiments the VENUS-F facility was adopted for the measurement of:

- integral parameters, as critical mass (*i.e., k* multiplication factor), worth of absorbing elements (CRs and SRs), effective delayed neutron fraction and neutron generation time;
- local parameters, as radial and axial flux traverses, spectrum indexes, void worth, etc..

For almost all the measured quantities, the values obtained with the ERANOS code (§2) resulted to be very accurate [12]. As examples of C/E results Table 1 reports:

- on the left columns, the reactivity worth of the CR close to the AIAs (named as CR1 in Fig. 1) at different insertion heights (Z);
- on the right columns, the values of the spectrum indexes of main interest in fast spectrum measured in the EFA-2 position. The measured indexes are the ratio between the fission rate of the U^{238}, Pu^{239} and Np^{237} nuclides (F28, F49 and F37, respectively) and the fission rate of U^{235} (F25).

Z	C/E for CR1 worth			Spectral	C/E for spectral indexes	
[mm]	JEFF-3.1	ENDF/B-VI.8		Index*	JEFF-3.1	ENDF/B-VI.8
375	0.985	0.997		F28 / F25	0.945	0.966
425	0.935	0.948		F49 / F25	1.011	1.010
475	0.921	0.965		F37 / F25	0.964	0.951
525	0.921	0.942				
575	0.987	0.975		* Fission rates ratio		

Table 1: ERANOS C/E values for the CR1 worth (left) and spectrum indexes in EFA-2 (right).

Besides the reproduction of the measured quantities, the ERANOS code was adopted for in-depth sensitivity and uncertainty analyses on the *k* multiplication factor value. The sensitivity coefficients (S_k) give the rate of change of the parameter of interest (*k*) as a function of the variation of any other one the former depends upon, notably as the cross-sections (σ):

$$S_k = \frac{\partial k}{\partial \sigma}\frac{\sigma}{k} \tag{1}$$

The coefficients (1) permitted to evaluate the uncertainty on the *k* value (U_k) starting from the uncertainties on nuclear data per each isotope and energy group:

$$U_k^2 = S_k B S_k^t \tag{2}$$

through the BOLNA covariance matrix (*B*) [13]. As examples of results obtained in VENUS-F:

- the top part of Fig. 2 shows the ERANOS/JEFF-3.1 sensitivity coefficients per each cross-section and per each energy group (summed over the isotopes considered). The highest values occur for the average number of neutrons emitted per fission (NU), the fission and capture cross-sections in the energy range between 0.1 and 2.3 MeV;
- the bottom-left part of Fig. 2 shows the ERANOS/JEFF-3.1 sensitivity coefficients per each isotope and per each cross-section (summed over the 33 energy groups). As expected, the highest values occur for the NU, capture and fission cross-sections of the U^{235} and U^{238} nuclides;
- the bottom-right part of Fig. 1 shows the ERANOS/ENDF/B-VI.8 uncertainty on the *k* value

per each isotope and per each cross-section. The highest values occur for the U^{235} capture cross-section. As a whole, the total uncertainty resulted to be of about 2%.

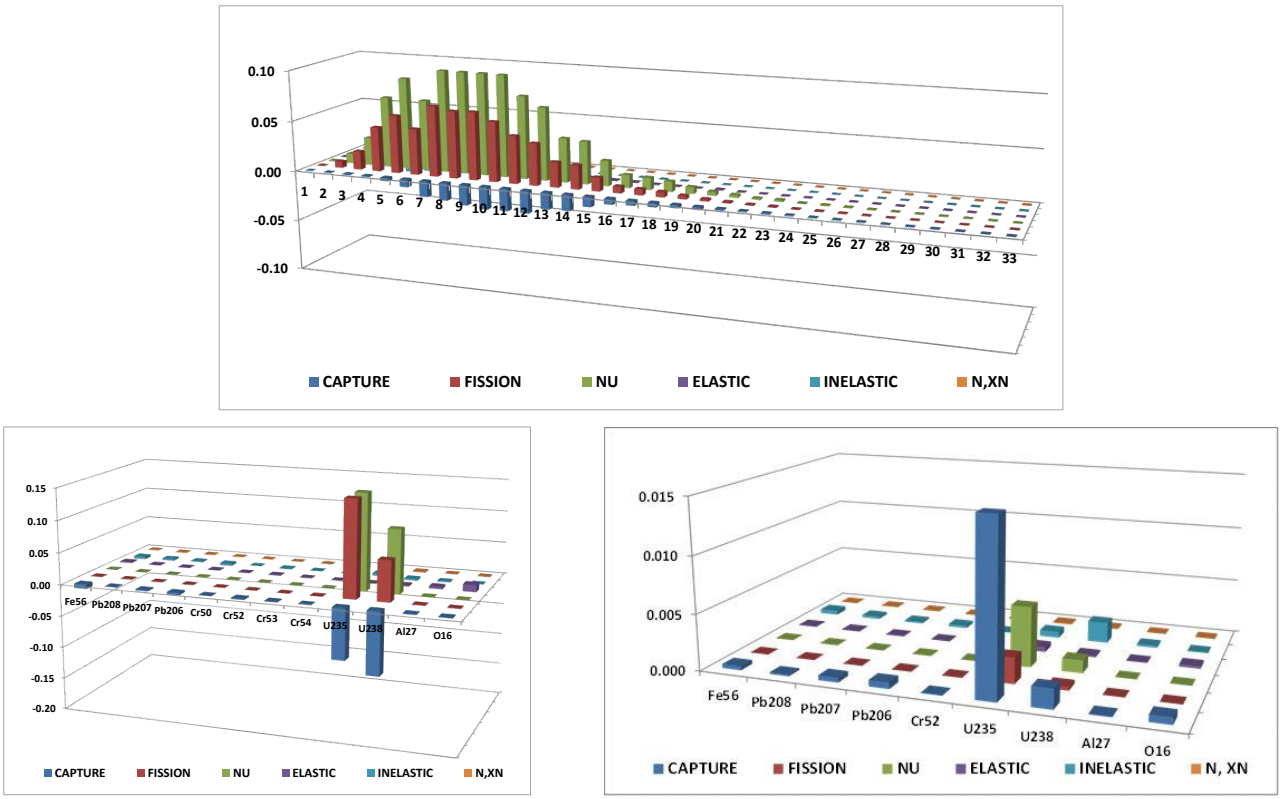

Fig.2: Examples of ERANOS/JEFF-3.1 sensitivity coefficients (top and bottom-left frame) and ERANOS/ENDF/B-VI.8 uncertainty on k values (bottom right frame).

References

[1] OECD/NEA, 2014. "Technology Roadmap Update for Gen. IV Nuclear Energy Systems".
[2] ESNII, 2013." Strategic Research and Innovation Agenda of the European Sustainable Nuclear Industrial Initiative", http://www.snetp.eu/.
[3] GRASSO, G., *et al.*, 2014. "The core design of ALFRED, a demonstrator for the European lead-cooled reactors", Nucl. Eng. and Des., Vol. 278, 287-301.
[4] KOCHETKOV, A., *et al.*, 2013. "Current progress and future plans of the FREYA Project". Proc. Int. Conf. TCADS-2, Nantes, France, May 21-23.
[5] https://www.euronuclear.org/e-news/e-news-43/ansaldo.htm.
[6] LODI, F., *et al.*, 2015. Characterisation of the new ALFRED core configuration. Ricerca di Sistema Elettrico, Technical Report ADPFISS-LP2-085.
[7] RIMPAULT, G., et al., 2002. "The ERANOS code and data system for Fast Reactor neutronic analyses", Proc. Int. Conf. PHYSOR 2002, Seoul, Korea, *October 7-10*.
[8] RIMPAULT, G., 1997. "Physics documentation of Eranos: the Ecco cell code", CEA report DERSPRC-LEPh-97-001.
[9] KONING, A. et al., 2006. "The JEFF-3.1 Nuclear Data Library", OECD/NEA N_6190, JEFF report 21.
[10] https://www-nds.iaea.org/exfor/endf.htm.
[11] RUGGERI, J.M., et al., 1993. "TGV: a coarse mesh 3 dimensional diffusion-transport module for the CCRR/ERANOS code system", CEA report DRNR-SPCILEPh-93-209.
[12] SAROTTO, M., et al., 2017. "Results of the validation campaign of neutronic codes and recommendations for the correct application to LFR systems", Workshop AdP MiSE – ADP PAR2016 B.3.1 LP2, LFR-GEN IV Stato attuale della tecnologia e prospettive di sviluppo, Bologna, September 26-27.
[13] SALVATORES, M., *et al.*, 2008. "Uncertainty and target accuracy assessment for innovative systems using recent covariance data evaluations", OECD/NEA report WPEC-26 ISBN 978-92-64-99053-1 N. 6410.

Emergent explosive synchronization in adaptive complex networks

V. Avalos-Gaytán[1], J. A. Almendral[2,3], I. Leyva[2,3]*, I. Sendiña-Nadal[2,3] and S. Boccaletti[4]

[1] *Research Center in Applied Mathematics, Univ. Autónoma de Coahuila, Saltillo, Coahuila, Mexico*

[2] *Complex Systems Group & GISC, Universidad Rey Juan Carlos, 28933 Móstoles, Madrid, Spain*

[3] *Center for Biomedical Technology, U. Politécnica de Madrid, 28223 Pozuelo de Alarcón, Madrid, Spain*

[4] *CNR- Institute of Complex Systems, Via Madonna del Piano, 10, 50019 Sesto Fiorentino, Florence, Italy*

Abstract. Adaptation plays a fundamental role in shaping the structure of a complex network and improving its functional fitting. Even when increasing the level of synchronization in a biological system is considered as the main driving force for adaptation, there is evidence of negative effects induced by excessive synchronization. This indicates that coherence alone can not be enough to explain all the structural features observed in many real-world networks. In this work, we propose an adaptive network model where the dynamical evolution of the node states towards synchronization is coupled with an evolution of the link weights based on an anti-Hebbian adaptive rule, which accounts. Our results can enlighten the shaping mechanisms at the heart of the structural and dynamical organization of some relevant biological systems, namely brain networks, for which the emergence of explosive synchronization has been observed.

1 Introduction

Adaptivity is a key feature in the construction and function of many real complex systems. In the brain, for instance plasticity is at the heart of memory and learning processes, and governs the huge functional versatility of this system. In many approaches adaptation has been considered to be the improvement of the level of synchronization [15, 7]. Most of the works in this area have implemented different versions of the Hebbian adaptation rule to enhance the strengths of the links of a network [2, 9, 4]. However, improving the coherence cannot be the only mechanism at work in brain networks. In fact, oversynchronization can lead to pathological states as epilepsy [6]. For this reason, inhibition and anti-Hebbian coupling have been investigated in neural systems, and they have been shown to play an important role in the control of synchronization [10, 8].

In this work, we show that the competition between the attractive coupling and the anti-Hebbian link dynamics generates networks that are able to sustain explosive synchronization (ES). Explosive synchronization, i.e. the sudden, discontinuous and irreversible transition from an incoherent state to a fully synchronized one, is a phenomenon that has attracted special attention in last few years [12, 13, 14, 5]. Our results indicate that the frustration induced by an anti-Hebbian adaptation rule

*Corresponding author. E-mail: inmaculada.leyva@urjc.es.

that promotes links between nodes in anti-phase dynamics, can be the main responsible of the phenomena observed empirically in neuroscience. This results have been recently published in Ref. [3].

2 Model and methods

We consider a system of $N = 300$ all-to-all coupled Kuramoto oscillators [11]:

$$\begin{aligned} \dot{\theta}_l &= \omega_l + \frac{\sigma_c}{N} \sum_{m=1}^{N} \alpha_{lm} \sin(\theta_m - \theta_l) \\ \dot{\alpha}_{lm} &= (p_c - p_{lm})\ \alpha_{lm}(1 - \alpha_{lm}) \end{aligned} \tag{1}$$

where ω_l is the natural frequency associated to the oscillator, that is assigned randomly from a uniform distribution in the interval [0.8, 1.2], $\alpha_{lm} \in [0, 1]$ is the weight of the connection between the units l and m, and σ_c is the *coupling strength*. Here $p_{lm} = p_{lm}(t) = \frac{1}{2}\left|e^{i\theta_l(t)} + e^{i\theta_m(t)}\right|$ is the instantaneous phase correlation and p_c has the following meaning: once the value of p_c is fixed, the links connecting pairs of oscillators with a higher (lower) level of instantaneous synchronization will be weakened (reinforced). As we will show, such a mechanism of frustration of the local synchronization process, which affects a larger number of pairs the higher is the value of p_c, is an essential ingredient for the emergence of explosive synchronization. Notice that $\alpha_{lm}(t)$ will tend to converge to either 0 or 1. As a consequence, for any choice of σ_c and p_c, and a random sampling of the initial conditions, the coevolution of oscillator states and link weights will result in a progressive pruning of the links of the initially complete graph, until the system approaches an asymptotic state, defined by $\dot{\alpha}_{lm} = 0$, $\forall\, l, m$, corresponding to a specific dynamically-induced network topology.

2.1 Numerical methods and use of computational resources

For the numerical integration of the above model and the analysis of the results we used homemade C codes implementing fix-step fourth-order Runge-Kutta integration algorithms. The standard GCC compiler was used. Extensive serial simulations have been performed for large parameters ranges, with statistical validation of the results. The calculations were performed in Cresco 3 and Cresco 4, using the *h144* queues for full evolution simulations. Homemade MatLab scripts were used for visualizing the results.

3 Results

For a large range of parameters σ_c and p_c we measure the final degree of global synchronization by means of the Kuramoto order parameter $R := \left\langle \frac{1}{N} \left| \sum_{l=1}^{N} e^{i\theta_l(t)} \right| \right\rangle_t$. In Fig. 1(a) we characterize the asymptotic dynamics of the network by reporting the average value of R as a function of p_c for different values of σ_c. As expected, for small values of the coupling σ_c the network is not able to synchronize for any value of p_c. However, above the critical coupling for the Kuramoto model $\sigma_c^* = \frac{2}{\pi g(0)} = 0.8/\pi \simeq 0.255$ [1], the global synchronization shows an abrupt transition at $p_c \simeq 0.625$. For slightly smaller values of σ_c, the global strength, defined as $S = \sum_{l,m>l}^{N} \alpha_{ml}$, suffers also a sharp transition, as shown in Fig. 1(b), pointing out to the fact that the networks go through a phase of strong local synchronization before global coherence is achieved. We characterize the microscopic properties of the emerging networks associated to the original weighted graphs $A = \{a_{lm}\}$, after a binarization process. In Fig. 2 we show for three representative values of p_c, for a fixed value $\sigma_c = 0.6$. In the first row of Fig. 2, k_l is pictured as a function of ω_l. Before the transition ($p_c = 0.62$), the two features are uncorrelated. However,

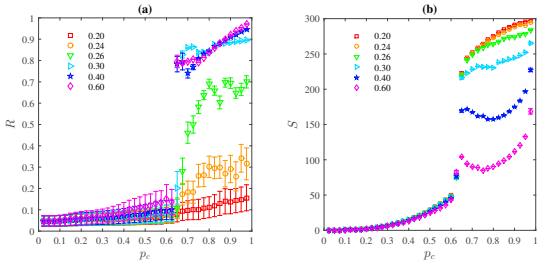

Figure 1: Asymptotic values of (a) global synchronisation, R, and (b) total strength, S, in coevolving weighted networks governed as a function of p_c

after the transition, a strong correlation between k_l and ω_l appears, meaning that the nodes with ω_l at the two edges of the natural frequency distribution are much more connected. This is a surprising and noticeable feature, as V-shape k-ω relationships are well known to be characteristic of networks capable of sustainaing explosive synchronization [12, 13, 5]. The finding is confirmed by the fact that the dynamics in Eq. (1) forces the network to acquire *frequency dissasortativity*, i.e., nodes are much more likely to link to those with distant frequencies, as can be seen in the central row of Fig. 2.

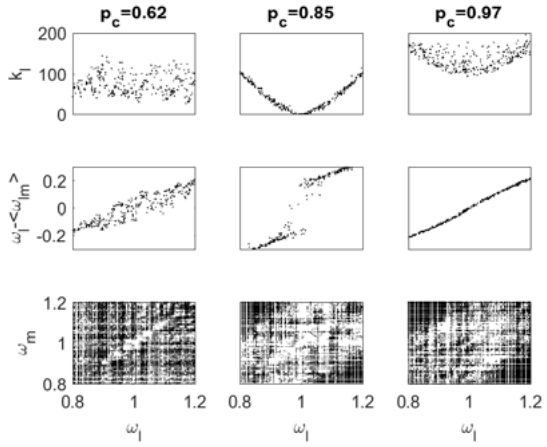

Figure 2: Scatter plot of the node degree k_i (upper row panels) and of the node neighborhood detuning $\omega_i - \langle\omega_{im}\rangle$ (central row panels) as a function of the natural frequency ω_i of a node for $\sigma_c = 0.6$. The connectivity of the resulting networks are shown as matrices where nodes are placed according to their natural frequencies ω (bottom row panels).

These results show that the link evolution has actually reinforced links connecting nodes whose frequencies are as far as possible, progressively pruning the remaining connections. This process can be followed through the panels in the bottom row of Fig. 2, where the full connectivity matrix is plotted. Before the transition to synchrony (first column, p_c=0.62), the pruning affects only nodes with frequencies close to the center of the distribution. As p_c grows, the link suppression affects a larger number of links connecting nodes with higher detuning, and therefore $\langle k\rangle$ and eventually $N_g(\sigma_c, p_c)$ decrease.

The observed frequency dissasortativity hints that such networks could be able to sustain first-order synchronization. We check this prediction by using the resulting networks as the fixed connectivity support of a system of interacting Kuramoto oscillators $\dot{\theta}_l = \omega_l + \frac{\sigma}{N(\sigma_c,p_c)} \sum_{m=1}^{N(\sigma_c,p_c)} a_{lm} \sin(\theta_m - \theta_l)$ where $l = 1, \ldots, N(\sigma_c, p_c)$, being $N(\sigma_c, p_c) \leq N$ the size of the binarized network and $A' = \{a_{lm}\}$. The coupling strength σ is now set to be the only control parameter, regardless of the original value of σ_c

used to create A'. R is monitored as a function of σ in forward and backward simulations [5].

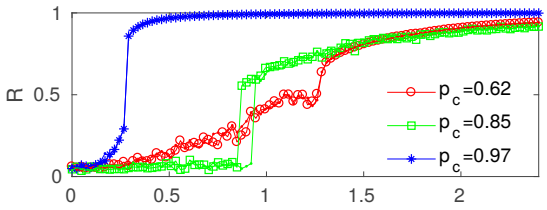

Figure 3: Global synchronization R for forward and backward synchronization schemes for the binary networks considered in Fig. 2.

In Fig. 3(a) we show the synchronization schemes for the same examples whose structures have been studied in Fig. 2. For networks obtained with p_c below the transition, the network synchronizes in a second order transition (red circles). For p_c values beyond the critical value, a first order transition happens, as suggested by the strong frequency-degree correlations. For intermediate values (green squares), this transition to synchrony presents an hysteresis loop as a consequence of the bi-stability generated in the detuning distribution. For even larger p_c, (blue diamonds), the synchronization occurs abruptly but reversibly.

4 Conclusions

In conclusion, in this work we suggested a novel adaptive network model based on the competition between attractive coupling at the node level and anti-Hebbian repulsive dynamics at the link level. We showed how an initial set of fully interacting phase oscillators can naturally evolve towards a complex networked system, under the action of an adaptation mechanism which promotes interactions between elements that are not synchronized. Indeed, in many biological systems synchronization needs to be both promoted and controlled in order to avoid excessive redundancy. We characterized how the dynamical organization of the emerging systems leads spontaneously to degree-frequency correlation at the node level, a structure typically associated to networks able to sustain explosive synchronization. Our results can widen our understanding of the shaping mechanisms behind the structural organization of some real-world systems such as brain networks where the emergence of explosive synchronization has been observed. The stability analysis of a simplified model reveals the microscopic mechanisms that are at the heart of the observed emerging structural and dynamical features, and their non-trivial correlations, observed in the networks described by our adaptive coevolving model.

References

[1] Juan A Acebrón, Luis L Bonilla, Conrad J Pérez Vicente, Félix Ritort, and Renato Spigler. The kuramoto model: A simple paradigm for synchronization phenomena. *Reviews of modern physics*, 77(1):137, 2005.

[2] Salvatore Assenza, Ricardo Gutiérrez, Jesús Gómez-Gardenes, Vito Latora, and Stefano Boccaletti. Emergence of structural patterns out of synchronization in networks with competitive interactions. *Scientific reports*, 1:99, 2011.

[3] Vanesa Avalos-Gaytán, Juan A Almendral, I Leyva, F Battiston, V Nicosia, V Latora, and S Boccaletti. Emergent explosive synchronization in adaptive complex networks. *Physical Review E*, 97(4):042301, 2018.

[4] Vanesa Avalos-Gaytán, Juan A Almendral, David Papo, Satu Elisa Schaeffer, and Stefano Boccaletti. Assortative and modular networks are shaped by adaptive synchronization processes. *Physical Review E*, 86(1):015101, 2012.

[5] S Boccaletti, JA Almendral, S Guan, I Leyva, Z Liu, I Sendiña-Nadal, Z Wang, and Y Zou. Explosive transitions in complex networks structure and dynamics: Percolation and synchronization. *Physics Reports*, 660:1–94, 2016.

[6] Mario Chavez, Miguel Valencia, Vincent Navarro, Vito Latora, and Jacques Martinerie. Functional modularity of background activities in normal and epileptic brain networks. *Physical review letters*, 104(11):118701, 2010.

[7] Pietro De Lellis, Mario Di Bernardo, and Franco Garofalo. Synchronization of complex networks through local adaptive coupling. *Chaos*, 18(3), 2008.

[8] Daniel E Feldman. The spike-timing dependence of plasticity. *Neuron*, 75(4):556–571, 2012.

[9] Ricardo Gutiérrez, A Amann, Salvatore Assenza, Jesús Gómez-Gardenes, V Latora, and Stefano Boccaletti. Emerging meso-and macroscales from synchronization of adaptive networks. *Phys. Rev. Lett.*, 107(23):234103, 2011.

[10] Erik Harvey-Girard, John Lewis, and Leonard Maler. Burst-induced anti-hebbian depression acts through short-term synaptic dynamics to cancel redundant sensory signals. *Journal of Neuroscience*, 30(17):6152–6169, 2010.

[11] Y Kuramoto. Chemical oscillations, waves and turbulence. 1984.

[12] I Leyva, I Sendina-Nadal, J Almendral, A Navas, M Zanin, D Papo, JM Buldú, and S Boccaletti. Explosive transitions to synchronization in networked phase oscillators. *Scientific Reports*, 3:1281, 2013.

[13] I Leyva, I Sendina-Nadal, JA Almendral, A Navas, S Olmi, and S Boccaletti. Explosive synchronization in weighted complex networks. *Physical Review E*, 88(4):042808, 2013.

[14] A Navas, JA Villacorta-Atienza, I Leyva, JA Almendral, I Sendiña-Nadal, and S Boccaletti. Effective centrality and explosive synchronization in complex networks. *Physical Review E*, 92(6):062820, 2015.

[15] Changsong Zhou and Jürgen Kurths. Dynamical weights and enhanced synchronization in adaptive complex networks. *Physical Review Letters*, 96(16):2–5, 2006.

THE REGIONAL EARTH SYSTEM MODEL REGESM: DESIGN AND EVALUATION OVER THE MED-CORDEX DOMAIN DURING THE ERA-INTERIM PERIOD 1980 – 2012

Maria Vittoria Struglia[1*], Sandro Calmanti[1], Adriana Carillo[1], Alessandro Dell'Aquila[1], Emanuele Lombardi[1], Giovanna Pisacane[1], GianmariaSannino[1], Ufuk Turunçoğlu[2]

[1]*ENEA, SSPT-MET-CLIM, Via Anguillarese 301, 00123 Rome, Italy*[1]

[2]*Informatics Institute, Istanbul Technical University, Istanbul, Turkey*

ABSTRACT. We present the results of a climate simulation performed with the Regional Earth System Model (RegESM) over the MED-CORDEX domain. The simulation covers the period 1980-2012 and its forcing is based on the regional downscaling of the ERA-interim re-analyses.

1 Introduction

In the framework of global climate studies, there is an increasingly growing concern about the vulnerability of the Mediterranean region, where high population density and intense exploitation activities pose severe questions on the sustainability of terrestrial water management, both for the present and the future. On the other hand, also global feedback processes are expected in the Atlantic Ocean through the altered Mediterranean thermohaline circulation in conditions of global greenhouse warming. Due to the socioeconomic relevance of the expected climate impacts in the region, including water shortages, floods, and extreme winds, both experimental and numerical efforts have been devoted in the last years to fill the gaps of our knowledge of the current and future Mediterranean climate and its variability, in order to provide robust climate change information for use in vulnerability–impact–adaptation assessment studies.
The Mediterranean Coordinated Regional Downscaling Experiment (Med-CORDEX) [1] initiative aims at coordinating the Mediterranean climate modeling community toward the development of fully coupled regional climate simulations, improving all relevant components of the system from atmosphere and ocean dynamics to land surface, hydrology, and biogeochemical processes. In this framework, we present the results of the climate simulations performed at the Climate Modeling laboratory of ENEA with the Regional Earth System Model (RegESM) [2]. The performance of the model has been tested by performing an evaluation run, i.e. a realistic simulation driven by the regional downscaling of the ERA-interim re-analyses.

2 Setup and main results

In its current configuration, RegESM active components are the 20 km horizontal resolution atmosphere (RegCM 4.5), 1/12° ocean (MITgcm) and river routing (HD), all of which are merged

[1] Corresponding author. E-mail: mariavittoria.struglia@enea.it.

and managed by the driver, the Earth System Modeling Framework (ESMF) which is responsible for the interaction between the components (i.e. boundary data exchange, regridding) and their synchronization. The parameterizations of the atmospheric component of the RegESM model had been calibrated in a previous stand-alone (SA) experiment [3] using the ERA-interim reanalysis dataset as initial and lateral boundary condition for the atmosphere. The calibrated RegCM has been included in the current version of the fully coupled climate model and a companion coupled simulation (CPL) was run, covering the whole period 1980-2013. Results are compared to observations on the available common periods, while the two simulations, CPL and SA, were directly compared in order to highlight the effects of the direct exchange of energy and fresh water between the air and the sea.
The model was run on CRESCO4 in a sequential mode on 256 cpus, which turned out to be the best choice in terms of scalability of the models, over the given domain at the given resolution. The average CPU time for one year of simulation is around 1 day. However, given the relatively low requirements in terms of CPUs, multiple simulation can be performed if necessary.
Three-dimensional 6-hourly output data are stored during the model simulation. Therefore, the amount of storage required for the whole hindcast simulation, covering the years from 1980 to 2013, is of the order of 10 Tb. NetCDF libraries are used by RegESM to manage I/O format.

2.1 Atmospheric circulation

The present climate atmospheric circulation has been evaluated comparing the mean near surface wind speed over the sea with the satellite observations from the QuickSCAT dataset. Figure 1 shows the difference between the CPL simulation and satellite observations for the summer season (JJA) for the years 2000-2010. Wind speed over the sea is in good agreement with satellite observations and the difference between the two datasets is in general below ± 0.5 m/s, with the exception of the Aegean Sea region where such difference increases up to ± 2 m/s. Such discrepancy is due to the moderate horizontal resolution of the atmospheric model (20 km) that is not sufficient to describe the complex orography in the Cretan Sea and subsequently the peculiar wind circulation of the region.

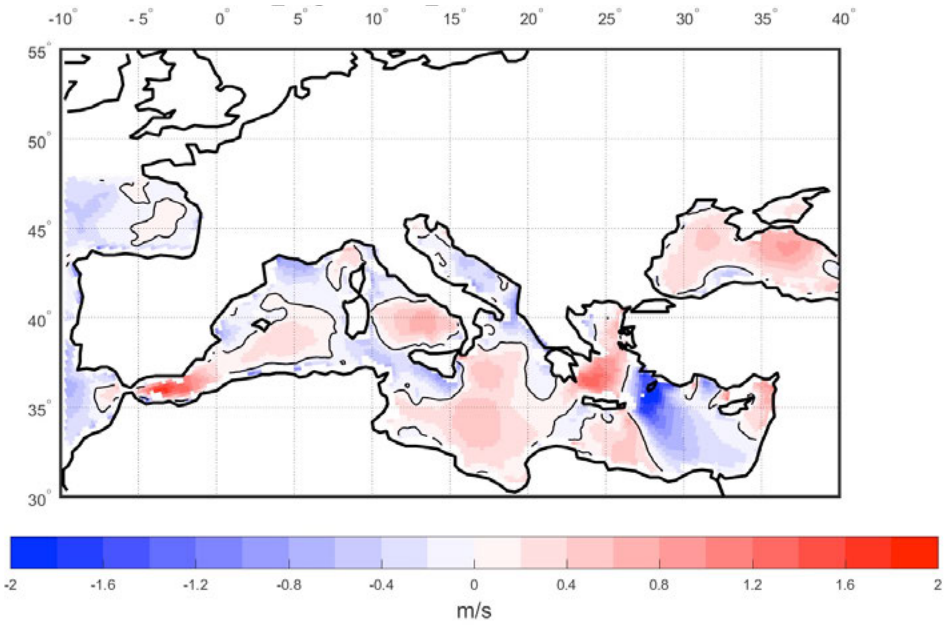

Fig.1: Near surface wind speed, JJA mean for the years 2000-2010: CPL-QuickSCAT .

The direct coupling of atmosphere and ocean affects the air-sea interactions, resulting in a general reduction of precipitation over the sea in the CPL simulation with respect to its companion SA simulation. Figure 2 shows the difference (CPL – SA) of the time series of precipitation averaged over the Mediterranean Sea.

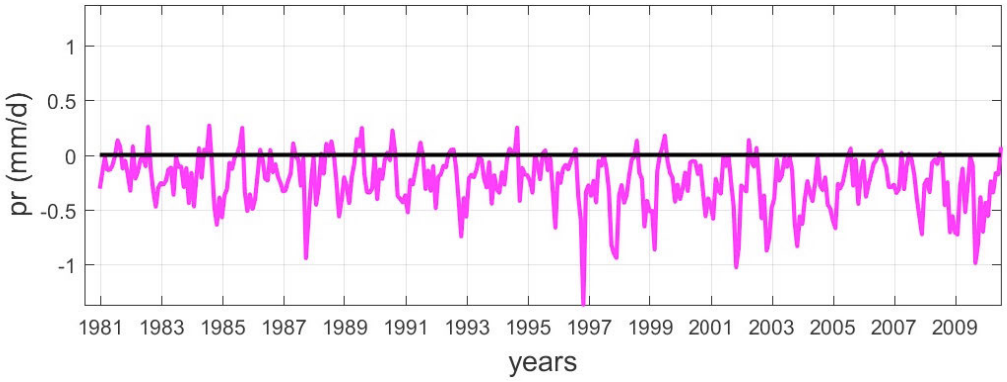

Fig. 2: Time series of precipitation over the Mediterranean Sea, CPL - SA

2.2 Sea Surface Temperature

The Sea Surface Temperature (SST) is a crucial variable to monitor in coupled climate simulations, as it simultaneously regulates and is affected by the air sea fluxes. The difference (CPL – SA) of climatological (1981-2010) atmospheric surface temperature (ts) over the whole domain has been analysed. Over the land this difference is lower than half degree, while over the sea a cold bias is detectable, mainly localized in the Eastern basin. We note that the stand-alone simulation uses the 6-hourly ERA-Interim SST dataset as a surface boundary condition. The seasonal cycle of ts, averaged over the sea, shows that the cold bias is higher during fall, winter and spring. The cold bias over the sea is frequent in climate coupled simulations, coherently with other experiments [2, 4].
Figure 3 shows the time series of surface temperature differences between the CPL simulation and the ERA-interim SST dataset, and no significant trend is detectable.

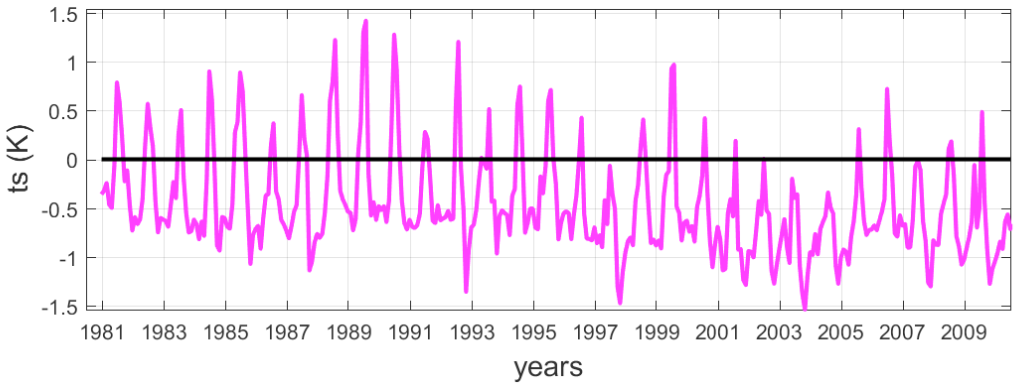

Fig.3: Time series of near surface temperature over the Mediterranean Sea, CPL - SA.

2.3 Ocean circulation

The Mediterranean is a marginal sea characterized by its own peculiar thermohaline circulation (MTHC). The Mediterranean Sea acts as a machine that modifies the incoming fresh Atlantic Water (AW) into a denser Mediterranean water through a series of complex processes of sinking and mixing both in the open ocean and on the shelves, driven by both winds and buoyant fluxes. AW enters the basin through the Gibraltar Strait, where is first trapped in the Alboran Gyre, then follows the African coast. Approaching the Sicily Channel the flux splits in two parts, one enters the Tyrrhenian Sea and the other enters the Eastern Basin where it undergoes processes of dense water formation. The so formed intermediate and deep waters go back to the Western basin and close the MTHC with an outflow to the Atlantic Ocean in the intermediate levels, acting as a modulating signal for the global ocean circulation. The main deep water formation sites of the Med Sea are the Gulf of Lion, the Adriatic, the Levantine, as clearly reproduced in our simulations.

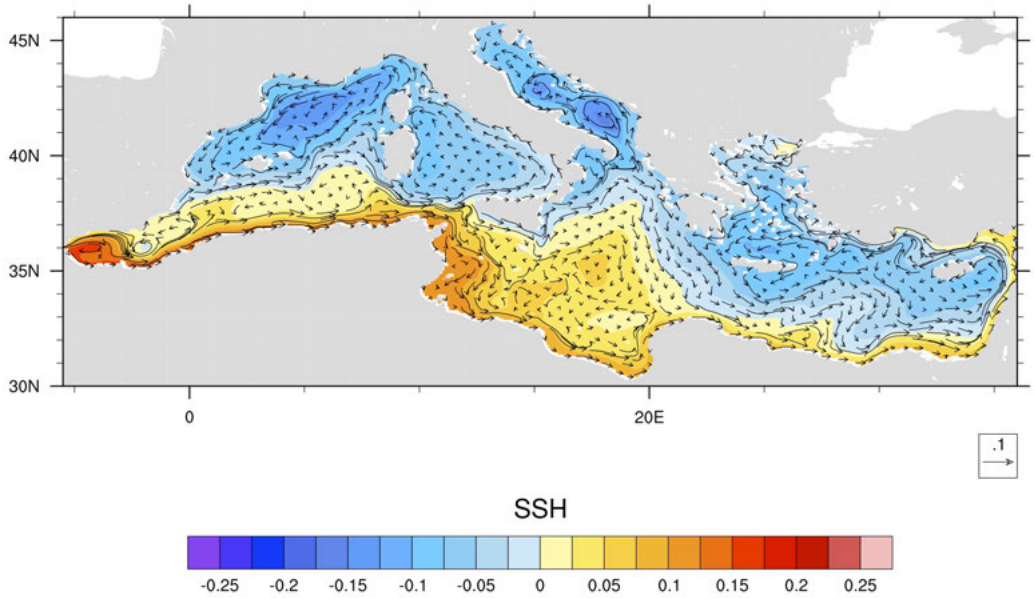

Fig.4: Mediterranean surface circulation (15 m depth) and Sea Surface Height (color shadow).

References

[1] P. Ruti et al (2015) MED-CORDEX initiative for Mediterranean Climate studies, BAMS, doi:10.1175/BAMS-D-14-00176.1, (2015)

[2] Turuncoglu U.U. and G. Sannino. Validation of newly designed regional earth system model (RegESM) for Mediterranean Basin. Clim. Dyn (2017) 48:2919–2947 DOI 10.1007s00382-016-3241-1 (2015)

[3] Struglia M.V., Calmanti S., Carillo A, Dell'Aquila A., Lombardi E. and Sannino G. Calibration of the high resolution regional earth system model (RegESM) over the Med-CORDEX domain. In *High performance computing on CRESCO infrastructure: research activities and results 2016* . ISBN: 978-88-8286-362-3 (2017)

[4] Sevault et al. A fully coupled Mediterranean regional climate system model: design and evaluation of the ocean component for the 1980 2012 period. Tellus A 2014, 66, 23967, http://dx.doi.org/10.3402/tellusa.v66.23967 (2014)

AIR QUALITY MODELLING AT THE URBAN SCALE: THE PMSS MODELLING SYSTEM APPLIED TO A CASE STUDY IN MODENA WITHIN THE CRESCO-HPC ENVIRONMENT

Villani Maria Gabriella*, Russo Felicita, Vitali Lina, Adani Mario, Ciancarella Luisella and Piersanti Antonio

ENEA, National Agency for New Technologies, Energy and Sustainable Economic Development,
SSTP-MET-INAT, Division Models and Technologies for Risks Reduction, Laboratory of Air Pollution

ABSTRACT. We present an urban application of the modelling system Micro-SWIFT-SPRAY (PMSS), a high resolution transport and dispersion model to represent air pollutants concentrations at the microscale. We apply PMSS in the city of Modena (Italy) with the focus of evaluating the impact of a green infrastructure, a CityTree structure, on potential PM concentration reductions. We describe the set-up of the simulation, also referring to the CRESCO/ENEAGRID High Performance Computing cluster. We found that PMSS can represent a very useful and interesting tool in evaluating the impact of green infrastructures, such as CityTrees, on urban air pollutants concentrations.

1 Introduction

Here we show an application of a very high resolution (order of meters) transport dispersion model, Micro-SWIFT-SPRAY (PMSS) [1, 2, 3] to a case study in presence of an urban green infrastructure, the CityTree [4] in viale Verdi-Modena (Italy). The Citytree (hereafter indicated "CT") is a $3\times0.6\times4$ [L×W×H] m^3 panel, with the vertical walls covered with special types of plants that act as depositing surfaces for particulate matter and pollutant gases. We applied PMSS to evaluate potential air pollutants concentrations reductions in the CT nearby area.

2 Methodology

The modelling system PMSS is the parallelized version of the MSS model suite [1, 2, 3]. As MSS, PMSS is composed of two main model units: PSWIFT, a 3D wind field model for complex terrain, and PSPRAY, a three-dimensional Lagrangian particle dispersion model. PSWIFT produces a mass-consistent wind field using data from a dispersed meteorological network or from simulated meteorological data at lower resolution. PSPRAY reproduces the transport, the dispersion and the dry and wet deposition of airborne chemically inert species released. Meteorologically complex conditions (low wind speed, flow over complex topography) can also be taken into account. PSPRAY can simulate emissions from point, area or line sources.

In PSPRAY the pollutant concentration is simulated by means of a certain number of "virtual" particles, each of them representing a determined portion of the pollutant mass. These particles follow the turbulent

*Corresponding author. E-mail: mariagabriella.villani@enea.it.

motion of the air as passive tracers and their spatial distribution at a certain time represents the concentration of an emitted substance. The velocity of the particles is composed by a mean velocity component defined by the local wind computed by PSWIFT, and a stochastic velocity component, characteristic of the atmospheric turbulence. PSPRAY can compute mean and instantaneous concentrations on a three-dimensional grid defined by the user, differentiating the calculation by "chemical species" or by "source". PSPRAY and PSWIFT allow taking into account the presence of obstacles, which are represented as filled cells in the meteorological field.

The modelling system PMSS is a commercial software produced and belonging to ARIA(NET) [5]. PSWIFT and PSPRAY codes were compiled with Intel14 compiler, using Mvapich2 library, and we used the versions PSWIFT-1.2.1, and PSPRAY-3.4.3. We set a 1×1 km^2 domain that was centred in viale Verdi, where the CT was located (Fig. 1). The domain is shown by the red square in Fig. 1, and covers an adequate fraction of the emissions of the city while providing that CT unit was far enough from the domain border, where the model uncertainty is generally higher. The spatial resolution of 2 m was chosen to ensure that the model can correctly represent the CT unit while keeping run time to acceptable values.

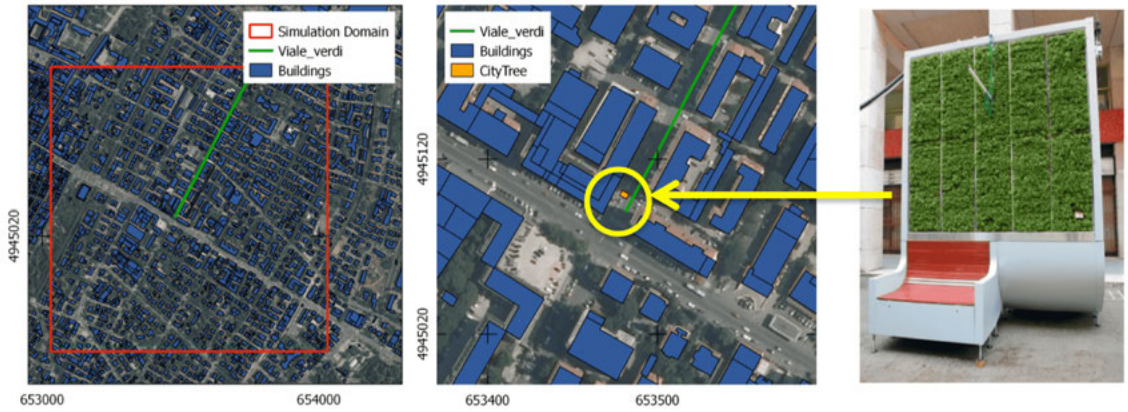

Figure 1: Simulation domain and location of the CT unit within the urban area of Modena, which includes viale Verdi, indicated by a green line.

A 15-day-time period from 12 to 26 May 2017 was chosen for the simulations. These days were selected since they are representative of typical meteorological conditions where Lagrangian models can be applied.

Meteorological data at lower resolution, used to feed the diagnostic model PSWIFT, were provided by the prognostic non-hydrostatic meteorological model RAMS [6]. Simulations were performed over Italy, at a resolution of 4×4 km^2, for the time period 12-26 May 2017. Hourly data of lower resolution meteorological fields were used by PSWIFT to reconstruct a three dimensional wind, temperature and turbulent flow at 2 m resolution.

To evaluate the impact of the CityTree unit on the air quality over the domain considered, we focused on its deposition characteristics, particularly for particulate matter. We used a value of PM10 deposition velocity equal to 0.001 m/s, which was found in the literature [7]. In order to quantify the effect of the presence of the CT on PM10 concentration, we set up two simulations that are equivalent to considering the case with and without the CT. Then, from the results, we calculated the percentage difference of the PM10 concentrations as metrics of the impact of the CT on the air quality.

The emissions were evaluated on the base of a flow assignment model for 2010, combined with a hourly traffic modulation. The traffic modulation was retrieved from a traffic flow measurement campaign held in 2016 in viale Giardini in Modena, a street nearby with a similar hourly traffic pattern. The vehicle fleet composition was retrieved from the public registry of motor vehicles data for the year 2014 (which is the latest published online). The emission input for PSPRAY has been calculated by Trefic, a software designed by ARIA(NET) [5] for the elaboration of the quantitative emitted input based on COPERT 4 methodology for the calculation of road vehicles EFs, taking into account vehicle type, fuel consumption, average travelling speed and road type.

2.1 Parallel Run Details

PMSS allows parallelization in time for PSWIFT and, for PSPRAY, either in domain, as referring to a multi tiles domain, or in sources/particles decomposition [1]. Our domain consisted of a 1×1 km^2 area, which is suited to be represented by a single tile [3]. Therefore, our PSPRAY simulations were handled by a single tile of 501×501 cells, and we parallelized over particles. We conducted our runs by using 30 cores on the CRESCO/ENEAGRID High Performance Computing infrastructure funded by ENEA [8]. In particular, we submitted our simulation on `cresco3_h144`. Each 15-day-simulation consisted of 15 single model runs, simulating 24 h. The restart option was applied, i.e. for each simulated day the values for the PM concentrations calculated for the last hour were saved, and used for the following run. The main features of our simulation are shown in Tab. 1. The simulation duration does depend also on the number of emitted particles. In our study, with a single tile of 501×501 cells, the simulation took into consideration *seven chemical species* with a total number of emitted particles equal to about *14.7 million particles* per each day of the simulation.

	Simulation run (15 d)		**What to expect for 1 day**	
VARIABLES	**PSWIFT**	**PSPRAY**	**PSWIFT**	**PSPRAY**
Days Simulated	15	15	1	1
Number of Cores	30	30	30	30
Simulation Duration	∼11 h	∼2 d	∼45 min	∼3-3.5 h
CPU time	∼14 d	∼60 d	∼22.5 h	∼4 d
Output Storage Space	∼149 GB	∼138 GB	∼10 GB	∼9.2 GB
Total Storage Space	**∼303 GB**		**∼29 GB**	

Table 1: Summary of the main features of PMSS simulations from a computational point of view.

3 Results

The results of the simulations are presented here as averages over the entire simulation period (15 days). Here we calculated the percentage differences in PM10 concentration between the 15-days averaged values from the simulation with and without the CT. Figure 2 shows: on the left i) the PM10 concentration difference (e.g. with and without CT), and on the right ii) the corresponding PM10 concentration differences in percentage. For a single CT, the area affected by the concentration reduction extends for 48 m along the street canyon and 20 m across. The major reduction is located within the CT premises.

The modelling system PMSS, with consistent input data and at an appropriate spatial resolution, has proven to be a very useful and interesting tool in evaluating the impact of green infrastructures, such as CityTrees, on air pollutants concentrations relevant to urban environments.

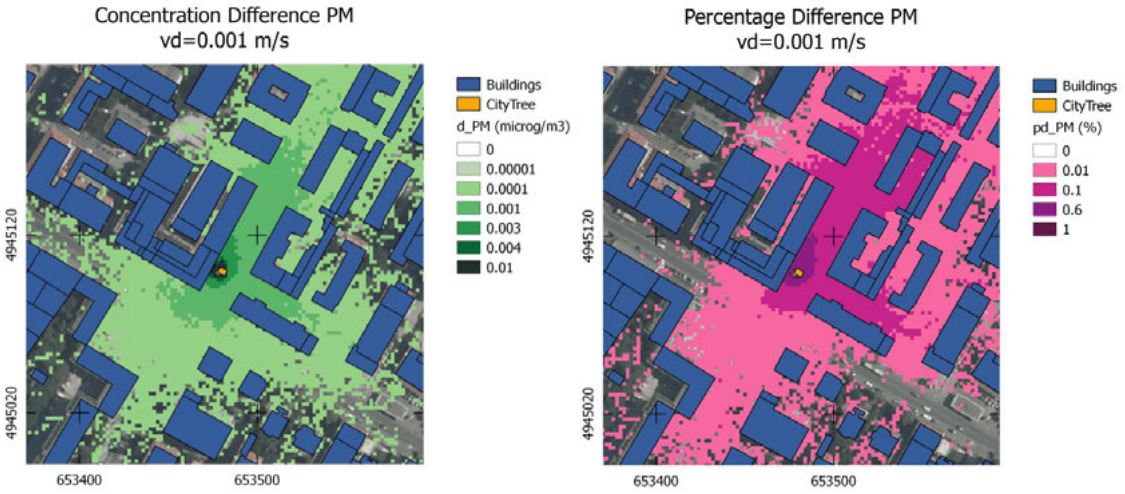

Figure 2: Results of the average of 15 days simulation of PM10 concentrations at human height level nearby the CT unit, in viale Verdi, Modena (Italy). Left: Map of the PM10 concentration difference (absolute values). Right: Map of the PM10 concentration difference (in %).

4 PMSS work activities during January 2017-December 2017 performed on CRESCO

The urban case study presented is related to the work in [9]. The modelling system PMSS has been also employed to simulate a plume release from the heating power station in ENEA Centro Ricerche Casaccia, Roma (Italy) [10].

References

[1] O. Oldrini, P. Armand, C. Duchenne, C. Olry, J. Moussafir, and G. Tinarelli. Description and preliminary validation of the PMSS fast response parallel atmospheric flow and dispersion solver in complex built-up areas. *Environmental Fluid Mechanics*, 17(5):997–1014, 2017.

[2] S. Trini Castelli, G. Tinarelli, and T.G. Reisin. Comparison of atmospheric modelling systems simulating the flow turbulence and dispersion at the microscale within obstacles. *Environmental Fluid Mechanics*, 17(5):879–901, 2017.

[3] G. Tinarelli, L. Mortarini, S.T. Castelli, G. Carlino, J. Moussafir, C. Olry, P. Armand, and D. Anfossi. Review and validation of MicroSpray a Lagrangian particle model of turbulent dispersion. *Geophysical Monograph Series*, 200:311–327, 2013.

[4] V. Splittgerber and P. Saenger. The CityTree: a vertical plant wall. *WIT Transactions on Ecology and the Environment*, 198(6):295–304, 2015.

[5] ARIA(NET). `http://www.aria-net.it/`. Accessed on 31 May 2018.

[6] W.R. Cotton, R.A. Pielke, R.L. Walko, G.E. Liston, C.J. Tremback, H. Jiang, R.L. McAnelly, J.Y. Harrington, M.E. Nicholls, G.G. Carrio, and J.P. McFadden. RAMS 2001: current status and future Directions. *Meteorology and Atmospheric Physics*, 82:5–29, 2003.

[7] T. Litschke and W. Kuttler. On the reduction of urban particle concentration by vegetation a review. *Meteorologische Zeitschrift*, 17(3):229–240, 2008.

[8] G. Ponti, F. Palombi, D. Abate, F. Ambrosino, G. Aprea, T. Bastianelli, F. Beone, R. Bertini, G. Bracco, M. Caporicci, B. Calosso, M. Chinnici, A. Colavincenzo, A. Cucurullo, P. d'Angelo, M. De Rosa, P. De Michele, l A. Fune, G. Furini, D. Giammattei, S. Giusepponi, R. Guadagni, G. Guarnieri, A. Italiano, S. Magagnino, A. Mariano, G. Mencuccini, C. Mercuri, S. Migliori, P. Ornelli, S. Pecoraro, A. Perozziello, S. Pierattini, S. Podda, F. Poggi, A. Quintiliani, A. Rocchi, C. Scio, F. Simoni, and A. Vita. The role of medium size facilities in the HPC ecosystem: the case of the new CRESCO4 cluster integrated in the ENEAGRID infrastructure. Proceedings of the 2014 International Conference on High Performance Computing and Simulation HPCS 2014, (6903807):1030–1033, 2014.

[9] M.G. Villani, L. Vitali, F. Russo, A. Piersanti, and L. Ciancarella. Internal report for EIT Climate KIC, WP3, TEST RUN, 2017.

[10] S. Taraglio, L. Blasi, G. Cupertino, C. Moriconi, V. Nanni, S. De Vito, F. Formisano, G. Zanini, F. Russo, M.G. Villani, and L. Vitali. Sviluppo di un Monitoraggio Aereo per lo Smart District, 2017. Report ENEA RdS/PAR2016/021, Ricerca di sistema elettrico.

NEUTRONICS ANALYSIS FOR THE DESIGN AND INTEGRATION OF EC LAUNCHER IN DEMO

Rosaria Villari*[1], Denise Trombetta[2], Fabio Moro[1], Davide Flammini[1] and Andrea Colangeli[1]

[1]*ENEA, Department of Fusion and Nuclear Safety Technology, I-00044 Frascati (Rome), Italy*[1]

[2] *University LA Sapienza of Rome, DIAEE department, I-00186 Rome, Italy*

ABSTRACT. Three-dimensional nuclear analyses with MCNP5 Monte Carlo code have been performed to support design and integration of Electron Cyclotron (EC) launchers in DEMO reactor. Strategies to improve the EC design and its shielding capability have been studied to guarantee self-sufficiency and reduce the impact of nuclear loads to other components.

1 Introduction

In the frame of this activity within EUROfusion PMI program, three-dimensional nuclear analyses with MCNP5 code [1] and JEFF3.2 nuclear data library [2] have been performed in CRESCO cluster to support design and integration of Electron Cyclotron (EC) in DEMO reactor. Two configurations have been analyzed and the impact on Tritium Breeding Ratio (TBR), neutron flux, nuclear heating and damage on Breeding Blanket (BB), Vacuum Vessel (VV) and Toroidal Field (TF) coil was studied as well nuclear loads on the integrated systems. Strategies to improve EC design and shielding capability have been suggested to reduce the interface with other systems [3].

2 Design and integration of EC launchers

Neutronics analyses have been performed to support design and integration of the Electron Cyclotron (EC) launchers in equatorial port of Water Cooled Lithium Lead (WCLL) DEMO reactor. The proposed heating system consists of 5 EC launchers based on 8 Remote Steering Antennas (RSA). Two different configurations have been considered for integration in DEMO: two horizontal rows with four RSA each and one vertically stacked array of eight RSA (Figure 1). The present integration strategy consists in removing the equatorial outboard WCLL BB modules impacted by EC opening, and in replacing them with shielding plug made of steel and water [4].

[1] Corresponding author. E-mail: rosaria.villari@enea.it

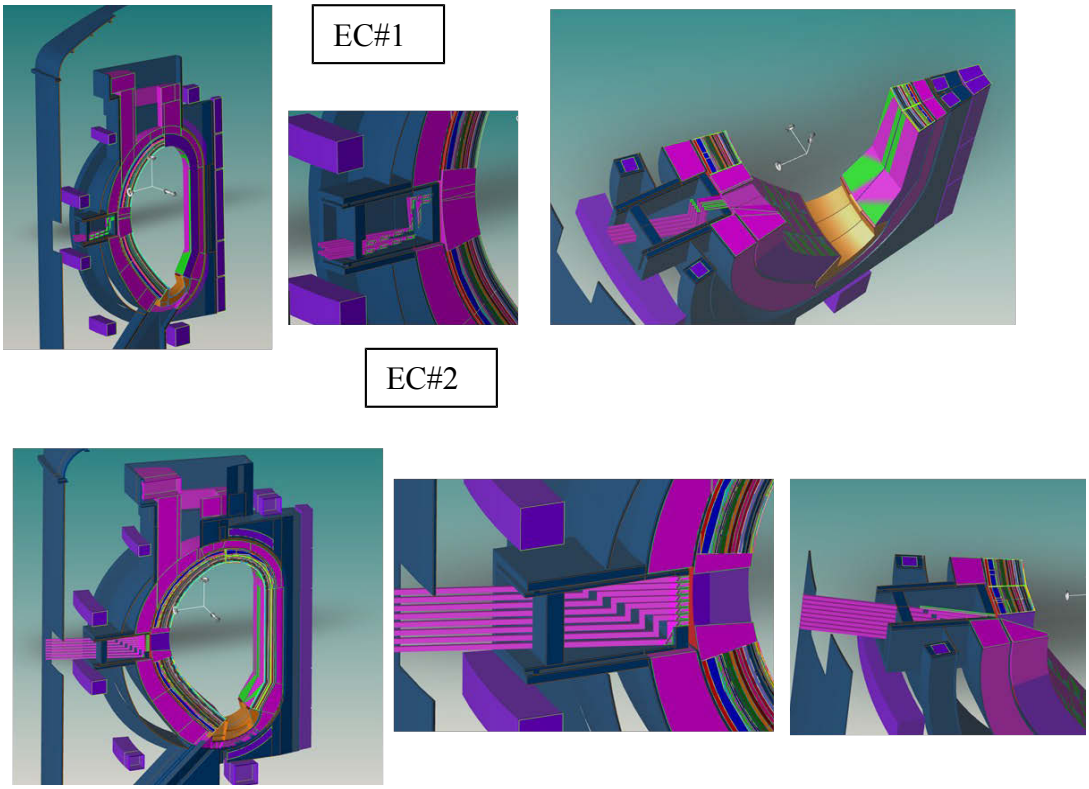

Fig.1: MCNP model of EC configuration #1 (top) and#2 (bottom)and integration in WCLL 20° DEMO model

3 Results

The impact on Tritium Breeding Ratio (TBR) of 5 EC#1 launchers is significant, -0.0057 with respect to WCLL baseline (i.e. 1.156), due to the complete replacement of 10 OB4 equatorial modules with steel-water plugs and the total TBR is 1.099, slightly below the design target. The effect of 5 EC based on conf. #2 is lower than EC#1, -0.030 with respect to baseline, due to the complete replacement of 5xOB4 equatorial modules with steel-water plugs and the total TBR is 1.126, above the margin.
The main results obtained from neutronics analyses of the other significant nuclear quantities and impact on Vacuum Vessel (VV) and Toroidal field coil (TFC) loads for EC#1 and EC#2 are reported in the Table 1. Due to EC openings and lack of in-port shield, all the neutronics quantities increase compared to the Baseline model. In particular, at the EC rear flange neutron flux increases of 3 orders of magnitude for both EC#1 and EC#2 configurations compared to the baseline (see Figure 2).

These configurations do not satisfy the TFC nuclear heating density limit (i.e. $5 \cdot 10^{-5}$ W/cm^3) or the Helium production limit on VV (i.e. 1 appm over 6 FPY). Moreover, for both the EC#1 and the EC#2 the neutron damage on VV shows great increase, in particular, for the first configuration the limit on VV (2.75 dpa over 6 FPY) is still satisfied while it does not occur for the second one.

In general, the results of these analyses indicate a high neutron flux and insufficient shielding capability to protect the surrounding components to the EC port plug such as TFC and VV.

Two shielding options have been studied for EC#1 and EC#2 to reduce the loads on VV and TFC. A 35 cm thick shield made of the same material as the VV, i.e. 60% vol. of SS316L and 40% vol. of water, has been inserted behind the front SS shield of EC#1 plug. The neutron flux at the level of EC#1 rear flanges is reduced by more than one order of magnitude ($7.82 \cdot 10^{9}$ n/cm^2/s**)** and the nuclear heating density on TFC decreases of one orders of magnitude ($1.54 \cdot 10^{-5}$ W/cm^3) compared to EC reference configuration without shield, the limit is respected.

Table 1: Comparison of neutronics quantities between EC#1 & EC#2 configurations.

Nuclear quantity	**EC#1 configuration**	**EC#2 configuration**
Neutron Flux (n/cm^2/s)	$1.66 \cdot 10^{11}$ on port rear flange	$1.95 \cdot 10^{11}$ on port rear flange
	$9.87 \cdot 10^{12}$ on VV	$6.28 \cdot 10^{13}$ on VV
	$6.38 \cdot 10^{10}$ on TFC	$1 \cdot 10^{11}$ on TFC
Nuclear Heating Density (W/cm^3)	0.32 on VV	1.80 on VV
	$1.85 \cdot 10^{-4}$ on TFC	$4.63 \cdot 10^{-4}$ on TFC
Neutron Damage (dpa/FPY)	$5.28 \cdot 10^{-2}$ on VV	$6.25 \cdot 10^{-1}$ on VV
	$1.89 \cdot 10^{-4}$ on TFC	$2.89 \cdot 10^{-4}$ on TFC
Helium Production (appm/FPY)	1.66 on VV	9.87 on VV
	$4.80 \cdot 10^{-4}$ on TFC	$6.57 \cdot 10^{-4}$ on TFC

Two shields have been introduced in the EC#2: 70 cm of VV-like shield behind the front SS flange of EC plug and a cover plate made of SS316 behind the EC cone opening (in the gap between VV and EC port). With this configuration, the neutron damage on VV is slightly still above the margin but design limit on the TFC nuclear heating density is satisfied (the maximum value decreases to $1.09 \cdot 10^{-5}$ W/cm^3).

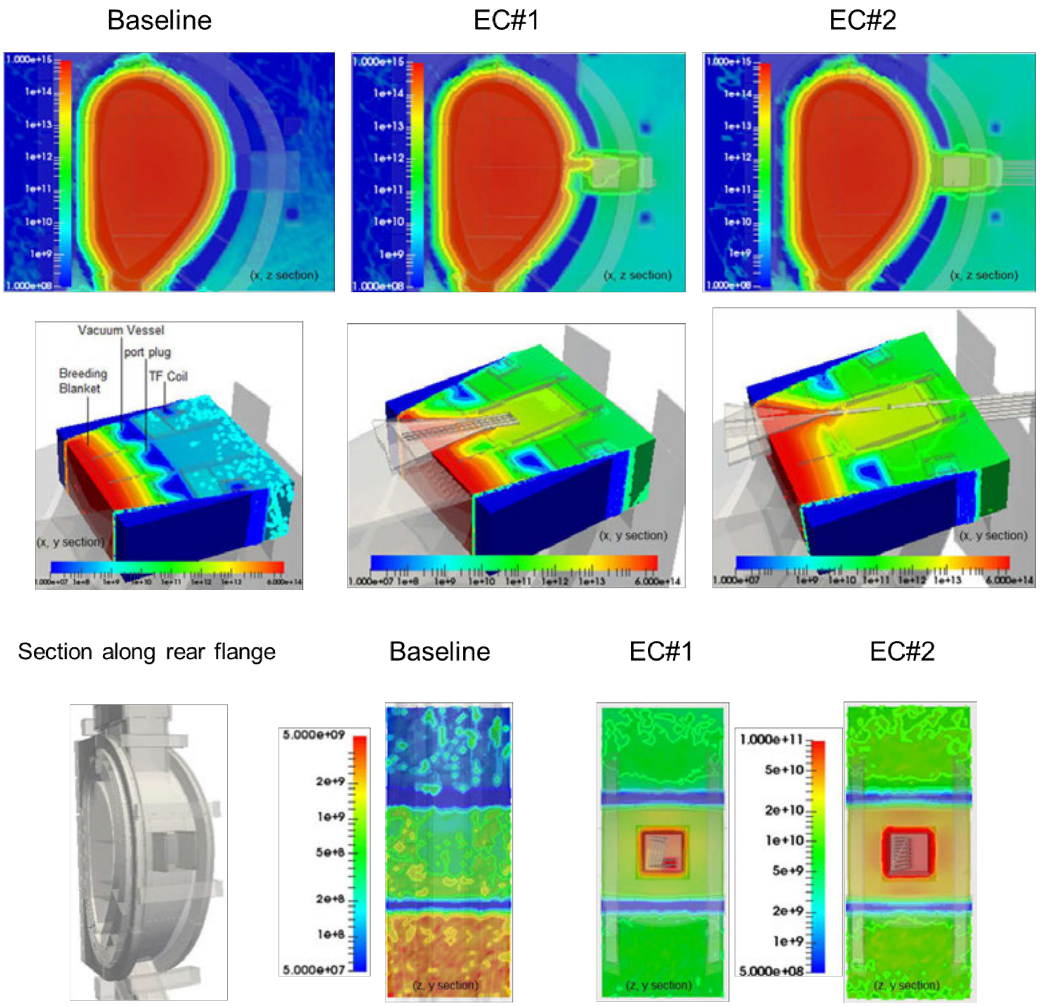

Fig.**2**: Neutron flux maps for Baseline, EC#1 and EC#2

These results imply that the EC#1 shield is a suitable option for its plug while the EC#2 option guarantees the protection of the TFC but the cover plate is not sufficient to reduce the neutron damage to the VV below the limit.

From the neutronic point of view, the EC#1 configuration with shield guarantees all the shielding requirements, however it has a severe impact on Tritium self-sufficiency, which could be mitigated through a more efficient integration in breeding blanket (e.g. reduction of shield plug extension to reduce the breeding blanket losses).

References

[1] X-5 Monte Carlo Team: MCNP - A General Monte Carlo N-ParticleTransportCode, Version 5,LosAlamosNationalLaboratory, Los Alamos, New Mexico, USA, April 2003.
[2] JEFF3.2 nuclear data library, http://www.oecdnea.org/dbforms/data/eva/evatapes/jeff_32/.
[3] R. Villari,A. Colangeli, D. Flammini, F. Moro, D. Trombetta. Neutron transport analysis through openings in in-vessel components, Final Report WP PMI-3-3-T007, EFDA_D_2MTM7F (2018)
[4] G. Grossetti1, L.V. Boccaccini, F. Cismondi, A. Del Nevo, U. Fischer, T. Franke, G. Granucci, F. Hernández, R. Mozzillo, D. Strauß, M. Q. Tran, A. Vaccaro, R. Villari. DEMO Port Plug Design and Integration studies. *Nuclear Fusion* **57**, 116068 (2017)

Employing Carbon Nanotubes Electrical Properties to Build New Intelligent Materials

Y. Zhao[1], G. Donati[2], A. De Nicola[3], A. Pizzirusso[2], G. Munaò[2], S. Caputo[2], G. Milano[2,3]

[1] Dalian Minzu University, Institute of Nano-Photonics, School of Physics and Materials Engineering, 116600, Dalian, China.

[2] Salerno University, Department of Chemistry and Biology "Adolfo Zambelli", 84084, Via Giovanni Paolo II, 132, Fisciano (SA), Italy.

[3] Department of Organic Materials Science, Yamagata University 4-3-16 Jonan Yonezawa, Yamagata-ken 992-8510, Japan

Abstract

The unique electric properties of carbon nanotubes (CNTs) have opened new scientific and technological fields based on the investigation and optimization of CNT filled polymers. CNTs, when added to polymer matrices, make them conductive once they overcome a specific (so-called percolative) concentration. When this percolative threshold is reached, a CNT electric circuit is formed and the composite materials become conductors. We simulate the self-assembly processes of carbon nanotubes dispersed in different polymer phases using a hybrid particle-field molecular dynamics technique (MD-SCF). This efficient computational approach allowes simulations of large-scale systems (up to ∼1 500 000 particles) of flexible rod-like particles in different matrices on the millisecond time scale. The equilibrium morphologies obtained for longer CNTs are in good agreement with those proposed by several experimental studies that hypothesized a two level "multiscale" organization of CNT assemblies. The calculated behavior of the conductivities for longer CNTs is consistent with the power laws obtained by numerous experiments.

We are also working on the modeling of the Joule effect and piezoresistivity, two interesting features of CNTs, that can be employed to realize smart materials able to monitor their own conditions and that can be employed for several applications ranging from automotive and aeronautics to civil engineering infrastructures.

1 - Introduction

Carbon nanotube (CNT)/polymer nanocomposites have received attention from the scientific and technological point of view since CNTs were first observed by Iijima[1] in 1991. The interest of CNT/polymer nanocomposites has grown widely in experimental and theoretical research fields because of the dramatic increase of the electrical conductivity of nanocomposites once the CNTs concentration increases (percolation threshold). So, when the volume fraction of CNTs rises above the critical value there is a continuous CNT cluster that extends throughout the entire CNT/polymer nanocomposite structure. Therefore, the distribution of CNTs in the CNT/polymer nanocomposites plays a key role in determining the percolation threshold, which depends primarily on the aspect ratio (AR), polymer types, alignment of CNTs, and composite processing methods.

Despite significant experimental success in this regard a full understanding of the behavior and potentialities of CNTs composite materials is still missing, and in this context, computer modelling and simulations play an important role because can give the molecular insight necessary to understand the main mechanisms ruling CNTs electric conduction. A correct description of self-

assembly processes, including interactions between the fillers and between the filler and the matrix, is necessary for a reliable prediction of the final network structure and its basic role in influencing the calculated electrical properties.
In this project an efficient Molecular Dynamics (MD) simulation scheme, based on hybrid particle-field representation called Molecular Dynamics-Self Consistent Field (MD-SCF)[2] is employed.

We investigate the percolation threshold and electrical conductivity of nanocomposites in homopolymer and block copolymer matrices using parallel hybrid particle-field MD-SCF simulations[3]. Self-assembly processes of flexible rod-like particles (mimicking CNTs) dispersed in polymer phases have been examined. In particular, dispersions of rod-like nanoparticles having three different ARs (10, 20 and 30) in different polymer matrices have been simulated at different concentrations near percolation. The obtained CNT morphologies have then been used to calculate the conductivity behavior using a resistor network approach.

2 – Methods

The hybrid MD-SCF approach is based on the evaluation of the non-bonded force and its potential between atoms of different molecules by the evaluation of an external potential dependent on the local density at position **r**. According to the spirit of SCF theory, a many-body problem such as molecular motion can be reduced to a problem of deriving the partition function of a single molecule with an external potential V(**r**). Then, the nonbonded force between atoms of different molecules can be obtained from a suitable expression of V(**r**) and its derivatives. In the framework of SCF theory, a molecule is regarded to be interacting with the surrounding molecules through a mean field, rather than direct interactions among the molecules. Assuming that the density dependent interaction potential **W**, where each species is specified by the index K, takes the following form:

$$W[\{\phi_K(\mathbf{r})\}] = \int \mathrm{d}\mathbf{r} \left(\frac{k_\mathrm{B}T}{2} \sum_{KK'} \chi_{KK'} \phi_K(\mathbf{r}) \phi_{K'}(\mathbf{r}) + \frac{1}{2\kappa} \left(\sum_K \phi_K(\mathbf{r}) - \phi_0 \right) \right)$$

where φK(**r**) is the coarse-grained density of species K at position **r** and χKK' are the mean field parameters for the interaction of a particle of type K with the density fields due to particles of type K', it can be shown using the so-called saddle point approximation that the external potential is given by:

$$V_K(\mathbf{r}) = \frac{\delta W[(\phi_K(\mathbf{r}))]}{\delta \phi_K(\mathbf{r})} = k_\mathrm{B}T \sum_{K'} \chi_{KK'} \phi_{K'}(\mathbf{r}) + \frac{1}{\kappa} \left(\sum_K \phi_K(\mathbf{r}) - \phi_0 \right)$$

The main advantage of this scheme is that the most computationally expensive part of the MD simulations (i.e. evaluation of the non-bonded force between atoms of different molecules), is replaced by an evaluation of forces between single molecules with an external potential.
All simulations (MD-SCF) reported in the present work have been performed using the parallelized version of the OCCAM MD code.[4]
The system is composed by an insulator part (polymer matrix) and conductive part (CNTs). The calculation of the CNT resistor network conductivity has been performed by using the transfer-matrix method, a very efficient approach that importantly decreases the computational cost for this calculation.[5]

Both the intrinsic and contact (to take into account the tunnel effect) CNT resistance, have been considered, according to the following expression for the intrinsic resistance:

$$R_{ij} = \frac{4l_{jk}}{\pi\sigma_{\mathrm{CNT}}D^2}$$

where l_{jk} is the length of the CNT between the nodes j and k, D is the CNT diameter (1.4 nm), and σCNT is the intrinsic conductivity of the CNT (1×10^5 S m^{-1}).

And according to the following expression for the contact resistance:

$$R_{\mathrm{con}} = \frac{h}{2e^2}\frac{1}{MP}$$

where h is Planck's constant, e is the electron charge, h/2e2 = 12.9054K is the quantized resistance, M is the total number of conduction channels, and the transmutation probability P.

3 - Results

In our work, we considered three different lengths for CNTs, that we will indicate as AR10, AR20, AR30 (CNTs of length of about 15, 28, 43 nm). The different CNT length influences the percolation threshold, that is lower for longer CNTs as shown in the following Figure (where the matrix is a homopolymer):

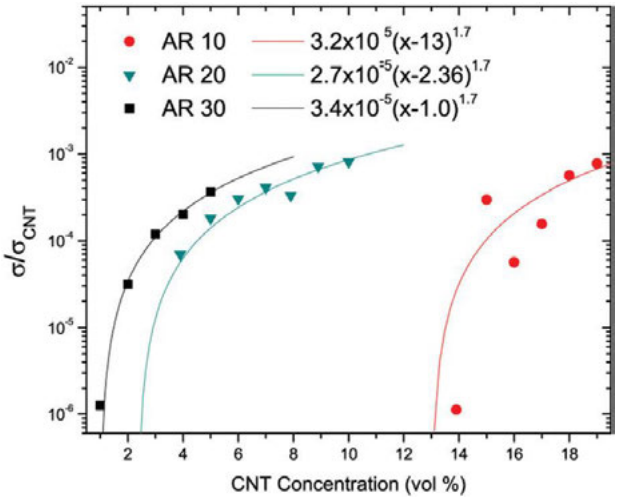

These calculated data can be well-fitted by the following power law:

$$\sigma/\sigma_{\mathrm{CNT}} = \eta(f - f_c)^t$$

where η is a prefactor, f is the CNT volume%, fc is the percolation threshold and t is the exponent of the power law. It is evident that in the case of AR10, the power law does not work, meaning that another percolation behavior rules that particular shape. Moreover, the CNTs networks are different: lamellar like for AR20 and AR30 and ellipsoidal and spherical for AR10.
The evolution of the conductive behavior at different times is also investigated, as shown in the following Figure:

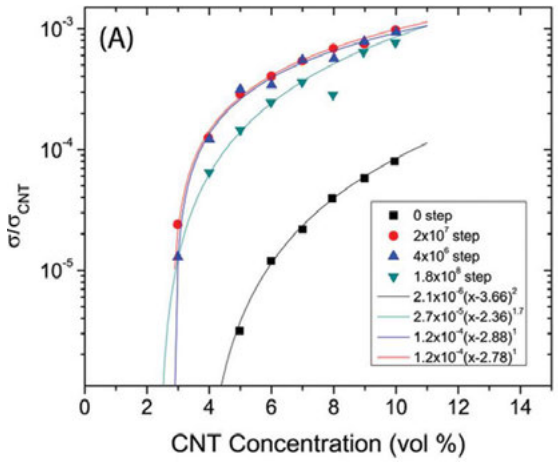

The behavior is clearly different at the beginning of the simulation, where the CNTs have a random distribution. However, we can see that at the beginning and at long time the conductivity is lower compared to intermediate times, where the self-assembly of CNTs is not concluded. The behavior of the exponent is also notable, changing from t = 2 for the homogeneous dispersion to approximately 1 at the early stages of CNT assemblies close to the maximum time conductivities, giving t = 1.7 when the self-assembly is complete. The results obtained here are in agreement with several studies, supporting the notion that the formation of nanotube clusters favors the formation of networks.

We also simulated CNTs in block co-polymers. In the first case, both CNTs and the polymer are randomly distributed in the simulation box. In this case, lower percolation thresholds (compared to the homopolymer case), are found as shown in the following Figure:

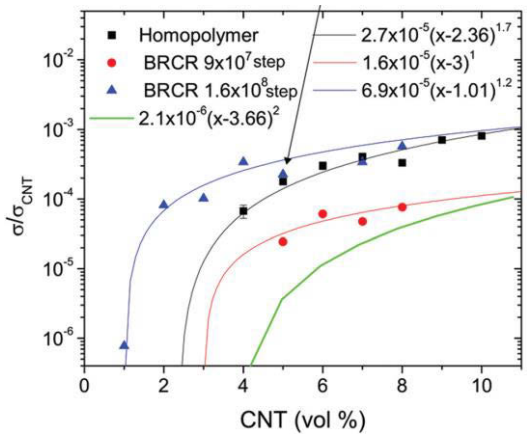

In this case the percolation threshold is lower compared to the homopolymer case. Conductive percolated structures are found in all directions because of the defects in the block copolymer phase and crossing of the CNT assemblies, which give perforated lamellar structures.

When CNTs are placed in an already ordered polymer matrix, they remain randomly generated but are positioned in a regular lamellar block co-polymer template from the start of the simulation.

In the last case, when CNTs are placed in a lamellar co-polymer template, randomly distributed but parallel to the lamellar place, the percolation threshold is larger: connections between the CNTs distributed in different lamellae are not obtained and the CNTs are confined in spherical or ellipsoidal shapes without forming a network. Only by increasing the CNT concentration the percolation threshold decreases.

4 – Conclusions and Perspectives

In this work an accurate insight on the percolative behavior of CNTs in different polymer matrices is obtained by using a computational approach. We showed the dependence of the percolation threshold of the CNT resistor network from the aspect ratio, concentration and matrix environment. Especially regarding the block co-polymers as matrix there is still a lot to understand.
We are currently working on the CNT Joule effect modeling, i.e. the heat dissipation of the conductive CNTs is simulated. The CNTs Joule effect can be employed to build smart materials able to have specific properties (i.e. self-deicing under certain temperatures) or to repair their own cracks (self-healing). We are also building a modeling strategy for the simulation of the piezoresistivity, i.e. the change in the electric resistance of the CNTs due to an applied strain or stress. This feature allows these composites to be sensitive to an external stress or damage (self-sensing), in this way an immediate and efficient repair can be performed.

References:

1 - S. Iijima, Nature, 1991, 354, 56-58.
2 - G. Milano and T. Kawakatsu, J. Chem. Phys., 2009, 130, 214106.
3 - Y. Zhao, M. Byshkin, Y. Cong, T. Kawakatsu, L. Guadagno, A. De Nicola, N. Yu, G. Milano, B. Dong, Nanoscale, 2016, 8, 15538-15552.
4 - Y. Zhao, A. DeNicola, T. Kawakatsu and G. Milano, J. Comput. Chem., 2012, 33, 868–880.
5 - M. S. Byshkin and A. A. Turkin, J. Phys. A: Math. Gen., 2005, 38, 5057.

THE FRANCK CONDON EFFECT ON THE BT2N LIGHT ABSORPTION SPECTRA: SINGLE AND DOUBLE MOLECULE ABSORPTION

Giuseppe Zollo*and Fabrizio Gala

Dipartimento di Scienze di Base e Applicate per l'Ingegneria, Universitá di Roma "La Sapienza", Via A. Scarpa 14–16, 00161 Rome Italy

ABSTRACT. First principles calculations based on density functional theory, density functional perturbation theory and many body perturbation theory are employed to explain the optical absorption peak of a newly synthesized oligo-tiophene molecule that has been considered for bulk-heterojunction solar cells. The GW approach is used to obtain quasiparticle energies as a pre-requisite to solve the Bethe-Salpeter equation for the excitonic. The Franck-Condon effect has been considered through the Huang-Rhys method in the context of the density functional perturbation theory in order to calculate the vibration assisted ionization spectrum. It is shown that the vibrational peak enlargement is necessary to explain the peak shape features arising from both isolated and π-stacked molecules.

1 Introduction

Organic cells have many appealing properties such as: low fabrication cost, solution processability, transparency and flexibility that make them appealing for solar energy conversion Moreover, power conversion efficiencies (PCEs) of polymer based solar cells (PSCs) with bulk-heterojunction (BHJ) architecture have been greatly improved in the recent years [1].

In BHJ materials [2] light absorption at the donor generates strongly bound Frenkel-type excitons[3, 4] that, at the donor-acceptor interface, have to be separated to generate the electrical current between the electrodes. Fullerene derivates are commonly considered as good acceptors BHJs while good donor materials are still under intense research to improve the organic solar cells performances.

In particular, π-conjugated small molecules, made of a push-pull structure with an electron-donating central unit (D) and peripheral electron-accepting groups (A) as end groups, have been considered as donors in BHJ solar cells, with an increased PCE up to 9$\sim$10% [5, 6, 7, 8] in the last years. However, solution-processed small molecule organic solar cells have not reached these performances so far. On the other hand, their properties of manageable synthesis and stability, high purity, batch to batch control, and easier energy level design are quite attractive and that's why research is pushing on them, especially concerning the quantitative understanding of the exciton formation [9, 5, 10, 11] that is still poor.

Indeed, accurate description of electron-hole (eh) interactions could be addressed in the context of

*Corresponding author. E-mail: giuseppe.zollo@uniroma1.it.

quantum-chemical approaches but with prohibitive computational effort. Alternatively, Many-body perturbation theory (MBPT) techniques, namely the GW approximation[12] and the Bethe-Salpeter equation (BSE), ensure good accuracy with reasonable computational cost and have been already employed in organic crystals and small molecules [13, 14, 15, 16, 17, 18].

It should be stressed, however, that some relatively important phenomena, such as dynamical effects in exciton screening or electron-phonon coupling, are not included in the GW-BSE scheme. Among them, the absorption peak shape that is related to the so called Frank-Condon (FC) effect due to vibrational modes of the molecule in its ground and excited states.

In this work we study the full absorption spectrum of a modified version of the BT2N molecule, the diethyl 3,3'-(3,3"'-dioctyl-[2,2':5',2":5",2"'-quaterthiophene]-5,5"'-diyl)(2E,2'E)-bis(2-cyanoacrylate), with chemical formula $C_{44}H_{52}N_2O_4S_4$, a newly assembled oligomer-like molecule for organic solar cells. BT2N has been already considered showing that the absorption spectrum can be explained if a π-stacking between the molecules is taken into account [18]. However in this previous work, only the peak position was taken into account and no attempt to predict the peak broadening and shape was performed. The molecule here considered (BT2Na in the following) has the following chemical formula $C_{28}H_{20}N_2O_4S_4$ and has been obtained from BT2N by removing the aliphatic chains. The absorption spectrum is calculated by GW-BSE and the Huang-Rhys (HR) formula is employed to calculate the peak shape connected with the FC effect. Due to the computational workload involved in the HR calculation, we adopt the present case as a good approximation to tread broadening and shape also for all the BT2N absorption spectra considered.

2 Theory

The ground state electronic and geometric properties of a single isolated BT2Na, BT2N and stacked BT2N systems have been obtained by density functional theory[19, 20] (DFT) with a generalized gradient approximation based on the Perdew-Burke-Ernzerhof formula [21](PBE) for the electron exchange and correlation potential $V_{xc}[n(\mathbf{r})]$, and norm-conserving pseudopotentials have been constructed with the Troullier-Martins schemeTM in the framework of a plane-wave basis set expansion. DFT calculations have been performed using the QUANTUM-ESPRESSO packageEspresso, with a plane-wave energy cutoff of 70 Ry for the wave functions. Structural optimization has been achieved in a cubic box of 20x40x20 $Å^3$ using the Broyden-Fletcher-Goldfarb-Shanno (BFGS) methodBFGS together with the Hellmann-Feynman forces acting on the ions; an empirical dispersion forces [22] is included to handle the long range interactions (π stacking) between the molecules. The chosen box size is large enough to prevent any spurious interaction arising from the effects of the periodically repeated images of the molecules. Concerning BT2Na, the atomistic configuration of the excited state has been obtained in the same context and with the same parameters as the ground state, but with a constrained occupation with both the HOMO and the LUMO occupied by one electron. While this approach is, in general, wrong, it has been demonstrated that it leads to an atomistic configuration quite close to the real one of the excited state if it is characterized by a single, well defined transition[16], as in the present case (see below). All the calculations have been performed using the Γ point for the Brillouin zone sampling, and the ionic minimization was done until the convergence threshold of 0.001 a.u. for the total force was achieved.

Theoretical band gaps have been obtained with three different levels of accuracy: in the context of ground state DFT either as the difference between the lowest unoccupied molecular orbital (LUMO) and the highest occupied molecular orbital (HOMO) (simply referred as ε_{gap}), or as the difference

between the electron affinity and the ionization potential $\varepsilon_{gap}^{\Delta SCF} = E_{N+1} - E_N - (E_N - E_{N-1})$ (the so called Δ-SCF method) where E_x is the DFT ground state total energy of the system containing x electrons [23], and lastly through the GW method that allows the calculation of the quasi-particle (QP) energies in the context of MBPT; the last task has been attained using the YAMBO code[24].

In particular, QP energies are computed to first order as:

$$\varepsilon_n^{\text{QP}} = \varepsilon_n^{(0)} + Z_n \langle n|[\Sigma(\varepsilon_n^{(0)}) - V_{xc}]|n\rangle \tag{1}$$

where $\varepsilon_n^{(0)}$ and $\langle \mathbf{x}|n\rangle = \phi_n(\mathbf{r})$ are the eigenvalues and eigenfunctions of the DFT hamiltonian respectively, and

$$Z_n = \left(1 - \frac{\partial \Sigma_n}{\partial \omega}\bigg|_{\omega=\varepsilon_n^{(0)}}\right)^{-1} \tag{2}$$

where $\Sigma_n(\omega) = \langle n|\Sigma(\mathbf{r}_1\mathbf{r}_2, \omega)|n\rangle$ is the Fourier transform of the dynamical electron self-energy operator Within the GW approximation[25], $\Sigma(\mathbf{r}_1\mathbf{r}_2, \omega)$ can be cast in terms of the ground state DFT Green's function $G(\mathbf{r}_1\mathbf{r}_2, \omega)$ as:

$$\Sigma(\mathbf{r}_1\mathbf{r}_2, \omega) = i \lim_{\eta \to 0^+} \int \frac{d\omega'}{2\pi} e^{i\omega'\eta} G(\mathbf{r}_1\mathbf{r}_2, \omega - \omega') W(\mathbf{r}_1\mathbf{r}_2, \omega') \tag{3}$$

with

$$G(\mathbf{r}_1\mathbf{r}_2, \omega) = \lim_{\eta \to 0^+} \sum_n \frac{\phi_n(\mathbf{r}_1)\phi_n^*(\mathbf{r}_2)}{\omega - [\varepsilon_n^{(0)} + i\eta \text{sgn}(\mu - \varepsilon_n^{(0)})]} \tag{4}$$

and

$$W(\mathbf{r}_1\mathbf{r}_2, \omega) = \int d\mathbf{r}_3 \frac{\epsilon^{-1}(\mathbf{r}_3\mathbf{r}_2, \omega)}{|\mathbf{r}_1 - \mathbf{r}_3|} \tag{5}$$

is a dynamically screened interaction, expressed in terms of the inverse dielectric function ϵ^{-1} of the system and of the bare Coulomb interaction V.

The inverse dielectric matrix is related to the response function $\chi(12) = \delta\rho(1)/\delta V_{ext}(2)$ (where (1) is a short-hand notation for $(\mathbf{r}_1, t_1)$) via the relation:

$$\epsilon^{-1}(12) = \delta(12) + \int d(3) \frac{\chi(32)}{|\mathbf{r}_1 - \mathbf{r}_3|} \tag{6}$$

In the RPA approximation[24], χ is related to the non-interacting response function $\chi^{(0)}(12) = G(12)G(21^+)$, through the Dyson-like equation:

$$\chi(12) = \chi^{(0)}(12) + \int d(34) \chi^{(0)}(13) \frac{1}{|\mathbf{r}_3 - \mathbf{r}_4|} \chi(42) \tag{7}$$

Another common approximation for the screened interaction is the plasmon pole approximation (PPA)[26, 24], in which it is assumed that the imaginary part of W is characterized by a strong peak corresponding to a plasmon excitation at the plasmon frequency; both methods (the GW-RealAxis and the GW-PPA schemes in the following), will be employed to evaluate the quasiparticle corrections to DFT energy gaps. The reader is referred to the recent literature for details on the calculation parameters [18]

Using the above obtained dynamically screened interaction, the macroscopic complex dielectric function that includes the excitonic effects is obtained by solving BSE in the electron-hole (e-h) space made of e-h pairs $|eh\rangle$ and antipairs $\overline{|he\rangle}$; its solution, in fact, can be mapped onto an eigenvalue problem for a two particle excitonic Hamiltonian[27, 28] of the form:

$$\mathcal{H}^{\text{exc}} = \begin{bmatrix} H^{\text{res}} & H^{\text{coupl}} \\ -(H^{\text{coupl}})^* & -(H^{\text{res}})^* \end{bmatrix} \tag{8}$$

where the resonant term $H^{\text{res}} = (E_e - E_h)\delta_{e,e'}\delta_{h,h'} + \langle eh|K|e'h'\rangle$ is Hermitian, the coupling part $H^{\text{coupl}} = \langle eh|K\overline{|h'e'\rangle}$ is symmetric, and $K = W - 2V$ is the excitonic kernel (the reader is referred to [28] for a detailed explanation of the block terms in $\mathcal{H}^{\text{exc}}$).

The macroscopic dielectric function $\epsilon_M(\omega)$ is calculated from the eigenvalues E_λ and the eigenstates $|\lambda\rangle$ of $\mathcal{H}^{\text{exc}}$ as:

$$\begin{aligned} \epsilon_M(\omega) &= 1 - \lim_{\mathbf{q}\to 0}\lim_{\eta\to 0^+} v_0(q) \sum_{\lambda\lambda'}\sum_{n_1 n_2} \langle n_1|e^{-i\mathbf{q}\cdot\mathbf{r}}|n_2\rangle \frac{A^{\lambda}_{n_1 n_2}}{\omega - E_\lambda + i\eta} \\ &\times S^{-1}_{\lambda\lambda'} \sum_{n_3 n_4} (f_{n_3} - f_{n_4}) \langle n_4|e^{i\mathbf{q}\cdot\mathbf{r}'}|n_3\rangle (A^{\lambda'}_{n_3 n_4})^* \end{aligned} \tag{9}$$

with $A^{\lambda}_{nn'} = \langle nn'|\lambda\rangle$, and $S_{\lambda\lambda'}$ is an overlap matrix of the generally non-orthogonal eigenstates of $\mathcal{H}^{\text{exc}}$.

Lastly we calculate the absorption spectra from the imaginary part of the system polarizability along the molecule axis (the transverse polarizability $\alpha_\perp$ figures out to be with respect to $\alpha_\parallel$) obtained through the Clausius-Mossotti relations[17]:

$$\alpha_\parallel = \frac{3\Omega}{4\pi}\frac{\epsilon_\parallel - 1}{\epsilon_\parallel + 2} \tag{10}$$

Dynamical effects in the excitonic hamiltonian have been neglected, since it has been shown[16] that they affect optical gaps of oligothiopehens by a small uniform reduction of 0.1 eV in the corresponding optical gaps. The absorption peak broadening and shape depends on the vibrational properties and has been calculated in the context of Density Functional Perturbation Theory. Indeed the FC effect can be calculated through the HR of method as [29]: the spectral function (SF) of the electron-local vibrations coupling is:

$$S(\hbar\omega) = \sum_\lambda S_\lambda \delta(\hbar\omega - \hbar\omega_\lambda) \tag{11}$$

The sum is over all the vibration modes λ of energy $\hbar\omega_\lambda$ and S_λ is the partial SF of the λ mode is defined as:

$$S_\lambda = \frac{\omega_\lambda q_\lambda^2}{2\hbar} \tag{12}$$

where

$$q_\lambda^2 = \sum_{\alpha i} m_\alpha^{1/2}(R_{I,\alpha i} - R_{N,\alpha i})\Delta r_{\lambda,\alpha i} \tag{13}$$

$m_{\alpha i}$ is the mass of the atom α, $i = , x, y, z$, $R_{[N,I]\alpha i}$ are the equilibrium positions of the atoms in the neutral [N] and the ionized [I] configurations, $\Delta r_{\lambda,\alpha i}$ is a normalized vector (expressed in mass

reduced coordinates) representing the atomic displacements of the atom α along the i direction of the λ mode. It can be shown [30] that the absorption peak is obtained from the quasi-particle excitation energy spectrum convoluted with the function $A(\hbar\omega)$:

$$A(\hbar\omega) = \frac{S^n}{\Gamma(n+1)}\delta(\hbar\omega - n\hbar\bar{\omega}) \quad n = 0, 1, \ldots \tag{14}$$

with $\bar{\omega} = \frac{1}{S}\sum_\lambda \omega_\lambda S_\lambda$.

3 Results

The ground state configurations of BT2Na and BT2N, the last one either isolated or π stacked are shown in Fig 1. Some important structural data including bond lengths and angles are reported in Table 1 were some differences between BT2N and BT2Na are found in the thiophene groups. The corresponding

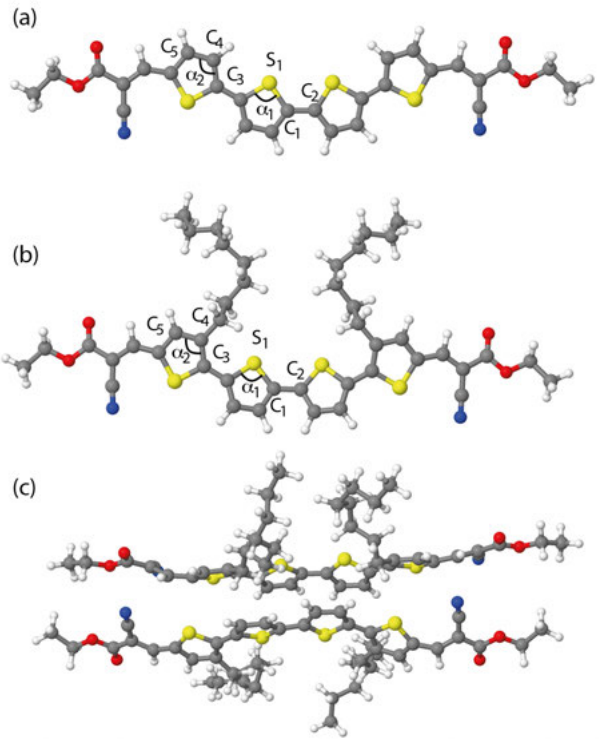

Figure 1: (Color online) Different ground state configurations isolated BT2Na (a) and BT2N (b) and π-stacked BT2N (c) molecules.

band gap data reported in Table 2. Isolated BT2N and BT2Na show the same band gap value obtained at the DFT-PBE theory level. Indeed it has been shown that the HOMO and LUMO orbitals in isolated BT2N are spread along the molecule axis but do not affect the aliphatic chains that have been removed in the case of BT2Na [18].

The BT2N/BT2Na chemical structures suggests a typical acceptor-donor-acceptor (A-D-A) configuration; such an A-D-A character emerges from the orbital localization, even though it is not marked probably because of the reduced length size of the molecule; indeed previous studies [18] have shown

Table 1: Some relevant structural data of isolated BT2N, BT2Na and the BT2Na excited configurations.Bond lengths are in nm

Molecule	C_1-C_2	C_1-S_1	C_2-S_1	C_3-C_4	C_3-C_4	$\hat{\alpha_1}$	$\hat{\alpha_2}$
BT2N	0.145	0.171	0.177	0.141	0114	92.5	111.1
BT2Na	0.144	0.174	0.175	0.14	0.1139	93.2	113.4
BT2Na-exc	0.141	0.176	0.176	0.142	0.1138	92.9	114.3

Table 2: DFT-PBE band gap energies of BT2N (π-stacked BT2N molecules in parenthesis) and BT2Na molecules. Experimental values for BT2N molecules are taken from the literature [18]

Molecule	DFT-PBE	Exp.	Chemical formula
BT2N	1.39 (1.30)	2.02	$C_{44}H_{52}N_2O_4S_4$
BT2Na	1.389	-	$C_{28}H_{20}N_2O_4S_4$

that the HOMO is only partially localized on the electron-donating unit (i.e. the two central thiophene units) and the HOMO state is almost equally spread between the electron accepting and donating parts of the molecule while the LUMO is preferentially located at the acceptor ends of the molecule.

As expected, the HOMO-LUMO gap is largely underestimated (being nearly of 1.39 eV for both the isolated molecules) at the DFT-PBE level with respect to the experimental value obtained for BT2N by CV (see Table 2) [18].

The correct theoretical band gap are obtained from quasi-particle band gaps, calculated by GW (with either GW-RealAxis or GW-PPA approximation) and are reported in Table 3. We see that BT2Na has a slightly larger theoretical QP band-gap that the BT2N molecule. Previous studies have demonstrated that GW quasi-particle band gaps, that are theoretically correct, severely overestimate the experimental absorption peak of BT2N, that is a clear sign of excitonic behaviour of the absorbance phenomenon. Therefore the absorption peak has been calculated by solving the BSE starting from both GW-PPA and

Table 3: Band Gaps (in eV) for the BT2N structures studied obtained with three different computational schemes.

Structure	GW-RealAxis	GW-PPA	Δ-SCF
BT2N	3.84	3.93	3.89
BT2Na	-	4.04	-
BT2Nx2	3.52	3.60	3.33

GW-RealAxis energy levels; concerning isolated BT2N, we know that the absorption peak calculated from BSE starting from the GW-PPA is red-shifted from the experimental absorption peak by nearly $\Delta\lambda \sim 50$ nm while the situation is worse in the case of the BSE absorption peak obtained from the GW-RealAxis QP energy levels that are red-shifted by $\Delta\lambda \sim 100$ nm. Indeed, the calculated values of the QP electronic gap (3.93 eV and 3.84 eV for GW-PPA and GW-RealAxis respectively) are much larger than the optical band gap obtained from the optical spectrum, it is clear that the calculated optical spectrum reflects the existence of strong excitonic transitions, with high excitonic binding energy (1.92 eV and 1.96 eV for GW-PPA+BSE and GW-RealAxis+BSE, respectively) that is found to be entirely associated to single particle $\pi \rightarrow \pi^*$ transition from the HOMO to the LUMO levels.

The difference of the calculated absorption peak with respect to the experimental one has been attributed to the π stacking arrangement of the molecules [18]. Indeed the experimental peak energy

is fully recovered by considering the absorption in π stacked molecules where the GW corrections to DFT-PBE energies, with both GW-RealAxis and GW-PPA schemes, result in a gap opening ($\varepsilon_{gap}^{\mathrm{QP}}$ =3.6 eV for GW-RealAxis and 3.5 eV for GW-PPA). The experimental absorption main peak is, indeed, obtained by solving the BSE using the GW-RealAxis approximation of the GW QP levels thus showing the fundamental importance of the local molecular ordering. This order, indeed, affects the main HOMO-LUMO transition because it has been demonstrated that the two molecular orbitals involved reside onto adjacent molecules thus involving a charge transfer. Moreover also other transitions contribute to the absorption peak lying on the two adjacent BT2N molecules.

The above discussed data concerns only the absorption peaks and do not account for the peak shape and broadening that is due to the FC effect depending on the vibrational modes of the molecules. The peak broadening has been calculated using the approximate HR formula Eq. 14 and the local vibrational spectra have been calculated with reference to the modified BT2Na molecule, i.e. the simplified version of the BT2N molecule obtained by removing the aliphatic chain. This choice is basically justified by the fundamental argument that the MO involved in the absorption are, in all the cases treated, even in the case of the π stacked geometry, located along the tiophene chain and do not affect significantly the aliphatic chains. Of course the vibrational spectra of the molecules might be affected by the aliphatic chains vibrations also but, due to the strong bonding of the central thiophenes, we are confident that the local vibrational spectra should be only slightly affected by the aliphatic chains. As mentioned in the section 2, the molecular configuration of the excited state has been obtained by an occupation constrained optimization of the BT2Na molecule. Indeed it has been demonstrated that, while this method is rigorously wrong from a theoretical point of view, the atomistic configuration of the pseudo-excited state obtained with a constrained occupation with both the HOMO and the LUMO occupied by one electron is rather close to the one of the real excited state if this excited state is characterized by a single, well defined transition, that is exactly the present case for isolated BT2N and BT2Na molecules [16]. Of course this is not the case for the π-stacked BT2N configuration that just means that the atomic configuration of the excited state, needed to calculate the HR SF, in this case cannot be obtained with the same method. The structural data of the excited BT2Na molecule are reported in Table 1 and show that the central C_1-C_2 bond is shortened, while the two central thiophenes are elongated with respect to the ground state configurations. The local vibrational spectrum, needed in the HR formula, is calculated in the context of the DFPT and the partial HR factors are calculated from Eq. 12. Both of them are reported in Fig. 2 and show that there are two main modes involved in the peak broadening located at 780 THz and 1410 THz with partial HR factors of $S_\lambda \approx 0.23$ and $S_\lambda \approx 0.22$ respectively. Moreover there are also other, less important, modes at 120, 550 and 580 THz with partial HR factors of $S_\lambda \approx 0.13$ and $S_\lambda \approx 0.1$.

The whole HR factors is $S \approx 1.15$ indicating that, in average, one vibrational mode affect the peak broadening. The HR broadened absorptions spectra of isolated BT2N and BT2Na molecules are reported in Fig. 3. The absorption spectra, that have been normalized to their maxima, show that, at the GW-PPA+BSE level of theory, the two molecules BT2N and BT2Na have the same absorption peak calculated starting from the PPA of the GW QP energy. The BT2N and the BT2Na have rather close values of the HR broadening also. In the seme figure is reported the absorption peak of the isolated BT2N molecule calculated using the RealAxis approximation of the GW QP energy. The full width at half maximum (FWHM) measured for BT2N in both the employed approximations is $\Delta E_{FWHM} \approx 0.40eV$ while for BT2Na is nearly $100meV$ smaller mainly because in this case we have not employed an artificial broadening that simulates the collision and rotation effects.

The HR factor causes a small shift of the absorption peak maximum to larger energy so that $\alpha_{max} \approx 2.13eV$ instead of the nominal $\alpha_{max} \approx 2.05eV$ of the peak position obtained from the GW-PPA+BSE

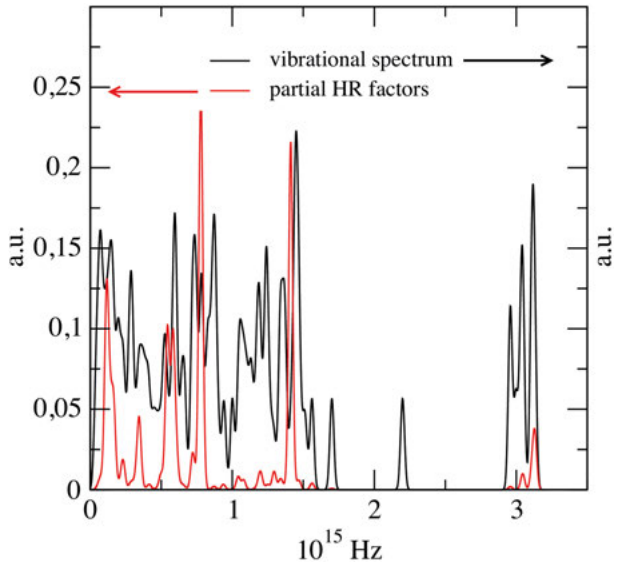

Figure 2: (Color Online) Local vibrational spectrum of the BT2Na molecule calculated by DFPT and the partial HR factors.

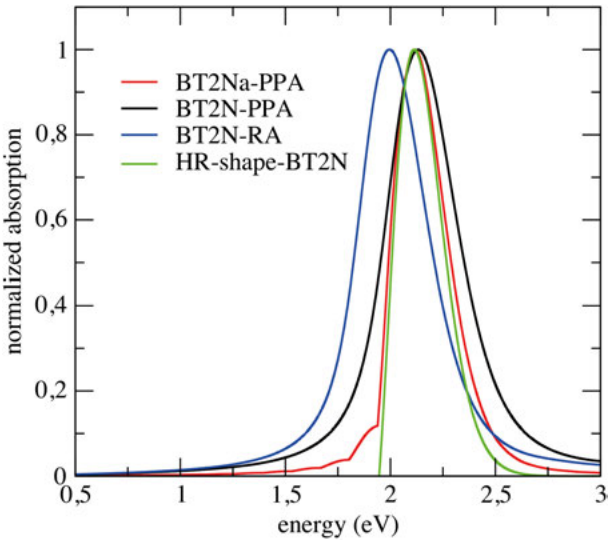

Figure 3: (Color online) Normalized absorption of light polarized parallel to the main axis of the molecule for spectra for BT2N and BT2Na isolated molecules. In the same figure the HR broadening and peak shape is reported calculated for an ideal absorption with one peak with zero standard deviation at $E = 2.05eV$.

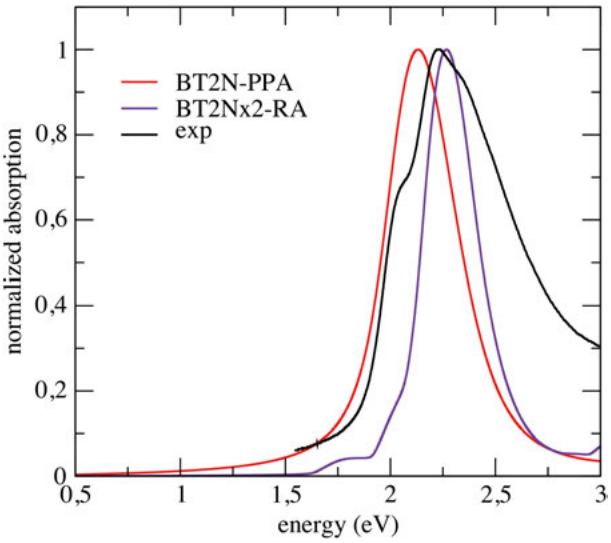

Figure 4: (Color online) Normalized absorption of light polarized parallel to the main axis of the molecule for spectra for BT2N and two π-conjugated molecules compared to the experimental absorption peak [18].

level of the theory. Nevertheless we see from Fig. 4 that this shift is not sufficient to fully recover the experimental absorption peak position already reported in the literature. The same HR factor is, then, applied to the absorption peak obtained in the case of two π-stacked BT2N molecules that, as reported in the recent literature, show the existence of two, very close peaks exactly at the experimental absorption peak and an additional one at $E \approx 2eV$. The absorption peak obtained from the calculated HR factor, again shown in Fig. 4 has the correct position but its width is severely underestimated with a FWHM of $\Delta E \approx 260meV$ instead of the experimental $\Delta E \approx 650meV$. We see, however that a superposition of the two peaks accounts for the main peak position and its largest satellite and that the sum of the two peak widths is consistent with the experimental measured absorpion peak width. Therefore it is likely that the experimental absorption spectrum features, namely the main peak position, additional satellites, the peak broadening and shape, could be explained through an appropriate superposition of the absorption characteristics of both the isolated and the π-stacked BT2N molecules.

4 Conclusions

In summary we have calculated in the context of the MBPT, using the GW approximation and the BSE for the excitonic Hamiltonian, the absorption spectra of two different systems made either of one isolated BT2N or BT2Na molecule or two π conjugated BT2N molecules evidencing the the excitonic nature of the measured absorption onset and main peak. Moreover we have calculated the FC broadening of the absorption peak on the basis of the HR formula. The absorption peaks of the isolated BT2N and BT2Na molecules are quite similar thus enforcing the idea that, in spite of the slight differences found for the ground sate configurations of theses two molecules, the absorption phenomena is entirely confined in the main molecular axis with thiophene groups. The theoretical absorption spectrum of BT2N and BT2Na have been discussed and, by including an artificial broadening that accounts for the molecular rotation and collisions, the simplified HR factor accounts for a peak broadening of nearly

$\Delta E_{FWHM} \approx 400meV$ that is still unfit to explain the broadening and the shape of the experimental results. However the HR factor broadening causes a shift of the single molecule absorption peak to higher energy by nearly $\Delta E_{shift} \approx 80meV$. In previous articles it has been shown that π conjugated geometry of BT2N molecules should be considered in order to recover the absorption energy of the main peak showing that inter-molecular transitions are needed to recover the peak position. However, playing with shape and broadening caused by the FC effect, a strong indication is obtained that the peak shape and broadening could be explained invoking both inter-molecular and intra-molecular transitions of both isolated and π-conjugated molecules. Further studies are in course to better clarify this aspect.

Acknowledgements

Computational resources have been provided by CRESCO/ENEAGRID High Performance Computing infrastructure and its staff [31]. CRESCO/ENEAGRID High Performance Computing infrastructure is funded by ENEA, the Italian National Agency for New Technologies, Energy and Sustainable Economic Development and by Italian and European research programmes, see http://www.cresco.enea.it/english for information.

References

[1] L. Dou, J. You, Z. Hong, Z. Xu, G. Li, R.A. Street, and Y. Yang. 25th anniversary article: A decade of organic/polymeric photovoltaic research. *Adv. Mater.*, 25:6642–6671, 2013.

[2] A.J. Heeger. 25th anniversary article: Bulk heterojunction solar cells: Understanding the mechanism of operation. *Adv. Mater*, 26:10–28, 2014.

[3] C.W.Tang. Two-layer organic photovoltaic cell. *Appl. Phys. Lett.*, 48(2):183–185, 1986.

[4] J.-L-Brédas, J.E. Norton, J. Cornil, and V. Coropceanu. Molecular understanding of organic solar cells: The challenges. *Acc. Chem. Res.*, 42(11):1691–1699, 2009.

[5] Y. Liu, C-C. Chen, Z. Hong, J. Gao, Y.(M.) Yang, H. Zhou, L. Douand G. Li, and Y. Yang. Solution-processed small-molecule solar cell: breaking th 10x7/power conversion efficiency. *Sci. Rep.*, 3356:3, 2013.

[6] B. Kan, Q. Zhang, M. Li, X. Wan, W. Ni, G. Long, Y. Wang, X. Yang, H. Feng, and Y. Chen. Solution-processed organic solar cells based on dialkylthiol-substituted benzodithiophene unit with efficency near 10/*J. Am. Chem. Soc.*, 136:15529–15532, 2014.

[7] Q. Zhang, B. Kan, F. Liu, G. Long, X. Wan, X. Chen, Y. Zuo, W. Ni, H. Zhang, M. Li, Z. Hu, F. Huang, Y. Cao, Z. Liang, M. Zhang, T. P. Russel, and Y. Chen. Small-molecule solar cells with efficency over 9%. *Nature Photonics*, 9:35–41, 2015.

[8] B. Kan, M. Li, Q. Zhang, F. Liu, X. Wan, Y. Wang, W. Ni, G. Long, X. Yang, H. Feng, Y. Zuo, M. Zhang, F. Huang, Y. Cao, T. P. Russel, and Y. Chen. A series of simple oligomer-like small molecules based on oligothiophenes for solution-processed solar cells with high efficiency. *J. Am. Chem. Soc.*, 137:3886–3893, 2015.

[9] H. Bai, Y. Wang, P. Cheng, Y. Li, D. Zhu, and X. Zhan. Acceptordonoracceptor small molecules based on indacenodithiophene for efficient organic solar cells. *ACS Appl. Mater. Interfaces*,

6(11):8426–8433, 2014.

[10] Y.Sun ad G.C. Welch, W.L. Lin Leong, C.J. Takacs, and G.C. Bazan. Solution-rocessed small-molecule solar cells with 6.7% efficiency. *Nature Materials*, 11:44–48, 2012.

[11] D. Patra, T.-Y. Huang, C.-C. Chiang, R.O.V. Maturana, C.-W. Pao, K.-C. Ho, K.-H. Wei, and C.-W. Chu. 2-alkyl-5-thienyl-substituted benzo[1,2-b:4,5-b']dithiophene-based donor molecules for solution-processed organic solar cells. *ACS Appl. Mater. Interfaces*, 5:9494–9500, 2013.

[12] L. Hedin. New method for calculating the one-particle green's function with application to the electron-gas problem. *Phys. Rev.*, 139:A796–A823, 1965.

[13] Cudazzo P., M. Gatti, and A. Rubio. Excitons in molecular crystals from first-principles many-body perturbation theory: Picene versus pentacene. *Phys. Rev. B*, 86:195307, 2012.

[14] S. Sharifzadeh, A. Biller, L. Kronik, and J. B. Neaton. Quasiparticle and optical spectroscopy of the organic semiconductors pentacene and ptcda from first principles. *Phys. Rev. B*, 85:125307–1/125307–11, 2012.

[15] M. Palummo, C. Hogan, F. Sottile, P. Bagalá, and A. Rubio. Ab initio electronic and optical spectra of free-bas porphyrins: The role of electronic correlation. *J. Chem. Phys.*, 131:084102, 2009.

[16] B. Baumeier, D. Andrienko, Y. Ma, and M. Rohlfing. Excited states if dicyanovinyl-substituted oligothiophenes from many-body greenś functions theory. *J. Chem. Theory Comput.*, 8:997–1002, 2012.

[17] C. Hogan, M. Palummo, J. Gierschner, and A. Rubio. Correlation effects in the optical spectra of porphyrin oligomer chains: Exciton confinement and length dependence. *J. Chem. Phys.*, 138:024312–1/024312–12, 2013.

[18] F. Gala, L. Mattiello, F. Brunetti, and G. Zollo. *J. Chem. Phys.*, 144:084310, 2016.

[19] P. Hohenberg and W. Kohn. Inhomogeneous electron gas. *Phys. Rev.*, 136:B864–B871, Nov 1964.

[20] W. Kohn and L. J. Sham. Self-consistent equations including exchange and correlation effects. *Phys. Rev.*, 140:A1133–A1138, Nov 1965.

[21] J.P. Perdew, K. Burke, and M.Ernzerhof. Generalized gradient approximation made simple. *Phys. Rev. Lett.*, 77(4):3865–3868, 1996.

[22] S. Grimme. Semiempirical gga-type density functional constructed with a long-range dispersion correction. *J. Comput. Chem.*, 27(15):1787–99, 2006.

[23] R. M. Martin. *Electronic Structure: Basic Theory and Practical Methods*. Cambridge University Press, 2008.

[24] A. Marini, C. Hogan, M. Grüning, and D. Varsano. *Comput. Phys. Comm.*, 180:1392–1403, 2009.

[25] L. Hedin and S. Lundqvist. *Solid State Physics: Advances in Research and Application*. Academic Press: New York, San Francisco, London, 1969.

[26] F. Aryasetiawan and O. Gunnarsson. The gw method. *Rep. Prog. Phys.*, 61:237–312, 1998.

[27] M. Rohlfing and S. G. Louie. Electron-hole excitations and optical spectra from first principles.

Phys. Rev. B, 62(8):4927–4943, 2000.

[28] G. Onida, L. Reining, and A. Rubio. *Rev. Mod. Phys.*, 74:601–659, 2002.

[29] K. Huang and A. Rhys. *Proc. Roy. Soc.*, 204:407, 1970.

[30] A. Gali, T. Demián, M. Vörös, G. Thiering, E. Cannuccia, and A. Marini. *Nat. Comm.*, 7:11327, 2016.

[31] G. Ponti, F. Palombi, D. Abate, F. Ambrosino, G. Aprea, T. Bastianelli, F. Beone, R. Bertini, G. Bracco, M. Caporicci, B. Calosso, M. Chinnici, A. Colavincenzo, A. Cucurullo, P. dAngelo, M. De Rosa, P. De Michele, A. Funel, G. Furini, D. Giammattei, S. Giusepponi, R. Guadagni, G. Guarnieri, A. Italiano, S. Magagnino, A. Mariano, G. Mencuccini, C. Mercuri, S. Migliori, P. Ornelli, S. Pecoraro, A. Perozziello, S. Pierattini, S. Podda, F. Poggi, A. Quintiliani, A. Rocchi, C. Scio, F. Simoni, and A. Vita. The role of medium size facilities in the hpc ecosystem: the case of the new cresco4 cluster integrated in the eneagrid infrastructure. *IEEE HPCS*, 6903807:1030–1033, 2014.

COEVOLUTIONARY DYNAMICS OF ROCK-PAPER-SCISSORS GAMES WITH THREE-AGENT INTERACTIONS

Filippo Palombi[1]*, Stefano Ferriani[2] and Simona Toti[3]

[1]*ENEA, Via E. Fermi 45, 00044 Frascati (IT)*

[2]*ENEA, Via Martiri di Monte Sole, 4, 40129 Bologna (IT)*

[3]*ISTAT, Via C. Balbo 16, 00184 Roma (IT)*

ABSTRACT. The origin of biodiversity, intended as the amount of genes expressed in a given eco-system, is a major issue among biologists and ecologists. Over the past twenty years experimental as well as theoretical evidence has been established to support the idea that cyclic dominance is a viable mechanism of maintenance of biodiversity. Cyclic dominance is to be understood as a non-hierarchical set of interactions controlling a group of species, according to which each species dominates and is dominated by another one, resulting in a circular dominance chain. In the simplest case one has three species behaving like children playing rock-paper-scissors (RPS). We studied an agent-based model with coevolutionary RPS dynamics ruled by three-agent interactions.

1 Introduction

The huge biological diversity present on Earth is one the most fascinating things we all experience in our own lives. What determines the diversity of species in Nature is still a matter of scientific investigation. Classical mathematical models of predator-prey dynamics predict that a dominating species in an eco-system survives by consuming the weaker ones, the result being that all species go extinct by lack of food in the long run.

A possible way out is to postulate the existence of non-hierarchical food-chains, where no species is placed on top or at the bottom. In this assumption each species is thought of as dominating and being dominated by another species, thus resulting in an overall closed chain. Is this weird idea also unrealistic? Not at all! As an example, cyclic dominance is observed in communities of E. coli bacteria, where three strains, namely a colicin-producing one (P), a colicin-resistant one (R) and a colicin-sensitive one (S) play a survival game closely resembling rock-paper-scissors (RPS), the famous children's game. The colicin-producing strain produces both colicin and its antidote and so it has the lowest reproduction rate among the three strains. The colicin-resistant strain produces only the antidote to colicin, hence it has more resources to reproduce. Finally, the colicin-sensitive strain does not produce neither colicin nor its antidote, therefore all its resources can be used for reproduction. When P proliferates, S goes close to extinction. At that point R can expand thus subtracting resources to P. When R takes full dominance, S can expand in turn thus subtracting resources to R. Finally, when S proliferates, it paves the way for the return of P.

*Corresponding author. E-mail: `filippo.palombi@enea.it`.

outcome	payoffs
RRR, PPP, SSS	all players receive 0 points
RRP, PPS, SSR	the dominant player receives 1 point
RRS, PPR, SSP	each dominant player receives 1/2 point
RPS	all players receive 0 points

Table 1: Payoff table.

RPS games have been extensively studied in the scientific literature as agent-based models in coevolutionary game theory. It has been shown that cyclic-dominance relations in a population of agents allow for biodiversity preservation, provided agents are spatially displaced and motile. Biodiversity is then realized in the form of fascinating spatial patterns, such as spiral waves where each species is hunted by its predator species, while hunting in turn its prey species along the arms of a spiral.

2 A model with three-agent interactions

In almost all models studied in literature, interactions involve two agents, respectively a predator and a prey. Yet, it is both clear and known the importance of studying group predation. The latter can be modeled as a multi-agent interaction, in which several agents partake as predators or preys. We can figure out a situation where either several predators hunt an isolated prey or a single predator approaches a group of preys. In the minimal case one would consider interactions involving three agents, meaning two predators vs. one prey or one predator vs. two preys. In the language of classical game theory, this would correspond to a variant of the standard game with three children playing according to the following rules. On each round all children deliver simultaneously one of the usual hand signals representing respectively rock (**R**), paper (**P**) and scissors (**S**). Payoffs are assigned to the players round by round, based on the dominance relation R $\prec$ P $\prec$ S $\prec$ R (read "$\prec$" as "beaten by") and the specific combination of signals being realized, as reported in Table 1.

In the language of coevolutionary game theory, we assume a population of $N \gg 1$ agents, each adopting one of the competing strategies R, P or S. We let the relative abundances of the strategies, respectively denoted by r, p and s in the sequel and subject to the constraint $r + p + s = 1$, vary in time due to microscopic interactions inspired by Table 1. Specifically, in place of payoffs we consider stochastic transitions mediated by a dominance-replacement mechanism, namely

$$\begin{array}{lcll} \text{RRP} & \to & \text{RPP} & \text{occurring with rate} \quad d_{\text{RRP}}\,, \\ \text{PPS} & \to & \text{PSS} & \text{"} \qquad\quad d_{\text{PPS}}\,, \\ \text{SSR} & \to & \text{SRR} & \text{"} \qquad\quad d_{\text{SSR}}\,, \\ \text{RRS} & \to & \text{RRR} & \text{"} \qquad\quad d_{\text{RRS}}\,, \\ \text{PPR} & \to & \text{PPP} & \text{"} \qquad\quad d_{\text{PPR}}\,, \\ \text{SSP} & \to & \text{SSS} & \text{"} \qquad\quad d_{\text{SSP}}\,, \end{array} \tag{1}$$

with rates (transition probabilities per unit time) depending on the interacting strategies. We leave out transitions where all involved agents adopt the same strategy before they interact and we also leave out possible transitions where they initially adopt three different strategies. Rate equations including all

contributions from eqs. (1) read

$$\begin{aligned}
\dot{r} &= r^2\left(d_{\mathrm{RRS}}s - d_{\mathrm{RRP}}p\right) + r\left(d_{\mathrm{SSR}}s^2 - d_{\mathrm{PPR}}p^2\right)\,,\\
\dot{p} &= p^2\left(d_{\mathrm{PPR}}r - d_{\mathrm{PPS}}s\right) + p\left(d_{\mathrm{RRP}}r^2 - d_{\mathrm{SSP}}s^2\right)\,,\\
\dot{s} &= s^2\left(d_{\mathrm{SSP}}p - d_{\mathrm{SSR}}r\right) + s\left(d_{\mathrm{PPS}}p^2 - d_{\mathrm{RRS}}r^2\right)\,.
\end{aligned} \tag{2}$$

Altogether, these cubic equations depend on 6 parameters. One of the them can be absorbed into a redefinition of time, thus yielding 5 effective parameters. Moreover, the equation for $\dot{s}$ can be dropped provided we insert $s = 1 - r - p$ into those for $\dot{r}$ and $\dot{p}$. Eqs. (2) describe correctly the evolutionary dynamics induced by eqs. (1) in the mean field approximation as $N \to \infty$. They define mathematically a cyclic Lotka-Volterra model [**?**, **?**, **?**, **?**, **?**, **?**, **?**, **?**] encompassing three-agent interactions.

3 Degenerate Hopf bifurcation

We notice that in a reaction such as RRS $\to$ RRR, the species R is dominant in the initial state and even more dominant in the final one. Therefore this reaction (and similarly those obtained by cyclically rotating the species) tends to polarize the system in favor of the currently dominant species. By contrast, in a reaction such as RRP $\to$ RPP, the species R is dominant in the initial state but inferior in the final one. Therefore this reaction (and similarly those obtained by cyclically rotating the species) tends to equilibrate the system in favor of a currently inferior species. We conclude that the system is driven by two opposing forces. To study eqs. (2), we consider a symmetric case, where we let

$$d_{\mathrm{RRP}} = d_{\mathrm{PPS}} = d_{\mathrm{SSR}} = d_{\mathrm{e}} = 1\,. \qquad\qquad d_{\mathrm{RRS}} = d_{\mathrm{PPR}} = d_{\mathrm{SSP}} = d_{\mathrm{p}} = 1 + \epsilon\,, \tag{3}$$

with ϵ being a positive or negative parameter. Accordingly, polarizing and equilibrating forces are neutral with respect to the species. Eqs. (2) have four fixed points,

$$(r_*, p_*) = (1, 0)\,, \quad (r_*, p_*) = (0, 1)\,, \quad (r, p_*) = (0, 0)\,, \tag{4}$$

$$(r_*, p_*) = (1/3, 1/3)\,, \tag{5}$$

independently of ϵ. The first three ones are absorbing points, for which the dynamics stops. The fourth one is a reactive fixed point. We can show that eqs. (2) undergo a Hopf bifurcation around the latter point for $\epsilon = 0$. To this aim, we let $r = x_r + 1/3$ and $p = x_p + 1/3$. Upon expanding the eqs. (2) in Taylor series to first order around the stationary point $(x_r, x_p) = (0, 0)$, we get

$$\begin{aligned}
\dot{x}_r &= -\frac{1}{3}x_r - \frac{2+\epsilon}{3}x_p\\
\dot{x}_p &= \quad \frac{1+\epsilon}{3}x_p + \frac{2+\epsilon}{3}x_r
\end{aligned} \tag{6}$$

i.e.

$$\dot{x} = \begin{bmatrix} \dot{x}_r \\ \dot{x}_p \end{bmatrix} = \frac{1}{3}\begin{bmatrix} -1 & -(2+\epsilon) \\ (2+\epsilon) & (1+\epsilon) \end{bmatrix} \cdot \begin{bmatrix} x_r \\ x_p \end{bmatrix} \equiv J \cdot x\,. \tag{7}$$

The eigenvalues of the Jacobian matrix J are given by

$$\lambda = \frac{\epsilon}{6} + \frac{\mathrm{i}}{2\sqrt{3}}(2+\epsilon)\,, \tag{8}$$

$$\bar{\lambda} = \frac{\epsilon}{6} - \frac{\mathrm{i}}{2\sqrt{3}}(2+\epsilon)\,. \tag{9}$$

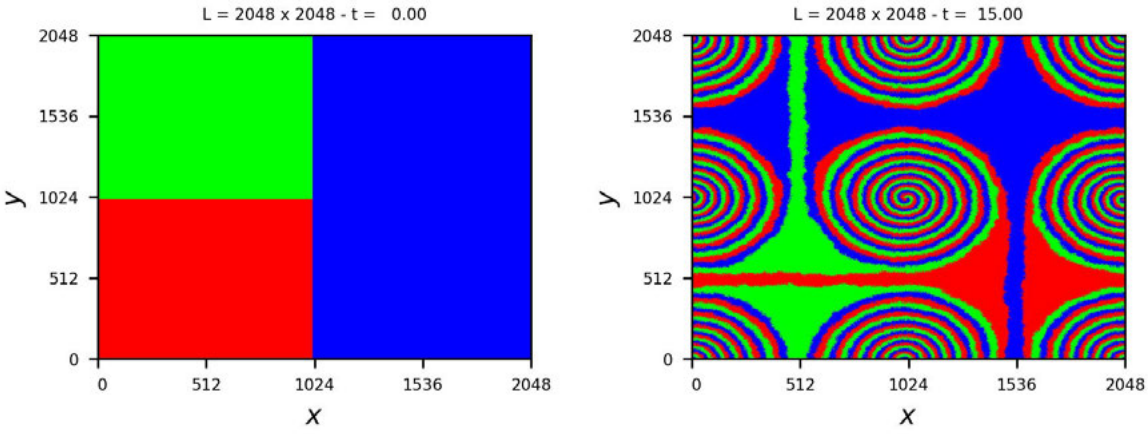

Figure 1: Results of a numerical simulation of the system via the Gillespie algorithm at simulation times $t = 0$ (left) and $t = 15.0$ (right) for $L_1 = L_2 = 2048$, $M = 20$, $\gamma = 64$, $\epsilon = 29.56$

For $\epsilon = 0$ we have $\mathrm{Re}\{\lambda\} = 0$. According to the Hartman-Grobman theorem, the linear stability analysis is not predictive for $\epsilon = 0$, hence we have to keep all terms (in principle we have to expand the system in Taylor series around $(x_r, x_p) = (0, 0)$ to third order, in practice the full system is already a polynomial with third degree) and bring it to Hopf normal form. The latter amounts to a single complex equation

$$\dot{z} = \lambda z - c(\epsilon)\lambda|\lambda|^2\,, \tag{10}$$

with

$$c(\epsilon) = a(\epsilon) + \mathrm{i}b(\epsilon)\,, \quad a(\epsilon) = \frac{3}{2}\frac{4\epsilon^2 + 15\epsilon + 15}{7\epsilon^2 + 27\epsilon + 27}\epsilon\,, \quad b(\epsilon) = \frac{9\sqrt{3}}{4}\frac{(\epsilon+2)(\epsilon^2+3\epsilon+3)}{7\epsilon^2+27\epsilon+27}\,. \tag{11}$$

Since $a(\epsilon)$ vanishes for $\epsilon \to 0$, the bifurcation for $\epsilon = 0$ is neither super- nor sub-critical. In fact it is a degenerate Hopf bifurcation. The system features no limit cycle. Nevertheless, the bifurcation is responsible for the formation of spiralling waves in presence of agent mobility.

4 Numerical simulations

Mobility is an extremely important feature to describe realistic systems. We assume that the agents are placed on a 2-dimensional lattice with size $N = L \times L$. They move via exchange reactions occurring at neighboring lattice points, namely

$$\mathrm{RP} \to \mathrm{PR}\,, \quad \mathrm{RS} \to \mathrm{SR}\,, \quad \text{with rate } \gamma\,, \tag{12}$$

$$\mathrm{PS} \to \mathrm{SP}\,, \quad \mathrm{PR} \to \mathrm{RP}\,, \quad \text{with rate } \gamma\,, \tag{13}$$

$$\mathrm{SR} \to \mathrm{RS}\,, \quad \mathrm{SP} \to \mathrm{PS}\,, \quad \text{with rate } \gamma\,. \tag{14}$$

Each lattice point is thought of as a patch hosting a number M of agents. Accordingly, we can define local densities $r(\mathbf{x}, t)$ and $p(\mathbf{x}, t)$, with $\mathbf{x} = (x_1, x_2)$ being a vector of lattice coordinates. Under this

assumption, the system is governed in the thermodynamic limit $N, M \to \infty$ by partial differential equations

$$\frac{\partial r}{\partial t} = D\nabla r + r^2 \left(d_{\mathrm{RRS}} s - d_{\mathrm{RRP}} p\right) + r\left(d_{\mathrm{SSR}} s^2 - d_{\mathrm{PPR}} p^2\right) , \tag{15}$$

$$\frac{\partial p}{\partial t} = D\nabla p + p^2 \left(d_{\mathrm{PPR}} r - d_{\mathrm{PPS}} s\right) + p\left(d_{\mathrm{RRP}} r^2 - d_{\mathrm{SSP}} s^2\right) , \tag{16}$$

with $D = \gamma/2N$. We can study the system by either solving the above equations numerically or by simulating a lattice of interacting agents. These two descriptions are similar in many respects. Yet, an important difference is that noise in numerical simulations can bring the system to one of the absorbing fixed points, thus destroying biodiversity. The algorithm to simulate the system is not a standard Monte Carlo. Systems with several reactions characterized by different rates can be simulated via a stochastic algorithm introduced by Gillespie many years ago in the context of Chemical Kinetics. We have produced a full implementation of the algorithm in C language. In Fig. 1, we report the spatial pattern obtained at simulation time $t = 15.0$ for $L_1 = L_2 = 2048$, $M = 20$, $\gamma = 64$, $\epsilon = 29.56$ with initial conditions

$$\begin{aligned}
&(r(\mathbf{x},0), p(\mathbf{x},0)) = (1,0) \text{ if } x_1 < L_1/2 \text{ and } x_2 < L_2/2\,,\\
&(r(\mathbf{x},0), p(\mathbf{x},0)) = (0,1) \text{ if } x_1 < L_1/2 \text{ and } x_2 \geq L_2/2\,,\\
&(r(\mathbf{x},0), p(\mathbf{x},0)) = (0,0) \text{ if } x_1 \geq L_1/2\,,
\end{aligned} \tag{17}$$

and periodic boundary conditions. We observe four single-armed spiral waves propagating across the lattice. It is possible to characterize analytically both the propagation speed, the angular velocity and the wavelength of the spirals. This goes beyond the aims of this report. It will be discussed in a forthcoming paper together a full analysis of the phenomenology of the spirals for a range of values of ϵ.

5 Conclusions

We have studied a variant of the cyclic Lotka-Volterra model with three-agent interactions. In particular, we have a full analytic description of the well-mixed system (mean-field theory) with a complete characterization of the degenerate Hopf bifurcation responsible for the spiralling patterns arising on a lattice. We also have extensive numerical results for the partial differential equations and for the agent-based simulations of the system in presence of agent spatial displacement and mobility. Results will be further detailed in a forthcoming paper.

References

[1] L. Frachebourg and P. L. Krapivsky. Fixation in a cyclic Lotka - Volterra model. *Journal of Physics A: Mathematical and General*, 31(15):L287, 1998.

[2] L. Frachebourg, P. L. Krapivsky, and E. Ben-Naim. Segregation in a One-Dimensional Model of Interacting Species. *Phys. Rev. Lett.*, 77:2125–2128, Sep 1996.

[3] L. Frachebourg, P. L. Krapivsky, and E. Ben-Naim. Spatial organization in cyclic Lotka-Volterra systems. *Phys. Rev. E*, 54:6186–6200, Dec 1996.

[4] A. Provata, G. Nicolis, and F. Baras. Oscillatory dynamics in low-dimensional supports: A lattice Lotka–Volterra model. *The Journal of Chemical Physics*, 110(17):8361–8368, 1999.

[5] T. Reichenbach, M. Mobilia, and E. Frey. Coexistence versus extinction in the stochastic cyclic Lotka-Volterra model. *Phys. Rev. E*, 74:051907, Nov 2006.

[6] G. Szabó and G. Arial Sznaider. Phase transition and selection in a four-species cyclic predator-prey model. *Phys. Rev. E*, 69:031911, Mar 2004.

[7] G. Szabó and T. Czárán. Phase transition in a spatial Lotka-Volterra model. *Phys. Rev. E*, 63:061904, May 2001.

[8] G. A. Tsekouras and A. Provata. Fractal properties of the lattice Lotka-Volterra model. *Phys. Rev. E*, 65:016204, Dec 2001.

CRESCO6: TECHNICAL SPECIFICATIONS AND BENCHMARKS

F. Ambrosino[1], G. Aprea[1], T. Bastianelli[1], I. Bellagamba[1], R. Bertini[1], G. Bracco[1], L. Bucci[1], F. Buonocore[1], M. Caporicci[1], M. Caiazzo[1], B. Calosso[1], M. Celino[1], M. Chinnici[1], A. Colavincenzo[1], A. Cucurullo[1], P. D'Angelo[1], D. De Chiara[1], M. De Rosa[1], D. Di Mattia[1], S. Ferriani[1], G. Ferro[1], C. Ferrelli[1], A. Funel[1], D. Giammattei[1], M. Galli[1], S. Giusepponi[1], G. Glorioso[1], R. Guadagni[1], G. Guarnieri[1], M. Gusso[1], F. Iannone[1]*, M. Marano[1], A. Mariano[1], G. Mencuccini[1], S. Migliori[1], M. Mongelli[1], P. Ornelli[1], S. Pagnutti[1], F. Palombi[1], S. Pecoraro[1], A. Perozziello[1], S. Pierattini[1], S. Podda[1], G. Ponti[1], A. Quintiliani[1], G. Santomauro[1], A. Scalise[1], F. Simoni[1], D. Visparelli[1].

[1]*ENEA- ICT Division, Piazzale E.Fermi, 80055, Portici (NA) , Italy*

ABSTRACT. A new cluster named CRESCO6 has been installed at the ENEA Research Center of Portici. The effort was made possible by the framework of the ENEA CINECA agreement signed in 2015. CRESCO6 has the objective to offer a computational resource of high-level to the scientific community and the world of production high-performance computing, by providing the user advanced systems of high-performance computing by providing the users with an advanced high-performance-computing system for modelling, integrated in a distributed architecture and accompanied by tools for advanced graphics. It supports multiple Research & Development activities (including those defining the institutional mission of the Agency), carried on in collaboration with national and international governmental institutions and with Italian private industrial partners. The new supercomputer refreshes the complex computational infrastructure of ENEA, granting a performance increase of a factor 5 compared with so-far-available resources. The technical specification and the benchmarks tests of CRESCO6 will be described in this paper.

1 Introduction

In 2015 ENEA and CINECA signed a strategic partnership agreement aimed at providing supercomputing and data storage services to EUROfusion, the European consortium for the Development of Fusion Energy. CINECA is currently the main supplier of HPC services in Italy. The agreement signed with ENEA aimed at promoting the joint devlopment of research activities in the field of HPC and was the basis for the purchase and installation of CRESCO6, a TIER1 cluster at the Portici ENEA Research Centre.
CRESCO6, a machine with a nominal power of about 0.7 Pflop/s succeeds CRESCO4 and CRESCO5, two older supercomputers already installed at the same centre and still operating, with a nominal computing power of 0.1 and 0.025 Pflop/s respectively. As such, CRESCO6 alone increases the total computing power currently available for research at ENEA by a factor of 7.

2 Technical specifications

CRESCO6 is a high performance computing system (HPC) consisting of 216 nodes for a total of 10,368 cores. Each node is equipped with:

- 2 Intel Xeon Platinum 8160 CPUs, each with 24 cores with a clock frequency of 2.1 GHz
- A RAM of 192 GB, corresponding to 4 GB/core
- A low-latency Intel Omni-Path 100 Series Single-port PCIe 3.0 x16 HFA network interface.

The nodes are interconnected by an Intel Omni-Path network with 15 switches of 48 ports each, bandwidth equal to 100 GB/s, latency equal to 100ns. The connections between the nodes have 2 tier 1:1 no-blocking tapered fat-tree topology (fig.1). The consumption of electrical power measured during the HPL tests amounts to 95 kW.

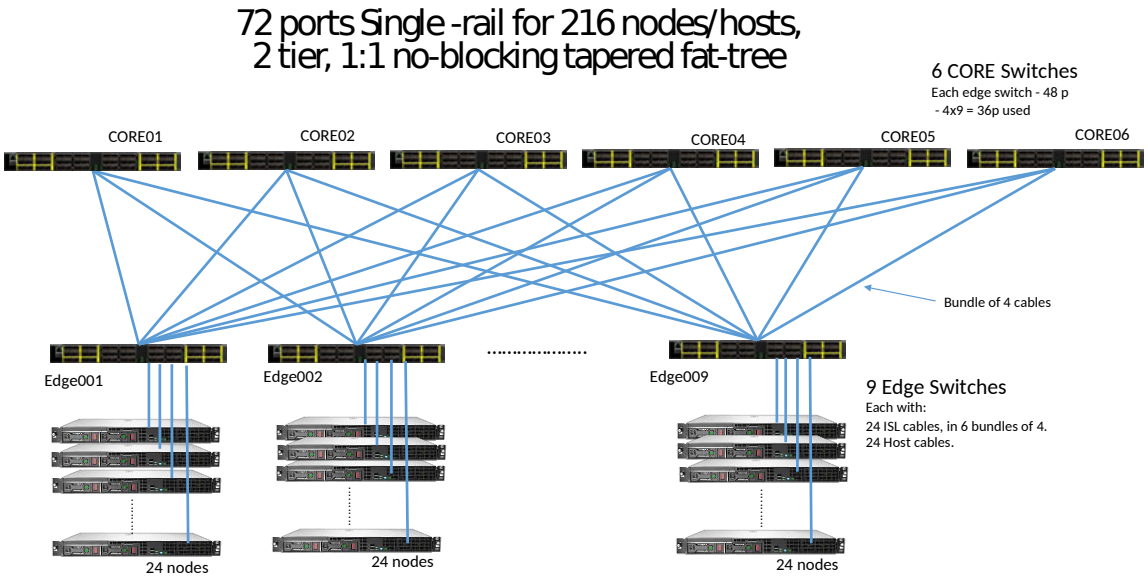

Fig.1: CRESCO6 Omni-Path network

3 OSU benchmarks on bandwidth and latency

Bandwidth tests were carried out by having the sender sending out a fixed number (equal to the window size) of back-to-back messages to the receiver and then waiting for a reply from the receiver. The receiver sends the reply only after receiving all these messages. This process is repeated for several iterations and the bandwidth is then calculated.

Latency tests are carried out in a ping-pong fashion. The sender sends a message with a certain data size to the receiver and waits for a reply from the receiver. The receiver receives the message from the sender and sends back a reply with the same data size. Many iterations of this ping-pong test are carried out and average one-way latency numbers are thus obtained. The benchmark test of bandwidth and latency are depicted in fig.2a/b

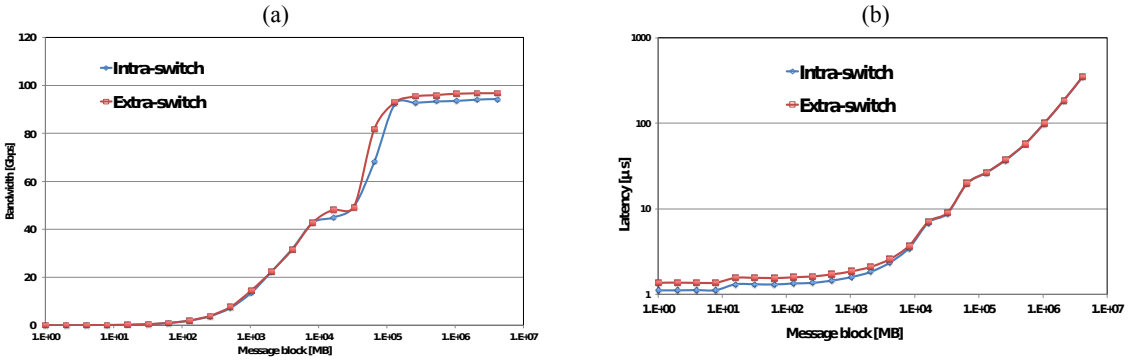

Fig.2:OSU Benchmark tests of Bandwidth (a) and latency (b)

4 HPL benchmark

HPL (High Performance Linkpack) solves a (random) dense linear system in double precision (64 bits) arithmetic on distributed memory computers.

The algorithm used by HPL can be summarized by the following keywords: Two-dimensional block-cyclic data distribution - Right-looking variant of the LU factorization with row partial pivoting featuring multiple look-ahead depths - Recursive panel factorization with pivot search and column broadcast combined - Various virtual panel broadcast topologies - bandwidth reducing swap-broadcast algorithm - backward substitution with look-ahead of depth 1.

The HPL was run on CRESCO6 and the MARCONI A3 systems. The MARCONI A3 system is the Tier-0 system, co-designed by CINECA. A Marconi A3 node is based on dual socket 24-cores Intel Xeon 8160 (SkyLake) at 2.10 GHz with Intel Omni-Path.

The graph below summarizes the performance as run on 1, 64, 128 and 216 nodes. The benchmark shows good performance around 63% efficiency and up to 434 Tflop/s for the CRESCO6 system on 216 nodes.

The benchmarks were made with the Intel/IntelMPI compiler v.18 and MKL library, 2 MPI processes per node (one for each socket). The CPU clock frequency was set on max performance. The benchmarks on MARCONI A3 were performed while the machine was in production mode (jobs were running on the other nodes). The results of the benchmark tests are depicted in fig.3.

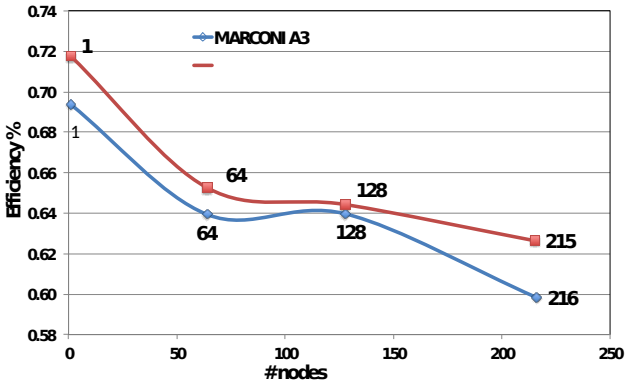

The *n-body* simulation integrates the Newton's equation by means the following numerical method.

$$\vec{r}_i(t+\Delta t)=\vec{r}_i(t)+\Delta t\cdot\frac{\vec{F}_i}{m_i}$$
$$\vec{r}_i(t+\Delta t)=\vec{r}_i(t)+\Delta t\cdot\vec{r}_i(t)$$

A case study of the n-body simulation is used to compare an hybrid MPI+OpenMP algorithm running on different HPC systems in operation at CINECA and on the new ENEA HPC system CRESCO6.

An hybrid master-only model is used with one MPI rank per node and OpenMP threads scattered on the cores of the node, with no MPI calls inside MP parallel regions.

It is the trend of the HPC systems is towards architectures with many cores integrated in a processor, composing a SMP compute node, sharing main memory and interconnected to other nodes by means a low latency network. That trend changed the parallel programming model over the years schematically shown in Fig.4.

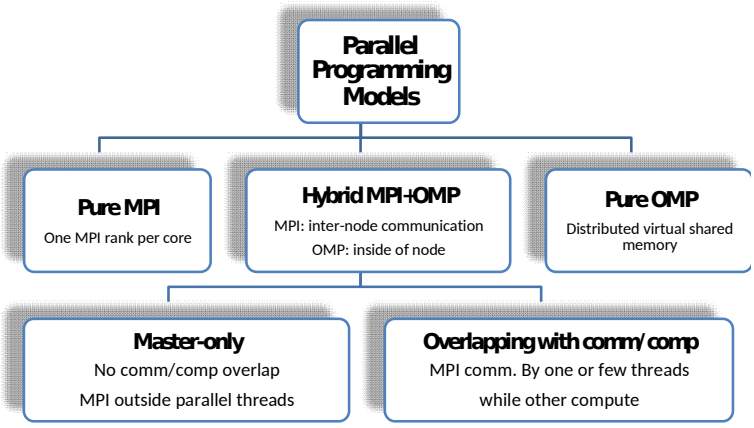

At beginning the parallel programming was based on pure MPI libraries in order to reach high scalability with the number of nodes. Instead OpenMP was easily deployed for parallel applications limited to a single node. Thanks to a multi-thread handling in a SMP node, hybrid parallel applications, using MPI and OpenMP (or others threading API) become more interesting for large HPC systems with the growing the number of cores. Each MPI process or ranks spawns several threads with #ranks×#threads = #logical processors, where logical processors can be the number of available cores or available core times the number of hyper-threading cores. Maximize the number of threads and minimizing the number of ranks will reduce the overhead communication that grows with the number of ranks. This overhead is due to the memory consumption of internal buffers and limited scaling potential of collective MPI functions. In order to avoid additional MPI communication within a node, the MPI+X (generally X = OpenMP) hybrid paradigm develops applications using OpenMP within the node and MPI communication among nodes having to share memory domains. The best performance of a hybrid applications can be achieved by allowing ranks and threads to get execute the core which is as close as to the memory domain requested. Thanks to cache-coherent NUMA, a core access its own memory domain faster than other domain within a multi-core node. Therefore additional environment variables control process pinning (affinity) for

hybrid MPI+OpenMP applications. These environment variables are used to define a number of domains of logical processors on a node and how MPI ranks are bounded to these domains with one MPI ranks per one domains. Each MPI rank can launch a number of children threads within the corresponding domain.

As the n-body PP method has a complexity of $O(n^2)$, tests were carried out getting the execution time for one time-step adopting two cases for the number of particles: 10^6, 10^7.

The following tables shown the results of the tests.

	BDW Intel E5-2697 v4 @2.3GHz 18 cores MARCONI A1		
N-body	8 nodes (sec.)	16 nodes (sec.)	32 nodes (sec.)
10^6	42.81	21.58	10.98
10^7	4296	2145	1072

Tab.1: N-body on MARCONI A1 (Broadwell CPU)

	KNL Intel Phi 7250 @1.4 GHz 68 cores MARCONI A2		
N-body	8 nodes (sec.)	16 nodes (sec.)	32 nodes (sec.)
10^6	110.34	57.20	30.19
10^7	10805	5405	2705

Tab.2: N-body on MARCONI A2 (Knight-Landing CPU)

	SKL Intel Xeon 8160 @2.1 GHz 24 cores MARCONI A3		
N-body	8 nodes (sec.)	16 nodes (sec.)	32 nodes (sec.)
10^6	22.95	11.72	6.03
10^7	2478	1208	617

Tab.3: N-body on MARCONI A3 (SkyLake CPU)

	SKL 2 x Intel Xeon 8160 @2.1 GHz 24 cores CRESCO 6		
N-body	8 nodes (sec.)	16 nodes (sec.)	32 nodes (sec.)
10^6	23.85	12.5	6.62
10^7	2361	1181	590
	64 nodes (sec.)	128 nodes (sec.)	
10^6	3.3	1.93	
10^7	296	150	

Tab.4: N-body on CRESCO6 (SkyLake CPU)

6 Conclusions

CRESCO6 benchmarks tests has shown good results comparing with similar HPC systems. The new facility is already ready for an upgrade that will double its own peak power computing.

References

[1] Cineca: https://www.cineca.it/en

Author Index

ENEA
Promotion and Communication Service

www.enea.it

Printed at the ENEA Technographic Laboratory – Frascati

November 2018